Atomic layer deposition of alumina and zinc oxide for optoelectronic devices

Claire Hannah Burgess

Department of Materials, Imperial College London
2016

Declaration

The work presented in this PhD thesis was carried out between September 2012 and September 2016 in the Department of Materials, Imperial College London. The research is my own, and contributions from other people and sources have been appropriately cited. Elements of Chapter 2 were included in the paper: C. H. Burgess, "Review of tailoring ZnO for optoelectronics through atomic layer deposition experimental variables", Materials Science and Technology, DOI: 10.1080/02670836.2016.1198578, and data in Chapter 7 was presented at the 16th International Conference on Atomic Layer Deposition (ALD2016) in a talk entitled "The role of orientation and composition of ALD ZnO on perovskite photovoltaics". All the experimental work in this thesis was carried out by me, except for the following measurements:

- Kelvin probe and integrating sphere UV-visible spectroscopy measurements (Maurizio Morbidoni)
- fabrication and testing of organic solar cells (Jiaqi Zhang)
- optical microscope imaging (Stefan Bachevillier)
- deposition of perovskite layers, and fabrication and testing of solar cells (Tian Du)
- Cu_2ZnSnS_4 nanoparticle growth, and fabrication and testing of photocathodes (Xuemei Zhang)

Acknowledgements

I would firstly like to acknowledge funding for this research from the Engineering and Physical Sciences Research Council (EPSRC) through the Imperial College Doctoral Training Award scheme. I would like to thank my supervisor Martyn McLachlan for guidance and support throughout my PhD studies.

The building of the ALD system could not have been done without help and guidance from other people. Thanks to my dad for help building the framework and to Ev Donchev for leak testing the ALD. Also thank you to the researchers at Tyndall National Institute and those I met at the Baltic ALD and international ALD conferences for their advice on setting up an ALD system.

I would like to thank the people I have worked with during my PhD and made it such a great experience, including those who have contributed to the work in this thesis: Xuemei, Maurizio, Tian, Jiaqi, Stefan; other people I have worked and who have helped me along the way: Richard, Freddy, Andreas and Xueting; the other members of the McLachlan group: Rob M, Yoann, Jorge, John, Joe, Kirsty, Rob H, Becky, Bob, Jaspreet, Ahmed; and to fellow PhD students Rob W, Dan, Caro and Jasvir.

I would like to thank my parents and brother for their huge support, and my friends for their encouragement, especially Fran, Sarah, Sammy D, Clare, Emma, Jenny M, Tom, Rob, Jenny C, Daniel, Dean, Valentijn, Junko and Ashley. And big thank you to Shaun for his incredible help and love throughout my PhD.

Abstract

Atomic layer deposition (ALD) uses surface reactions of gaseous precursors to grow thin films of materials. Exceptional uniformity and thickness control is possible due to the separation of the different precursors, allowing each to undergo reactions with substrate surface groups until, on chemisorption of a complete monolayer, self-termination occurs. Purging after the precursor release removes by-products and remaining precursor, ensuring that the material growth proceeds layer-by-layer. These and other benefits such as relatively low deposition temperatures, and the ability to coat large areas and complex 3D surfaces, have led to ALD being a key and increasingly popular technique in research and industry.

One area of application of ALD is in optoelectronics; this thesis describes the design and construction of an ALD system for research into optoelectronics, including thin film transistors, solar cells and photoelectrodes. A conventional, thermal ALD system was custom-built, and the deposition of Al_2O_3, ZnO and Al doped ZnO (AZO) using trimethyl aluminium, diethyl zinc and H_2O was characterised through techniques including X-ray diffraction, UV-visible spectroscopy, cross-sectional TEM, resistivity and Hall measurements. The growth per cycle and the properties of the materials were consistent with literature values, confirming self-saturating ALD was achieved. The conductivity of ZnO was seen to increase with temperature and doping, and the ZnO (wurtzite crystal structure) out-of-plane preferential orientation was increasingly [100] at lower temperature and with higher Al content. Reducing purge times below 10 s resulted in a slight increase in ZnO film thickness due to a chemical vapour deposition contribution to growth, but the more significant effect was a reduction in mobility and carrier concentration and a higher hysteresis when the ZnO was employed as a thin film transistor channel layer.

The crystal orientation of ALD ZnO deposited at 100 °C was investigated on different substrates such as amorphous quartz, polycrystalline ITO and single crystal sapphire. A method of using multilayers of [100] oriented AZO, ultrathin Al_2O_3 (<20 ALD cycles) and ZnO was developed as an alternative way to control the ZnO orientation whilst ensuring compatibility with devices. A dependency on ZnO crystal orientation was seen for the rate of $CH_3NH_3PbI_3$ perovskite degradation when $CH_3NH_3PbI_3$ was deposited on top of an ALD ZnO layer. The stability of $CH_3NH_3PbI_3$ was studied by temperature controlled XRD and film colour change; Al doping of ZnO reduced degradation rates. High aspect ratio track-etched membranes were coated by ALD to produce nanotubes, and Cu_2ZnSnS_4 nanoparticle films were coated with Al_2O_3 layers which increased stability as a photocathode. The ALD system built and the principles explored for tuning material properties presented in this thesis can be used to further optimise optoelectronic devices in the future.

Contents

List of Figures

List of Tables

Chapter 1

Introduction

The majority of electronic devices have historically been based on Si single crystals as this technology has proved very successful and the manufacturing processes are now well developed. There are, however, disadvantages and limitations to this technology. Silicon itself has an indirect bandgap, resulting in thick layers needed for applications such as solar cells, and the mobility of electrons is relatively low compared to other materials. The processing requires high temperatures for the formation of the high quality single crystals necessary to obtain good device performance, resulting in several years of operation being needed for the energy cost in manufacturing solar cells to be returned. The design of devices is also limited by the rigidity and opacity of the material, so flexible, transparent electronics are not possible. Due to these limitations there is increasing demand for, on the one hand, the development of devices that can compete with the Si technology through e.g. better performance or reduced processing costs, and, on the other hand, for devices which can be used in otherwise unachievable, novel applications. There is a rise in newer technologies such as organic electronics being used in commercial products, and further research into the myriad of other opportunities is crucial. The research in this thesis is focused on atomic layer deposition (ALD), a technique for growing thin layers of materials which can be applied in many devices.

ALD, having already been used in manufacturing for a number of years, e.g. silicon chips and luminescent displays, is becoming increasingly important, with growth in the industry predicted and orders for equipment rising. The technique has also proven key in research, as the control offered by the layer-by-layer deposition enables detailed investigations into the performance-limiting factors in devices. Two of the most popular and successfully employed materials grown by ALD are ZnO and Al_2O_3, using diethyl zinc, trimethyl aluminium and H_2O precursors. Using this material combination, conducting, semiconducting and insulating layers can be formed, allowing use in a wide range of applications. These materials and their employment in several different devices are investigated in this thesis.

Chapter 2 discusses the fundamentals of ALD, the material properties of ZnO and Al_2O_3, and examples of their use in devices. The fabrication and characterisation details used in this work are included in Chapter 3, and the design and construction of the ALD system is described in Chapter 4. The system-specific calibration of Al_2O_3, ZnO and Al doped ZnO (AZO) deposition is presented in Chapter 5 along with an investigation into the effect of purge time variation on the performance of thin film transistors and organic solar cells with ALD ZnO layers. In Chapter 6 the control of ZnO crystal orientation using different substrates and multilayers is explored, and in Chapter 7 some of these techniques are used to investigate the dependence of $CH_3NH_3PbI_2$ perovskite stability on underlying ZnO-based electron transport layers for solar cells. Finally, investigations into coating high aspect ratio substrates, i.e. nanoparticle thin films for photocathodes and track-etched membranes, are presented in Chapter 8 and the conclusions from this work are given in Chapter 9. References are listed in the Bibliography and there is also an Appendix with further details on the ALD system constructed.

Chapter 2

Background

Atomic layer deposition (ALD) is a relatively new growth technique; it was invented separately by researchers in the Soviet Union and Finland in the 1960s and 1970s respectively.[19–21] The drive to grow high quality, pin-hole free layers for use in luminescent displays led the researchers in Finland to develop ALD reactors for manufacturing. Research then progressed into growing thin films of a wide range of different materials and gradually more potential applications arose which require the unique combination of uniformity and conformality provided by ALD. As devices became miniaturised ALD became of interest in silicon chips, and the ability to passivate Si solar cells also raised the status of this technique in industry,[22,23] leading to the used of ALD in multiple manufacturing processes.[24] Accompanying the industrial interest in ALD, the involvement of ALD in research has also increased. The yearly number of publications on ALD was around 150 from the 1990s until 2001,[4] then it rose hugely over the subsequent years reaching 800 per year in 2010,[1] with figures still increasing year-on-year. Optoelectronics is an area where ALD has been used to investigate device performance and where there is potential for further improvements. This chapter outlines how ALD occurs, why ALD is such an invaluable deposition technique, how it compares to other techniques, the materials deposited for this thesis (ZnO, Al_2O_3) and how their properties can be tailored for use in optoelectronic devices.

2.1 Fundamentals of ALD

ALD can be used to deposit a wide range of materials but for each material growth variables have to be tailored to obtain the best properties. Figure 2.1 shows the range of binary and elemental materials that had been achieved by 2011,[1] and researchers are regularly reporting new precursor options as well as new materials. Ternary and quaternary compounds can also be deposited[1] and along with hybrid materials such as ZnO:hydroquinone.[25]

ALD growth is achieved with the use of two or more gaseous precursors to grow a material through separated surface reactions. The deposition of ZnO using diethyl zinc and H_2O precursors in a conventional, thermal ALD reactor will be used as an idealised example here. A substrate with appropriate surface groups e.g. glass with polar –O–H groups is loaded into an ALD reaction chamber. The chamber is under vacuum with a continuous inert gas flowing e.g. N_2, resulting in a viscous

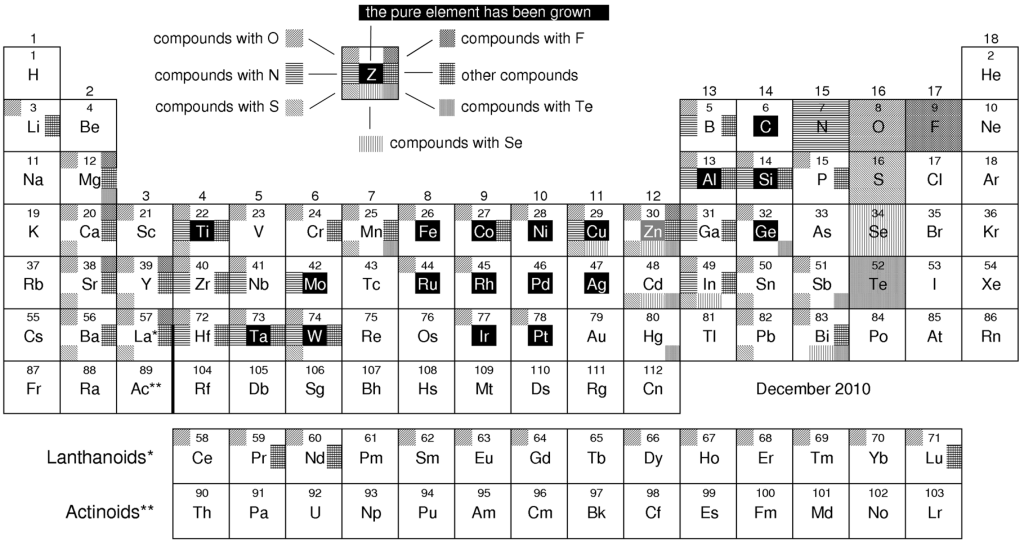

Figure 2.1: Diagram demonstrating the binary compounds which had been grown by ALD up to January 2011. The shading indicates the possible elements and oxide, nitride, sulphide, selenide, telluride and fluoride compounds. Reprinted with permission from reference,[1] ©AIP Publishing LLC 2013.

gas flow regime (pressure >0.3 mbar).[26] After an initial purging and temperature equilibration period, ALD cycles are begun (Figure 2.2 shows a schematic). Firstly, diethyl zinc (DEZ) is released into the chamber by opening a valve connected to a cylinder of liquid DEZ precursor; release times (the valve open times) for DEZ and H_2O are often <0.5 s. The DEZ molecules are carried through the chamber by the N_2 flow. Whilst in the chamber the DEZ is able to react with the surface of the substrate loaded inside. The DEZ molecules react with the surface groups e.g. –O–H* (where the * denotes the surface species), forming bonds with oxygen, releasing C_2H_6, and leaving a surface consisting mainly of $–O–Zn–CH_2CH_3*$ species. The reaction of DEZ with the surface is self-terminating because DEZ does not react with $–CH_2CH_3*$, so no further change occurs once the all original compatible surface groups have been reacted with (excluding those blocked by steric hindrance). Purging with the N_2 flow follows to ensure all remnant DEZ and by-products are removed from the chamber before the next precursor exposure. H_2O is then released, which is able to react with the surface $–Zn–C_2H_5*$, releasing ethane and leaving a mostly –Zn–O–H* surface on self-saturation. Purging follows, and this sequence of DEZ-H_2O release and purging can be repeated, the number of cycles directly controlling the thickness of the ZnO produced. This idealised description of ALD is equally applicable to other binary materials, and a monolayer or less of the material is deposited each ALD cycle, typically ≈ 0.2 nm/cycle ZnO with DEZ-H_2O and ≈ 0.1 nm/cycle Al_2O_3 with trimethyl aluminium (TMA)-H_2O .

To obtain ternary or doped materials additional precursors are generally needed; Al doped ZnO (AZO) is of particular interest in this thesis. In ALD, the selected dopant source (e.g. metal or oxygen source) usually needs to be capable of ALD growth with the opposite precursor (e.g. oxygen or metal source respectively). One method of doping is to mix the dopant precursor vapour with the usual precursor vapour in a chosen ratio. They can be mixed in the gas phase[27] or come from a mixed

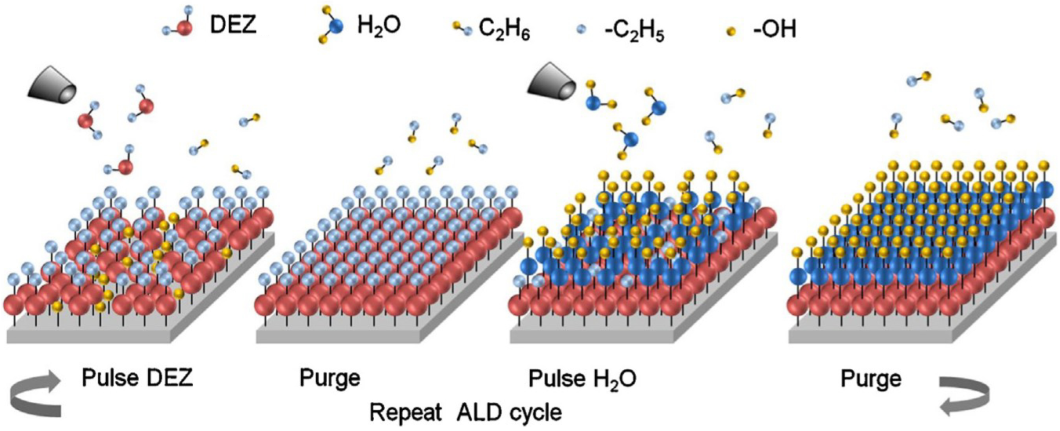

Figure 2.2: Schematic showing the DEZ release – purge – H_2O release – purge sequence of an ALD cycle for depositing ZnO. Reprinted with permission from reference,[2] ©Elsevier 2014

source e.g. NH_4OH (source of NH_3 and H_2O).[28] This is known as co-doping. Alternatively, delta-doping can be used, where a cycle of dopant precursor is included in the deposition sequence after a chosen number of regular cycles. This method is commonly used in ALD as it has proved quite successful and allows flexibility of composition (adjusted through doping cycle ratio) and the precursors can also be used separately for other material depositions. For AZO the supercycle sequence often used is (DEZ-H_2O) $\times x$, (TMA-H_2O) $\times 1$ where x is on the order of 10s, which is repeated to produce the desired thickness. There are, however, problems which sometimes arise with delta-doping, as the deposited material can have a laminar nature, with localised layers of dopant.[29,30] To overcome this, several techniques have been explored: precursors with larger steric hindrance can be used to reduce the density of dopant in a layer;[31] timings of the deposition can be adjusted[32] e.g. TMA release time;[29] or a chemical can be released before or after dopant precursor to reduce the amount chemisorbed,[33,34] for example release DEZ of before TMA reduces the density of Al as the DEZ acts as a sacrificial layer protecting the underlying material from etching by TMA.[35] Note that with both co-doping and delta-doping the composition of the film is often different from the ratio of dopant precursor used due to differences in reactivity,[36] exchange reactions[37] etc.

The gaseous nature of the precursors used in the ALD deposition and the self-termination of the surface reactions give ALD the unique ability of being able to deposit films with subnanometer thickness control over surfaces irrespective of whether they are planar or have a convoluted, 3D geometry. Some ALD reactions, including generally those of DEZ-H_2O and TMA-H_2O, show behaviour near to the ideal discussed above. However, there is a series of factors that need to be tuned to obtain this ALD behaviour in order to get the optimal material properties and the most repeatable films. Different precursors and substrates affect the nature of the material grown, and optimum deposition conditions tend to be fairly reactor specific. The material thickness deposited per ALD cycle, known as growth per cycle (GPC), is often used as the measure of whether ALD is occurring properly as it should be quite consistent for a given combination of precursors. These areas are discussed in Section 2.3.

2.1.1 ALD reactor types

There are many types of ALD reactors, some designed for coating of specific substrates or for reaction studies, others for general material deposition. The ALD system custom-built for this project, described in detail in Chapter 4, is conventional-type, operating under vacuum and designed for deposition of materials for devices. In conventional ALD reactors, deposition is possible in two different pressure regimes: molecular flow (high vacuum, mean free path of molecules is greater than chamber size) is more compatible with high vacuum in-situ analysis techniques, whereas viscous flow (usually 0.3 mbar $>$ pressure $>$ 10 mbar) allows good precursor diffusion for porous substrates and quick purging times for higher deposition rates. Reactors can be fitted with plasma and ozone sources, which can be used in ALD deposition cycles, e.g. DEZ-O_2 plasma for ZnO ALD. Having a plasma source increases the variety of materials that can be deposited as there are many precursors that are only compatible with plasma reactants, and lower substrate temperatures are often possible.

The study of the reactions occurring during ALD is very important for understanding and improving the deposition processes, and so there are many reports of techniques for this in the literature. Some researchers use analysis systems that can be installed in general ALD systems, such as electrical conductivity measurement set-ups[38] and quartz crystal micro-balances for measuring mass changes,[39] whereas others have completely designed ALD reactors around the analysis method. Interesting examples include reactors with windows for ellipsometry measurements,[40] quantitative measurements of amounts of precursor released,[41] and portable systems compatible with synchrotron analysis.[42]

(a) Cross-flow ALD reactor

(c) Linear AP-SALD reactor

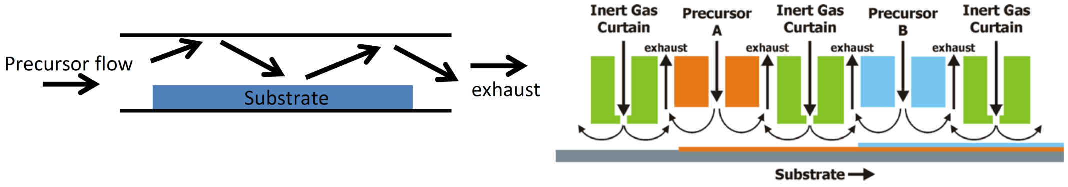

(b) Perpendicular flow ALD reactor

(d) Roll-to-roll AP-SALD reactor

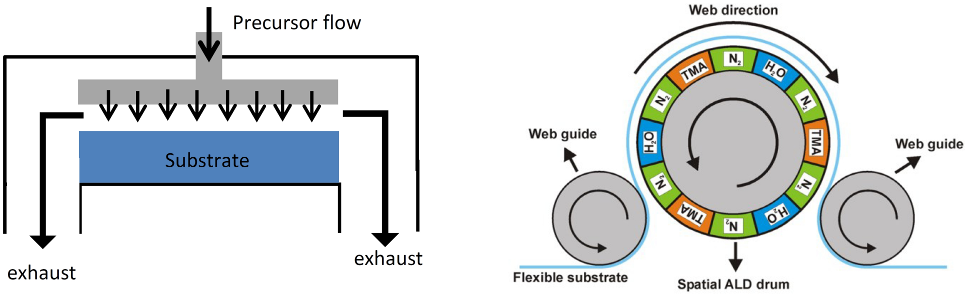

Figure 2.3: Example diagrams of ALD reactors. (a),(b) show the conventional cross-flow and (shower-head) perpendicular reactor designs. AP-SALD reactors are shown in diagrams (c),(d), reproduced with permission from reference[3] ©2012 AIP Publishing LLC

Alternatively, reactors have been specifically designed for the material and substrate they are coating. For example, when precursors with unusual risks are used, e.g. H_2S for metal sulphide deposition, the parts and materials in a general ALD system may not be compatible.[43] In industrial manufacturing, large batch reaction chambers are often favoured as they increase the wafer-per-hour throughput.[44] Alternatively, high throughput ALD can be achieved using an increasingly popular ALD reactor type known as atmospheric pressure spatial (AP-S)ALD.[3,27,45] The idea of spatial ALD has existed from around the time of ALD invention, and originally it involved moving a substrate between different zones of precursor separated by an inert gas so the substrate precursor exposures were effectively separated in space rather than time (i.e. in location rather than with purging periods between precursor releases).[3] More recently, open-air AP-SALD systems have enabled ALD to become compatible with continuous manufacturing processes, rather than being limited to batch. AP-SALD uses a deposition head consisting of a series of channels which are each constantly releasing precursor vapour or inert gas, or pumping away the gases. A substrate moves across the deposition head in very close proximity to it, and through this movement each area on the substrate is sequentially exposed to a first precursor (e.g. DEZ) followed by an inert gas curtain, then a second precursor (e.g. H_2O) followed by another inert gas curtain, etc. Rapid deposition rates are achievable using AP-SALD (>1.2 nm/s has been reported) compared to conventional ALD, which is usually limited by purging time (<0.1 nm/s, often <0.01 nm/s). Many different variations of AP-SALD reactors have been developed, including linear (for continuous lines of substrates or large area substrates), roll-to-roll (for continuous, flexible substrates) and rotary (for wafers) reactors, and this technology enables ALD to be a competitive process in the manufacturing of many types of optoelectronic devices. Many other ALD reactors have been designed to broaden the applicability of ALD even further,[46] including fluidised-bed reactors for deposition on powders.[47] Figure 2.3 demonstrates the appearance of some of the described reactors.

2.1.2 Comparison with other deposition techniques

There are many different thin film growth techniques which can be used instead of ALD. The options include other chemical deposition techniques where liquids and gases undergo chemical reactions to form a new material on substrate. Examples of this include:

Chemical vapour deposition (CVD) - similar to ALD, but without separated, self-limiting reactions (sometimes ALD precursors can be used).[27] Gaseous reactants are released into a chamber under vacuum and react with the surface of a heated substrate, depositing material.

Spray pyrolysis - sometimes considered to be a form of aerosol-assisted CVD. Droplets of a precursor solution are sprayed at a heated substrate, the solvent evaporates and the chemicals pyrolyse on their approach to the substrate and the resulting material is deposited on its surface.

Sol-gel - reactant solution is coated onto a substrate, often using spin coating, and as the solvent evaporates an interconnected network of the desired material gradually forms (post-deposition annealing usually required).

Alternatively, physical deposition techniques can be used, which involve a source of the desired material composition (or multiple sources consisting of the elements needed) from which small amounts of material are physically transferred and deposited onto the substrate surface. Types of physical deposition include:

Molecular beam epitaxy (MBE) - under the ultrahigh vacuum conditions used, atoms and molecules from the material sources travel unscattered through the chamber until they impinge on the substrate surface, resulting in high purity, epitaxial films.

Pulsed laser deposition (PLD) - a high energy laser ablates material from a target (the source) and the plume travels through the vacuum chamber and deposits material on the substrate.

Sputter deposition - particles collide with a target, causing atoms to be ejected from it, which are then deposited on the substrate across from the target in the vacuum chamber.

Evaporation - a source is heated in a boat under vacuum and the material which evaporates from it is deposited on a substrate located above.

These techniques all offer different advantages. While ALD is more expensive than sol-gel and spray pyrolysis and requires more complicated equipment, it can offer higher purity films and materials can be grown at lower temperatures and without post-deposition annealing. ALD also uses lower temperatures than CVD, but has a slower growth rate. ALD does not produce films with as high purity as MBE, PLD, sputter and evaporation, but it is scalable to very large areas, can be used in continuous manufacturing processes and is less sensitive to variations in e.g. background gas pressure than PLD and sputtering. Stoichiometry is more complicated to control with ALD than physical vapour deposition techniques, but different compositions of materials are easily deposited using variations in precursor cycles instead of fabricating new targets of different compositions.

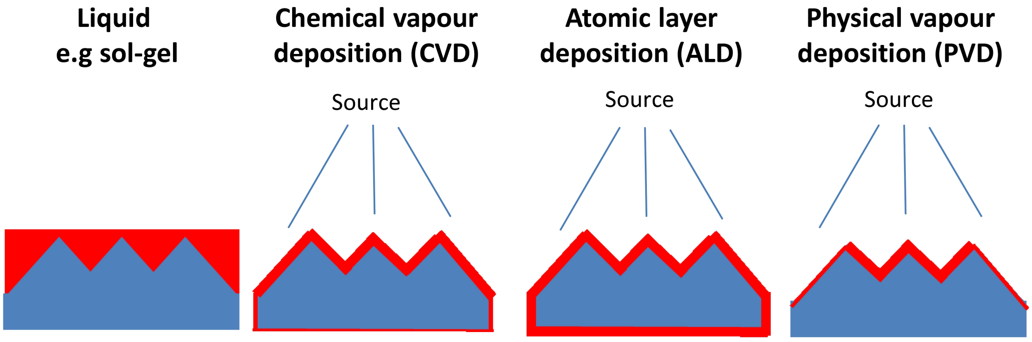

Figure 2.4: Diagram demonstrating the difference in coatings (in red) on a non-planar substrate (in blue) produced by different thin film deposition methods.

However, in addition to these comparative merits, ALD has certain capabilities that cannot be matched by any other deposition techniques. In ALD gaseous precursors and self-saturating reactions allow extremely repeatable coatings, with subnanometer thickness control over an entire substrate surface of any area and with any structure from planar to high aspect ratio features.[48] Figure 2.4 illustrates this ability.

2.2 Alumina and zinc oxide

Alumina is a wide bandgap, insulating material. There are different polymorphs of Al_2O_3, for example single crystal Al_2O_3 (sapphire) of hexagonal crystal structure is a commonly used substrate for epitaxial growth (used for ZnO growth in Chapter 6 and 7). However, Al_2O_3 grown by ALD at temperatures below 500 °C is almost always amorphous.[1] The optical bandgap of amorphous ALD Al_2O_3 is 6.4 eV which is lower than the crystalline bandgap (8.8 eV) but still very wide so no parasitic absorption occurs when employed in solar cells.[49]

Applications of relatively thicker Al_2O_3 layers, especially by ALD, include diffusion barrier layers, where the amorphous nature of the Al_2O_3 is generally beneficial as it results in a complex diffusion path;[50] in polycrystalline films the grain boundaries have a defective crystal structure so are often pathways of more rapid diffusion.[51] The amorphous, pin-hole free nature of Al_2O_3 is also advantageous for its use as a dielectric gate oxide layer in thin film transistors (TFTs), and its dielectric constant (7-9)[52] is higher than that of SiO_2 (3.9),[53] allowing thicker films to be used (the equivalent oxide thickness is relatively low).[54] Al_2O_3 has been found to be effective at passivating silicon surfaces, reducing recombination in silicon solar cells. This is due both to passivation of the surface defects by the hydrogen incorporated in the ALD films and to the negative charge formed at the interface, linked to the aluminium vacancies and oxygen interstitials in the Al_2O_3.[49]

Al_2O_3 layers can also be used for ultrathin interlayers in devices, which is the main area of interest in this project. The detailed description of how the devices studied in later chapters specifically function is included in Section 3.2. Generally $<$ 2 nm layers are required in optoelectronics so the Al_2O_3 does not provide too much of a barrier to current flow, as bulk films have a resistivity on the order of 10^{16} Ωcm.[55] Ultrathin Al_2O_3 layers are generally used to passivate surface states in devices, form a protective coating and to act as a tunnelling layer between interfaces with high recombination rates e.g. semiconductor absorber/metal electrode interfaces. A 3 TMA-H_2O cycle layer deposited at the interface between p-type Si and ZnO reduced recombination in the diode,[56] and ultrathin Al_2O_3 layers passivated surface trapping states on hematite photoanodes[57] and reduced recombination in perovskite solar cells.[58] Al_2O_3 has acted as both an electron selective[59] and a hole selective layer[60] on indium tin oxide (ITO) and gold electrodes in organic and perovskite solar cells. In quantum dot[61] and dye sensitised solar cells[62,63] Al_2O_3 blocked recombination, and also a few TMA-H_2O cycles aided dye attachment.[64] ZnO electron transport layers were protected from degradation with perovskite absorbers by Al_2O_3 interlayers, which can also protect perovskite from moisture.[65] Additionally, TMA-H_2O beneficially reduced Cu_2S carrier concentration and improved the nucleation of further ALD layers on top.

Zinc oxide is a semiconducting material which is transparent to visible light due to a bulk bandgap of around 3.37 eV.[66] ZnO deposited by ALD has a hexagonal, wurtzite structure and is generally highly crystalline even at the typical, low ALD deposition temperatures of 85 - 250 °C. ZnO is intrinsically n-type and, when deposited by ALD, has a charge carrier concentration of around 10^{18} - 10^{19} cm^{-3}. The origin of the generally n-type nature is not yet clear,[66] but in ALD ZnO films higher electron concentrations are linked to increased oxygen deficiency.[67,68] ZnO deposited by a variety of techniques is used widely as a semiconducting layer in devices, and ALD ZnO layers have had success as electron transport layers (ETLs, also known as hole blocking layers), TFT channels and buffer layers in solar cells.[3,12,23,27,69–74] Advantages over rival materials include non-toxicity and higher transparency (compared to CdS),[75] higher mobility (compared to TiO_2),[76] elemental abundance and reasonable stability. However, surface states on ZnO are complicated, in part due to polarity in the [001] crystal lattice direction,[77] which can sometimes lead to poorer charge transfer characteristics compared to e.g. TiO_2.[76] Lower carrier concentrations tend to be favourable for ALD ZnO due to reduced interface recombination.

ZnO can be doped with various elements to change the electrical behaviour and band alignments for specific applications. Doping with Mg, Sn and S has been used to adjust the band alignment through orbital hybridisation, and has been used to reduce recombination at interfaces in e.g. copper indium gallium selenide solar cells where the negative conduction band alignment of undoped ZnO is unfavourable.[78] The electrical and crystal properties of these doped films are also affected. To lower the intrinsically high carrier concentration in ALD ZnO, doping with N has been reported, resulting in improved switching in transistors[79] and reduced recombination in certain solar cells compared to undoped ZnO.[80,81] For transparent conducting applications, ZnO is often doped with Al (AZO). This can be carried out with the same precursors used for the Al_2O_3 and ZnO depositions, so is of particular interest for this project. Al^{3+} substitutes onto a Zn^{2+} site, donating an electron, which raises the carrier concentration and conductivity of the film. AZO has frequently been deposited by ALD,[29,30,35,43,82–88] using a variety of doping sequences as discussed in Section 2.1. The lowest resistivity of AZO tends to occur at doping levels of 2 - 7 % AZO, beyond this point the Al content is above the solid solubility limit.[12,31] AZO is often suggested as an alternative, more earth abundant transparent conductor with which to replace ITO, and additionally tuning the ALD AZO work function and band alignment through doping has lead to use as an effective electron transport layer.[89–91]

The range of material properties available when depositing ALD Al_2O_3, ZnO and AZO, and their reported wide applicability in optoelectronic devices were the motivation and guidance for the investigations in this thesis. To be able to obtain good quality layers which can then be incorporated into devices, ALD-specific variables need to be considered and optimised. These general ALD requirements are described in the following section along with specific effects of tuning the variables on ZnO and Al_2O_3 properties.

2.3 Tailoring ALD deposition variables

When specific materials are chosen to be deposited, in this case ZnO, Al_2O_3 and AZO, the choice of precursors is important as the deposition conditions and film properties will be affected. Saturated ALD growth should be very reproducible between different deposition systems, but for each new precursor and substrate combination used in an ALD system a series of variables need to be tuned. Growth per cycle (GPC), i.e. amount of material deposited each ALD cycle, is frequently used as the guide for variable optimisation, and saturated ALD at a specific temperature should have a GPC consistent with literature values for the precursors. The steps for optimising ALD are outlined below, along with how changing these variables can affect ZnO and Al_2O_3 films, especially in devices.

2.3.1 Precursors

There are a variety of successful types of ALD precursor, and the development of new precursor chemicals is a popular and in-demand area of research. To be viable for ALD, precursors have to meet the following conditions:[92]

- Adequate vapour pressure which, generally in research, would be $\gtrsim 0.1$ mbar for a new precursor.[92] Heating precursor sources or bubbling carrier gas through liquid precursors can raise the amount of precursor vapour released.
- No self-decomposition of the precursor, as the deposition reactions would no longer be self limiting.
- A fast and complete reaction of the precursor with surface groups.
- No etching of the substrate or deposited material by the precursor or the by-products, and the by-products must be inert and volatile.

In addition to these requirements for a precursor to be functional, other properties such as purity, synthesis, toxicity, safety of handling and cost are important.

Solid, elemental sources were initially used in ALD but high temperatures were needed to obtain adequate vapour pressures. Metal halide sources were also popular as they are highly reactive and thermally stable, however the HCl by-product is corrosive and can etch the deposited film and equipment. Organometallics are one of the alternatives for metal oxide deposition, and they are very reactive due to the metal–carbon bond. Other alternative metal organic precursors have an e.g. metal–oxygen bond so are more stable and can be used for higher temperature depositions. Organometallics, however, are very popular in ALD research and can produce high quality films at low temperatures which is favourable for optoelectronics as flexible and temperature-sensitive substrates are often desired. The organometallics used in this project are diethyl zinc ($Zn–(CH_2CH_3)_2$) and trimethyl aluminium ($Al–(CH_3)_3$), which are pyrophoric liquids. Deposition using both is easily achievable as they have high vapour pressures (21 mbar[93] and 15 mbar[94] at room temperature respectively), are very reactive with surface groups under ALD conditions, and produce films with low levels of contamination and a high GPC (≈ 0.2 and 0.1 nm/cycle respectively).

In devices there has not been much variation in choice of Zn precursor. Other than DEZ, dimethyl zinc has been reported in devices with similar results to DEZ,[74] but DEZ is better characterised and is likely to remain the most popular Zn precursor.[12] An alternative to trimethyl aluminium (TMA) for the deposition of Al_2O_3 is dimethylaluminium isopropoxide (DMAI, $Al–(CH_3)(O–(CH(CH_3)_2))$) which is not pyrophoric and can be used under similar conditions to TMA to produce good quality films.[49,95] DMAI has a larger steric hindrance, which is an advantage in AZO deposition as higher doping efficiencies are achieved due to the disperse Al atoms,[31] but the GPC is lower for Al_2O_3. TMA has been the more widely used precursor and was chosen on balance.

The oxygen precursor selected for ZnO and Al_2O_3 ALD in this project was H_2O. It has a high vapour pressure (31 mbar at room temperature),[96] produces high quality materials at low temperature in combination with DEZ and TMA, and is safe, inexpensive and readily available. There are many alternatives to H_2O, such as H_2O_2, N_2O, O_2 plasma, O_3 etc.[1, 12] Plasmas result in lower film contamination at low deposition temperatures due to higher oxidative power,[97] and O_3 can be more easily purged than H_2O for e.g. batch Al_2O_3 depositions.[49] ZnO deposited using O_2 and H_2O plasma has lower carrier concentration which proved to be beneficial for channel layers in thin film transistors compared to DEZ-H_2O,[98] however solar cells with electron transport layers fabricated using DEZ-O_2 plasma were not improved due to the increased defects in the films.[99] There are cases were alternative precursors have excelled in devices, such as H_2O_2 which was used in controlling the oxidation state of copper to form an improved Cu_2O-ZnO solar cell heterojunction,[100] and O_2 which proved more compatible for ZnO deposition on top of water-sensitive organic-inorganic perovskite for use in a hybrid LED.[101] However, H_2O was chosen, as it is easily incorporated in an ALD system, has well established deposition properties and there have been good performances reported when it is used as a precursor for both ZnO and Al_2O_3 in a wide range of optoelectronic devices, from layers in TFTs to solar cells and photoelectrodes.

2.3.2 Release and purge times

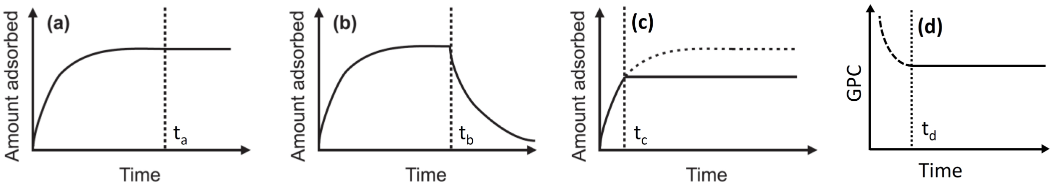

Figure 2.5: (a) Graph representing the amount of precursor adsorbed during a precursor release of time t_a. The chemisorption is irreversible. (b) The amount of precursor adsorbed with release time t_b, where the adsorption is reversible. (c) The amount of precursor adsorbed with release time t_c, which is too short for reaction self-saturation. (d) The GPC with purge time, where t_d is the minimum time needed for true ALD to occur. (a)-(c) adapted with permission from reference,[4] ©AIP Publishing LLC 2005.

The release and purge times need to be tuned to obtain optimal saturated ALD growth and quick deposition rates. Release times need to be long enough so that sufficient precursor is present to ensure chemisorption self-saturation over the entire substrate surface. Figure 2.5(a) demonstrates the Langmuir isotherm behaviour for irreversible chemisorption, which is required for ALD, whereas if the adsorption is reversible, the behaviour in Figure 2.5(b) occurs and repeatable, high GPC film growth is not possible. If subsaturation release times are used then films may be non-uniform and will have a lower GPC (Figure 2.5(c)), but if long release times are used unnecessarily there will be a large amount of precursor wastage. For DEZ-H_2O and TMA-H_2O in the literature, generally short release times are reported due to the high vapour pressures and reactivities of the precursors, but the exact times are reactor dependent. At very low temperatures (e.g 58 °C) there may still be slight increases in GPC with prolonged release times due to the much longer reaction completion times, known as "soft saturation".[52] In situations when high aspect ratio substrates are used, the precursor exposure time may have to be extended by using a valve to isolate the reaction chamber from the pump, retaining the precursor inside to allow diffusion into the substrate so saturation occurs on all surfaces. This was necessary, for example, when coating mesoporous TiO_2 with ultrathin layers of Al_2O_3 for dye stabilisation.[64]

Figure 2.5(d) demonstrates the affect of purge times on ALD deposition. The shorter purge times are, the quicker a deposition can be completed, but if precursors and by-products are not completely removed from the reaction chamber before the next precursor arrives, gas phase reactions result. This adds a CVD contribution to growth and reduces film uniformity and repeatability. Generally the shortest purge times possible are used in ALD, however in ZnO deposition varying purge times beyond those needed to avoid CVD growth has also been seen to have an effect on electrical properties. The very short (tens of milliseconds) purge times possible in AP-SALD have produced ZnO with much lower carrier concentrations, which improved switching performance in TFTs[102] and is promising for solar cells.[103] However, with the conventional ALD system used in this project these purge timescales are not possible; times on the order of seconds are necessary. With extended purge times, changes in film composition have been reported due to changes in the amounts of –OH groups.[32,104] Prolonged purging at 90 °C improved mobility and thus organic solar cell performance,[104] so this is an aspect should be studied to obtain the best films for ZnO incorporated into devices.

2.3.3 Number of cycles, substrates and film nucleation

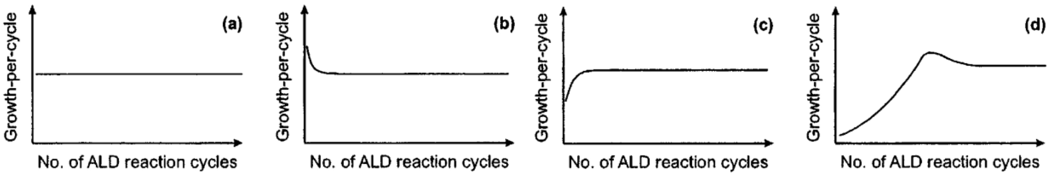

Figure 2.6: Graphs illustrating GPC trend with (a) linear, (b) substrate enhanced, (c) substrate inhibited and (d) island growth nucleation behaviours. Reproduced with permission from reference,[5] ©AIP Publishing LLC 2005.

The GPC of an ALD film should have a steady-state value at high cycle numbers as the ALD material e.g. Al_2O_3 is being steadily deposited onto a reasonably unchanging Al_2O_3 surface. The GPC at the start of the deposition, however, is very dependent on the substrate surface (Figure 2.6). The growth rate might be identical to the steady state growth which could indicate similar surface species and density. In other cases there is substrate enhanced growth, such as Al_2O_3 on ITO or Cu_2O where oxygen diffusion out of the substrate leads to high initial GPCs.[105,106] Often, there is a lower GPC initially (substrate inhibited growth) due to lower density of surface groups or to the less reactive surface species initially formed.[4,107] If nucleation occurs in sparse locations, growth is island type (Volmer-Weber), as has been seen for e.g. ZnO on SiO_2 and Si.[108,109] A low initial GPC will be seen, then GPC will rise as the islands grow and it may become higher than the steady-state GPC as the islands offer higher surface area for deposition. As the islands coalesce the GPC will tend towards the steady state value.

Growth on polymers tends to occur differently compared to dense, inorganic substrates. Sometimes growth can occur at on the surface, but both TMA and DEZ precursors have also been reported to diffuse into polymers, remaining beneath the surface during purging, causing the formation of sub-surface islands of Al_2O_3 and ZnO on the release of the H_2O precursor. Eventually the islands start to coalesce and a complete layer of oxide is formed on the polymer surface. This layer blocks any further diffusion into the polymer and growth proceeds at the steady-state rate.[110,111] The diffusion of ZnO into organics and the reaction with specific polymer groups has been used as a tool to map bulk heterojunctions to aid understanding in organic solar cells.[112] ZnO has also been deposited on organic poly(3-hexylthiophene-2,5-diyl) (P3HT) layers to form a P3HT/ZnO heterojunction for a hybrid solar cells, although resulting devices had a very low power conversion efficiency.[113] Attempts have also been made to coat similarly challenging organic-inorganic perovskite materials such as $CH_3NH_3PbI_3$. The perovskite was found to degrade with some precursors (e.g. O_2 plasma), and although Al_2O_3 growth is possible using TMA-H_2O,[114] self-saturation of reactions cannot be observed.[115] AP-SALD was able to deposit Mg doped ZnO on top of pervoskite for use in a hybrid LED, and an O_2 precursor was less damaging to the film than H_2O.[101] Using the delay before a continuous film is grown on a polymer is one of the methods available for patterning ALD films.[116] Investigations into AP-SALD ZnO on different films revealed there was a long nucleation delay on polyvinyl pyrrolidone, enabling layers of 200 nm thickness to be grown on uncovered areas and the inhibitor later removed.[117] Whole TFTs have been made using only AP-SALD and inhibitor print patterning which is potentially a good technique for manufacturing transparent flexible electronics.[95]

Al_2O_3 deposited by ALD is generally amorphous whereas ZnO tends to grow crystalline. The substrate on which ZnO grows has an effect on the orientation of crystals (other variables e.g. deposition temperature also contribute). Epitaxial ZnO films can be grown on lattice matched substrates, for applications such as LEDs.[118] The growth conditions e.g. temperature generally need to be tuned carefully to obtain monocrystalline films.[119] Controlling the growth of thin ALD ZnO layers on lattice-matched ZnO nanorods has also proved an effective way to produce different nanostructures through hydrothermal growth.[120]

As discussed in Section 2.2, this project focuses on the use of Al_2O_3 as an ultrathin (<2 nm) functional layer in devices, rather than as a relatively thick layer for dielectric or diffusion barrier applications. In contrast, ZnO in the majority of optoelectronic devices of interest here (e.g. TFTs, solar cells, photoelectrodes) generally has a thickness of around 10 - 150 nm when deposited by ALD or otherwise. In this thickness range the properties of the ZnO may not be representative of bulk values due to surface effects, changing grain boundary concentrations (boundaries are likely to contain traps)[121] and film stress.[30,122] The performance of e.g. a solar cell is sometimes independent of ZnO thickness above a threshold value.[123,124] Alternatively, ZnO thickness can have an optimum intermediate value due to the balance of the increasing series resistance with the increasing hole blocking,[125] shunt resistance[126] or exciton dissociation[127] with thickness. Effects such as optical spacing and Schottky barriers can also have thickness dependent contributions.[128,129]

Beyond typical thickness ranges of ZnO (10 - 150 nm), extra ALD-specific possibilities exist due to the ability to deposit very uniform ultrathin films. Ultrathin ZnO layers have found uses in organic solar cells at interfaces,[130,131] where the behaviour of the initiation of growth has had significant effects on performance. ZnO growth sometimes initialises as crystalline,[132] but in other situations it grows as amorphous for the initial cycles and then undergoes a transition once a threshold thickness is reached, becoming crystalline.[109] In one solar cell, performance was optimum with a ZnO electron transport layer of thickness just greater than the amorphous-to-crystalline transformation point.[133] In a separate study, when there was island growth of ZnO on ITO the solar cell performance was superior with ZnO thickness below coalescence, thought to be due to the traps created at grain boundaries.[134] In addition to material deposition purposes, use of a single or a few cycles of DEZ-H_2O precursors also enabled modification of substrate surfaces, as was discussed for TMA-H_2O in Section 2.2, through control of oxidation states[100,135] and by increasing photocurrents.[136]

2.3.4 Deposition temperature

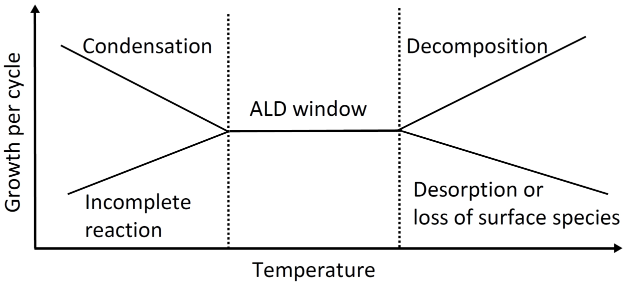

Figure 2.7: Schematic showing typical GPC behaviour with temperature

ALD precursors tend to have a temperature range in which the growth reactions occur optimally and the GPC remains fairly constant; this is known as the ALD window..[137] Figure 2.7 shows a schematic of the general behaviour GPC may not necessarily be constant with temperature within the window, there might be a small increase or decrease due to slight changes in surface species, but outside of the window more dramatic changes tend to be seen. At low temperatures precursors may condense, resulting in non-saturating reactions and thus higher GPC. Alternatively precursors may not have enough energy to complete reactions and the GPC decreases. At high temperatures, an increase in GPC might be seen due to decomposition of precursors or a decrease might occur due to decreasing density of surface species with which to react. TMA-H_2O can be used from 30°C up to 300 °C.[1] There is less hydrogen contamination in films deposited at higher temperature[52] but low temperature layers are also often used and prove effective in optoelectronics with temperature sensitive substrates.[18,114,138]

The DEZ-H_2O ALD window is from around 120 - 180 °C but is also regularly deposited outside this range. This is possible as the reactions are still self-saturating but the GPC is lower.[12] The preferential crystal orientation of ZnO changes with temperature. At temperatures at the lower end and just beyond the ALD window, the out-of-plane preferential orientation tends towards [100] due to adsorption of negatively charged organic by-products to the polar (002) ZnO planes.[139] At higher deposition temperatures the films become more [002] oriented and above 220 °C the films are strongly [002] oriented. This is also the case at temperatures below 70 °C.[140] At increasingly lower temperatures ($\lesssim$ 120 °C) the carrier concentration and mobility of tends to ZnO decrease, which is probably linked to changes in crystallinity and the ZnO becoming increasingly less oxygen deficient.[67,68] At temperatures of around 120 °C and above, ALD ZnO has a steady carrier concentration of around 10^{18} - 10^{19} cm^{-3} and a carrier mobility above 20 cm^2 $(\text{Vs})^{-1}$.[74] For this reason, generally higher temperatures of around 200 °C are used for applications where high carrier concentrations and mobilities are desired; AZO is often deposited at these temperatures.[30] When ZnO is used as a semiconducting layer in devices, often lower carrier concentration interlayers are favourable as they reduce charge carrier recombination, so low deposition temperatures ($\lesssim$ 100 °C) have often proved optimal when temperature dependence is studied,[104,125,141–143] or effective without a specific temperature study.[113,127,131,134,144,145] This is not exclusively the case though, as higher deposition temperatures have also produced some good performances.[90,123,130,133,146,147] In TFTs, higher temperature channel layers failed to switch off due to the higher carrier concentration.[148–151]

2.4 Summary

- ALD occurs through repeated, separated, self-limiting reactions of two or more precursors with the surface species on a substrate.

- ALD reactors can operate under low vacuum with a N_2 purge (conventional ALD) or in open atmosphere (AP-SALD), and there are many different forms of reactors designed for different applications.

- ALD is more expensive than solution processing techniques, and tends to have a much slower deposition rate than CVD and PVD techniques (although AP-SALD allows more rapid deposition than conventional ALD). However, ALD cannot be rivalled in repeatability, uniformity and conformality over complex surfaces, and also has generally low deposition temperatures and is scalable for manufacturing.

- Using TMA, DEZ and H_2O precursors, Al_2O_3, ZnO and AZO can be readily deposited which have a variety of uses in optoelectronic devices. Al_2O_3 is an amorphous, insulating material which is of interest for ultrathin passivation, protection and recombination barrier layers; ZnO is a transparent semiconductor which can be used as electron transport layers, TFT channel layers and solar cell buffer layers; and AZO is a degenerate semiconductor with high carrier concentration and applications as a transparent, conducting electrode or electron transport layer.

- To confirm true ALD is occurring with each precursor combination used in a reactor, the variation in GPC with release time, purge time, number of cycles, and temperature needs to be investigated. GPC should match literature reports and material properties may also be affected by the variables.

Chapter 3

Experimental techniques

In this chapter, an overview is presented of the different material and device characterisation techniques used in the rest of this thesis. The ALD system and experimental variables are the key areas of investigation in Chapters 4 and 5 so are not discussed here. The deposition parameters for the organic photovoltaics (discussed in Section 5.2.3 and 6.3.2) and perovskites (discussed in Chapter 7) are included with the solar cell measurements, Section 3.2.2. The deposition of CZTS nanoparticles (discussed in Section 8.2) is included with the photoelectrochemical measurements, Section 3.2.3.

3.1 Material characterisation

3.1.1 UV-visible spectroscopy

UV-visible spectroscopy (UV-vis) is a method for measuring the optical properties of a material. The equipment uses a lamp which emits wavelengths from UV to infrared, and a monochromator steps through the chosen wavelength range set by the user. Each specific wavelength of light is shone through the sample and a detector receives the transmitted waves. The percentage of the light transmitted is calculated by the system through comparing the detector current at each wavelength to an air reference value. The measurements were made either with a Bentham 605 single beam system with BenWin+ software or a Cary series spectrophotometer (Agilent Technologies).

Transmission data provides information on which wavelengths of light are absorbed by a material, which is a useful in e.g. characterising light absorbing and transparent layers for solar cells. Light with photon energies above the bandgap of a semiconducting material will be absorbed, so the bandgap can be calculated using the transmission, T. From the Beer-Lambert law, absorbance $\alpha \propto -ln(T)$. For a direct bandgap material like ZnO the absorbance is related to the bandgap energy, E_g, by the following equation:

$$(\alpha h\nu)^2 \propto (h\nu - E_g)$$

where h is Planck's constant and ν is the light frequency. By plotting $(\alpha h\nu)^2$ against $h\nu$ the bandgap can be found by fitting a line to the absorption edge and extrapolating it to $(\alpha h\nu)^2 = 0$. This construction is called a Tauc plot. For the samples in Chapter 6 the transmission and reflection of the samples were measured, using an integrating sphere set-up (carried out by Maurizio Morbidoni). The absorbance was then instead calculated using $\alpha \propto -ln(T+R)$ where R is the reflection.

For wavelengths of light with energy less than the bandgap, samples will generally show high transmission. There may be some transmission oscillations in this region due to light interference. If the sample is a smooth multilayer, for example ZnO on quartz, the light reflected at the interfaces between the materials of different refractive index will constructively and destructively interfere at different wavelengths.[152]

3.1.2 Spectral reflectance

Spectral reflectance is another optical characterisation technique, which is used in this thesis to measure the thickness of ALD Al_2O_3 layers on Si/native SiO_x. A Filmetrics F20-UV system measures the reflection for wavelengths 190 - 1100 nm and a model is fitted to it by the Filmetrics software. The model is created from the reference wavelength-dependent refractive index and dielectric values of each material in the multilayer combined with the known thickness values of the layers. The possible range of thickness of the layer being measured is entered i.e. the Al_2O_3 layer, and then the program uses a Cauchy model to calculate the expected spectrum with varying thickness to find the best matching model to the data. The reference values for Si/native SiO_x (2 nm) and air used are from the Filmetrics database and the Al_2O_3 refractive index was found from a representative ALD sample of known thickness (Section 5.1).

3.1.3 Optical microscopy

An optical microscope was used in examination of perovskite layers with temperature. Transmission images of the samples were taken with a camera at programmed time intervals, and between times the light was blocked to limit the perovskite exposure as in some situations light contributes to degradation.[153] The samples were enclosed in a box heated internally to the set temperature (100 °C), under a constant flow of N_2 ensuring a H_2O and O_2 free atmosphere. The microscope equipment was set up by Stefan Bachevillier.

3.1.4 X-ray diffraction

Information on the crystal structure of a material can be obtained by X-ray diffraction. Cu Kα X-rays are produced when thermionically emitted electrons are accelerated at a Cu target, knocking out core electrons, leading to electron transitions from higher energy shells which emit photons of characteristic energies. A beam of these X-rays is directed at a sample, which in all the cases here is a thin film on a substrate of e.g. glass. The detector and source move in an arc of selected angle range, θ, about the sample, and large numbers of X-ray counts are measure at angles where there is diffraction from a specific crystal plane oriented parallel to the substrate surface. The substrate also rotates about the vertical so that all in-plane orientations are measured, not just those in a certain direction. The angles at which there are strong diffraction peaks correspond to constructive interference of the X-rays following the Bragg equation:

$$n\lambda = 2d_{hkl}\sin(\theta)$$

where n is an integer, λ is the Cu Kα wavelength (0.15405 nm) and d_{hkl} is the plane spacing of the (hkl) plane. The geometry of diffraction is discussed further in Section 3.1.6 in the context of electron diffraction.

The relative intensity of an X-ray diffraction peak in a powder sample is dependent on a number of contributions:

- Structure factor (depends on atomic electron density, lattice motif, thermal motion of atoms)
- Lorentz-polarisation factor (measure of the time planes can diffract constructively and the scattering dependence on polarisation)
- Multiplicity (number of equivalent planes)

The diffraction of a thin film may show different relative peak intensities to those of a reference powder. This indicates that film is textured i.e. there is a preferential orientation of crystals relative to the substrate surface.

The peak centres may be shifted to different angles; this can be an indication of a uniform out-of-plane lattice strain and the Bragg equation can be used to calculate the difference in plane spacings. If there is a distribution of strain this manifests as peak broadening. Other contributions to peak full width half maximum (FWHM) are instrument broadening and small crystallite size. In these studies the Scherrer equation was often used to estimate crystallite size for ALD films (note other the factors were not corrected for). The out-of-plane crystal size, D, is found using:

$$D = \frac{0.9\lambda}{FWHM\ \cos(\theta)}$$

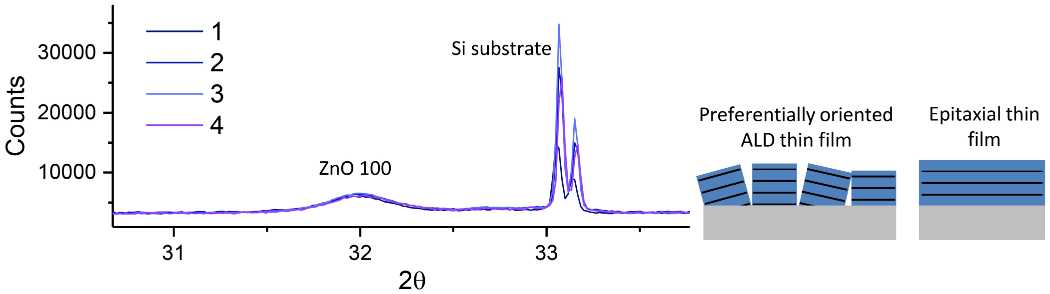

Figure 3.1: XRD pattern of ALD ZnO film on a Si substrate loaded four separate times with the ZnO and Si substrate peaks identified (note there is no epitaxial orientation of ZnO to the Si single crystal due to the presence of the native oxide). The schematics show the crystal alignment range in preferentially oriented ALD films compared to single crystal, epitaxial films.

XRD patterns were taken using a Bruker D2 Phaser or a Panalytical X'Pert Pro system, both using a spinning stage and with the substrate held in place by plasticine and the sample surface aligned by pressing flat. This is an approximate method of substrate alignment. Figure 3.1 shows XRD patterns from an ALD ZnO film on a Si substrate loaded four separate times. It can be seen that there are only small variations in the ZnO (100) peak position, height and width, but the Si substrate peak shows a large variation, demonstrating that the approximate alignment procedure is adequate for studying ALD ZnO thin films but not for single crystal, epitaxial thin films. From 10 repeated measurements the peak centre, 2θ, had a standard deviation of 0.028 and the peak FWHM had a standard deviation of 0.047, so these values were used to calculate the error bars in figures showing XRD data.

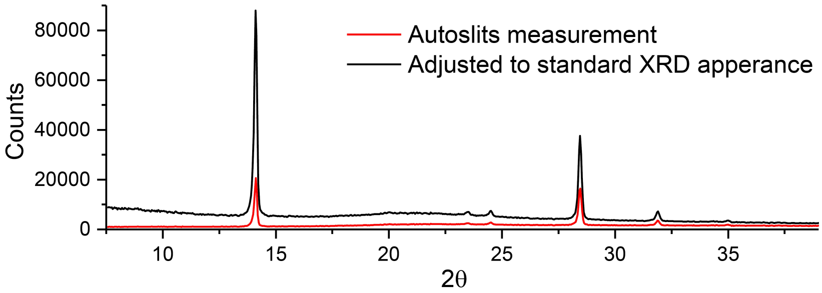

Figure 3.2: XRD pattern taken using the ‘Autoslits’ program compared with the same data processed by the Panalytical software to appear as a standard XRD measurement would.

Degradation studies were carried out in a different Panalytical X’Pert Pro system with a heated stage and vacuum chamber, and substrate surface height and tilt were carefully adjusted using micrometers. In usual measurements the slit width through which the X-ray beam passes is constant, which means the beam has a larger area at low angles than high angles. For most situations this is not an issue, however, in the temperature controlled XRD where the temperature is only uniform in the central area of the sample, a changing beam area with angle will mean a changing area of the sample is being monitored. At lower angles there will be more of a contribution from the lower temperature areas further from the sample centre than at higher 2θ. To overcome this some XRD systems have programmable slit widths. The ‘Autoslits’ program that was used for these measurements adjusts the slit width whilst scanning 2θ to ensure that the area being measured is a constant 0.7 mm × 0.7 mm area in the centre of the sample. It must be noted that XRD patterns taken with ’Autoslits’ will have a different background appearance and peak height from standard XRD measurements so cannot be directly compared, as demonstrated in Figure 3.2.

3.1.5 Scanning electron microscopy

Scanning electron microscopy (SEM) involves a beam of electrons being rastered across a sample surface, and the signal detected for each location is used to build an image of the sample pixel-by-pixel. The SEM used in these studies (LEO Gemini 1525) had a field emission gun enabling high resolution imaging, and a 5 kV accelerating voltage and an in-lens detector were used for the image formation. Electrons undergo a number of different interactions with matter, producing a variety of signals that can be monitored in SEM (Figure 3.3), and in this case secondary electrons were used to gain information about the topography and work function of the sample. Secondary electrons are produced when an electron from the beam inelastically

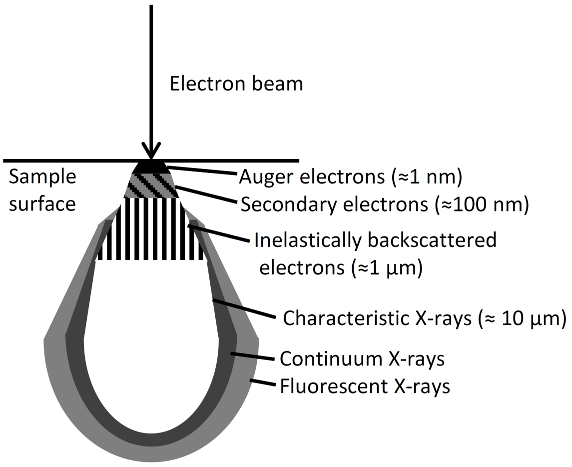

Figure 3.3: Schematic of the signals received from different depths within a substrate, produced due to interactions of the electron beam with the atoms of the substrate.

scatters, transferring some of its energy to an electron within the valence or conduction bands of an atom which subsequently has enough energy to escape the atom. The secondary electrons only have enough energy to escape from $\gtrsim$ 100 nm depth so at edges of features etc. where there is a shorter route to the surface a greater number of electrons can escape. Additionally, the number of electrons that can escape is dependent on the work function of the material. The contrast in an image represents the amount of electrons received by the in-lens detector, with brighter areas being locations from which more secondary electrons were received. Some samples need to be coated to reduce charging during imaging; in these cases Cr was sputtered on the surface to provide a conductive layer.

3.1.6 Transmission electron microscopy

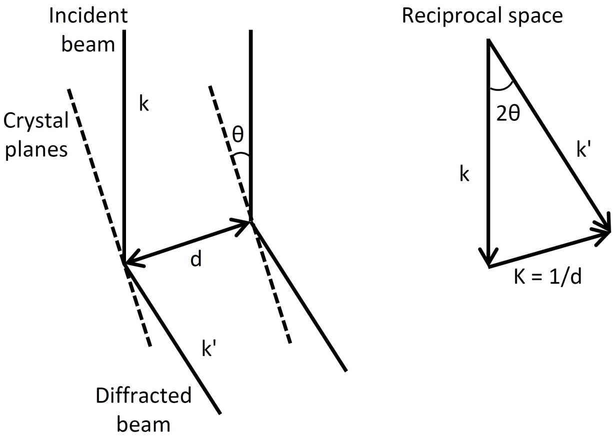

Figure 3.4: Diagram showing diffraction of electron beam from crystal planes in real and reciprocal space, where d is the plane spacing, k is the wavenumber of the electron and θ is the Bragg angle.

In transmission electron microscopy (TEM) an electron beam, accelerated by a high voltage (200 kV), is used to image a sample by transmission of electrons through the sample. Like in an optical microscope, an area of the sample is illuminated with the electron beam and the electrons which pass through the sample are directed using electromagnetic lenses to form an image directly on a screen or camera, with the contrast in the image arising from different electron interactions in the imaged area of the sample. Electrons undergo interactions as in Figure 3.3 but for TEM imaging elastic interactions will be primarily considered. An electron which passes through the electron cloud of an atom is deflected by attraction to the positive nucleus without losing energy. This is incoherent elastic scattering. There is a higher probability of electrons being scattered incoherently when passing through an element of higher atomic number and/or a thicker layer of material (TEM samples need to have thickness $\lesssim$ 100 nm for enough electrons to pass through to form a TEM image). Electrons can also elastically scatter coherently, which occurs when the electron (considered now as a wave) passes through a regular crystal lattice. If the planes are at a spacing and angle to the incident beam which satisfies the Bragg equation (Section 3.1.4) the waves diffracted from the atoms will constructively interfere resulting in an electron diffraction pattern. Figure 3.4 shows a diagram of this diffraction, and because of the very small wavelengths ($\approx$ 3 pm), diffraction occurs at very small θ angles and often from multiple planes simultaneously. In images, lattice fringes can be seen as a result of this diffraction as well as effects such as bend contours.

Apertures and electromagnetic lenses in the TEM can be used to select differently scattered electrons from which to form an image or diffraction pattern on the screen. Figure 3.5(a) shows the ray diagrams for the imaging and diffraction arrangements, and an objective aperture of a smaller size can be used to select undiffracted electrons or electrons diffracted from a specific plane to form a bright or dark field image respectively.

The JEOL JEM-2100F microscope used can also be operated in scanning TEM (STEM) mode. As in SEM, an electron beam is rastered across an area of the sample and detectors on the transmission side of the sample are used to form bright field and dark field images pixel-by-pixel. In this mode energy dispersive X-ray spectroscopy (EDX) can be used to obtain an elemental map of the sample or determine the composition at a specific location. The X-rays which form the EDX spectra are produced when electrons inelastically scatter, transferring enough energy to a core electron for it to escape the atom. As explained in Section 3.1.4, an electron from a higher energy shell then drops down to fill the space, releasing a characteristic wavelength of X-ray which is then detected and attributed to a specific element. EDX spectra arise from an area of the sample larger than the focussed electron beam size due to the interaction volume (Figure 3.3) but the precise area is sample thickness dependent. EDX is more sensitive to heavier elements so cannot reliably be used to determine e.g. ZnO stoichiometry.

The thickness $\lesssim$ 100 nm requirement of TEM samples means sometimes a long preparation process is required. For nanoscale, dispersable samples, e.g. CZTS nanoparticles (Section 8.2) and ZnO nanotubes (Section 8.1), the particles can be suspended in a solvent and then the liquid can be dropped onto a holey carbon TEM grid. For cross-section preparation, a focussed ion beam microscope is needed

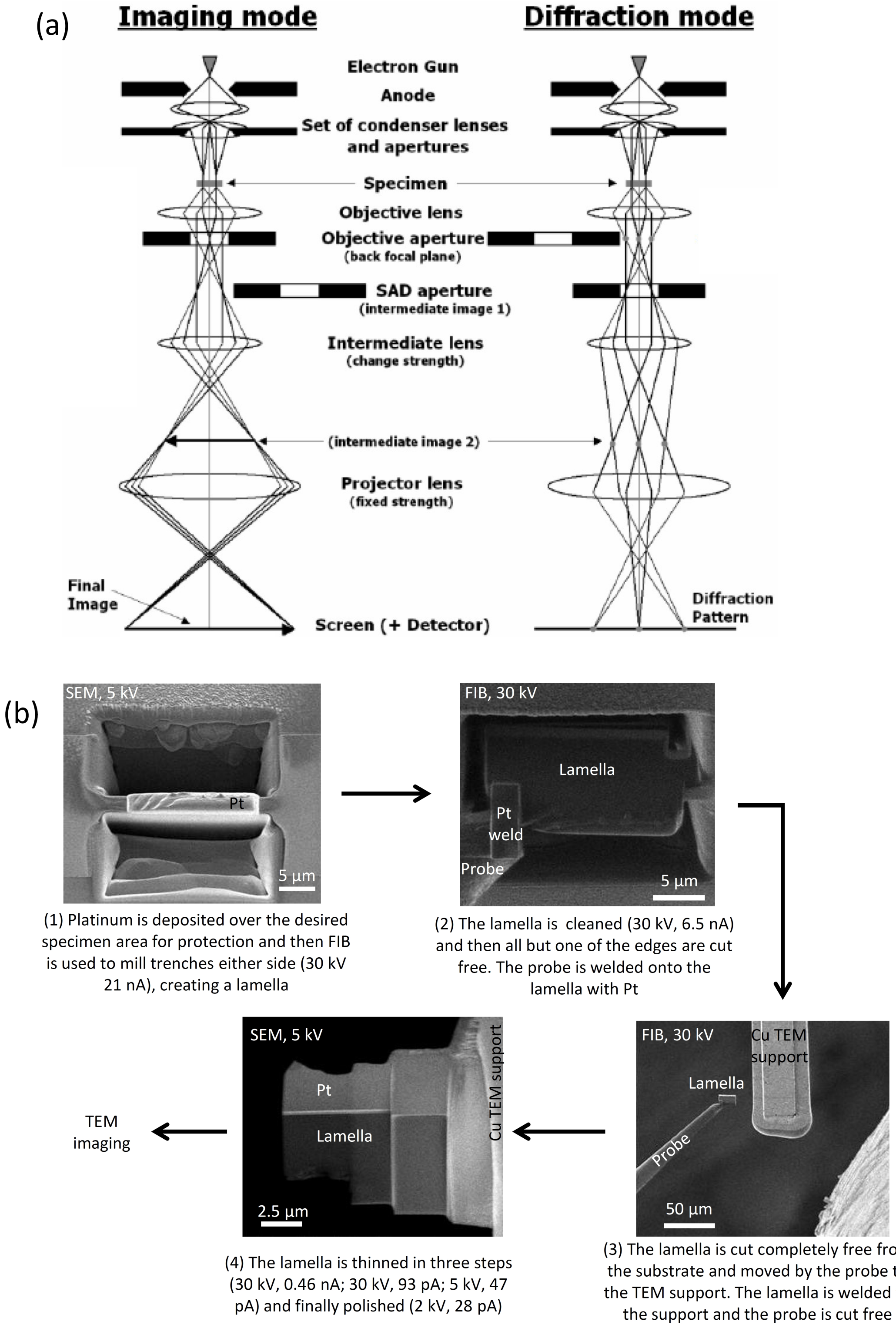

(1) Platinum is deposited over the desired specimen area for protection and then FIB is used to mill trenches either side (30 kV 21 nA), creating a lamella

(2) The lamella is cleaned (30 kV, 6.5 nA) and then all but one of the edges are cut free. The probe is welded onto the lamella with Pt

(3) The lamella is cut completely free from the substrate and moved by the probe to the TEM support. The lamella is welded to the support and the probe is cut free

(4) The lamella is thinned in three steps (30 kV, 0.46 nA; 30 kV, 93 pA; 5 kV, 47 pA) and finally polished (2 kV, 28 pA)

Figure 3.5: (a) Ray diagrams of the TEM in imaging and diffraction modes. Reproduced with permission from reference,[6] ©Springer US 1996. (b) Images and description outlining the series of steps taken to prepare a lamella for TEM imaging using the Helios DualBeam SEM/FIB microscope.

to cut a lamella free of the sample, weld it to a TEM support and thin it to electron transparency. The individual steps are shown in Figure 3.5(b).

3.1.7 Time of flight secondary ion mass spectroscopy

Secondary ion mass spectroscopy (SIMS) is a method which involves bombarding a sample with ions and analysing the secondary ions and charged groups of atoms which are released from the sample. Time of flight (TOF-)SIMS uses a focused pulse of primary ions from an analytical source, in this case a Bi liquid metal ion gun (LMIG), to sputter secondary ions from a location on the sample which are then accelerated using a potential, V. Their resulting velocity is determined by their mass to charge ratio, m/z. The ions travel through a long chamber, length L, to a detector and the time, t, taken to arrive is measured. The mass separation of the ions is given by:

$$\frac{m}{z} = \frac{2Vt^2}{L^2}$$

The peak pattern of counts from the detector is plotted against atomic mass units (amu) and is calibrated using known, easily identifiable ions, starting with $H^+ = 1$ amu. After calibration ions can be identified with a very high mass resolution. In this project SIMS was used to assess Al distribution in Cu_2ZnSnS_4 film, so positive ions were monitored to track the presence of the metals and a depth profile was carried out using Cs^+ ions to sputter a certain thickness between Bi primary ion analytical pulses. The resulting number of counts (secondary ion current of ion X, I_s^X) for each metal ion is dependent on several factors, expressed by the SIMS equation:

$$I_s^X = I_p \; C_X \; S \; \gamma \; F$$

where I_p is the primary ion current (Bi ions), C_X is the concentration of X, S is the sputter yield of X, γ is the ionisation efficiency of X, and F is the transmission of the analysis system.[154] An IONTOF TOF.SIMS5-Qtac[100] LEIS was the equipment used here.

3.1.8 Van der Pauw and Hall

Van der Pauw and Hall measurements were carried out on a Lakeshore 8404 HMS system to electrically characterise the ZnO films deposited by ALD. Contacts were confirmed ohmic (straight line V-I graph, fit >0.999) before the measurements were carried out. Van der Pauw was the technique used to measure the sheet resistance, R_s of the thin films. It can be used for a film of any shape as long as the four electrical contacts are all at the film edge. Voltages need to be measured between two contacts (e.g V_{12}), whilst running a current between the other two (e.g I_{34}), so resistance $R_{34,12} = V_{12}/I_{34}$ can be calculated. The Van der Pauw equation, for measured vertical resistance (e.g. $R_{34,12}$) and horizontal resistance (e.g. $R_{23,41}$), is:

$$1 = e^{-\pi R_{34,12}/R_s} + e^{-\pi R_{23,41}/R_s}$$

For these studies square samples were used with indium contacts positioned at the corners, which simplifies the sheet resistance calculation (see Figure 3.6 for contact arrangement). The sheet resistance can be calculated from two perpendicular resistance measurements by, for example:

$$R_s = \frac{\pi}{\ln(2)} \frac{R_{34,12} + R_{23,41}}{2}$$

Eight voltage measurements were made whilst applying current of magnitude I across the opposite contacts in order to determine the sheet resistance in two geometries, R_a and R_b.

$$\begin{aligned} R_a &= \frac{\pi}{\ln(2)} \frac{V_{12} - V_{21} + V_{23} - V_{32}}{4I} \\ R_b &= \frac{\pi}{\ln(2)} \frac{V_{34} - V_{43} + V_{14} - V_{41}}{4I} \end{aligned}$$

The final resistivity, ρ, was calculated using $\rho = x \times (R_a + R_b)/2$, where x is the sample thickness, and the measurement program also returned a fractional f value as a measure of the symmetry of the two geometries (f >0.95 is acceptable).

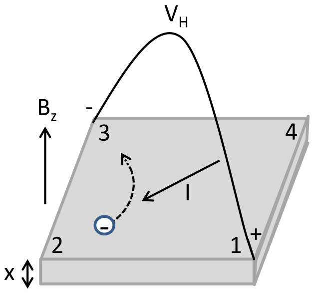

Figure 3.6: Schematic showing the measurement of the Hall voltage, V$_H$, induced by the current, I, following perpendicular to magnetic field, B$_z$. The film thickness is x and the electrical contacts are labelled 1 - 4.

The diagram for a conventional Hall measurement is shown in Figure 3.6. Whilst a current, I, is flowing, majority charge carriers are deflected by the magnetic field B_z applied normal to the thin film. A voltage is built up between the contacts perpendicular to the current flow. This is the Hall voltage, V_H, which is a balance between the Lorentz force and charge repulsion, and can be expressed by:

$$V_H = \frac{IB_z}{nxe}$$

where n is the charge carrier density (electron for ZnO) and e is the elementary charge. The mobility, μ, of the electrons can finally be calculated from $\mu = x/(e\ n\ R_s)$

The Hall measurements were generally carried out using an AC magnetic field, which has increased accuracy over the conventional DC magnetic field Hall for samples of mobility <10 cm^2 (Vs)$^{-1}$. This is due to the relatively high misalignment voltage, V_α, compared to the Hall voltage. The misalignment voltage arises when the contacts for the Hall measurement are not precisely symmetrical, and it scales with current ($V_\alpha = \alpha\rho I$). The measured voltage, V_{meas} is the sum of the misalignment voltage and Hall voltage (assuming other voltage errors have been accounted for).

$$V_{meas} \quad = \quad V_H + V_\alpha \quad = \quad \rho I(\mu B_z/x + \alpha)$$

where α is the misalignment factor. If μB_z is low then field reversal ($V_H = (V_{measured,+B} - V_{measured,-B})/2$) will not be effective in removing the α contribution as the result will be dominated by noise. However, because V_α is independent of magnetic field an AC field and a lock-in amplifier can be used to eliminate any DC voltage contributions. The resulting measured voltage is:

$$V_{meas}(t) \quad = \frac{I|B|\cos(\omega t)}{nxe} - A\omega|B|\sin(\omega t) \quad = V_H\cos(\omega t) - V_{ind}\cos(\pi/2 - \omega t)$$

where A is a constant related to the inductive pickup, $|B|\cos(\omega t)$ is the magnetic field which varies with time, t, with amplitude $|B| = 1.23$ tesla and frequency $\omega =$ 50 Hz. V_{ind} is the inductive voltage that arises as a result of the changing magnetic field and is 90° degrees out of phase with the Hall voltage so is easily separated by the lock-in amplifier.

3.1.9 Kelvin probe

A Kelvin probe can be used to indirectly measure the near-surface work function of a material. The sample and the oscillating Kelvin probe are electrically connected and the probe tip is brought into close proximity with the sample surface. A potential difference between the surface and the tip arises due to their difference in work function, and the voltage needed to counteract the AC current which oscillates with the varying tip distance is measured. This is the contact potential difference (CPD) and is used to calculate the work function by calibrating it with the CPD of a highly oriented pyrolytic graphite (HOPG) reference sample which has a work function of 4.48 eV. Due to the sensitivity of surface work functions to changes in atmosphere, Kelvin probe results that are to be compared should be made immediately after one another. HOPG is chosen as the reference as it has a work function which is relatively stable in air. Kelvin probe measurements are reliable for degenerate semiconductors like AZO but for non-degenerate semiconducting materials the measurements may be affected by band bending. The Kelvin probe results in this thesis were measured by Maurizio Morbidoni.

3.2 Device characterisation

3.2.1 Thin film transistors

Thin film transistor (TFT) measurements were used as another method of electrically characterising ALD ZnO layers. Pre-fabricated, bottom gate, bottom contact TFT substrates were bought from Fraunhofer IPMS, shown in Figure 3.7. The photoresists were removed and the substrates cleaned, then they were coated in the ALD system with a layer of ZnO which formed the transistor channels.

The TFTs use an applied gate voltage V_G to control the accumulation of electrons in the channel and thus the current that flows between the source and drain contacts, I_D. The operation regimes of TFTs and the model output and transfer curves are presented in Figure 3.8. When the TFT is in the accumulation regime (electrons accumulated at the dielectric/channel interface), the measured I_D initially scales linearly with applied source-drain voltage, V_D. As V_D approaches value of $V_G - V_T$ (where V_T is the threshold gate voltage for electron accumulation) the rate of I_D increase reduces. At the pinch-off point the applied V_D is too large for

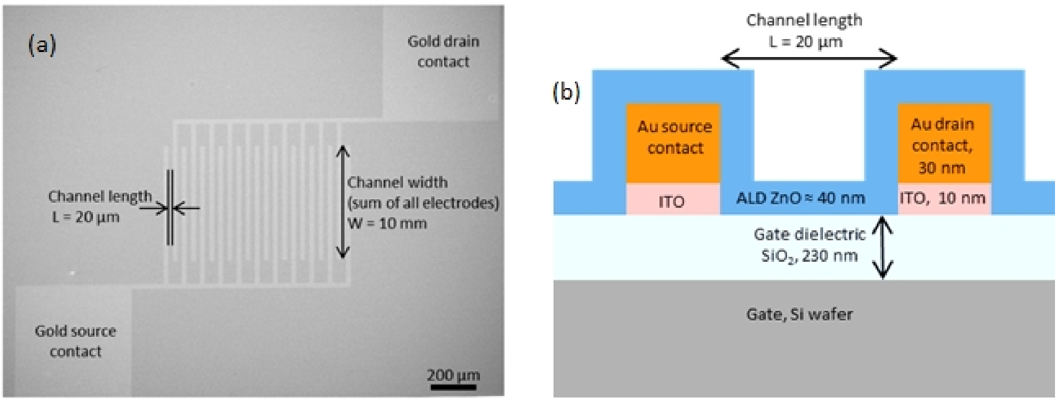

Figure 3.7: (a) SEM top-view image and (b) schematic cross-section (not to scale) of an ALD ZnO coated bottom gate, bottom contact TFT.

accumulation of electrons to occur across the whole dielectric/channel interface so the I_D value saturates.

By employing a V_D value at which I_D is saturated for the chosen V_G range, the saturated transfer curve of the TFT can be investigated. The measured I_D is low at small V_G values where the transistor is in the off state. Beyond a certain V_G value, the measured I_D starts to sharply rise. This in the on-voltage, V_{on}, where electrons are beginning to accumulate in the channel, attracted by the gate voltage, so increasingly more current can flow. For ALD ZnO V_{on} is often negative so the TFTs are depletion mode (i.e. normally on). In the region where V_G has just surpassed V_{on} the subthreshold swing, SS, can be measured. SS is the inverse of ΔV_G needed for an order of magnitude increase I_D, and can be used as measure of the traps at the dielectric/channel interface. I_D continues to increase at a slower rate as V_G is increased further as the accumulation of electrons completes (when V_T is reached). The transfer curve data can be plotted against $I_D^{0.5}$ to enable the saturated, field effect mobility, $\mu_{sat,FE}$, of the charge carriers to be calculated and also V_T to be found. A linear fit can be made to the $I_D^{0.5}$ data at higher V_G, the voltage at which the line intercepts $I_D^{0.5} = 0$ is the value of V_T, and the gradient of the line, $(dI_D^{0.5})dV_G$, can be used in the following calculation:

$$\mu_{sat,FE} = \frac{(\frac{dI_D^{0.5}}{dV_G})^2}{C_G \frac{W}{2L}}$$

where W is channel width, L is channel length and C_G is the capacitance per unit area ($C_{G,SiO_2} = \frac{\epsilon_{SiO_2}\epsilon_0}{x_{SiO_2}} = 1.50 \times 10^{-4}$ F m^{-2}).

3.2.2 Solar cells

Two different types of solar cell were investigated in this thesis: organic solar cells (OSC) and perovskite solar cells (PSC). In OSCs, the organic material absorbs a photon, exciting an electron from the highest occupied molecular orbital (HOMO) to higher energy, creating an exciton of the electron and corresponding hole. The exciton diffuses to the donor/acceptor interface where it is separated, with the hole travelling through the donor material to the anode, while the electron travels through

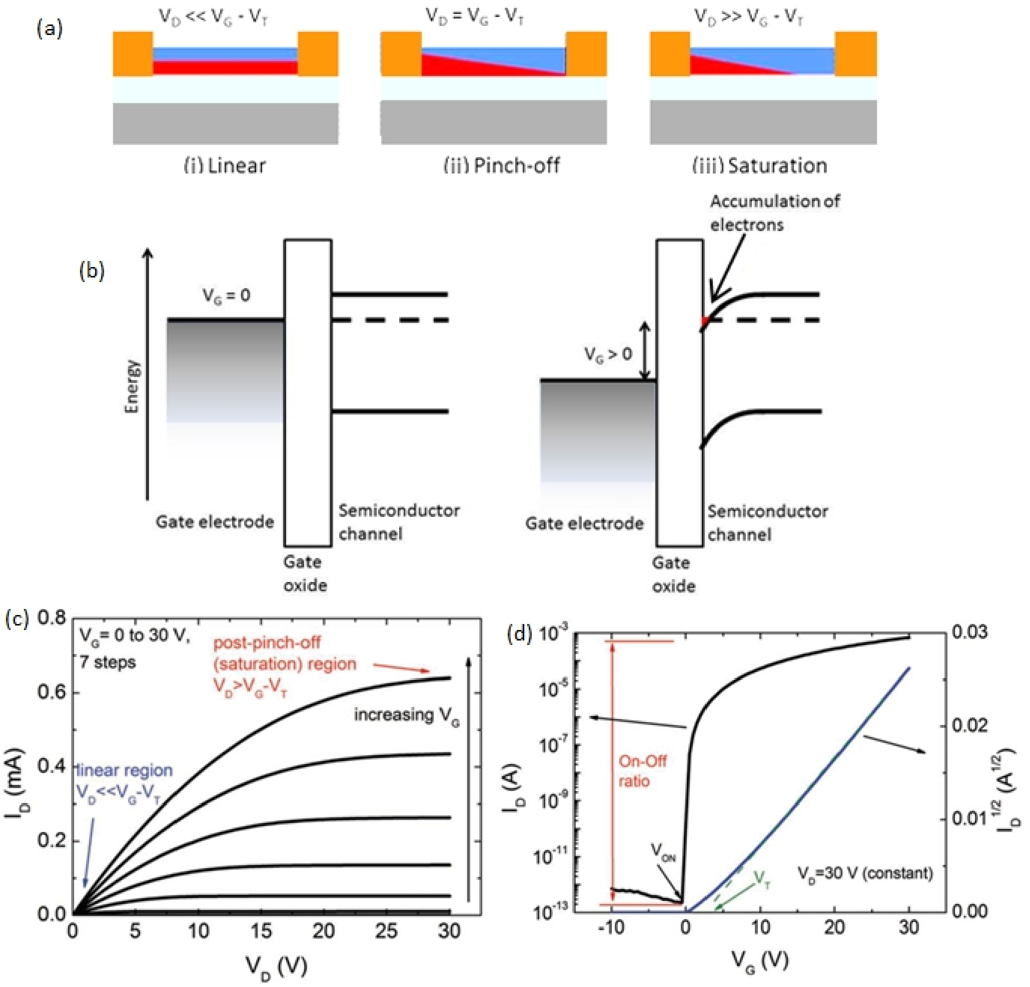

Figure 3.8: (a) Schematic showing how the accumulation of electrons (red area) at the gate dielectric/ZnO channel interface is affected by the magnitude of the applied source-drain voltage V_D compared to the threshold (V_T) and gate (V_G) voltages. The source-drain current, I_D, measured for the different regimes is illustrated by the output curves in (c). (b) shows the band diagram of a n-type semiconducting channel with and without applied gate voltage, V_G. The corresponding transfer curves of I_D variation with V_G are shown in (d). Graphs (c) and (d) are reproduced with permission from reference,[7] ©2012 John Wiley and Sons.

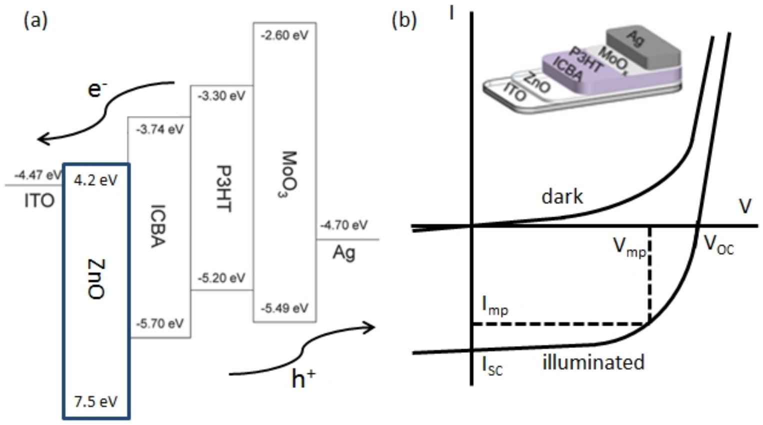

Figure 3.9: (a) Diagram of an OPV band structure with ZnO as an ETL, adapted with permission from reference,[8] ©2016 John Wiley and Sons. (b) Graph of the dark and illuminated electrical output of a solar cell, with inset device schematic.

the acceptor to the cathode. If the solar cell is suitably biased, the power produced by this process can be utilised. In OSCs metal oxide layers are frequently used as semiconducting, charge transport layers between the conductive electrodes and the organic blend. These layers are often referred to as electron transport layers (ETL) and hole transport layers (HTL). The ETLs, for example, block holes and selectively conduct electrons, reducing the recombination of charges which otherwise occurs when the organic blend is in direct contact with the conductive electrode. ALD ZnO is used as the ETL material for these OSCs and is deposited on top of an ITO electrode.

The OSCs investigated are bulk heterojuction type, where the donor and acceptor organic materials are blended rather than in planar layers. Two different donor:acceptor material combinations were used – poly(3-hexylthiophene-2,5-diyl) : 1',1",4',4"-tetrahydro-di[1,4]methanonaphthaleno[5,6]fullerene-C_{60} (P3HT:ICBA) and poly[[4,8-bis[(2-ethylhexyl) oxy]benzo[1,2-b:4,5-b']dithiophene-2,6-diyl] [3-fluoro-2-[(2-ethylhexyl)carbonyl]thieno[3,4-b]thiophenediyl]] : [6,6]-phenyl C71-butyric acid methyl ester (PTB7:$PC_{71}BM$). The band diagram for the P3HT:ICBA OSC is shown in Figure 3.9(a), where it can be seen that the band gap of ZnO is wide enough to block holes whilst having a suitably aligned conduction band which allows the transport of electrons to ITO. PSCs have a similar operating principle to OSCs. The so-called organic-inorganic perovskite material, in this case methylammonium lead iodide $CH_3NH_3PbI_3$, acts as the light absorbing layer and ALD ZnO is used as an ETL layer on top of an ITO electrode. Figure 3.9(b) shows the current-voltage (I-V) performance of general solar cells. A number of values can be extracted from the data to aid understanding of the cell performance. The short circuit current I_{sc} and open circuit voltage V_{oc} are labelled. The fill factor, FF, which is a measure of how 'square' the $I - V$ curve is and depends on the series and shunt resistance of the cell, can be calculated from $FF = \frac{V_{mp} I_{mp}}{V_{oc} I_{sc}}$. The overall power efficiency of the cell is $PCE = \frac{FF\ V_{oc}\ I_{sc}}{P_{incident}}$ where $P_{incident}$ is the incident power from the solar simulator xenon lamp (1 sun, AM1.5G). Processes such as carrier recombination and interfacial charge transfer can affect the performance of a device, and the above parameters are used in discussion of the results for solar cells later in this thesis.

For the OSCs in Chapter 5 and 6, once ZnO had been deposited on ITO by ALD, the rest of the layers in the OSCs were deposited by Jiaqi Zhang, who also performed the solar testing. The exact parameters for the OSC fabrication are described in reference.[8] Briefly, a layer of P3HT:ICBA or PTB7:$PC_{71}BM$ was spin coated on the ITO/ALD ZnO substrate, followed by evaporation of MoO_x and Ag. The perovskite layers used in the stability tests Chapter 7 were deposited by Tian Du, who also fabricated the additional layers of the PSCs and tested the cells. The perovskite was deposited on ITO/ALD ZnO or AZO substrates following the method from reference,[155] where a lead iodide and methylammonium iodide solution is spin coated with a part-way-through toluene drop casting step to improve uniformity. The substrates were then heated for only a short time, 20 s at 110 °C, to allow the formation of perovskite (observed by colour change from yellow to black) without affecting the later temperature stability tests. For devices a spiro-OMeTAD (2,2',7,7'-tetrakis[N,N-di(4-methoxyphenyl)amino]-9,9'-spirobifluorene) layer was spin coated on top of the perovskite, then finally MoO_x and Ag were evaporated. All the solar cells had a pixel area of 4.5 mm^2.

3.2.3 Photoelectrochemical testing

As part of the analysis ALD deposition on complex substrates, Cu_2ZnSnS_4 (CZTS) nanoparticle layers were deposited on FTO substrates for photoelectrochemical testing. CZTS nanoparticles were made by Xuemei Zhang through the simultaneous hot-injection of copper(II) acetylacetonate, zinc acetate, and tin(IV) acetate in oleylamine and sulphur powder in oleylamine as described in reference.[9] The remnant solution was removed using centrifuge separation and dispersion in toluene. The nanoparticles were dip coated onto glass/FTO substrates, carried out by hand in a N_2 glove box. Between subsequent dips the substrates were allowed to dry and were then dipped into a solution of ethylenediamine (EDA) in acetonitrile to exchange ligands as illustrated in Figure 3.10(a). The dip coating and photoelectrochemical testing of the CZTS photocathodes was carried out jointly, led by Xuemei Zhang.

The CZTS nanoparticle films underwent ALD coating and annealing as described in Chapter 8. They were then photoelectrochemically tested by submerging in a $Eu(NO_3)_3$ electrolyte with a Pt counter electrode and a Ag/AgCl reference electrode. The band structures of a p-type semiconducting layer such as CZTS film submerged in a an electrolyte is shown in Figure 3.10(b), although, due the nanoparticle nature of the CZTS used here it is expected that there would not be a built-in field as this would be cancelled out by electrolyte ions so instead chemical potential would drive the movement of the charges. Figure 3.10(d) shows the measured current during a voltage sweep of a typical CZTS photocathode under chopped illumination. The negative step in current when the photocathode is illuminated is the photocurrent and arise because the CZTS absorbs photons, exciting electrons to the conduction band which travel to the CZTS/electrolyte interface whilst holes flow through the CZTS and out of the FTO electrode. The photogenerated electrons reduce the Eu^{3+} in the electrolyte to Eu^{2+} which then diffuses to the Pt counter electrode and is re-oxidised, completing the circuit. The increase in dark current at below ≈ -0.55 V is due reduction of the Eu^{3+} directly on the CZTS surface, as expected from the reduction potentials shown in Figure 3.10(c). Note that photocurrent spikes on illumination then reduces to a steady state value with time; this is due to the

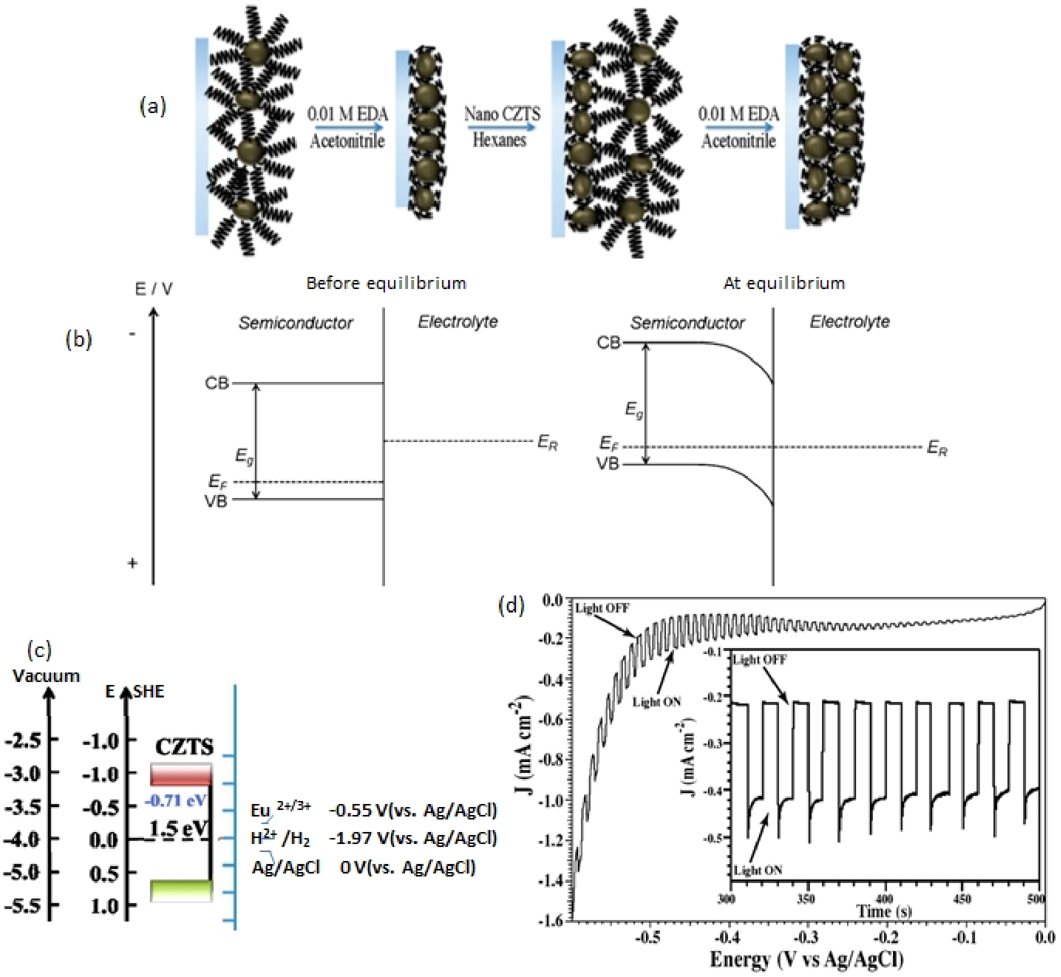

Figure 3.10: (a) Diagram demonstrating the ligand exchange process for CZTS nanoparticle dip coating. Long oleyleamine ligands are exchanged for shorted EDA ligands. Reproduced with permission from reference[9] ©2011 American Chemical Society. (b) The band alignment and bending for a p-type semiconducting layer submerged in an electrolyte. Reproduced with permission from reference[10] ©American Chemical Society. (c) The band structure of CZTS and its relation to the reduction potentials of the Eu^{3+} electrolyte and Ag/AgCl reference electrode. Adapted with permission from reference[11] ©2014 Elsevier. (d) An typical voltage sweep current measurement of a nanocrystalline CZTS photocathode under chopped light. The inset is a constant voltage measurement demonstrating stability with time. Reproduced with permission from reference[9] ©2011 American Chemical Society.

slow electron transfer kinetics of $Eu(NO_3)_3$ which cause a build up in charge and recombination.[156]

The characterisation of the photocathodes fabricated in this project was done through incident photon to charge carrier efficiency (IPCE) measurements. This is carried out by biasing the photocathode (-0.35 V) and illuminating it with a chopped series of wavelengths of light, measuring the photocurrent at each wavelength. The IPCE is the fractional number of carriers produced per incident photon. From measuring the power (P in Watts) of the light source at each wavelength (λ in nm) with a reference diode, the IPCE (in %) for each λ can be calculated from the photocurrent (I_{photo} in A):

$$IPCE = \frac{1240 \times I_{photo}}{P \times \lambda} \times 100$$

3.3 Summary

In this project, both materials and devices were characterised. The methods of materials characterisation were:

- UV-visible spectroscopy - optical transmission measured and bandgap fitted.
- Spectral reflectance - thickness calculated from fitted reflectance spectrum.
- Optical microscopy - imaging multilayer during degradation at high temperature.
- X-ray diffraction - characterising crystal structure.
- Scanning electron microscopy - imaging surface of films.
- Transmission electron microscopy - imaging nanoparticles and cross-sections of multilayers, and gaining elemental distribution information (EDX).
- Time of flight secondary ion mass spectroscopy - depth profiling to measure elemental distribution.
- Van der Pauw and Hall - measuring resistivity, carrier concentration and mobility.
- Kelvin probe - measuring surface work function.

The devices characterised were:

- thin film transistors - ALD ZnO channel layer.
- solar cells - organic and perovskite types, with an ALD ZnO/AZO electron transport layer.
- photocathodes - photoelectrochemical testing of Cu_2ZnSnS_4 with ultrathin ALD Al_2O_3 coating.

Chapter 4

ALD System Construction

4.1 Introduction

There are many different variations of ALD systems, some mentioned in Section 2.3.1, each with benefits depending on the intended use. A large portion of this PhD project was dedicated to constructing an ALD system which could then be used to coat a variety of substrates for optoelectronic purposes. Consideration of the precursors, substrates and deposited layers, along with system complexity, adaptability and expense all impacted on the type of ALD reactor that was chosen. The reasoning behind the choice is outlined below.

Conventional (temporal) ALD
In conventional, temporal ALD reactors substrates are placed in a vacuum chamber into which gaseous precursors are alternately released, separated by purging/pumping periods. A less common alternative is spatial ALD (SALD), where precursors are separated in space rather than time,[3] which can be carried out at atmospheric pressure (AP-SALD). In AP-SALD a deposition head, which contains a series of channels that constantly release and pump precursor and inert gas, passes over the substrate surface. AP-SALD reactors have several advantages including deposition speed but they require careful design of the gas flow from the deposition head. Contrastingly, the design of conventional ALD reactors is better established so guidance for construction is more readily available.[157,158] Also, when coating complex shaped, non-planar substrates it is much simpler to use conventional ALD as precursors can be held in the chamber to allow time for diffusion.

Thermal reactor
Energy can be provided to aid chemical reactions through heating (thermal) and also additional sources such as plasmas. As discussed in Section 2.3.1 ZnO, Al_2O_3 and Al doped ZnO will be the main materials deposited, using the precursors diethyl zinc (DEZ), trimethyl aluminium (TMA) and H_2O. No plasma, ozone etc. sources are needed for these depositions (although they can be used) as the surface reactions occur readily even at low temperatures. Therefore these options were not incorporated in the system as it would have involved significant extra effort without major benefits. Even with a purely thermal reactor there are a range of other precursors that can be used so there is flexibility for future research.

N_2 flow

Precursors are drawn into and evacuated from the reaction chamber by vacuum pumping which can be aided by an inert carrier/purging gas e.g. N_2. The choice of whether to solely use pumping or a combination of pumping and N_2 flow depends on the application because the pressure and gas flow inside a reactor determines the precursor movement and diffusion.[137] There are two pressure regimes possible: molecular flow and viscous flow. Molecular flow occurs at low pressures where there are few molecules present and so their mean free path between collisions is greater than the chamber size. In the absence of a purging gas extended pump down times are needed between precursor releases, as the removal of precursors on evacuation will be slow due to their molecular flow. These pump-down reactors can be more precursor efficient as precursor has a longer residency time due to not being whisked away by N_2 flow.[159] Also, for research where low deposition rate is not an issue (e.g. in studying reaction mechanisms), there is more flexibility in chamber shape and less design of gas flows necessary.[26] However, for the reactor in this project in-situ analysis is not required and a relatively high deposition rate is desired so that coatings which are tens of nanometres thick can be deposited and used in devices. Therefore a viscous flow reactor was chosen, with a N_2 gas flow used to aid diffusion and entrain the precursors and reaction products, enabling short residency times.

Hot wall

Substrates can be heated independently or through the same route as the walls of the reactor. It is generally inadvisable to have cold reactor walls as the precursors, especially H_2O, become much more difficult to purge. Some reactors have warm walls which are heated to a lower temperature than the substrates so, if ALD windows allow, less material is deposited on the reactor walls than the substrate surface, reducing the need for cleaning. In that case the substrates would sit on a heated stand (which could be heated by a system inside the vacuum chamber or from outside). A hot wall reactor is chosen in this case, with the substrates sitting on a stand in contact with the reactor walls so both are heated to the required deposition temperature from the heaters on the outside. This is a simple and well used method.

Cross-flow, tube reaction chamber

Although the design requirements are much less rigorous than those needed for CVD, the flow of gas in ALD reactors effects material growth and must be considered. There need to be no unswept volumes in the chamber where a precursor could remain to react in gas phase with the next precursor. There is the option of cross-flow or perpendicular-flow[160] of gas relative to substrate surface, and the choice can affect the uniformity of the coating. In cross-flow reactors the precursor flows parallel to the surface of the substrates, so substrates near the chamber entrance are exposed to a higher partial pressure of precursor than those further along as the precursor is gradually consumed. This can lead to a film thickness gradient, especially if there is too little remaining precursor for self-saturation.[44,161] Additionally the increasing partial pressure of gaseous by-product with increasing distance from the chamber entrance can affect growth if the by-product etches or adsorbs onto the surface. Shower head style and vortex funnel shape ports, where flow from the port is perpendicular to the substrate surface, have been designed to counteract this issue, especially when using large silicon wafers. They do, however, increase chamber volume and so lengthen purge times.

Cross-flow reactors allow smaller chamber volumes to be used. A tube-shaped chamber can be easily purged and uniformly heated compared to some alternative shapes and is a fairly common choice for ALD. Through design of the substrate stand the separation between substrate surface and roof can be made narrow, decreasing reactor volume and increasing the number of collisions which precursors will have with the substrates.

Despite some of the issues with cross-flow, tube shaped reaction chambers, the precursors used here have a high vapour pressures, so provided the release step is sufficiently long they will not suffer depletion and unsaturated growth. The growth behaviour of the precursors is also close to ideal (especially for TMA/H_2O) so should not suffer much from a partial pressure gradient and the by-products are not particularly inhibiting towards growth. Also, from a manual handling point of view, substrates can be easily loaded in from one end for tube shape reactors. If a removable interior tube is used to line the chamber walls this can also be slid out for cleaning/replacement without complete disassembly.

After the considerations above a conventional, thermal, cross-flow, hot wall, tube furnace type reactor operating with a N_2 was chosen as suitable for this project. Henning Urban of Oxford University very kindly provided the drawings for their custom-built ALD system and it is from those drawings that our ALD system was developed, with changes and improvements made to their original design. Literature, advice from colleagues, prototypes and trial experiments all contributed to the final, working ALD system.

In order to prepare for building and operating the system safely I attended courses on pipe fitting, fire safety, laboratory gases, gas cylinders and vacuum pumps. The ALD system was then constructed in several stages. The majority of the frame and system housing was built at home with the help and guidance of Pete Burgess. This structure was transported to the university and the rest of the system including vacuum, pneumatic and electrical components were assembled in the lab. Figure 4.1 shows photos and the schematic of the completed system. When discussing components which are labelled in Figure 4.1 a number or colour will be given in ⟨*triangular brackets*⟩ to help indicate the relevant part. This chapter describes the ALD system, the choices made for various components and how the system operates. For a comprehensive understanding of the ALD system this chapter should be used in combination with the ALD Handbook in the Appendix, which contains more precise engineering details including specifics on assembly and maintenance accompanied by diagrams and photos.

4.2 ALD reactor description

4.2.1 Precursor and N_2 Delivery to Reaction Chamber

The precursors used in the reactor are trimethyl aluminium (TMA), diethyl zinc (DEZ) and H_2O. DEZ and TMA are pyrophoric and corrosive chemicals, and they were bought packaged in cylinders isolated by a manual diaphragm valve, with a

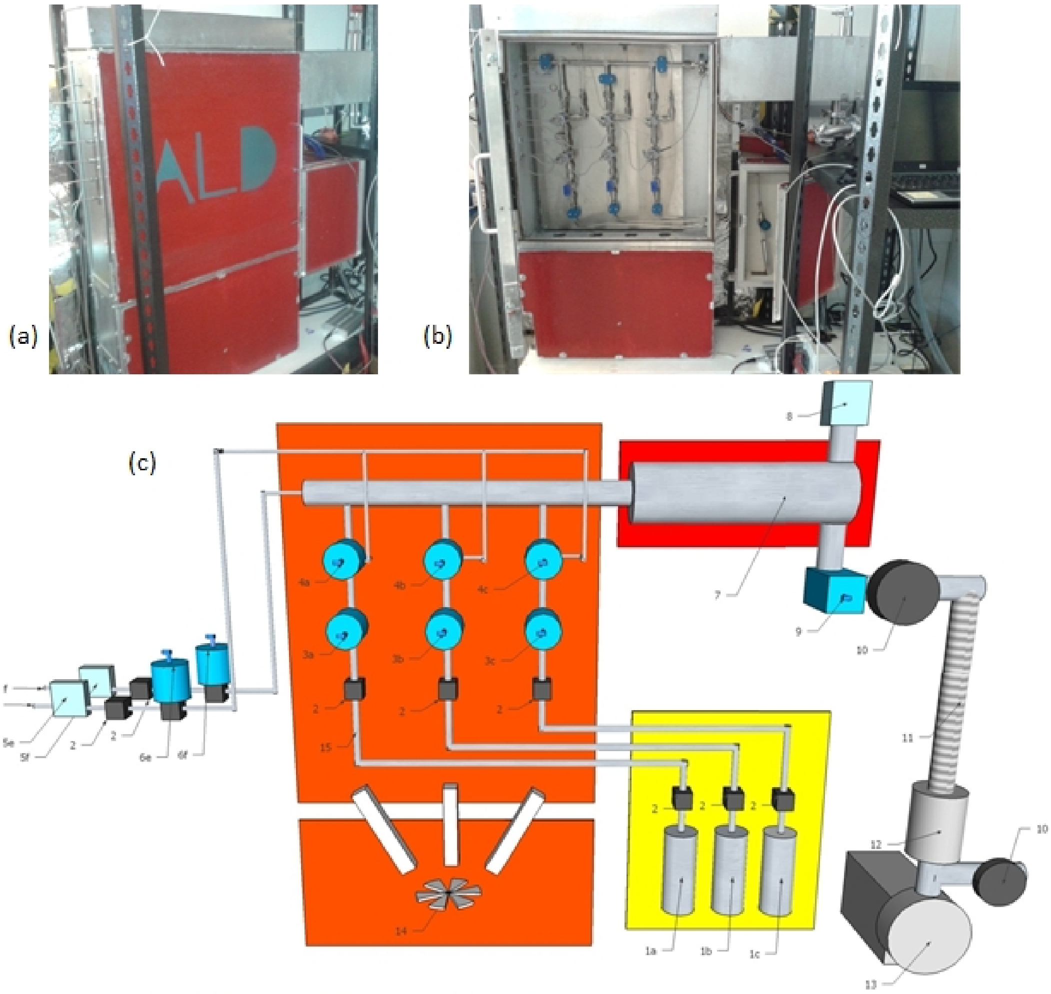

Yellow – Precursor box (room temperature)
Orange – Oven box (usually 100 °C)
Red – Reaction chamber box (usually 100 – 200 °C)
Blue – Devices which are controlled remotely/communicate with laptop

1 – Precursor flask (a TMA, b DEZ, c H_2O)
2 – Manual valve
3 – Pneumatic ALD valve (safety valve)
4 – Pneumatic ALD valve (release valve)
5 – Mass flow controller (e, f separate purified N_2 flows)
6 – Pneumatic diaphragm valve
7 – Reaction chamber
8 – Pirani vacuum gauge
9 – Pneumatic isolation valve
10 – Manual isolation valve
11 – Bellows
12 – Activated charcoal filter trap
13 – Scroll pump
14 – Fan to circulate heated air
15 – Place to attach heated precursor

Figure 4.1: Photographs of the ALD system (a) as in use and (b) open to show tubing. A schematic of the vacuum components of the system is shown in (c) with all compressed air tubing and heating systems excluded for clarity. The items numbers on the schematic are explained

VCR connection for easy attachment to the deposition system. For H_2O there are no safety risks so H_2O can simply be transferred into a suitable stainless steel cylinder with a valve and VCR connection. Chromatography grade H_2O was used, but H_2O of lower purity is often used in the literature (e.g. deionised H_2O,[162, 163]) so chromatography grade is not necessarily required. Precursors are degassed before use.

For ALD growth to self-saturate the amount of precursor in the deposition chamber needs to be above a certain minimum. For some precursors the vapour pressure at room temperature may not be sufficient to practically satisfy this minimum by lengthening valve opening times, so other methods such as heating the precursor flask or bubbling nitrogen through precursor liquid have to be employed. The vapour pressures of TMA, DEZ and H_2O at room temperature (20 °C) are 15,[94] 21[93] and 31[96] mbar respectively. These are sufficiently high to not require heating so the precursor flasks ⟨*1a,b,c*⟩ were installed in a fire proof box ⟨*yellow section*⟩ separate from the rest of the equipment for use at room temperature. In case a different, lower vapour precursor was desired in the future a junction ⟨*15*⟩ where an alternative precursor flask could be attached inside the heated oven was also added to the equipment.

When a deposition is being run the valves on the precursor cylinders are opened. Precursor vapour, which is in equilibrium with the liquid precursor in the cylinders, fills the available tubing up to the first pneumatic Swagelok ALD valves ⟨*3a,b,c*⟩. This tubing and the ALD valves are in the section of equipment labelled "oven" ⟨*orange section*⟩ and the oven is heated, usually to 100 °C, to prevent precursor condensation. In the lower section of the oven a fan ⟨*14*⟩ and system of pipes directs air flow from heaters over the ALD valves and vacuum system to ensure uniform heating. The ALD valves employed are specially designed for the very short open/close times and resistance to high temperatures needed for ALD experiments. The first set of ALD valves encountered by the precursors are used as safety valves ⟨*3a,b,c*⟩ which are opened for the duration of a deposition but will close as soon as a problem is detected, shutting off the precursors and so preventing potentially dangerous reactions. This was not the original purpose of this first set of valves, the original set up is discussed in Section 4.4.2.The next set of ALD valves are the release valves ⟨*4a,b,c*⟩, which open in sequence for a set amount of time. When a pair of ALD valves on the same tube line are both open the precursor is released by "vacuum draw" due to the lower pressure of the rest of the system relative to the precursor.[41] The released precursor is carried to the reaction chamber by N_2 carrier gas, a flow of which is constantly passing through the system to the vacuum pump. In the reaction chamber ALD occurs, as described in Section 2.1. Figure 4.2 shows how the opening sequence of the valves relates to the ALD reactions occurring on a substrate surface for a typical ZnO deposition cycle.

The purpose of the N_2 flow through the system is both as a carrier gas and a purge gas. It is important to keep the level of contaminants in the N_2 very low due to the high reactivity of DEZ and TMA to gases such as H_2O which will cause a partially CVD-type growth instead of true ALD. To reduce this issue the N_2 source used is N6 (99.9999 % pure) and is further purified by an Entegris Inert Gas Gatekeeper which lowers the contaminants significantly, for example the H_2O level to <100 ppt.

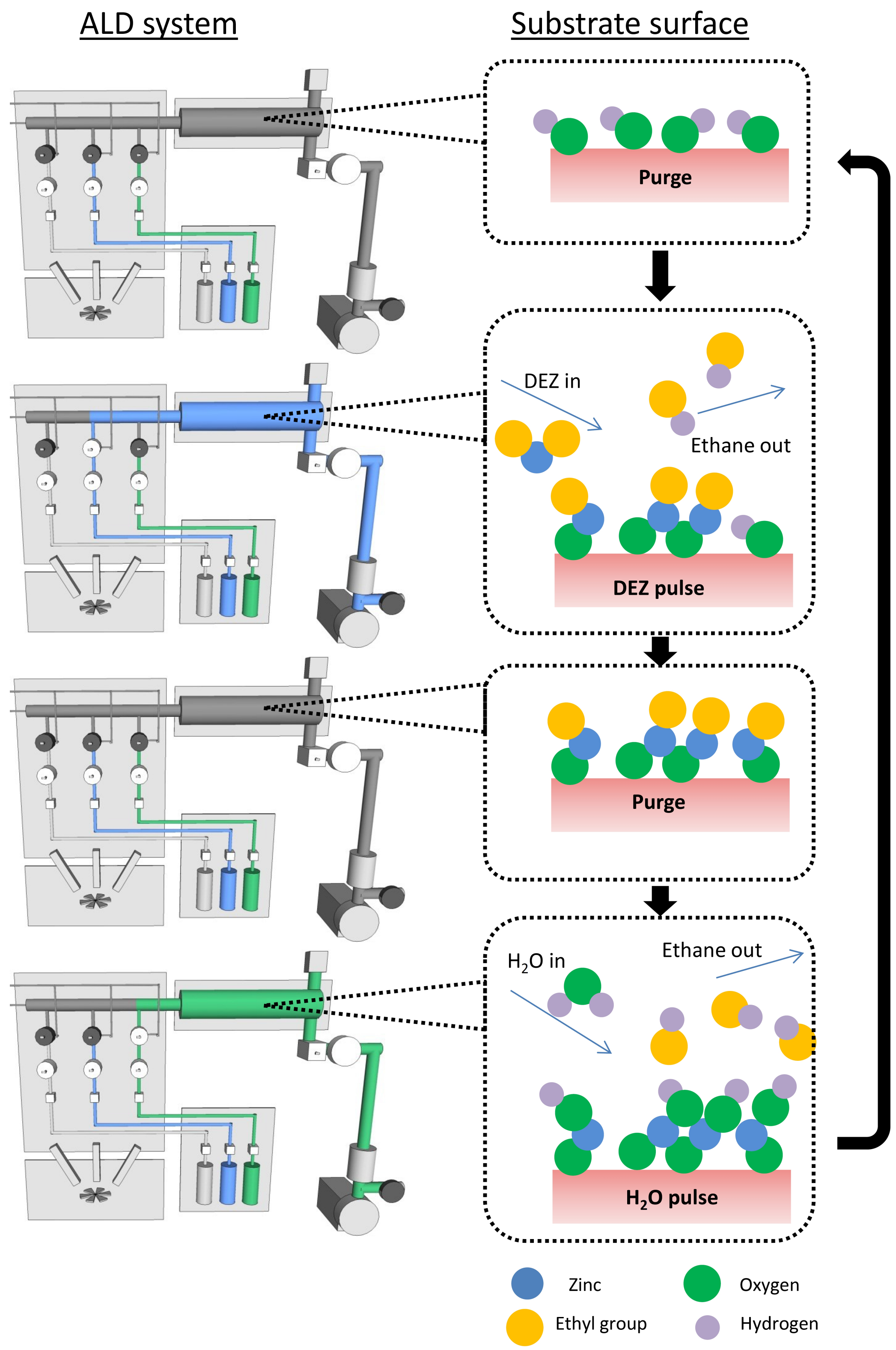

Figure 4.2: Schematic showing the state of the ALD system and the reactions at the substrate surface during a single ALD cycle

The rate of N_2 flow through the system is regulated by two computer-controlled mass flow controllers (MFCs) with maximum flow rates of 30 sccm (standard cm^3 per minute), making a total maximum of 60 sccm. With 60 sccm of N_2 passing through the system the pressure in the deposition chamber is 0.5 mbar, which is satisfactory for ALD, although often slightly higher pressures of around 1.3 mbar are used.

4.2.2 Deposition Chamber and Sample Holders

The substrates for a reaction are placed on a sample holder which is then loaded into the reaction chamber ⟨*7*⟩. Precursors are released as described in Section 4.2.1 and ALD occurs on the substrates' surface. The main requirements are: easy access into the reaction chamber for substrate loading and removal, a uniform heat distribution, a pressure gauge to monitor the chamber state and valves for isolating the chamber from the pump. The chamber is tube furnace style with a blank flange at the end which is removed for sample holder loading. Figure 4.3 shows the design of the reaction chamber and the different sample holders that rest inside. The reaction chamber contains a quartz tube which fits snugly inside the stainless steel outer. This quartz tube can be removed and cleaned or replaced for easy decontamination of the reaction area when necessary. Inside the quartz tube sits the sample platform and roof. The sample platform aids even heating of the sample holder and ensures it has an identical position inside the tube every deposition. Dimples are machined into the sample holder for repeatable substrate positioning whilst being shallow enough to ensure that substrates protrude above the holder top edge. The clearance between the sample roof and a substrate surface is approximately 1.5 mm so that the N_2 and precursors are directed over the substrate surface, enabling more efficient purging and better interaction because of the many collisions of the gases with the surfaces. Two different sample holders were fabricated to allow for the variety of substrates employed in this and future investigations.

Uniform heating of the reaction chamber was another important design consideration. Even though for depositions at temperatures within the ALD window the film thickness should not vary much with temperature, other critical properties may vary, for example crystallinity and stoichiometry. A consistent temperature across the entire sample holder ensures that all substrates coated in the same batch are comparable. Heating tape was wrapped around a copper surround clamped to the stainless steel vacuum tube for even heating; from this copper surround the temperature is monitored by a thermocouple. This design, although a remote way of heating the substrates and monitoring deposition temperature, avoids having to install wiring inside the vacuum system which would be more complicated and less accessible. For insulation, 45 mm of Rocklap and Rockwool surround the chamber and heating tape, followed by two air separated layers of fibre reinforced, fire resistant Masterboard. Two layers of Masterboard were also the chosen insulation for the oven section of the ALD system but further insulation was thought necessary here as the temperatures required will be higher and uniformity is even more crucial.

The pipes at the end of the chamber section, adjacent to the pressure gauge ⟨*8*⟩ and isolation valves ⟨*9,10*⟩, are heated to an intermediate temperature, usually 115 °C. This ensures a gradual temperature decrease away from the substrate location,

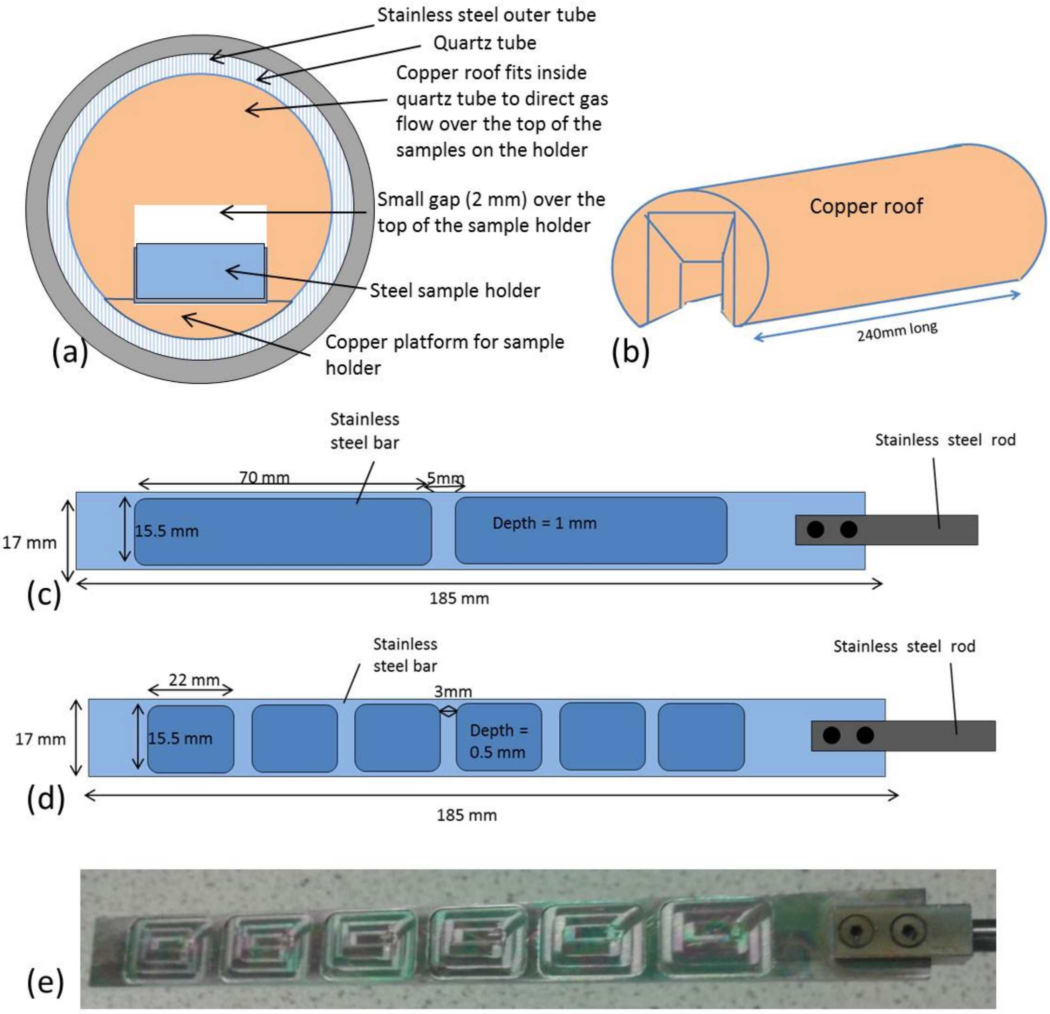

Figure 4.3: (a) Schematic cross-section of the reaction chamber interior and (b) side view of the copper roof. The two sample holders for different sample sizes are shown in (c) and (d), with (e) being a photograph of holder (d).

the shallow gradient preventing sudden precursor condensation whilst distancing the temperature sensitive components from potentially high deposition temperatures.

The pressure in the deposition chamber is monitored during sample loading, ALD growth, and sample removal. This pressure information is displayed to the operator and is necessary for a number of reasons:

- To indicate when the chamber has reached atmospheric pressure and can be opened for loading/unloading.
- To indicate when the correct baseline pressure has been achieved when pumping down the system. If the system is taking an unusually long time to evacuate or does not reach the usual level this can be suggestive of a leak.
- To check the N_2 gas flow and to measure the chamber pressure before and during depositions because this a variable which can affect ALD growth. An increase in chamber pressure above the norm may indicate, amongst many other possibilities, MFC malfunction, a leak, decrease in gas conduction through the trap or a decrease in vacuum pump performance.
- To observe pressure spikes as precursor enters the deposition chamber which confirm that the precursor release is occurring as programmed. If a release valve is faulty or a precursor has been used up there will be no pressure spike even though the release valves may be heard or seen operating.
- To alert the system if there is a sudden problem during deposition e.g. a vacuum pump failure, so the precursors can be safely isolated avoiding potentially hazardous reactions.

When choosing a suitable pressure gauge it was important to consider the way in which the gauges monitor the pressure and the pressure range required. The deposition pressure in the system is 0.5 mbar and the lowest pressure reachable by the vacuum pump is approximately 2×10^{-2} mbar, so a range of 10^{-2} - 10 mbar was targeted. In this pressure regime the thermal conductivity of gas present depends on the pressure and therefore this property can be used for indirect measurement. Pirani gauges function by monitoring a heated wire within the vacuum system: the resistance of the wire depends on its temperature. The gauges are designed to minimise the loss of heat via radiation and conduction through the wire base so that the dominant heat loss route is gas conduction. Gas molecules within the vacuum system continually remove heat on contact with the wire, so the higher the pressure, the larger the number of gas molecules, the greater the heat loss from the wire. Using a feedback system the resistance of the wire is kept constant by adapting the power supplied during any pressure change. By monitoring the resulting bridge voltage the pressure can be calculated. Accurate pressure measurements are limited in range by the insulating layer of hot gas which surrounds the wire when at relatively high pressures, and at low pressures the gas conduction becomes too small relative to the other heat loss mechanisms. The vacuum thermal conductivity is also gas dependant, so due to the variety of gases in ALD (carrier gas, precursors, reaction by-products) the calculated pressure from this method will not always be representative. Also the calculation assumes a room temperature gas whereas the gas in ALD is heated so this will add a systematic error. There are alternative, direct, gas-independent ways of measuring this pressure range, for example capacitance manometers which operate by measuring deflection of a diaphragm due to the pressure difference between system and gauge. This method is considerably more accurate than a Pirani gauge but comes at a much higher financial cost. Pressure accuracy is not a high enough priority for the ALD system to warrant the extra cost, the primary requirements are robustness and the ability to monitor the aspects listed earlier, all of which are provided by a Pirani gauge.

There will be occasions when coating of complex, high aspect ratio structures is required, so precursors will need to be held in the deposition chamber to ensure complete surface coverage.[164] To this end a pneumatic isolation valve ⟨*9*⟩ was positioned at the exit of the reaction chamber before the pump. This valve and the pneumatic N_2 valves ⟨*6e,f*⟩ are closed for the chosen period of time so there is a constant pressure and atmosphere within the chamber, allowing time for precursor diffusion. These valves are then opened for purging as usual.

A manual isolation valve ⟨*10*⟩ is positioned just after the pneumatic valve. This manual valve is closed when turning the pump on/off and is opened slowly to allow gradual pumping/venting of the system, thus avoiding rapid movement of gas which may disturb the samples and blow them from the sample holder.

4.2.3 Evacuation from chamber

After passing through the reaction chamber gases are then extracted from the system via a trap ⟨*12*⟩ and vacuum pump ⟨*13*⟩. To reduce the transfer of vibrations from the pump to the ALD system a flexible bellow ⟨*11*⟩ was positioned between the manual isolation valve ⟨*10*⟩ and pump. All the piping between the reaction chamber and pump is heated to 65 °C to reduce precursor condensation before the trap. This heating is achieved by rope heaters coiled around copper sheet clamped tightly to the pipes to distribute heat evenly, all wrapped with aluminium foil and rubber insulation.

Two different traps were explored in order to protect the vacuum pump from contaminant formed by reactions of the precursors. The first trap tried was a liquid nitrogen (LN_2) cooled trap. With this trap the precursor gases reach the trap and are condensed on the LN_2 cooled inner of the trap, preventing them from reaching the pump. This has been reported in literature[165, 166] but was not found to be practical or effective in this system. The main issues were that the LN_2 evaporated very rapidly from the trap, probably because the low vacuum and heated gases during deposition did not provide enough insulation between the LN_2 filled inner and the room temperature outer of the trap. Also, given that both precursors used in the deposition condensed at this same location a potentially dangerous reaction could occur between them. Instead an activated charcoal filter trap was chosen and proved effective in our system. The filter contains very small pores and so prevents particles from entering the pump and damaging it. The high charcoal surface area may also allow some precursor elimination through surface reactions, but it was observed that, despite the heating of the pipes preceding the pump, there is significant deposition within them so it is likely that only a small portion of the precursor reaches the trap.

The vacuum pump ⟨*13*⟩ used in this system is a scroll pump. This a dry pump that evacuates the system by orbiting a scroll which is interleaved with a stationary scroll. The movement traps gas from the vacuum system and compresses it inside a space with reducing volume, pumping it out to atmosphere. This pump choice does not risk contaminating the system with oil as with rotary vane pumps, and it does not need a backing pump like turbomolecular pumps. Problems can arise in scroll pumps if contaminant particles enter and wear away the bearing surface, but the activated charcoal filter trap prevents this.

4.3 Deposition control

Deposition using the ALD system is controlled by a set of programs written in LabVIEW on a laptop linked to the ALD system. During deposition the pneumatic ALD valves are operated and the pressure inside the reaction chamber is monitored as described previously. Figure 4.4 illustrates the signal transmission processes which enable this communication. Transmitting a signal to an ALD valve requires several steps including the manipulation of a solenoid valve within a compressed air system. When open (solenoid powered), the solenoid valve allows compressed air into the tube attached to the respective ALD valve; when closed (solenoid off), the valve releases to atmosphere any compressed air in the tube attached to the ALD valve. The ALD valve contains a diaphragm which responds to the pneumatic pressure signal. Using air pressure for remote control of the ALD valves is necessary because the ALD valves are in a heated area of the equipment incompatible with electronics.

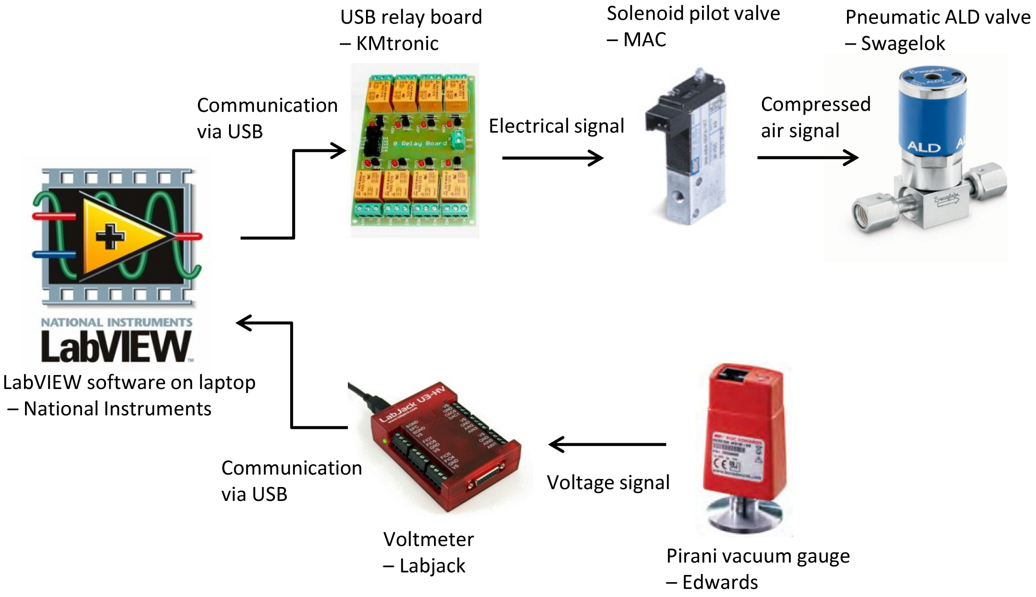

Figure 4.4: Schematic showing the steps in transmitting signals for ALD valve control and pressure monitoring by LabVIEW. The component images are sourced from the respective manufacturers' websites

4.3.1 LabVIEW program

LabVIEW is a very visual software, with programs arranged as flow diagrams and symbols instead of lines of text and many common functions for measurement and control are available already written. This software is therefore a good choice for the ALD system and enables easy editing of programs when different deposition sequences are designed; other groups have also chosen to use LabVIEW for their ALD systems with alternative program designs to the one here.[52, 167]

The ALD program was split into 5 separate programs which are run in sequence. The programs are Start up, Loading samples, Safety valve opening, Deposition program, Post deposition sequence. The purpose for splitting the programs was to enable the deposition sequence program to be modified independently, and to make the overall control more flexible and safer. Separating programs gives obvious, easy stopping points for when problems arise during an individual step e.g. sample loading. Also, the user is forced to be present when the ALD cycles start to check that they are occurring properly and that the correct conditions e.g. temperatures have been reached. Table 4.1 summarises the purpose of each program and details the main actions taken by the program (the deposition programs are discussed more later in this section). As mentioned in Section 4.2.1 the N_2 MFCs are also laptop-controlled but using a program provided by the manufacturer, Brooks. It was considered complicated and unnecessary to control the MFCs using LabVIEW, and there would be no significant advantage as their settings are adjusted only twice in a deposition (N_2 flow is started after sample loading and is stopped before sample unloading).

The valve opening sequence and timings for ALD depositions vary depending on the precursors, substrates and material being deposited. A general deposition program with adjustable purge and release timings was written and other deposition programs were developed from this basis when necessary. Figure 4.5 shows the general deposition program user screen and the two loops of the deposition cycle section of the program (one loop for DEZ-H_2O, the other for TMA-H_2O). Before the deposition is run, the user enters the timings and deposition conditions to be used. The general operating principle of the program is:

1. first ALD release valve is opened by running a subVI
2. program waits for a chosen interval (the precursor release time)
3. ALD release valve is closed
4. program waits for a longer time during which the released precursor is removed from the chamber
5. next ALD release valve is opened, etc.

The ratio of DEZ-H_2O to TMA-H_2O cycles, i.e. the number of times each “for loop” in Figure 4.5 is repeated before moving on, is chosen by entering values in the *No. of DEZ per overall* and *No. of TMA per overall* boxes. This determines what material is deposited e.g. 1:0 for ZnO (as set in Figure 4.5), 0:1 for Al_2O_3, x:1 for Al doped ZnO. The number of repetitions of the overall “while loop” (set through the *Number of overall cycles* box) controls the final film thickness. Whilst the deposition runs, the release of precursors can be followed on the pressure graph vs. time graph and the number of cycles completed counts upwards (see the *No. of overall cycles on* box). Once the deposition has finished a notice appears on the

Number	Program name	Description
0	Pressure monitoring	Reports the pressure in the system. This program runs constantly during all steps (except during Step 4) giving the user information on what is occuring in the system e.g. whether the system has reached atmospheric pressure. It is not set up to take action at any pressure due to the range of pressures encountered in these steps.
1	Start up	After the ALD system has been completely shutdown for a while preliminary checks and steps, e.g. opening gas cylinder valves, need to be followed before loading can begin. Step by step instructions are given.
2	Loading samples	The system is vented so that samples can be loaded. It is then evacuated and purging is started while the system heats to the required temperature.
3	Safety valve opening	The relevant safety valves are opened in preparation for deposition.
4	Deposition programs	The required deposition program is selected and the deposition sequence is carried out with the parameters entered. Pressure monitoring is incorporated into the program so the deposition can be stopped if the pressure is abnormal, therefore program 0 is not used.
5	Post-deposition	The safety valves are closed and the system is allowed to cool. The chamber is vented to allow the samples to be removed and then returned to vacuum with the system ending on either a pre-program 3 state or a stand-by state.
-	Individual control of valves	Consists of an array of on/off buttons for all the valves and can be used in unusual situations such as loading new precursors into the system or if one of the set programs has to be stopped midway and the system needs to be returned to a neutral state.

Table 4.1: Table showing the separate programs created for the ALD system control. The most frequent procedure is: start 0, run 2, 3, stop 0, run 4, start 0, run 5, stop 0.

screen and the program sends an email in case the user is not in the laboratory. The program automatically saves the pressure data along with the deposition conditions as an Excel file for future reference. Refer to the Appendix for a more detailed description of the program.

Safety features are an important part of the program, especially as the user will not necessarily be present whilst the ALD is running. Firstly, there is an emergency stop button on the program to stop the deposition. When the button is operated, the safety and release ALD valves close, isolating the precursors from the reaction chamber; the pneumatic furnace isolation valve is held open so that the furnace is being evacuated by the pump (it is usually open during deposition except when a program with a hold step is run); and the program halts and sends an email saying an emergency has occurred. The program is also set up to identify emergencies by monitoring pressure. On each opening of a release valve there is a spike in pressure indicating precursors reaching the deposition chamber followed by a rapid return to the N_2 purge pressure as precursors and by-products are removed (Figure 4.8). If there is a fault, for example the vacuum pump failing, the pressure will increase to an abnormally high value, above the usual pressure spike value. On detecting this, the ALD program responds with the same process described earlier for the emergency stop button. In the event of a power cut all the solenoid valves will switch off, closing the ALD valves and thus leaving the system in a safe state.

4.4 Preliminary investigations

After completion of construction of the fledgling ALD system, the primary aim was to confirm that ZnO and Al_2O_3 could be deposited and that the reactor performance was as desired and comparable to the literature. Trial depositions were run and modifications were made to the equipment.

4.4.1 Substrate cleaning

The cleaning procedure was found to be crucial in obtaining uniform films as contamination blocks the substrate's surface chemical groups. A procedure of cleaning the substrates through sonication and rinsing sequentially in acetone, H_2O and isopropanol, followed by immediate blowing dry under N_2 flow and cleaning by UV-ozone was adopted. The handling of the clean substrates was also crucial, touching with gloves can contaminate the surface so tweezers should always be used and the substrate should be held by the edges.

4.4.2 Valve operation and sample holder modifications

The initial sample holder design was different from the one shown in Figure 4.3. Samples were on a holder suspended centrally in the chamber which otherwise contained only the quartz tube lining. The holder was connected via a metal rod to the blank flange at the end of the chamber and had no contact with the chamber walls. Furthermore, the deposition sequence was not as in Figure 4.2, where the first set of valves $\langle \mathit{3a,b,c} \rangle$ are safety valves and the second set $\langle \mathit{4a,b,c} \rangle$ are release valves.

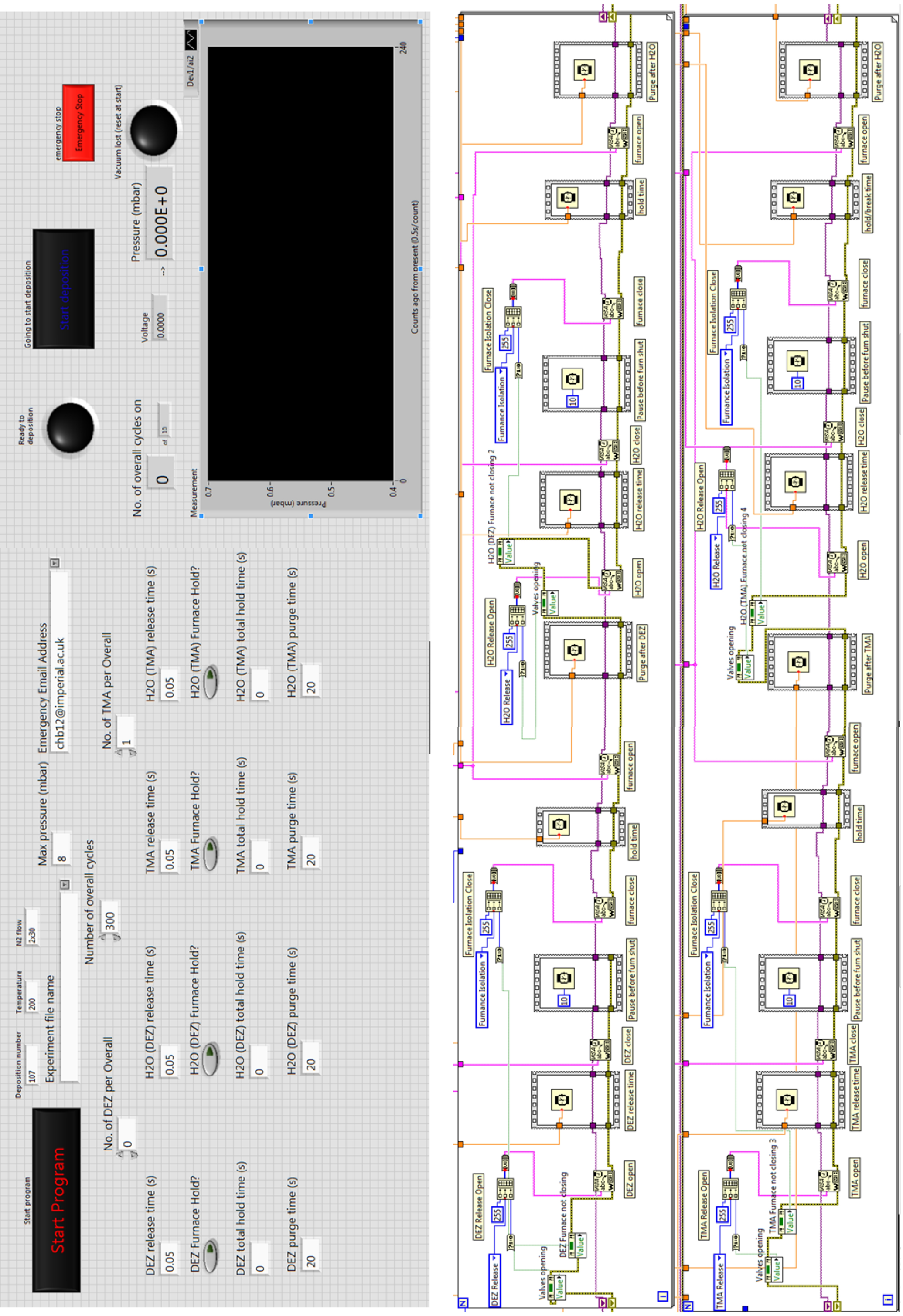

Deposition number 107

Temperature 200

N2 flow 2x30

Experiment file name

Max pressure (mbar) 8

Emergency Email Address chb12@imperial.ac.uk

Number of overall cycles 300

No. of DEZ per Overall 0

No. of TMA per Overall 1

DEZ release time (s) 0.05

DEZ Furnace Hold?

DEZ total hold time (s) 0

DEZ purge time (s) 20

H2O (DEZ) release time (s) 0.05

H2O (DEZ) Furnace Hold?

H2O (DEZ) total hold time (s) 0

H2O (DEZ) purge time (s) 20

TMA release time (s) 0.05

TMA Furnace Hold?

TMA total hold time (s) 0

TMA purge time (s) 20

H2O (TMA) release time (s) 0.05

H2O (TMA) Furnace Hold?

H2O (TMA) total hold time (s) 0

H2O (TMA) purge time (s) 20

No. of overall cycles on 0 of 10

Voltage 0.0000

Pressure (mbar) 0.000E+0

Figure 4.5: LabVIEW program user screen for a typical ALD deposition program and the deposition cycle section of the block diagram i.e. the DEZ-H_2O and TMA-H_2O ”for loops”

Instead, valves ⟨*3a,b,c*⟩ were buffer valves, opened for several seconds to allow the precursor vapour from the relevant cylinder to diffuse into the short tube section between the two ALD valves. The buffer valve was then closed so a fixed volume and therefore a repeatable amount of precursor was contained. Next the respective ALD release valve ⟨*4a,b,c*⟩ opened for a prolonged time, releasing all the precursor contained within the short tube section, and a purge time followed. This is a sequence which has been used in other reactors,[41, 168] often with additional vacuum pumps to evacuate the tube section between the valves before the buffer valve opens.

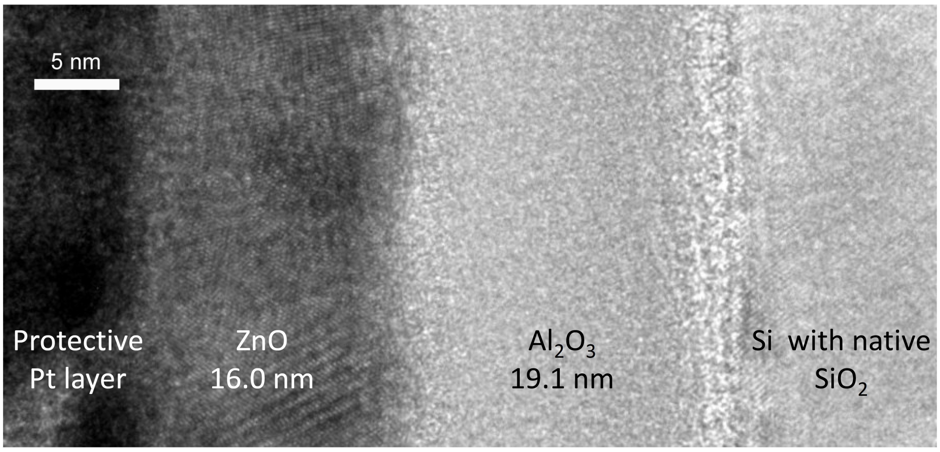

Figure 4.6: Cross-sectional high resolution (HR)TEM image of Al_2O_3/ZnO bilayer deposited by unsaturated ALD on a Si/native SiO_2 substrate. Al_2O_3 GPC = 0.06 nm/cycle (literature value 0.10-0.11 nm/cycle[4]), ZnO GPC = 0.08 nm/cycle (literature value 0.18-0.22 nm/cycle[12]). No beam block was available so a diffraction pattern image could not be taken, but diffraction spots due to crystalline ZnO were present, and Moiré fringes can be seen within the ZnO layer.

Using the original sample holder and valve opening sequence, ZnO and Al_2O_3 depositions were run. The correct material was confirmed deposited (from measurements using XRD, UV-vis, Hall (ZnO) and spectral reflectance (Al_2O_3), results not shown), however, cross-sectional TEM revealed that the growth per cycle (GPC) was significantly lower than expected for the ALD conditions (Figure 4.6). This indicated the surface reactions were unsaturated due to insufficient precursor exposure. To combat this the sample holder was redesigned to sit on a platform within the chamber, with only a small gap above the substrates for the precursor and purge gas to pass through. This design ensures the precursors pass directly over the sample resulting in many collisions with the surface, helping to saturate the reaction. The contact of the holder with the furnace wall will also help substrate heating; cool temperatures can give low GPC. The deposition sequence was switched to the direct draw method described in Section 4.2.1 in order to raise the amount of precursor released to also aid saturation.

4.4.3 Deposition uniformity

An important aspect in ensuring uniform deposition is temperature control. To check that temperature is even and the external thermocouple measurements give

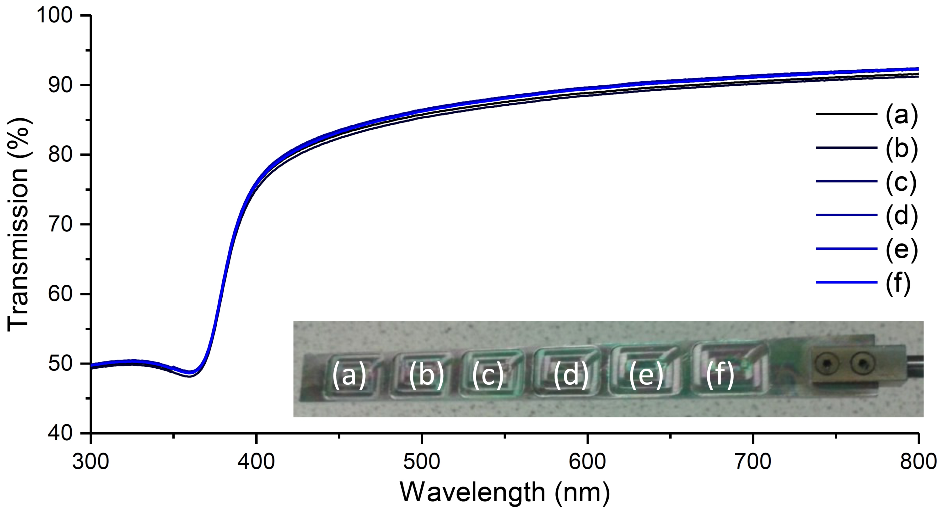

Figure 4.7: UV-Vis transmission spectra of ZnO on quartz deposited at different locations on the sample holder.

a representative substrate temperature, "temperature labels" were attached to the sample holders and heated under deposition conditions. Temperature labels have ten indicator circles with different temperature thresholds at which they undergo a permanent colour change (white to black). For temperatures of 70, 110 and 150 °C the temperature reached after a time equivalent to the pre-deposition equilibration time was equal to the thermocouple measurements to within the 6 °C precision of the indicator circles. Caution was taken to ensure deposition conditions (i.e. the correct chamber pressure and N_2 flow) were acquired before beginning the chamber heating and during chamber cooling after the temperature setpoint hold period had finished. This was to make sure the temperature measurement was due to the heating under a representative atmosphere and not due to heating at room pressure, as the indicator circles will show the maximum temperature reached but is not possible to know at what point that temperature was reached. In addition, a low temperature ramping rate was used to avoid significant overshoot.

To test the ALD growth uniformity, which will depend on gas flow and temperature, ZnO and Al_2O_3 were deposited on quartz and Si/SiO_2 substrates respectively. Figure 4.7 shows that the ZnO layers produced at the different substrate holder positions were consistent (very similar UV-Vis spectra). The Al_2O_3 coating was also of uniform thickness across the sample holder, with an average GPC of 0.115 nm/cycle at 150 °C. 500 ALD cycles produced Al_2O_3 of thickness ranging from 58.00 nm at the sample holder leading edge to 56.95 nm at the trailing edge, as measured by spectral reflectance fitting.

4.4.4 Precursor release times

Adjustment of precursor release times is one of the system-specific factors which needs to be adjusted for deposition optimisation. Shorter release times result in less precursor wastage, but release times need to be long enough to ensure there is enough precursor for saturated growth. The minimum possible release time for the ALD valves in the system is affected by the time taken for each step that the open/close (O/C) signal goes through as it is sent from the computer to the diaphragm valve (schematic of steps is shown in Figure 4.4). The time for each individual step is presented in Table 4.2.

	Step	Description	Opening Time	Closing Time
1	LabVIEW sending O/C signal	Milisecond timings are readily programmable in LabVIEW	negligible	negligible
2	O/C signal transfer	Signal from computer USB port to relay	negligible	negligible
3	Relay switch O/C	USB signal switches reed switch	<10 ms	<5 ms
4	Solenoid valve O/C	The solenoid in the valve is energised/de-energised moving the poppet, allowing compressed air to flow between chosen paths	3.4 ms	1.5 ms
5	Compressed air (5 bar) travelling into /out of tube to ALD valve	Compressed air flow rate through each tube is unknown but very rapid from observation. The shortest pipes reasonably practicable were used, with smooth bends for better flow	quick	quick
6	O/C of pneumatic ALD valve	The pressure of air in the ALD valve actuator assembly controls the position of the diaphragm which opens or closes the precursor paths through the valve	<5 ms	<5 ms
		Approximate maximum total time for process	18.4 ms	11.5 ms

Table 4.2: Table presenting the steps and timings associated with opening/closing (O/C) the ALD valves which control the release of precursors. Timings are taken from manufacturer data sheets.

To investigate the O/C behaviour experimentally, a series of different release times for DEZ and H_2O were carried out whilst monitoring the reaction chamber pressure to detect precursor release. Figure 4.8 shows the pressure signal during the experiment, and it can be seen that for short release times no DEZ pressure spike is seen. A faint sound of compressed air being released from the MAC solenoid valves can be heard with programmed times of 6 ms, indicating that that solenoids are operating, but a lack of detectable pressure spike for DEZ and a very small H_2O peak show that 6 ms is considerably too short for this ALD system. Below 6 ms release time there is no compressed air release heard at all. This tallies approximately with the calculated maximum O/C timings in Table 4.2, for which the opening time for an ALD valve was found to be around 6.9 ms longer than the closing time, so at times $\lesssim$ 6.9 ms no valve actuation would be expected.

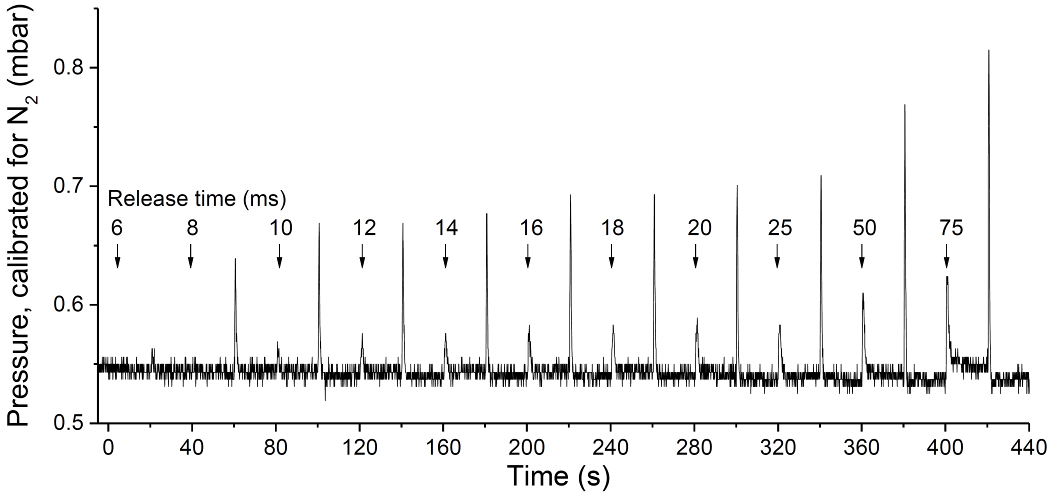

Figure 4.8: Pressure response of the Pirani gauge for DEZ - H_2O release pairs of different lengths. Each DEZ release instant is indicated with an arrow labelled with the release time length and there are 20 s purges between the sequential precursor releases.

From 10 ms onwards there are visible pressure spikes corresponding with both DEZ and H_2O release. The peaks increase in magnitude with time as larger precursor amounts are released. Depositions of 300 DEZ-H_2O cycles with different precursor release times were carried out at 125 °C to investigate the effects on the deposited films. For release times between 15 and 75 ms the thickness of ZnO films was 55.4 $\pm$ 1.3 nm (by SEM), corresponding to a GPC of 0.185 nm/cycle, indicating that saturated growth was reached. For a 10 ms release time there was no measurable ZnO layer deposited; Figure 4.9(a) shows the lack of characteristic ZnO absorbance for 10 ms compared to longer release times. In Figure 4.8 the pressure value does not appear to drop to the baseline 0.55 mbar after the 75 ms DEZ release. One explanation of this could be that the DEZ has not been completely purged from the pressure gauge area within the 20 s allotted time. If there was remnant DEZ surrounding the substrates then an increased GPC would be expected due to a CVD contribution to the growth. There is, however, no GPC increase so the volume surrounding the substrates must be sufficiently purged, but perhaps because the pressure gauge is connected to a port perpendicular to the tube chamber (Figure 4.1), the volume surrounding the gauge may not be as effectively purged. Ideally the arrangement of the gauge and purging would be redesigned to improve precursor removal, but for this newly built reactor longer release times were instead avoided.

The electrical properties of ZnO with precursor release $\geq$ 15 ms were found to be time dependant despite GPC having saturated (Figure 4.9(b)-(d)). The mobility and carrier concentration of ZnO were lower for the shorter release times, and plateaued for 50 ms and above. The anomalously low carrier concentration and mobility for the 25 ms release time is thought to be due to human error in substrate cleaning. Higher mobility is often preferable for ZnO, suggesting good crystal quality, therefore the longer release times seem desirable. There have been investigations in the literature into the effects of release times and generally the main results seen are slight changes to the electrical properties of ZnO,[169] as observed here. In order to limit the number of variables to investigate in Chapter 5, a fixed release time of 50 ms was settled on for DEZ, TMA, and H_2O. This time is around eight times

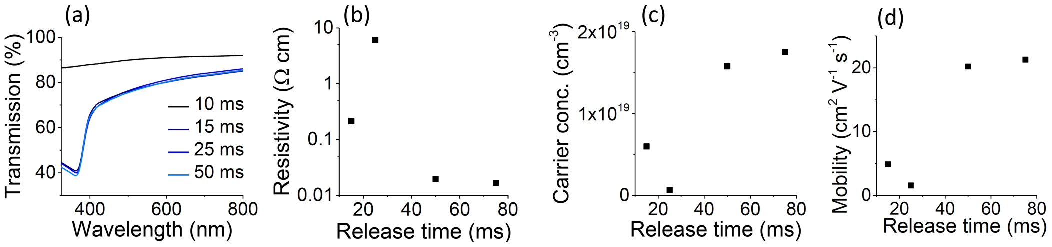

Figure 4.9: (a) UV-Vis transmission spectra for quartz substrates with ZnO deposited using different DEZ-H_2O release times. The 10 ms transmission is similar to lone quartz. (b) Van der Pauw resistivity and Hall (c) carrier concentration and (d) mobility measured for different release times. The depositions were at 125 °C with 20 s purge times.

greater than the minimum valve operation time, and the extra leeway is sufficiently large to ensure any variability in the opening times is small compared to the total opening time, allowing repeatable release times.

4.5 Conclusions

- The custom-designed ALD system was designed and constructed with successful operation demonstrated.
- Preliminary testing was used to improve the deposition chamber and the programmed deposition sequence.
- Precursor release times of 50 ms were chosen for DEZ, TMA and H_2O, being a compromise between saturated growth, high ZnO conductivity, remnant precursor issues and repeatable release time lengths.
- Both ZnO and Al_2O_3 were deposited successfully, with properties matching literature values. The ALD was ready for the system-specific deposition analysis and optimisation which follow in Chapter 5.

Chapter 5

Alumina and zinc oxide film calibration

A wide variety of materials have been successfully grown by ALD, and due to the fundamental self-limiting nature of ALD growth the properties of these materials should be the same irrespective of the ALD system used. This is a valuable quality which allows reproducible results between different researchers. The ALD system that has been constructed can therefore be thoroughly tested to check that ALD growth is occurring properly by comparing results to those in the literature. There are a large number of publications of ALD grown ZnO and Al_2O_3 so the general investigation of the growth itself is not novel, but this is a vital process that is required every time a new combination of precursors and reactor is used. There will be differences in the release and purge times needed for different ALD systems as these depend on features such as the substrate size, reactor shape and pumping rate. However once these timings are adjusted so that saturated growth is occurring the growth per cycle (GPC) and other properties will be consistent with the literature values.

Small variations in GPC both from and in the literature may arise for a number of different reasons. Obtaining sufficiently pure carrier gas can be a challenge and it is difficult to compare how pure the carrier gas is between different groups' equipment. Often papers will not include details on the purity of their carrier gas or extra purifying devices installed in their system. Small amounts of contaminants such as H_2O in the carrier gas will give rise to a CVD contribution to the GPC leading to a higher value than true ALD. Another source of variations is the method of determining the temperature of the substrate surface. Techniques vary from installing a thermocouple inside a heating block within the vacuum system, to heating the reaction chamber from outside and measuring the external temperature. It is clear that there will therefore be some variation in the accuracy of growth temperatures between different systems which will affect ensuing results. Fortunately, when depositing at a temperature within the ALD window there will only be a small variation in GPC and other properties with temperature differences of a few degrees. These and other origins of growth dissimilarities have to be considered when comparing results, but when true ALD is occurring the growth should be very similar.

In this chapter, growth of Al_2O_3, ZnO and Al doped ZnO (AZO) is characterised for the ALD system constructed. The effects of number of deposition cycles, precursor release times, purge times and deposition temperature are systematically investigated and comparisons with literature are made. From this study the conditions needed for ALD growth in this specific system will be found and optimised, and then the ALD reactor can be confidently used to deposit these layers in more complex, novel situations. Additionally, this chapter contains an analysis of the effects of purge time on the properties of ZnO and how this affects the performance of transistors and OPVs.

5.1 Alumina growth

The trimethyl aluminium (TMA)-H_2O combination of precursors for growing ALD Al_2O_3 is very popular and has a growth per cycle (GPC) $\approx$ 0.10 - 0.12 nm/cycle.[4] This GPC is around 30 % of an Al_2O_3 monolayer per cycle (monolayer $\approx$ 0.38 nm)[137] due to steric hinderance from methyl groups and surface species' densities. TMA-H_2O is often considered to exhibit near-ideal ALD behaviour although there are some apparently contradictory results, for example, on the chemistry behind GPC variations with temperature.[170]

Al_2O_3 is an insulating material and is used for a range of applications including as a dielectric layer in thin film transistors. However, in this project the intention was to use Al_2O_3 mainly as an ultrathin, passivating layer for coating materials such as ZnO without significantly inhibiting charge transfer at the interface, so during this calibration and optimisation section properties such as dielectric constant and breakdown voltage were not investigated. The properties that were focussed on were the thickness and GPC in order to confirm true ALD was achieved. The thickness was found through measuring the spectral reflectance of Al_2O_3 deposited on Si/native SiO_x and fitting the spectrum to a model using Filmetrics software, the details of which are in Section 3.1.2. The fitted thickness value, found using a model ALD Al_2O_3 layer created from a representative sample, was compared to a TEM cross-section to confirm that the model was accurate (Figure 5.1 (a), (b)). The coating of samples across the sample holder was found to only vary by 1 nm (2 % of deposited thickness) and therefore is sufficiently uniform for ALD (Figure 5.1 (c)). A slight Al_2O_3 thickness gradient with position in the sample holder was found, with thickness generally decreasing with distance from the leading edge of the holder, probably because the cross-flow design of the reactor results in samples experiencing slightly different precursor and by-product concentrations (Section 4.1). A slight variation in refractive index of the Al_2O_3 could have also affected the fitted thickness but when allowed to vary there was no obvious trend in refractive index across the sample holder.

From the brief study in Section 4.4 it was decided that a 50 ms release time would be used for the DEZ, TMA and H_2O ALD precursors. This choice was later supported with the investigation into Al_2O_3 on a higher aspect ratio substrates which revealed a uniform thickness coating within the pores, negating any sub-saturation concerns (Section 8.1). A purge time of 20 s was selected as adequate for TMA and H_2O precursor and by-product removal. This choice was made for several reasons. Firstly, a more detailed investigation into ZnO properties with purge time found that purges of 15 s or more were adequate for the DEZ-H_2O combination (Section 5.2.3),

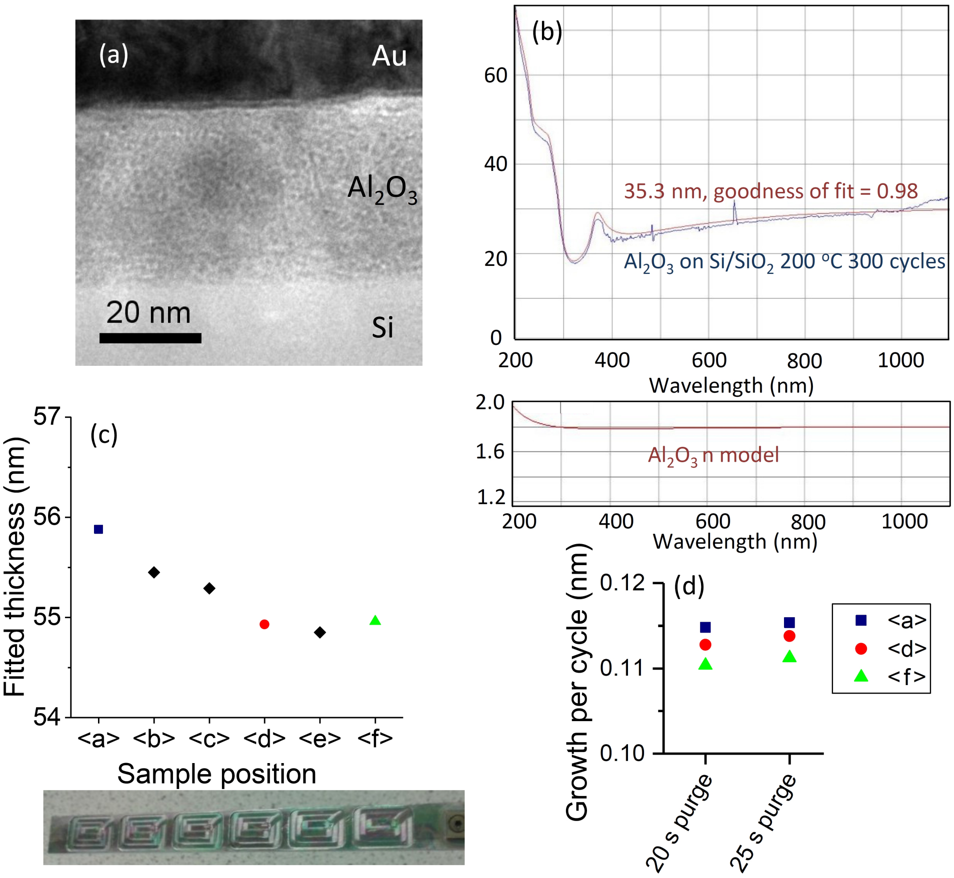

Figure 5.1: (a) cross-sectional TEM for a sample from position ⟨c⟩, with thickness of 35.5 ± 0.5 nm compared to (b) spectral reflectance of sample from position ⟨d⟩, with fitted thickness of 35.3 nm. The model refractive index, n, is also shown. (c) the variation of fitted thickness for the sample positions ⟨a⟩- ⟨f⟩ across the sample holder. Holder image is shown beneath (500 ALD cycles, 150 °C) (d) Comparison of fitted GPC found for samples deposited using 20 s and 25 s purge times (300 ALD cycles, 150 °C)

and although TMA, H_2O and DEZ have different properties the purge time would be expected to be of a similar magnitude due to similarities in vapour pressures etc. Secondly, there was no change in Al_2O_3 thickness when using a purge time of 20 s compared to 25 s at 150 °C (Figure 5.1 (d)). Additionally, the further studies in this section and in Section 8.1 showed the Al_2O_3 properties matched literature values when using a 20 s purge time.

The dependence of Al_2O_3 thickness on deposition temperature is shown in Figure 5.2(a), (b). The trend of increasing GPC with temperature to a peak value $\approx$ 0.12 at around 175 °C then decreasing at higher temperature agrees with literature trends.[4,52] At lower temperatures there is higher coverage of the surface with reactive species but the thermal activation barrier is harder to overcome so the GPC is lower. At higher temperatures reaction occurs more easily but there are fewer surface groups, although there are conflicting reports as to whether both –OH and –CH_3 groups decrease[137] or just –OH groups.[4] The quality of the deposited Al_2O_3 also changes with deposition temperature. It has been reported that the density of Al_2O_3 increases with temperature and the amount of hydrogen contaminant decreases.[52] Allowing the refractive index in the model of Al_2O_3 to vary, the fitted

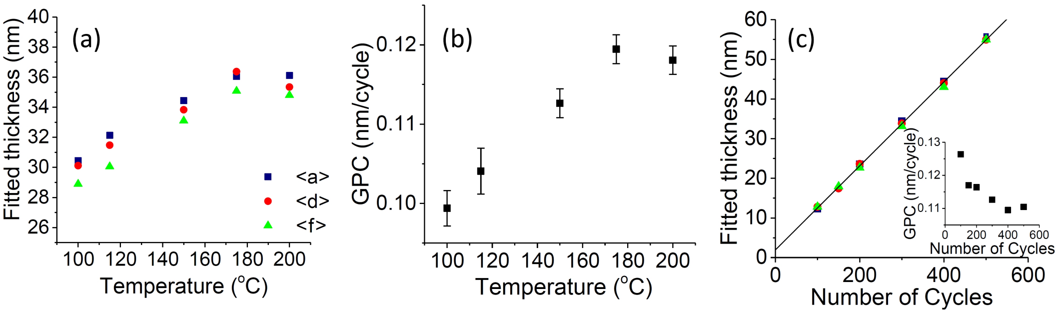

Figure 5.2: (a) Fitted Al_2O_3 thickness with temperature (300 TMA-H_2O cycles) and (b) the calculated GPC. (c) The fitted thickness with number of cycles (150 °C). Best fit line gradient = 0.106 nm/cycle, intercept = 1.9 nm. Inset shows calculated GPC (thickness divided by number of cycles) variation with number of cycles

value increased from 1.74 at 100 °C to 1.81 at 200 °C. This trend in refractive index agrees with results of Groner et al.[52] but is about 0.15 higher than their values, which might be due to the limitations of the spectral reflectance fitting used here, as discussed below.

The GPC in Figure 5.2(b) was calculated by dividing by the number of cycles. However, as shown in Figure 5.2(c), this is not necessarily precisely correct. Although general ALD has an approximately linear thickness increase with cycles, detailed studies often reveal some variation in growth rate, especially at the nucleation stage. The amorphous nature of Al_2O_3 allows the film to grow conformally over a surface so GPC is more easily studied without the added complication of increasing roughness with thickness which is often seen in crystalline films. The fitted thickness of the Al_2O_3 with number of ALD cycles is approximately linear, indicated by the best fit line which has a gradient (approximate GPC) of 0.106 nm/cycle which is fairly consistent with literature values. However, the line does not either pass through the origin, which would indicate an equal GPC on Si/SiO_x and Al_2O_3 surfaces, or intercept the x-axis, which would indicate a nucleation delay or reduced GPC for a number of cycles approximately equal to the value of the intercept. Instead, the line intercepts the y-axis at a value of 1.9 nm, which suggests enhanced GPC on the substrate compared to Al_2O_3. Substrate-enhanced GPCs have been reported for TMA-H_2O in combination with a few substrates, for example on Ru where the surface RuO_2 is reduced to Ru by TMA, producing in a relatively thick initial Al_2O_3 layer.[171] Nonetheless, to my knowledge there are not any reports of this phenomenon for Al_2O_3 on Si/SiO_x; SiO_x remains present and growth is usually reported to be linear[52] or substrate inhibited, which is attributed either to the lower density of –OH groups on SiO_2 which gradually increases with ALD cycles[4] or to the less reactive surface species initially formed after the first ALD cycle compared to Al_2O_3 surface species.[107] Given the abnormal behaviour here, alternative factors which could result in an apparent GPC enhancement were considered.

If there is truly a higher initial GPC, one explanation could be adsorbed species on the native SiO_x surface. The substrates were cleaned thoroughly as described in Section 4.4 so organic residues will have been removed. Adsorption of H_2O to the hydrophilic surface may have occurred which could increase the initial deposition rate, but the substrates were purged under N_2 at 0.5 mbar whilst ramping to and equilibrating at the deposition temperature of 150 °C, a process which took 1 hour, so it is likely that any H_2O would have desorbed. The change in deposition rate could instead be linked to changes in the precursor vapour pressure as the deposition proceeds, which is sometimes an overlooked consideration in ALD. The time between each subsequent release of TMA or H_2O is 40 s, which is relatively long for ALD and should allow reasonable equilibration but this does not entirely eliminate the possibility, especially for films with high numbers of cycles.

Alternatively, if the model to which the spectral reflectance is fitted is not sufficiently representative, this could also result in a systematic error which would have a more significant affect on the modelling of thinner films and thus lead to the best fit line 1.9nm intercept. One possible origin of this could be the modelling of the native SiO_x layer which is modelled as 2 nm thick. In a later cross-sectional TEM image (Figure 5.3) the SiO_x had a thickness of 2.0 ± 0.2 nm, but other substrates may have a different SiO_x thickness originally or after the 10 minute UV-ozone cleaning step. One study reported a 0.3 nm SiO_x increase after 10 minutes[172] which would be a large thickness percentage increase for the 2 nm used in the model. The spectral reflectance measurement and fitting system also has limitations on how thick a layer can be measured; the manufacturer states the limit to be material dependent and $\approx$ 15 nm. The GPC calculated from dividing thickness by cycles seems to plateau with thicker films of 400-500 cycles (Figure 5.2(c) inset) so the thinner layers might be beyond the accurate range of the measurement system.

The origin of the slight variation of GPC from expected behaviour could be clarified by further cross-sectional TEM measurements or by ellipsometry, but this was not a high priority for the project. The thickness of films of 300 cycles and above measured by spectral reflectance was considered to be a sufficiently good approximation. In the following chapters Al_2O_3 will be mostly employed as an ultrathin layer (<5 nm) in devices and will generally be discussed in terms of number of cycles rather than a thickness.

5.2 Zinc oxide growth

Initial investigations of ZnO growth confirmed that a thin film could be deposited on glass, quartz and Si with native oxide. The films were crystalline, as seen in cross-sectional TEM (Figure 5.3 (a)) where Moiré fringes indicate the presence of overlapping of ZnO crystals. UV-vis and XRD (shown later in this section) indicated the films grown had the expected band gap and crystal structure of ZnO. After this success, the deposition conditions were varied and the effects investigated. Deposition parameters, even for saturated ALD growth, can affect electrical and optical properties so optimising the growth of ZnO was important for incorporating the ZnO layers in devices. From the study in Section 4.4, a fixed precursor release time of 50 ms was chosen.

ZnO layer characterisation was carried out through the following techiques: thickness by cross-sectional SEM, optical properties by UV-vis spectroscopy, crystallinity by XRD and electrical performance by Van der Pauw and Hall. For Al_2O_3

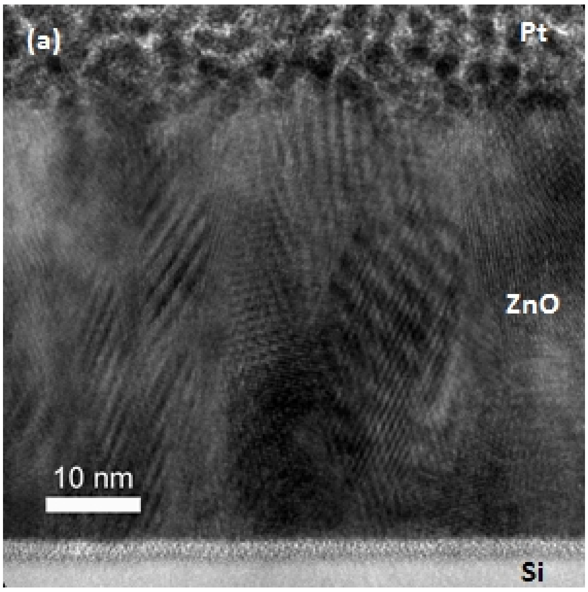

Figure 5.3: (a) Cross-sectional HRTEM image of 50 ± 1 nm thick ZnO film deposited on Si/native SiO_x using 300 ZnO-H_2O cycles, 30 s purge, 125°C.

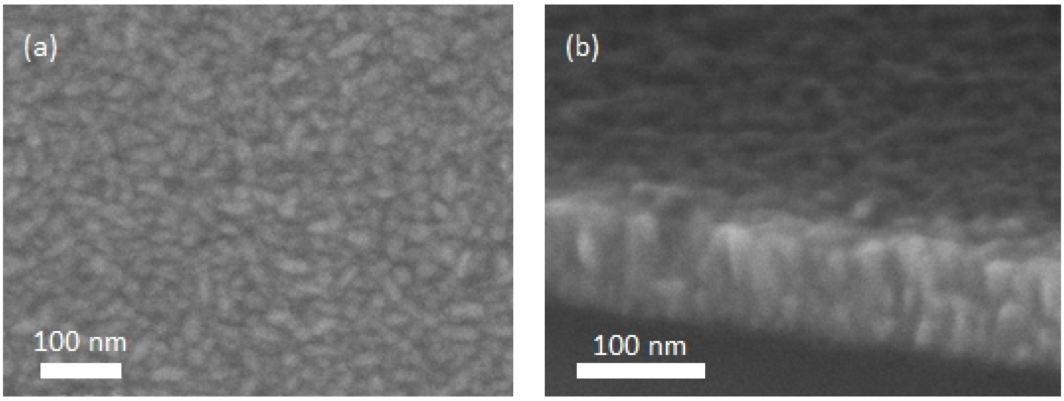

Figure 5.4: (a) Top-view and (b) cross-sectional view SEM images of a 400 cycle ZnO thin film deposited at 125 °C. Mean ZnO thickness is 79 ± 2 nm

spectral reflectance fitted to a model was used for thickness measurement (Section 5), but measurements were not possible for the ZnO films partially because of the more complex fitting parameters needed for semiconducting films and also due to the crystallinity and roughness of the films. Ellipsometry could have been used for thickness measurements of these films but was not readily available so instead SEM cross-sections were chosen as the measurement method. Using SEM cross-sections to measure thickness proved an adequate and quick enough method (Figure 5.4).

5.2.1 Number of cycles

The GPC of ZnO with number of cycles was found to be linear (Figure 5.5(a)). From the best fit line the GPC was calculated to be 0.201 nm/cycle with a 7.1 cycle intercept indicating delayed nucleation or slower initial GPC on the Si/SiO_x substrate. This matches the literature reports of a briefly lower intial GPC followed by a linear

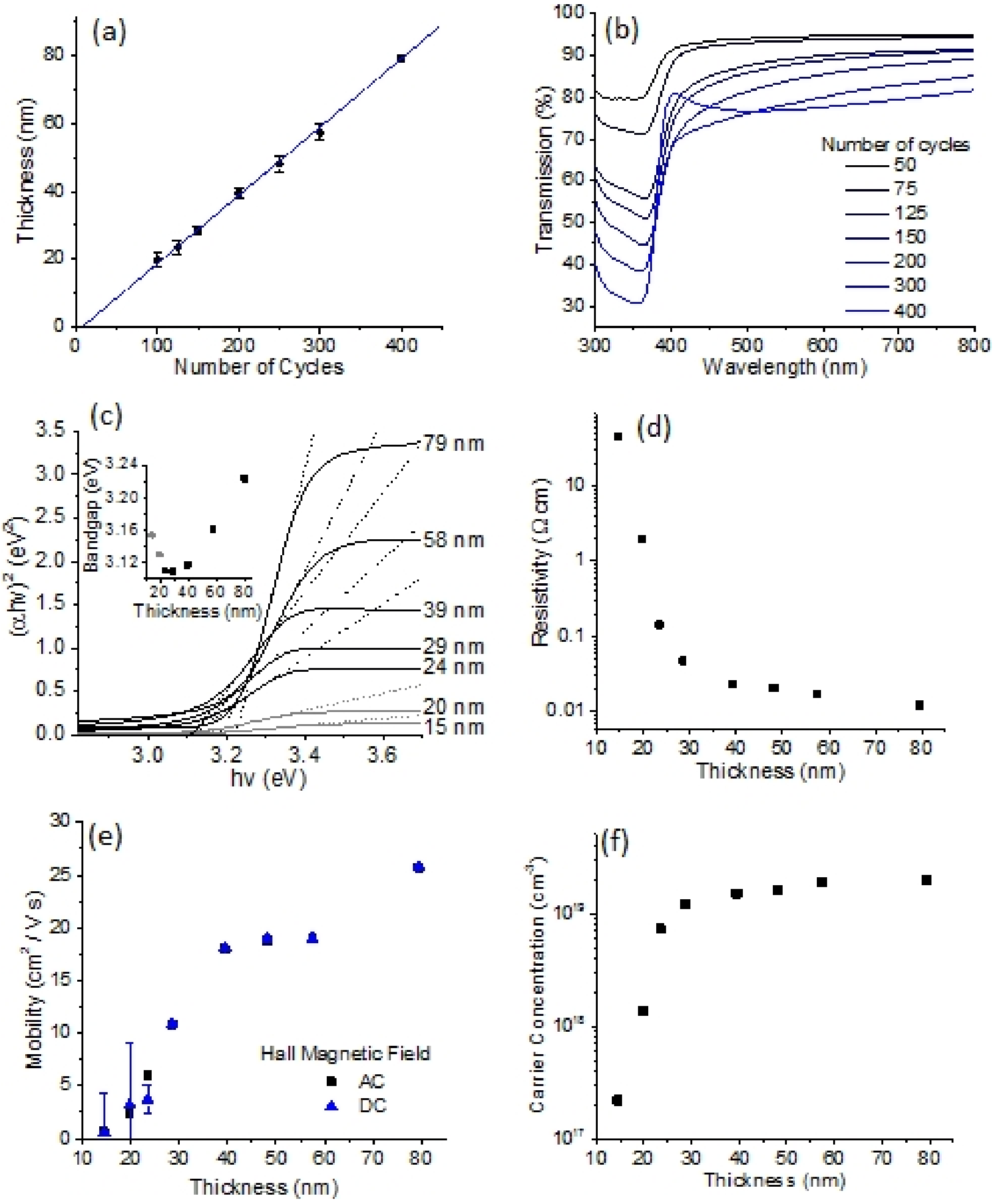

Figure 5.5: (a) Measured ZnO thickness for different numbers of DEZ-H_2O cycles on Si/native SiO_x from multiple SEM cross-sectional measurements. Best fit line gradient = 0.201 nm/cycle, intercept = 7.1 cycles. (b) UV-vis spectroscopy of ZnO on quartz and the (c) Tauc plots of the transmission data with an inset graph showing the calculated bandgap. The thickness of the 75 cycle sample was estimated from the best fit line of graph (a). (d) Resistivity of the ZnO films on quartz measured by Van der Pauw method. (e) The mobility measured by Hall using AC and DC magnetic fields, and (f) the carrier concentration calculated from the AC measurements.

GPC for ZnO on Si/SiO$_x$,[173] other substrates,[103] and with Al doping where in-situ studies revealed there is a lower GPC for about 5 cycles following a TMA-H_2O cycle until steady state is reached.[31,38] The increasing thickness with number of cycles leads to an increased amount of absorption in the UV range i.e. for photon energies above the ZnO bandgap (Figure 5.5(b)). The bandgap calculated using the transmission data varied significantly with thickness (Figure 5.5(c)). Above 30 nm the bandgap increased towards the bulk ZnO value of around 3.37 eV.[66] This increase is due to a decrease in the tensile biaxial stress in the film with thickness,[122,132] a factor that is investigated further in Chapter 6. Below 30 nm there is an apparent increase in bandgap with decreasing thickness. The thinnest film analysed is 14.5 nm and although it will probably contain grains of smaller dimensions, it is not likely that the apparent bandgap change is due to quantum confinement as the Bohr radius of ZnO is 1.4 nm.[174] The wider bandgap at thickness $<$24 nm is instead attributed to the limitations of using Tauc plot fitting for bandgap measurements as there is no sharp bandgap edge for the thinnest films.[175]

The charge carrier (electron) concentration of ZnO rapidly decreases at thickness below 30 nm, from the order of 10^{19} to 10^{17} cm^{-3}. The much smaller average crystal size of the thinner films results in a higher concentration of grain boundaries, observable at the substrate interface in Figure 5.4, and the grain boundaries contain high numbers of charge traps which reduce the overall carrier concentration. The resistivity of the ZnO films is also affected by the carrier mobility. The mobility of the ZnO is highest for the thickest (80 nm) film and is approximately equal to that of ZnO deposited at higher temperatures (Section 5.2.2). Due to this repeated observation, the bulk mobility for ALD ZnO is considered to be $\approx$ 25-28 cm^2 Vs^{-1}, which is also often the value reported in literature. For films between 40 - 60 nm the mobility is at an intermediate, transition value of approximately 18 cm^2 V^{-1} s^{-1} and rapidly decreases at lower thickness. Hall measurements were carried out using DC and AC magnetic field settings. As described in Section 3.1.8 the AC magnetic field is designed to obtain accurate results for films with mobilities of less than 10 cm^2 V^{-1} s^{-1} where DC becomes inaccurate. Figure 5.5 shows the measured mobilities where the representative error bars (calculated by propagating the standard deviation of the Hall voltages measured) are only large enough to be visible for the DC measurements. The lower thickness films have low mobilities because of scattering from the surface and the high concentration of grain boundaries. There are large errors in the DC measurements for these films, due to the signal to noise ratio which is very low because the Hall voltage is of a similar magnitude to the misalignment voltage. This confirms that AC magnetic fields should be used for low mobility ZnO films.

5.2.2 Temperature

The DEZ-H_2O ALD window is often reported as being from around 120 - 180 °C. The thickness of 300 cycle ZnO films deposited here was seen to peak around 150 °C with decreasing thickness with increasing departure from this maximum (Figure 5.6(a)). Again, the thickness change is due to increasing energy for reactions counteracted by reducing density of surface groups as temperature increases.[67] The GPCs varied from 0.167 - 0.2 nm/cycle within the 100 - 200 °C temperature range investigated. This is a relatively large GPC for ALD, close to the equivalent of a

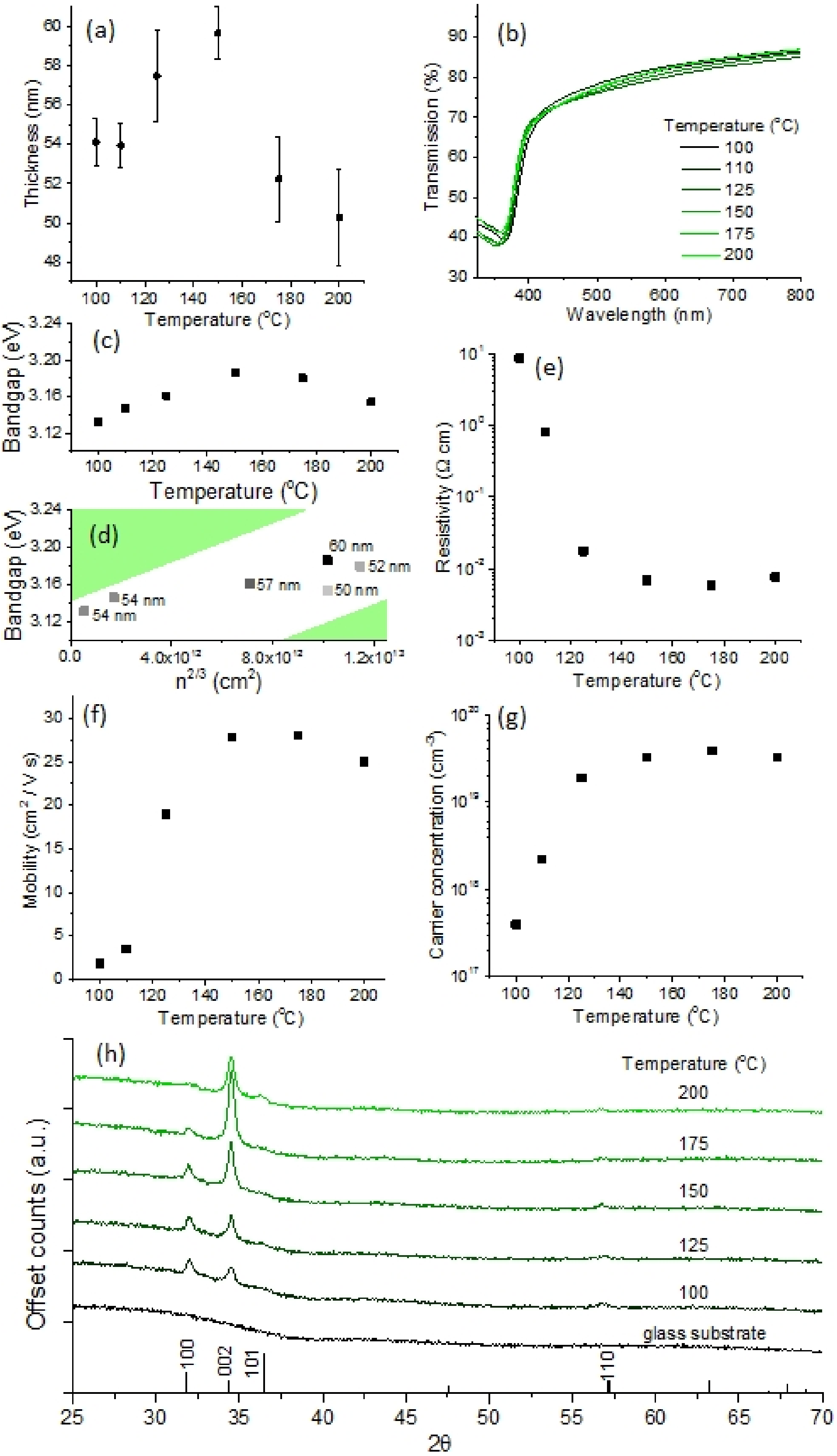

Figure 5.6: (a) The thickness of 300 DEZ-H_2O cycle ZnO films deposited at different temperatures, with glass substrate and powder ZnO stick pattern for reference. (b) the UV-vis transmission and (c) bandgaps of the films. (d) The bandgap plotted against sheet carrier concentration, $n^{2/3}$, with the theoretical gradient for the Burstein-Moss effect demonstrated by the green areas. The thickness of the ZnO is represented by the shade of the point and labelled adjacently. (e) Resistivity, (f) mobility and (g) carrier concentrations measured. (h) the XRD pattern of the films.

ZnO monolayer (≈ 0.26 nm) and is typical for these precursors, indicating that it is easy to grow reasonable thickness films over this entire temperature range.

The absorption of the ZnO is similar for the films, with the slightly thicker films absorbing slightly more, and the bandgap changes with temperature, being widest for 150 °C (Figure 5.6(b)(c)). The bandgap partially follows the trend thickness because, as found in Section 5.2.1, the stress within the film is more relaxed in slightly thicker films, although this affect is very small as XRD peak position (i.e. plane spacing) did not significantly change with temperature. Another effect that is contributing to the trend in bandgap is the Burstein-Moss effect: as the Fermi level of a semiconductor approaches and crosses into the conduction band there is an increase in carrier concentration (n) and also an increase in the optical energy required for an electron to be excited from the valence band to the conduction band as the lower conduction band states are occupied. The change in bandgap (ΔE_g) for a parabolic conduction band can be described by:[176]

$$\Delta E_g = \frac{h^2}{8m^*}(\frac{3}{\pi})^{2/3}\ n^{2/3}$$

$$\Delta E_g = 1.04 \times 10^{-14}\ n^{2/3}$$

Where h is Planck's constant, m* is the effective mass of an electron (0.35 x stationary electron mass),[177] and where ΔE_g and $n^{2/3}$ are in eV and cm^{-2} respectively. The change in n with temperature is shown in Figure 5.6(g). Carrier concentration is lower at lower temperatures due to the higher grain boundary defect concentration and the reduced oxygen deficiency of the ZnO,[67] but is fairly constant at 10^{19} for temperatures above 150 °C. Figure 5.6(d) shows the carrier concentration and bandgap approximately follow the expected Burstein Moss behaviour as it can be seen that, especially for films of similar thickness and therefore similar stress, the data points follow the 1.04×10^{-14} eV cm^2 theoretical gradient represented by the green shaded areas. The lower mobilities of the low temperature films are also due to high grain boundary defect concentration and electron scattering by impurities (e.g O–H, carbon)[178] within the ZnO crystals (Figure 5.6(f)).

Figure 5.6(h) shows there is a change in preferential orientation from mixed [100][002] out of plane at lower temperatures to [002] out of plane at higher. Small (101) peaks and (110) peaks can also be seen. The preference for [002] orientation is often seen in ZnO deposition by other techniques (the cause of the orientation is complex to determine though).[179] For ALD ZnO at lower temperature the orientation becomes mixed [100][002] due to adsorption of negatively charged hydrocarbon ligands, possibly produced via β-hydride elimination processes, to the polar (002) planes.[139] The ligands, from the breakdown of the ethyl groups of diethyl zinc (DEZ), disturb the charge distribution on (002) planes and suppress growth on them, causing [100] to become increasingly favourable.

5.2.3 Purge time

For ALD to occur it is important that precursors do not interact in the gaseous phase, only through substrate surface reactions. The purge time used has to be suf-

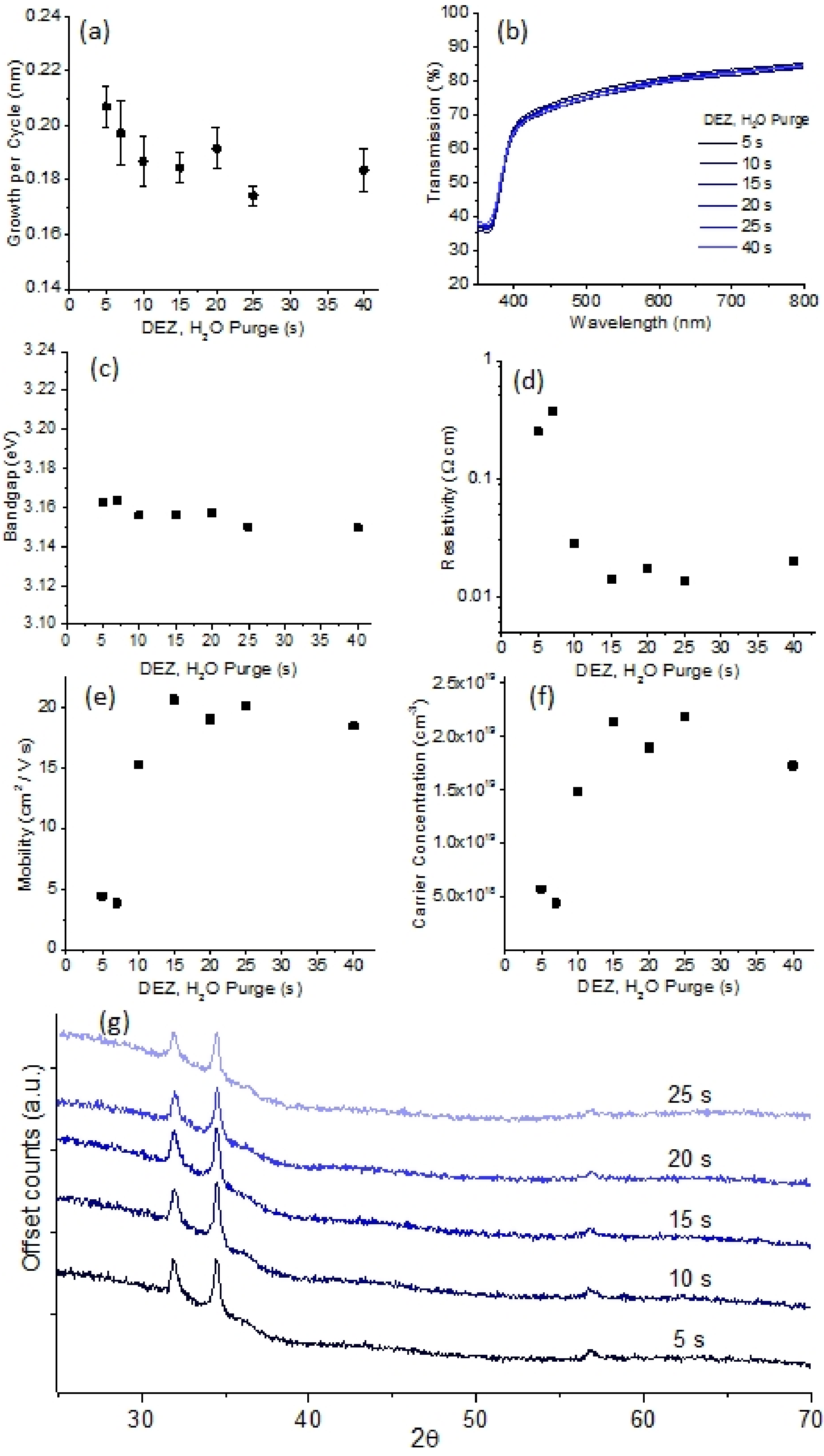

Figure 5.7: The affect of varying the DEZ, H_2O purge time on (a) GPC, (b) UV-vis, (c) bandgap, (d) resistivity, (e) mobility (f) carrier concentration, and (g) XRD pattern.

ficiently long to allow the removal of unreacted precursors before the next precursor is released. Using purge times longer those need to avoid this CVD contribution will increase the time taken for the deposition but may also affect the material properties. To investigate the effect of purge times for this system 300 cycle ZnO films were deposited at 125 °C using a broad range of purge times.

Figure 5.7(a) shows that increasing purge time from 5 - 10 s decreases the GPC which is probably the result of a CVD contribution to the growth at short purges times as not all the previous precursor has been removed from the reaction chamber before the next one is released. There is then an approximately constant GPC for above 10 s at a value consistent with the literature, so this should correspond to pure ALD growth. The UV-vis and XRD results were very similar for all the films investigated (Figure 5.7(b),(g)) and the bandgap did not vary significantly. The electrical properties, however, showed a wider variation. The mobility and carrier concentration of the films was fairly level, 18 - 21 $\mathrm{cm}^2\ (\mathrm{Vs})^{-1}$ and 1.7 - 2.2 x 10^{19} cm^{-3} respectively, for purge times $\leq$ 15 s. Both the mobility and carrier concentration decreased to approximately a quarter of those values for short purge times. This is likely due to changes in the composition of the crystals and grain boundaries of ZnO. To try to understand the purge time effects on these ZnO films more thoroughly the DEZ and H_2O purge times were varied separately and the GPC and electrical properties were studied.

Figure 5.8 shows the GPC and Hall results for independently varied purge times, with the top and bottom rows of graphs presenting the same information but as a function of H_2O and DEZ purge times respectively. From this data it can be seen that GPC of the films tends to decrease with purge time for both DEZ and H_2O although there is a large spread in the data. In a study by Park et al.[180] at 170 °C the GPC was seen to decrease significantly with H_2O purge times of longer than 40 s, which was due to desorption of hydroxyl groups. However, when using the same long purge times at 120 °C the magnitude of GPC reduction was greatly diminished because of the increased survival probably of hydroxyl groups. Thus, with the exception of increases in GPC for very short purge times due to CVD contributions, the GPC values are expected to be constant for the purge times used in this 125 °C experiment. A more marked difference is seen in the hall properties, and the behaviour differs visibly for H_2O and DEZ purge times. It can be seen carrier concentration and mobility follow the same trend, both increasing with purge time indicating improved film quality. The properties seem to be more dependent on the DEZ purge time than H_2O as the data points in Figure 5.8(f)-(h) are more closely grouped than (b)-(d), but there appears to be some dependence on both. Generally purge times below 10 s produce films of lower mobility and carrier concentration. This is due charge carrier traps such as O–H within the grain boundaries and the CVD contributions to growth.[104] In spatial ALD studies ultrafast (25ms) DEZ purge times have been used to reduce carrier concentrations but this effect was in tandem with increased mobilities and was attributed to prevention of DEZ precursor decomposition.[102] This effect is not expected to occur for purge times used in conventional ALD systems.

A clear variation in resistivity and Hall properties with purge time has been demonstrated for the ZnO films at 125 °C. To further investigate the effects of

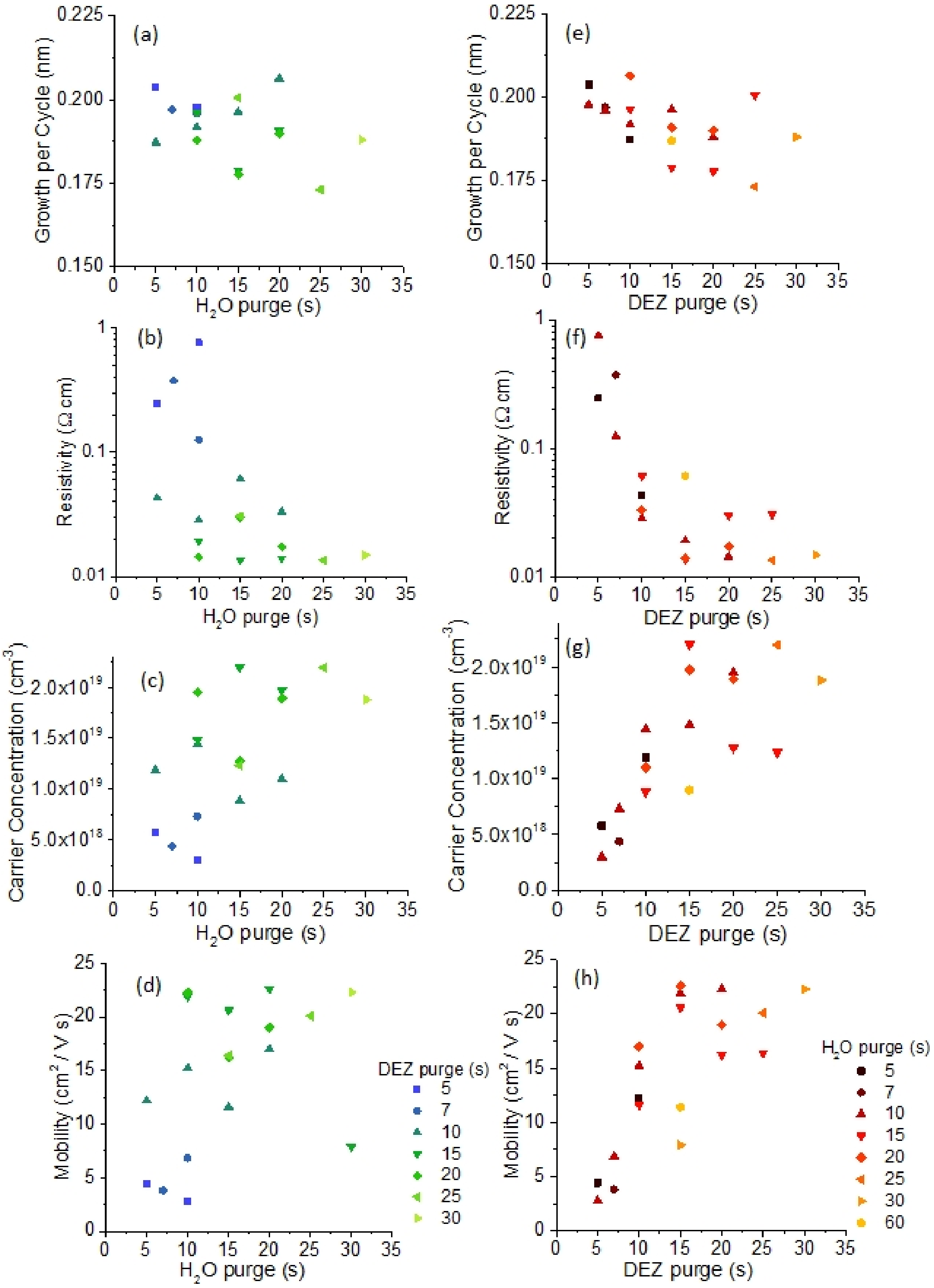

Figure 5.8: (a)(e) GPC, (b)(f) resistivity, (c)(g) carrier concentration (d)(h) mobility values for 300 cycle ZnO films with separately varied DEZ and H_2O purge times. Graphs (a)-(d) plot data as a function of H_2O purge time and graphs (e)-(h) show the same data as a function of DEZ purge time.

purge on the electrical behaviour a short (7 s) and normal (20 s) purge time were used in the deposition of ZnO films at 100 °C. The lower temperature was chosen as the carrier concentration is several orders of magnitude less than the otherwise $\approx 10^{19}$ cm^{-3} value; transistors and solar cells are often reported to perform better at lower carrier concentrations due to easier channel depletion and improved charge selectivity respectively. Figure 5.9 shows the Hall, transistor and solar cell data for the 7 and 20 s purge samples.

ZnO layers of 222 ALD cycles were deposited on bottom gate, bottom contact thin film transistor substrates, and in the same batch ZnO was deposited on quartz for Hall measurements (Figure 5.9(e)). The transistors deposited with 7 s purges showed a much higher hysteresis than for 20 s purge. Examples of representative output and transfer curves are shown in Figure 5.9(a)-(d). The shorter purge time results in a higher amount of charge traps e.g. O–H in the ZnO grain boundaries and at the SiO_x/ZnO interface resulting in the larger hysteresis for 7 s purges.[104] Initially the current I_{DS} is high but as carriers become trapped I_{DS} reduces.[181] Another source of hysteresis could be water adsorption onto the surface of ZnO although the films are quite thick (40 nm) and it is not expected that the adsorption would produce such a high magnitude of hysteresis.[182] Movement of ions thorough the channel could also produce hysteresis, which seems less likely than traps, but using varying scan rates in future would help differentiate between these effects (slower sweep leads to higher hysteresis with ions and lower hysteresis with traps).[181] The large subthreshold swing (SS) values of 4.8 - 6.1 V/decade, nonetheless, indicate that both layers suffer from relatively high amounts of interface traps compared to the theoretical ideal of 60 mV/decade. The ZnO films have a lower resistance with 20 s purges which results in a higher leakage current (I_{off}), but the on/off current ratio (I_{on}/I_{off}) is still higher for these TFTs.

The Hall data shows that the 7 s purge has a carrier concentration that is around five times smaller than the 20 s purge film. The lower amount of charge carriers could be the origin of the higher V_{on} (closer to 0 V) for the 7 s purge TFT, as having a lower amount of charge carriers means less gate bias is required for channel depletion. The $I_{DS}^{1/2}$-V_G plots do not become as linear at high V_G as ideally would be seen but the saturated mobility and V_t have been estimated. The Hall mobility for 20 s purge ZnO is 1.4 times higher than the 7 s purge, but the saturated mobility is 19 times higher. In Hall measurements current flows throughout the film thickness and will therefore take the path of least resistance. Electrons have a higher mobility in the top portion of the film due to the larger crystal size and thus lower grain boundary and trap concentration. In transistors, however, electrons accumulate at the interface with the dielectric, which is the bottom ZnO interface in these TFTs. This means the electrons will be forced to pass through the lower mobility portion of the film so the saturated mobility value was lower than the Hall mobility, and the difference between the 7 and 20 s purge ZnO was accentuated, supporting the theory of a higher amount of grain boundary traps arising from shorter purge times. Thin layers of different doping or temperature ZnO have been employed in similar situations to improve the electrical properties at the interface of TFTs.[148]

The performance OPVs with ZnO incorporated as an electron transport layer (ETL) were not found to be repeatable, but the results for a single pixel of a 7

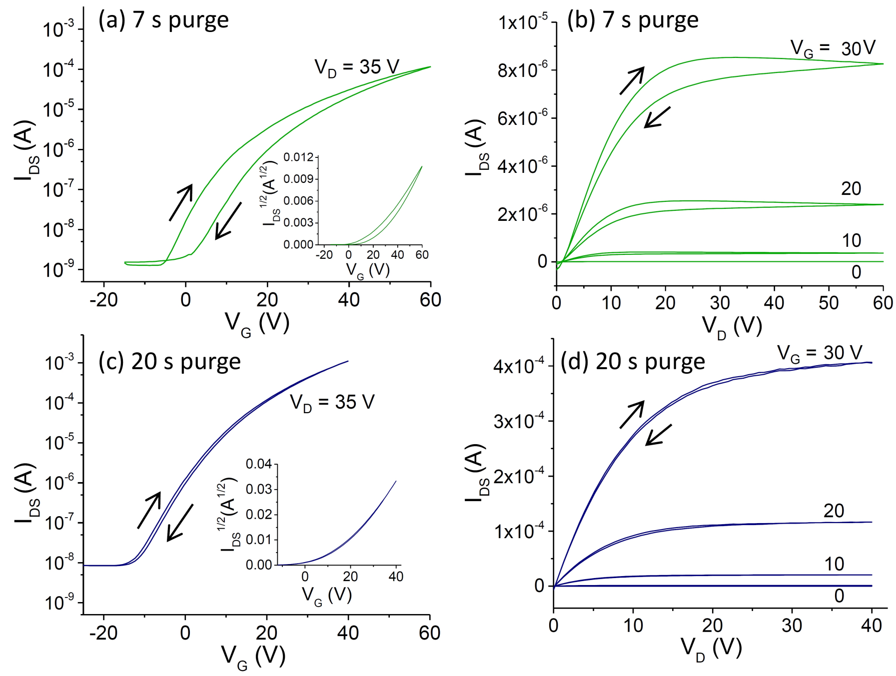

(e) Van der Pauw, Hall and transistor properties

Purge time (s)	ρ (Ω cm)	n (cm^{-3})	μ_{hall} (cm^2 Vs^{-1})	TFT scan direction	μ_{sat} (cm^2 Vs^{-1})	V$_t$ (V)	V$_{on}$ (V)	SS (V/decade)	I$_{on}$/I$_{off}$
7	714	4.2x10^{15}	2.1	Forward	0.020	37.4	-6.2	4.78	2.5x10^4
				Reverse	0.030	41.2	1.6	6.13	1.3x10^4
20	92.0	2.3x10^{16}	2.9	Forward	0.46	25.9	-15.4	5.75	1.3x10^5
				Reverse	0.49	26.2	-14.0	5.78	1.3x10^5

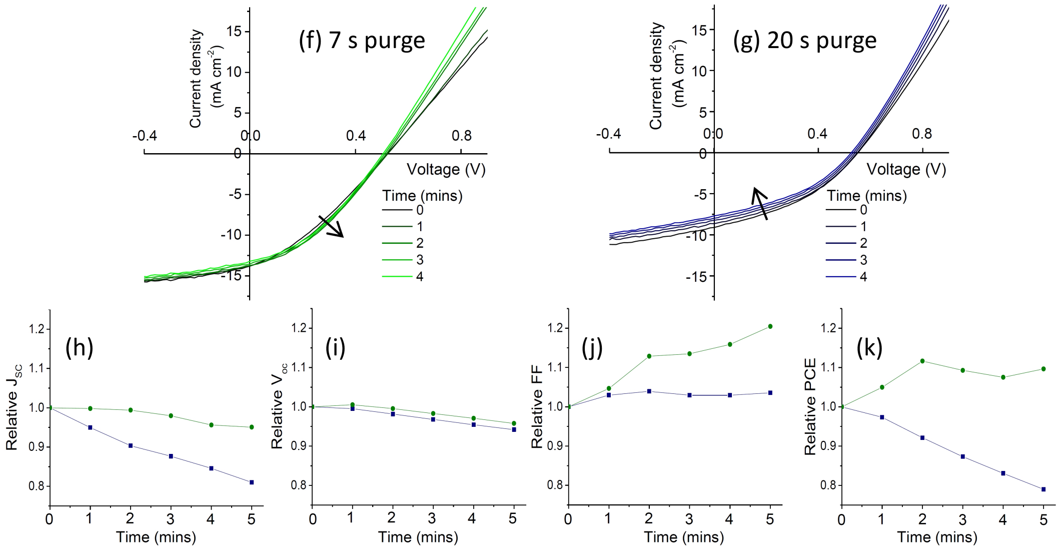

Figure 5.9: (a) The saturated transfer curve (V$_D$ = 35 V) with $I_{DS}^{0.5}$-V$_G$ inset for saturated mobility calculation, and (b) the I$_{DS}$-V$_D$ plot for ZnO deposited with 7 s DEZ, H_2O purges and 240 cycles. (c) and (d) show the equivalent plots for 20 s DEZ, H_2O purge ZnO. (e) Table showing Van der Pauw resistivity (ρ), Hall carrier concentration (n) and mobility (μ_{hall}), along with the TFT parameters of saturated mobility (μ_{sat}), threshold voltage (V_t), switch on voltage (V_{on}), subthreshold swing (SS) and on/off current ratio (I_{on}/I_{off}). The J-V behaviour change with 6 sequential measurements for a pixel of an OPVs with (f) 7 s and (g) 20 s purge time ZnO layers. (h)-(k) show the subsequent values, relative to the first J-V measurement, of short circuit current (J_{SC}), open circuit voltage (V_{OC}), fill factor (FF) and power conversion efficiency (PCE) of the pixel for each measurement.

s and 20 s purge, 120 cycle ZnO ETL with sequential voltage sweeps are shown in Figure 5.9(f)-(k). The OPVs had a bulk heterojuction structure consisting of glass/ITO/ZnO/P3HT:ICBA/MoO_x/Ag. Despite the absolute values of J_{SC}, V_{OC}, FF and PCE varying widely from device to device, there was a consistent trend with their change under light soaking. The performance for the 7 s purge ZnO OPV improves with repeated measurement and the most affected parameter is the fill factor (FF), which improves after subsequent measurements due to a decreasing series resistance. This behaviour has been reported for other devices and in those cases attributed to UV-induced oxygen desorption from grain boundaries, removing traps and reducing the resistivity of the ZnO and the charge transfer resistance at the interface with the organic layers.[123,183] It corresponds that the 7 s purge sample, which had the most traps from TFT measurements, then has a light soaking behaviour dominated by the removal of traps. The 20 s purge ZnO OPVs showed a different response to repeated measurements. There was a slight reduction in series resistance but the dominant effect of the repeated measurement was the reduction in J_{SC} and V_{OC}. As grain boundary traps as fewer in these films, the UV desorption of oxygen had a less significant affect. The reduction in J_{SC} is attributed to the photocatalytic reaction of ZnO with the organic layers causing degradation, which has a faster rate on 20 s purge ZnO. In a study by MacLeod et al.[184] the rate of degradation was different for two solution processed ZnO ETLs using different reactants, and the degradation rate was linked to the differing natures of the ZnO surfaces.

5.3 Aluminium doped ZnO Growth

Aluminium doped ZnO (AZO) can be deposited by inserting TMA-H_2O cycles at set intervals amongst DEZ-H_2O cycles as discussed in Section 2.1. The ratio of DEZ-H_2O:TMA-H_2O cycles can be varied to change the dopant concentration, affecting the electrical, optical and crystallinity of the AZO. Al acts as an electron donor, increasing the electron concentration within ZnO by substituting Zn^{2+} with Al^{3+}, but the delta doping method employed here gives added complications due to an uneven Al distribution through the film thickness. The incorporated concentration of Al in the AZO was not measured here, but EDX is used to analyse Al atomic percentage in a later study in Section 7.4.

Depositions of 300 cycles were carried out at 150 °C with varying doping cycle ratios. The resulting film thickness decreased with increasing TMA-H_2O cycle ratio (Figure 5.10(a)). This would be expected from the rule of mixtures as TMA-H_2O has a GPC of ≈ 0.11 nm/cycle compared to ≈ 0.2 nm/cycle for ZnO, but also TMA has been reported to etch surface groups and reduces the GPC of for a few subsequent ZnO-H_2O cycles.[35] For the same reason the concentration of Al in the resulting film is also higher than the amount expected from the doping cycle ratios. The crystal structure of AZO also changes with doping (Figure 5.10 (e)-(g)). Al ions are suspected of interrupting the surface polarity of the usually [002] preferentially oriented films ZnO films, reducing preference of growth in that direction.[86] The (002) peak height reduces and the (100) peak height increases slightly compared to undoped ZnO. For doping ratios between 29:1 and 19:1 there are only small changes in the orientation, with [002] being more preferential than [100], but for heavier dop-

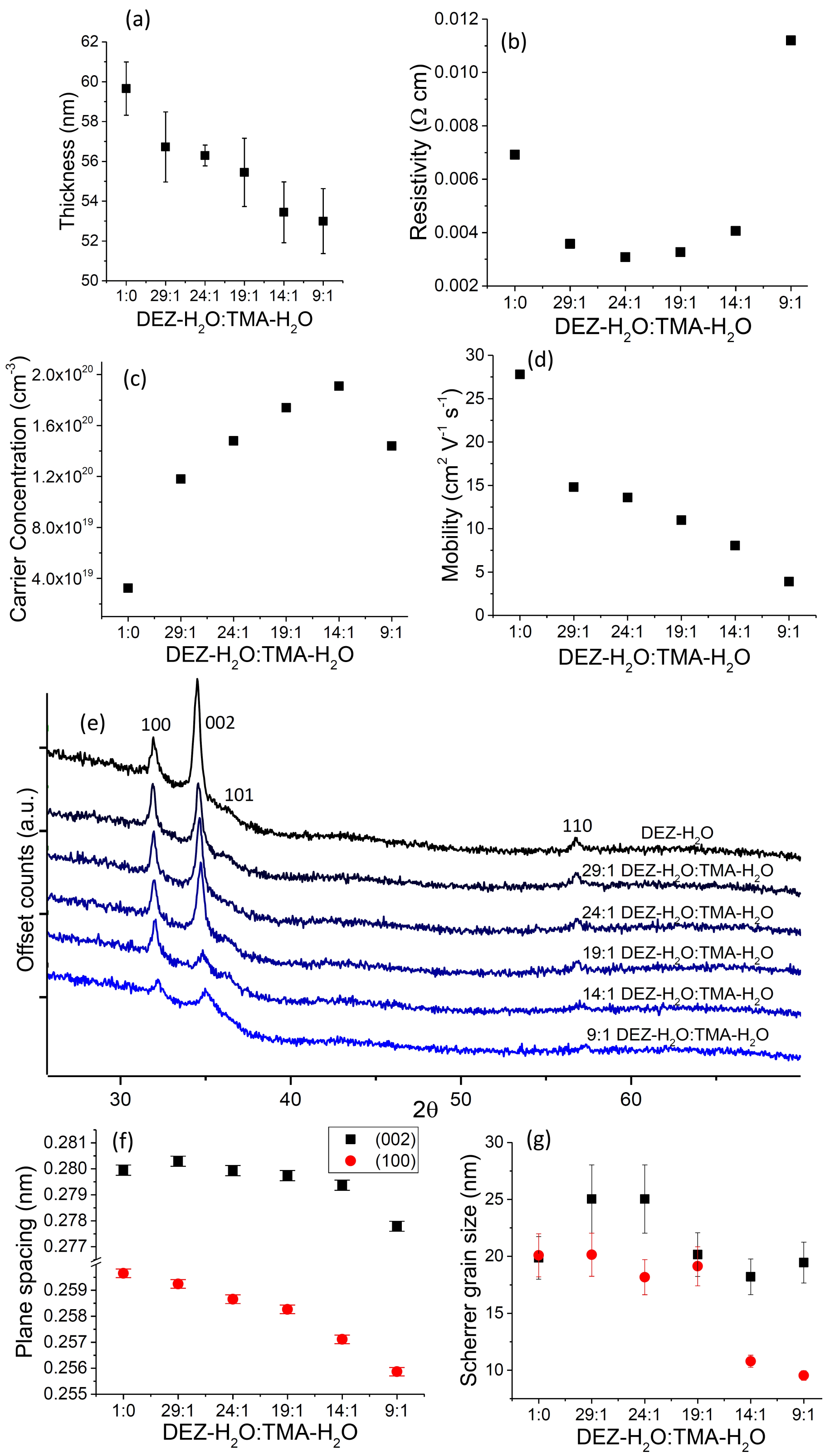

Figure 5.10: The variation of (a) GPC, (b) resistivity, (c) carrier concentration and (d) mobility with DEZ-H_2O:TMA-H_2O cycle ratios, with 300 total cycles. The crystal structure was investigated by (e) XRD, and the plane spacing (f) and Scherrer grain size (g) were calculated from the patterns.

ing (14:1) the [100] becomes preferential and the crystallinity of the film decreases dramatically due to further inhibition of the [002] growth direction, disruption of the crystal structure by closely spaced localised layers of Al and possibly an increase in the volume of amorphous areas. The smaller calculated Scherrer grain sizes with 14:1 and 9:1 doped films are also attributed to this and maybe an increase in non-uniform stress. There is an increase in (002) plane spacing and (002) Scherrer grain size and a decrease in the (100) spacing for 29:1 compared to 1:0 doped ZnO which may be due to a reduction in in-plane stress within the film. Otherwise, there is a generally decreasing lattice spacing with increasing Al doping. This is due to the smaller ionic radius of Al compared to Zn.[86]

As is the intention with Al doping, the conductivity of AZO was higher than that of ZnO (Figure 5.10(b)-(d)). The higher the doping, the higher the carrier concentration until 9:1 doping where the very disrupted crystal structure reduced the amount of active Al electron donors. The doping decreased the mobility for all Al concentrations due to Al^{3+} ions acting as scattering centres and the localised Al layers disrupting the ZnO crystal structure. The doping efficiency (number of electrons donated per Al atom) of TMA used in an ALD delta doping sequence is known to be low, around 8 %.[30] The localised Al layers contain a high density of Al atoms so the charge of one Al^{3+} ion prevents nearby Al atoms from donating electrons, resulting in fewer active donors than would be expected for AZO films with a uniform Al distribution of equal atomic percentage.[29] Using an Al precursor with more steric hindrance or increasing purge times have been reported as methods to reduce the density of Al atoms within the dopant layers.[31,32] Another is to release DEZ before and/or after the release of TMA.[33,35] A DEZ-H_2O:DEZ-TMA-H_2O deposition sequence with 14:1 ratio was adopted to investigate this. Figure 5.11 shows the properties of the film deposited with this doping sequence compared to the conventional 14:1 sequence.

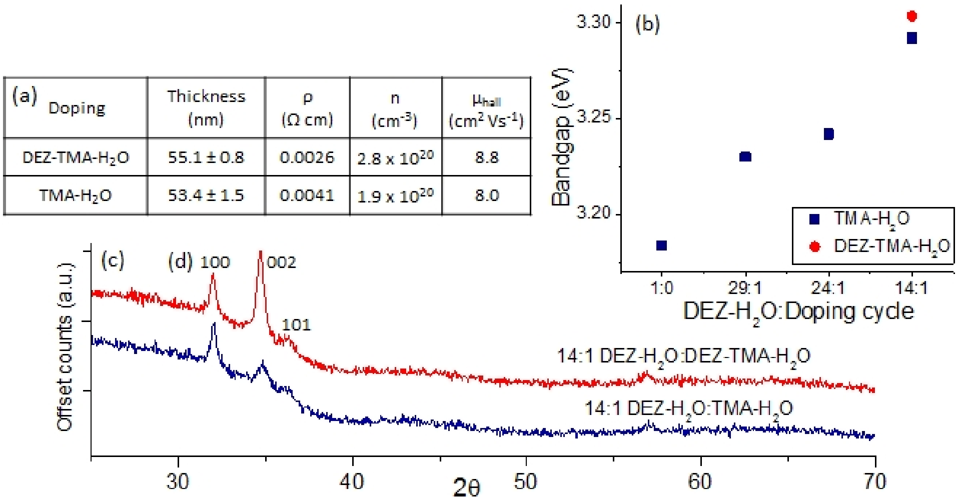

(a) Doping	Thickness (nm)	ρ (Ω cm)	n (cm^{-3})	μ_{hall} (cm^2 Vs^{-1})
DEZ-TMA-H_2O	55.1 ± 0.8	0.0026	2.8 x 10^{20}	8.8
TMA-H_2O	53.4 ± 1.5	0.0041	1.9 x 10^{20}	8.0

Figure 5.11: (a) Table comparing thickness, resistivity (ρ), carrier concentration (n) and Hall mobility (μ_{Hall}) for 150 °C, 300 cycle AZO films with DEZ-H_2O:doping cycle ratio of 14:1 where the doping sequence is either DEZ-TMA-H_2O or TMA-H_2O. (b) Bandgap of AZO films of different doping. (c) XRD patterns of 14:1 DEZ-TMA-H_2O and TMA-H_2O doped AZO.

The growth rate with the DEZ-TMA-H_2O doping cycle is higher than with TMA-H_2O because the release of DEZ reduces the amount of TMA chemisorption and acts as a sacrificial layer against the etching of the surface groups.[35] The GPC recovers to the steady state ZnO value more rapidly after the dopant cycles and the resulting film has a lower density of Al within each dopant layer. Correspondingly, the crystal structure is more [002] oriented, rather than the more [100] oriented film with conventional doping, and the mobility is higher due to less electron scattering. The carrier concentration of the DEZ-TMA-H_2O doped film is higher even though the number of Al atoms present is fewer, and resistivity of the DEZ-TMA-H_2O doped film is lower than any of the TMA-H_2O doped films in Figure 5.10. A change in AZO bandgap is also seen with doping. The bandgap generally widens with doping, which will be partially due to the Burnstein-Moss effect but the carrier concentration is high so the the conduction band can no longer be modelled as parabolic. Many body effects and film stress will have also contributed to the resulting bandgap.

5.4 Conclusions

Deposition of Al_2O_3, ZnO and AZO was achieved using the custom-built ALD system. The properties were in line with literature values, confirming ALD was successfully occurring. Additionally, studies on the effects of e.g. purge times were carried out and the following key results were found:

- For temperatures between 100 - 200 °C the measured GPC was $\approx$ 0.1 - 0.12 nm/cycle for Al_2O_3 and 0.167 - 0.2 nm/cycle for ZnO.

- ZnO had maximum GPC at 150 °C, maximum conductivity at 175 °C and had a mixed [100][002] orientation at 100 °C that transitioned to [002] with increasing temperature.

- At purge times < 10 s there is apparently a CVD contribution to ZnO growth, and the carrier concentration and mobility is reduced. The increase in charge traps resulted in greater TFT hysteresis and hugely reduced field effect mobility, but improved performance with light soaking when used as an ETL.

- 50 ms release times and 20 s purge times were chosen as the standard times for TMA, DEZ and H_2O.

- AZO conductivity was increased with low amounts of Al doping, and an increase in bandgap and [100] crystal orientation was also observed.

- Using a DEZ-TMA-H_2O doping sequence resulted in a higher doping efficiency than only TMA-H_2O.

Chapter 6

Controlling crystal orientation in ZnO

6.1 Introduction

As introduced in Section 2.2, ZnO grown by ALD exhibits the wurtzite structure. The ZnO crystal planes differ in nature: c-oriented crystals can be O or Zn terminated and the resulting (002) plane is polar, as is (101), whereas (100) and (110) planes are neutral (Figure 6.1). Control of the orientation of ZnO can be beneficial due to the variations in the surface and bulk properties. ZnO surface planes show different behaviours, such as adsorption selectivity[185] and photocatalytic activity.[186] The work functions and band bending varies between the different crystal surfaces,[187] which can be a crucial consideration for charge transfer at interfaces. ZnO thin films can be used as seed layers where the polarity/neutrality arising from the orientation acts to determine the subsequent growth of structures such as nanorods and platelets.[120] The orientations of ZnO within polycrystalline films also affects the dimensions of each crystallite and thus other interlinked properties such as the grain boundary density are affected. Grain boundaries are important as they can be barriers to electron transport and contain traps and recombination centres,[188] and the degradation of ZnO electrical properties, especially mobility, is also frequently attributed to O_2 and H_2O diffusion along grain boundaries.[123,189] The relative orientation of the crystal structures of adjacent grains can additionally effect the charge transfer between the grains, so preferentially oriented grains can be beneficial.

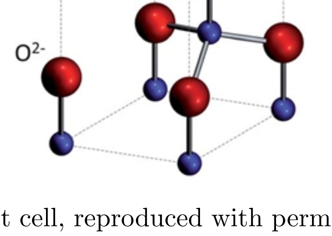

Figure 6.1: Diagram of ZnO unit cell, reproduced with permission from reference,[13] ©2013 Royal Society of Chemistry

It is well known that, along with optical and electrical properties, the orientation of ALD ZnO varies strongly with deposition temperature (Section 5.2.2). On amorphous substrates such as glass and quartz, low temperature deposition (around 100 °C) result in mixed [100][002] out-of-plane orientations, whereas higher temperatures (around 200 °C) give [002] preferential orientation. [002] growth is frequently favourable for ZnO, including with other deposition techniques, possibly due to the lower surface energy.[179] The deviance from the [002] orientation at low ALD temperatures is attributed to the adsorption of negatively charged hydrocarbon ligands to the polar (002) planes.[139] The ligands, from the breakdown of the ethyl groups of diethyl zinc (DEZ), disturb the charge distribution on (002) planes and suppress growth on them, causing [100] to become the more favourable growth direction. Doping ZnO with Al (AZO) gives [002] oriented crystals at high temperatures as with ZnO, but at low temperatures the AZO films are even more strongly [100] orientated, possibly due to exchange reactions and Al ions further disturbing the (002) plane charge.[86]

In addition to control the orientation of ALD ZnO through temperature and other deposition variables such as exposure time, the surface-sensitive nature of ALD growth also causes the orientation to be affected by the substrate. The majority of investigations into ZnO properties involve deposition on amorphous substrates including glass, quartz and Si with native SiO_2; these have been discussed in Section 5.2. However, for devices ZnO is often used as an interlayer and thus may be grown on top of an electrode layer, dielectric layer or active layer depending on the device architecture, potentially affecting ZnO growth and orientation. It is important to understand how the orientation of ZnO might be affecting the device, for example nitrogen doped ZnO in a hybrid solar cell showed improved exciton dissociation compared to undoped ZnO, but the difference in orientation of the films was mentioned as possibly also contributing to the improved dissociation.[81]

Epitaxial ZnO has been deposited on lattice-matched substrates for use in applications such as LEDs by ALD under carefully tuned conditions.[118] An alternative way of controlling ZnO orientation is to deposit multilayers of ZnO, as the initially deposited ZnO layer orientation will guide that of the following layer. Multilayers of ZnO have been employed in devices such as transistors, but usually for the improvement of the dielectric/ZnO interface rather than specifically to control the orientation. Thin high temperature ZnO and Al doped ZnO layers underneath a low temperature ZnO layer both improved the performance of transistors by combining the low carrier concentration of the low temperature ZnO with the improved mobility and reduced interface defects of the underlayers.[148,190,191] There is as yet no reports of using multilayers to investigate performance dependence on ZnO orientation in other devices. This would be an efficacious way to separate affects of orientation from other factors e.g. annealing is a common way to change crystal orientation but also affects ZnO stoichiometry and external factors such as residual organic species.[15]

An example of a way in which ALD multilayers have been used to vary ZnO orientation is in coating nanorods for the fabrication of more complicated structures. A thin Al_2O_3 layer was used to block the polarity of the ZnO nanorod surfaces and therefore controlled the orientation of the subsequently deposited ALD ZnO.[120] Ultrathin layers of Al_2O_3 are frequently used for passivation, surface protection and to reduce recombination in solar cells and photoelectrodes, allowing current to still pass when below a certain thickness.[56,57,192,193] The method of orientation control explored later in this chapter combines these abilities, using ultrathin Al_2O_3 to block certain orientations in ZnO multilayers whilst still allowing current flow, ensuring compatibility with general device architectures. Preceding the multilayer study, alternative methods of controlling the orientation of ZnO other than through deposition temperature are explored. This includes study of growth on amorphous, polycrystalline and single crystal substrates. The material properties are characterised in depth, and ALD multilayers are incorporated into organic photovoltaics (OPVs).

6.2 Substrate dependence

For organic solar cells indium tin oxide (ITO) is a common electrode due to its high conductivity and transparency. Selecting a deposition temperature of 100 °C (low carrier concentration, commonly used for ZnO in devices), deposition on this substrate was investigated. Both undoped and Al doped ZnO (AZO) were deposited. For this chapter an ALD process with a ZnO:dopant cycle ratio of 19:1 was used, with a DEZ-TMA-H_2O dopant release sequence unless otherwise stated.

As mentioned in Section 6.1 the growth of ZnO on quartz at 100 °C is seen to switch from mixed [100][002] to [100] when Al doped. Figure 6.2 shows that a difference in orientation with doping is also seen on pre-patterned glass/ITO substrates, along with a dependence on the locally underlying ITO crystal.

The crystal structure of ZnO is hexagonal and from a combination of SEM, XRD and knowledge of the crystal structure it was found to be possible to approximately judge the orientation of ALD ZnO grains from their shape as seen in SEM. This is discussed more thoroughly later in this chapter in Section 6.3.1, but, in brief, crystals with [002] out-of-plane orientation appear small and circular in shape, whereas [100] and [101] oriented crystals are long and needle shaped from top-view SEM. It can be seen that a mixed [100][002] orientation occurs for ZnO on glass, and on ITO there are areas of [002] oriented ZnO as well as areas of what is likely [100] and [101] crystals. Figure 6.3 shows the XRD pattern of ZnO on ITO, along with AZO on ITO, and a small (002) peak can be seen for the ITO/ZnO sample. The (002) ZnO peak is relatively small, in part due to the 40 nm layer thickness, and other ZnO peaks are not readily visible, so this is an clear example of how evaluation by SEM as well as XRD can be informative in the analysis ZnO orientation.

ITO has a cubic crystal structure, significantly different from hexagonal wurtzite ZnO, but it has been reported that ITO grown on [002] oriented ZnO adopts a [111] orientation. This is attributed to the similar O atom locations with this alignment, resulting in a favourably small 3 % lattice mismatch.[194] The ITO layer employed here is extremely flat and smooth with columnar grains, as shown in the inset of Figure 6.3, so it is likely that the ITO surface plane is parallel to the substrate and therefore the surface planes are the plane orientations identified by XRD. One of the out-of-plane preferential orientations of ITO is [111] (from the (222) XRD peak), so it is expected that ZnO will grow [002] oriented on these crystals. The other ITO

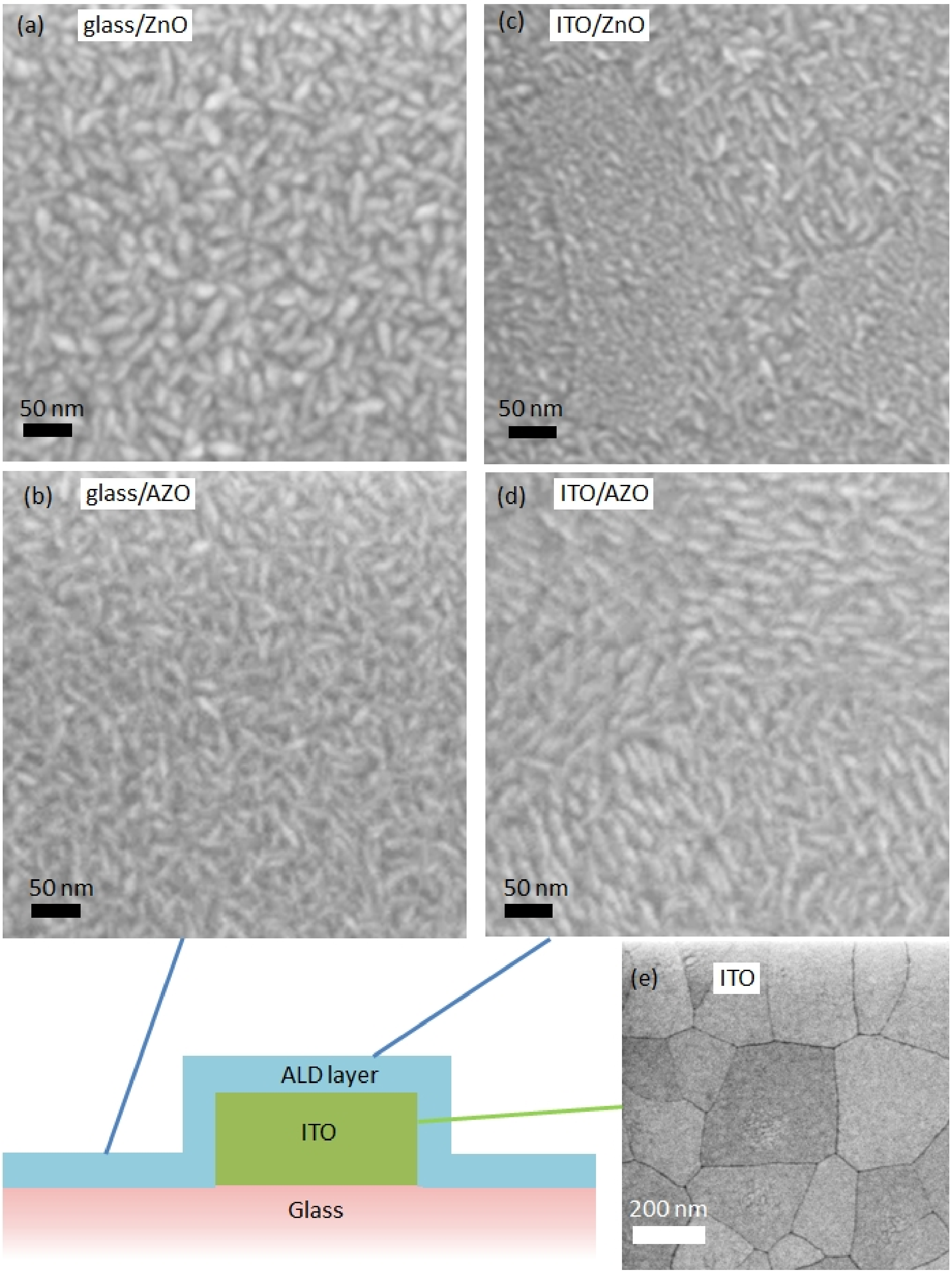

Figure 6.2: Schematic of a pre-patterned glass/ITO substrate and SEM images of the crystal growth of ZnO on (a) glass and (c) ITO, AZO (29:1 DEZ-H_2O:TMA-H_2O) on (b) glass and (d) ITO, and of (e) uncoated ITO grains. The SEM images of the ZnO or AZO were taken from different areas of the same glass/ITO substrate

orientations may also have low lattice mismatch with certain ZnO orientations. AZO grown on glass showed [100] orientation (as on quartz), and when grown on ITO the individual ITO crystallites determined the orientations, with [100] and [101] being preferential. The different orientations of ZnO and AZO on ITO are probably due to different film growth kinetics combined with Al doping affecting lattice spacings and therefore the mismatch of the ZnO and ITO lattices.

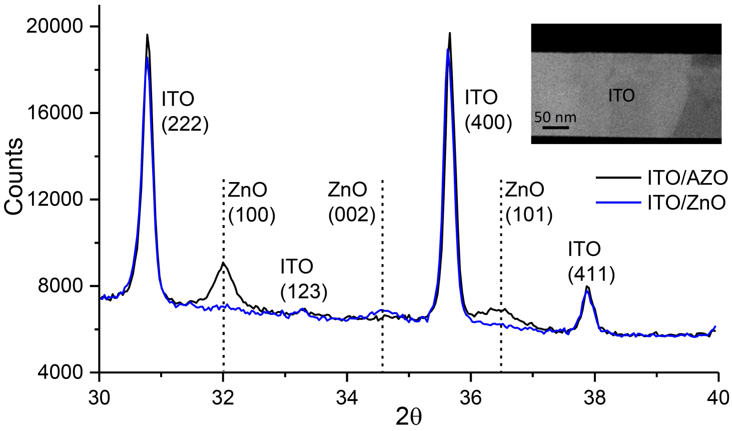

Figure 6.3: XRD pattern of ZnO and AZO (29:1 DEZ-H_2O:TMA-H_2O) on an ITO substrate. Inset shows a dark field STEM cross-section image of the ITO layer. An auto-slits program was used to fix the XRD beam size to a 0.7 x 0.7 mm area to prevent signal from the ZnO or AZO on glass areas of the substrate.

In addition to polycrystalline substrates like ITO, single crystal substrates can be used, and an investigation was carried out into ZnO grown on (100) (m-plane) and (001) (c-plane) cut sapphire substrates. Sapphire (Al_2O_3) has a hexagonal crystal structure like ZnO, and when deposited at 100 °C ALD ZnO shows (100) and (002) XRD peaks on (100) and (001) sapphire substrates respectively (Figure 6.4). Comparing the lattice dimensions of ZnO and sapphire (Table 6.1) it can be seen there is a relatively large lattice mismatch. However, this is a very simplified comparison, for example even though the calculated a-plane spacing mismatch is 32 % for ZnO grown on (001) sapphire, ZnO crystals have been seen to rotate 30° with respect to the sapphire, reducing the mismatch to 18 %.[195] Other substrates e.g. GaN have a better lattice match with ZnO, however sapphire is less expensive and still guides the orientation of the deposited ZnO, which is the area of interest in this investigation. Various ALD ZnO deposition parameters e.g. temperature and precursor exposure times can be adjusted to improve epitaxy on single crystal substrates, but to reduce the number of variables needing to be considered, the standard ALD parameters and a temperature of 100 °C without any post-deposition annealing were used here.

Figure 6.5 shows the XRD, UV-Vis, SEM and electrical properties of 240 ALD cycles of ZnO deposited on sapphire and quartz. Under the same deposition conditions, ZnO grown on m-plane sapphire is [100] oriented, on quartz there is a mixed [100][002] orientation and on c-plane sapphire ZnO is preferentially [002] oriented. The ZnO XRD peaks on sapphire show a shift to higher angles because out-of-plane lattice spacing is reduced due to in-plane tensile stress caused by the larger sapphire lattice dimensions. The ZnO deposited on sapphire shows a larger band gap than

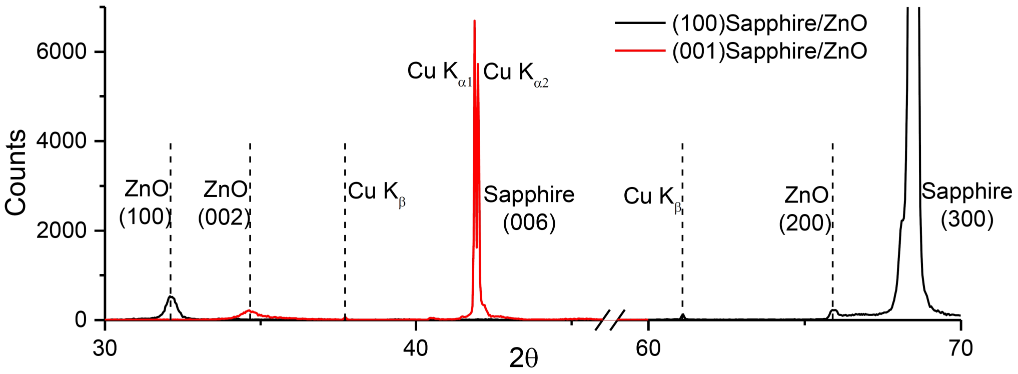

Figure 6.4: XRD patterns of ZnO grown on (100) and (001) oriented polished sapphire substrates. Note the ratio of Cu $K_{\alpha 1}$: Cu $K_{\alpha 2}$ is not 2:1 as would be expected due to the fast 2θ scan rate used compared to the substrate spinning rate

Plane	ZnO spacing (exp) (nm)	ZnO spacing (ref) (nm)	Sapphire spacing (nm)	mismatch (exp) (%)	mismatch (ref) (%)
a	0.32246	0.32498	0.4758	32	31
c	0.51916	0.52066	1.2991	25	25

Table 6.1: Comparison of experimental (exp) ALD ZnO a and c plane spacings (calculated from (100) and (002) diffraction peaks on quartz) with reference (ref) ZnO (ICCD: 00-036-1451) and the sapphire substrate(data from supplier, CRYSTAL Gmbh) lattice mismatches.

that on quartz, which is also common in cases of lattice strain e.g. in monocrystalline growth. ZnO on (001) sapphire shows an XRD peak with a maximum corresponding to (002) but the peak is broad and asymmetric indicating there is also some (101) contribution. From SEM (Figure 6.5(f)) it can be seen that there are [002] oriented grains but also some needle shaped grains which have [101] orientation. It is not possible to judge the in-plane orientation of [002] oriented crystals from SEM but the needle like [100] and [101] ZnO crystals grown on quartz and (001) sapphire respectively show random in-plane orientations whereas the [100] crystals grown on (100) sapphire have a preferential in-plane orientation, lining up with probably the [001] sapphire lattice direction (Figure 6.5(d)).

The electrical properties of the ZnO layer are different for the three substrates, as shown in Figure 6.5(c). There is a small change in electron mobility between the different orientation samples but the mobility appears inherently low. The (100) sapphire sample may have highest mobility due to the increased crystal alignment in this case compared to the other samples. Overall there is the suggestion that factors other than orientation are dominating the mobility e.g. defects within the ZnO crystals due to the 100 °C deposition temperature. The main electrical performance difference was the carrier concentration, rising from the order of 10^{16} for ZnO on quartz to 10^{18} cm^{-3} on sapphire. To investigate the cause of this unusual result, an investigation into the variation of ZnO properties with thickness was carried out for this 100 °C deposition temperature, similar to the investigation at 125 °C in Section 5.2.1 but with significantly different trends.

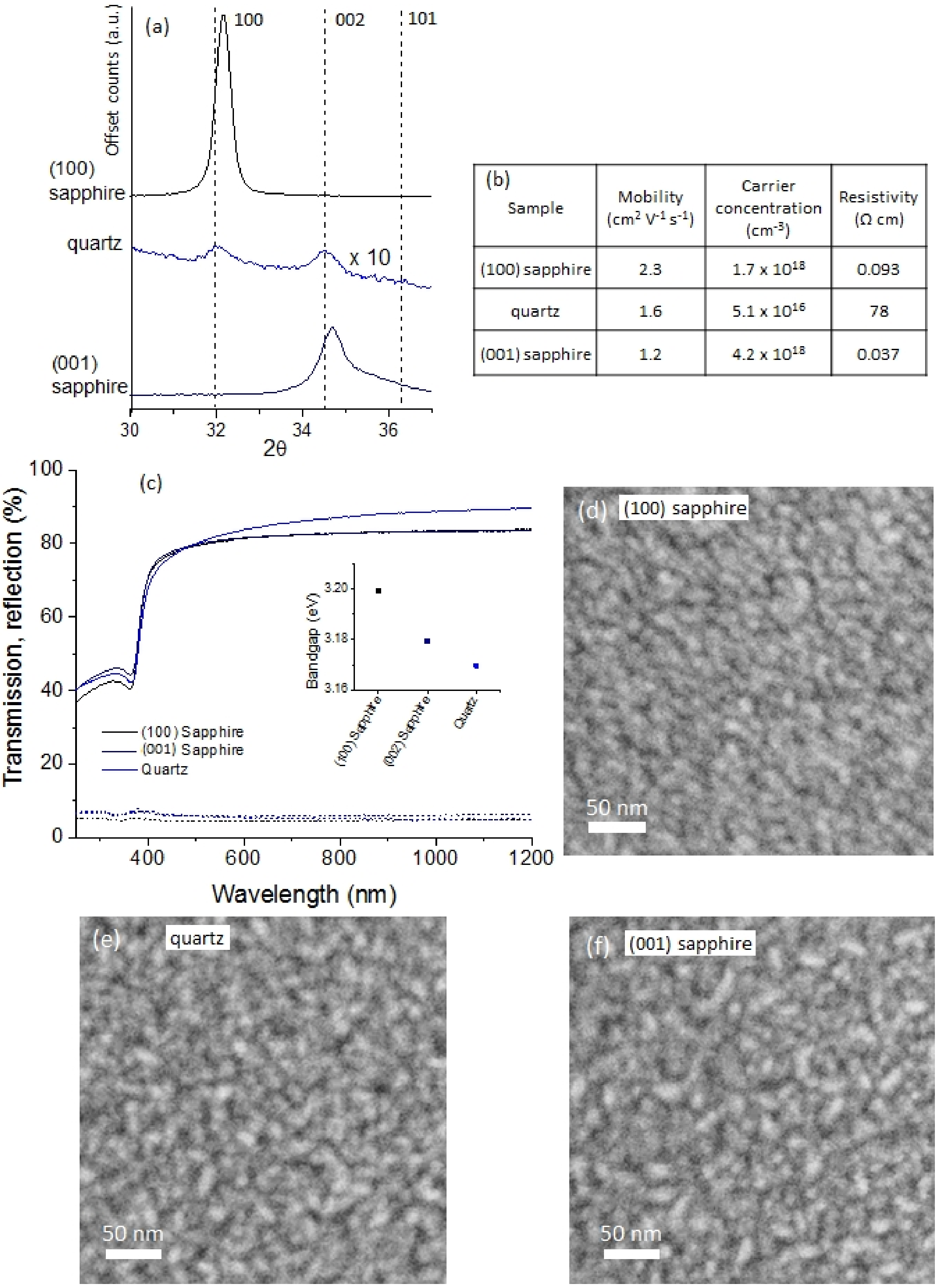

(b)

Sample	Mobility (cm^2 V^{-1} s^{-1})	Carrier concentration (cm^{-3})	Resistivity (Ω cm)
(100) sapphire	2.3	1.7 x 10^{18}	0.093
quartz	1.6	5.1 x 10^{16}	78
(001) sapphire	1.2	4.2 x 10^{18}	0.037

Figure 6.5: (a) XRD patterns of ZnO on (100) and (001) sapphire substrates compared to on quartz in the same deposition batch. Table (b) shows the electrical properties, and (c) shows UV-vis transmission (solid line) and reflection (dashed line) spectra with an inset showing the Tauc bandgap. The SEM images (d)-(f) show the film microstructure.

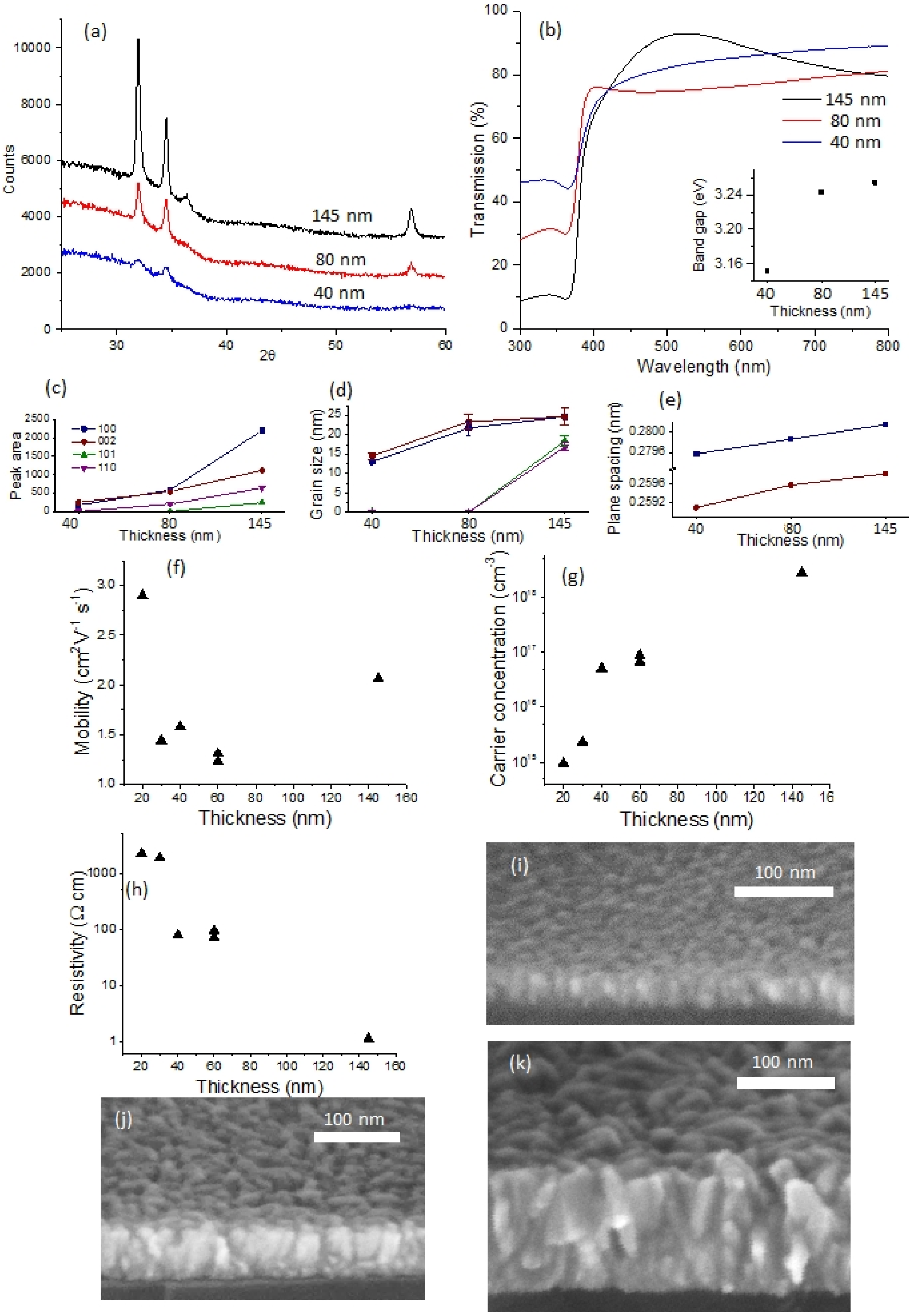

Figure 6.6: (a) XRD patterns with different thickness ZnO layers and the calculated (c) peak area, (d) Scherrer grain size (without instrument broadening correction) and (e) plane spacings. (b) UV-vis transmission spectrum with inset of Tauc bandgap (note Tauc was calculated using only transmission data). The electrical characterisation of different thickness films are shown in (f) mobility, (g) carrier concentration and (h) resistivity. (i),(j) and (k) show SEM cross-sectional views of 40 nm, 80 nm and 145 nm thickness films respectively.

For ZnO deposited at 125 °C the carrier concentration and mobility plateaued at around 35 nm, and it has been reported that, for a 300 °C deposition temperature, ALD ZnO resistivity becomes relatively thickness independent beyond 40 nm.[30] This is not the case for 100 °C ALD ZnO. Figure 6.6 shows mobility of ZnO films is consistently low for 100 °C films of any thickness, as was seen with the different sapphire substrates, compared to mobilities of around 20 $\text{cm}^2\ \text{V}^{-1}\ \text{s}^{-1}$ which were easily obtainable at higher temperatures. As with the sapphire films, the slight changes in mobility with thickness might be due to crystal alignment changes which can be studied by XRD (Figure 6.6(a)). The mobility is highest for thin films (20 nm) which could be due to the c-oriented ZnO crystal nucleation resulting in a film consisting of aligned [002] crystals. The mobility is reduced by 50 % for 30 nm films, perhaps as the film becomes more mixed in orientation, with a slight mobility increase at higher thickness possibly due to the again increasingly ordered crystal alignment, shown by the rapidly increasing (100) peak area with layer thickness (Figure 6.6(c)). The Scherrer grain size indicates the out-of-plane size is fairly similar for the [100] and [002] oriented crystals, with [100] size initial smaller but increasing at a slightly faster rate (Figure 6.6(d)). From SEM cross-section it can be seen that in-plane crystal size does increase with thickness but the crystals do not grow completely through the film thickness, explaining the nonetheless small Scherrer grain size for a 145 nm film. The UV-vis transmission showed a shift in bandgap which has been reported to be due to a reduction of stress within thicker films, and is supported by the increase plane spacing towards the larger reference values (Figure 6.6(e)).

The carrier concentration of the deposited ZnO depends strongly on thickness (Figure 6.6(g)). At higher deposition temperatures the carrier concentration tends to plateau at around 30 nm but at 100 °C the carrier concentration underwent a two order of magnitude increase for a thickness increase from 30 nm to 145 nm. The value at 145 nm was $10^{18}\ \text{cm}^{-3}$, which has been reported as the plateau value for studies on other 100 °C ZnO thin films. This is also the value for 40 nm thick ZnO on sapphire substrates. This suggests a link between the crystal orientation and carrier concentration. It is hypothesised that due to low depositions temperatures, the grain boundaries in ZnO are poorly aligned and contain crystal defects (and possibly hydrocarbon contamination) which trap electrons, keeping carrier concentrations low. As the film thickness increases the ZnO crystals become more favourably aligned and grain boundaries become less defective, so carrier concentration increases to the would-be bulk value for this deposition temperature, with the same affect achieved by deposition on a substrate which aligns the ZnO crystals.

6.3 ZnO and AZO multilayers

From the preceding section, the choice of the substrate on which ZnO is deposited has been shown to be important for ZnO growth. However, when considering devices there is often not a lot of flexibility in substrate choice. ZnO orientation control is important for investigating and improving certain devices, as has been reported for transistors, but there is as yet no method of controlling the orientation which has been developed to be compatible with solar cells and similar devices. This Section explores a method which would allow in-depth analysis of the ZnO orientation dependence without having to make changes in the deposition conditions or substrate which add additional variables to be analysed.

6.3.1 Multilayers on quartz

It is known that at 100 °C AZO grows with [100] orientation on quartz whereas ZnO grows with a mixed [100][200] orientation. If ZnO is grown on AZO then you would expect the AZO to affect the ZnO orientation. This is observed: ZnO grows with a strong [100] orientation on [100] AZO, as shown in Figure 6.7. For ZnO on quartz, films nucleated with [002] orientation but later growth favours [100] due to the adsorption of hydrocarbons on (002) so there is a stage of mixed orientation before [100] becomes dominant, as previously discussed for Figure 6.6. Using a [100] AZO underlayer alters this situation because then both nucleation and homogeneous growth favour [100] orientation so this results in a strong [100] orientation.

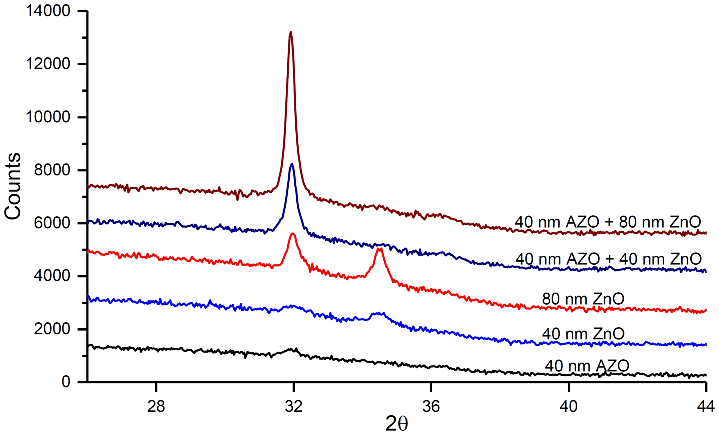

Figure 6.7: XRD patterns showing the main preferential orientations of AZO and ZnO, and AZO/ZnO multilayers.

Considering the reverse situation, if an AZO underlayer is used but the [100] preferential orientation is not desired then you would expect to be able to revert the orientation to a situation similar to on quartz by completely covering the AZO layer with a layer of amorphous material. To further investigate orientation control and the critical thickness needed to block it, a series of TMA-H_2O cycles were deposited on AZO to form an amorphous Al_2O_3 layer and the subsequent ZnO orientation was studied. Figure 6.8 (a) shows the gradual transition from [100] to mixed [100][002] orientation with increasing Al_2O_3 thickness, with the critical orientation-blocking thickness reached at around 10 cycles of TMA-H_2O, corresponding to approximately 1 nm of Al_2O_3.

There is a shift in the (100) peak position during orientation transition, demonstrated in Figure 6.8(b), which is an indication of changing plane spacing. One effect contributing to the (100) ZnO spacing change could be stress relaxation which is seen to occur when ZnO film thickness increases (Figure 6.6(e)). The growth of ZnO on AZO increases the effective film thickness compared to films nucleated on Al_2O_3.

Another possible contributing affect could be an epitaxial type relationship of ZnO on AZO. For AZO the out-of-plane (100) spacing is larger than for ZnO grown on a relatively thick layer of Al_2O_3 or on quartz, but when ZnO is grown on AZO the resulting ZnO adopts a larger out-of-plane (100) spacing. It could be that the in-plane lattice spacing of AZO is smaller than that of ZnO due to an affect of

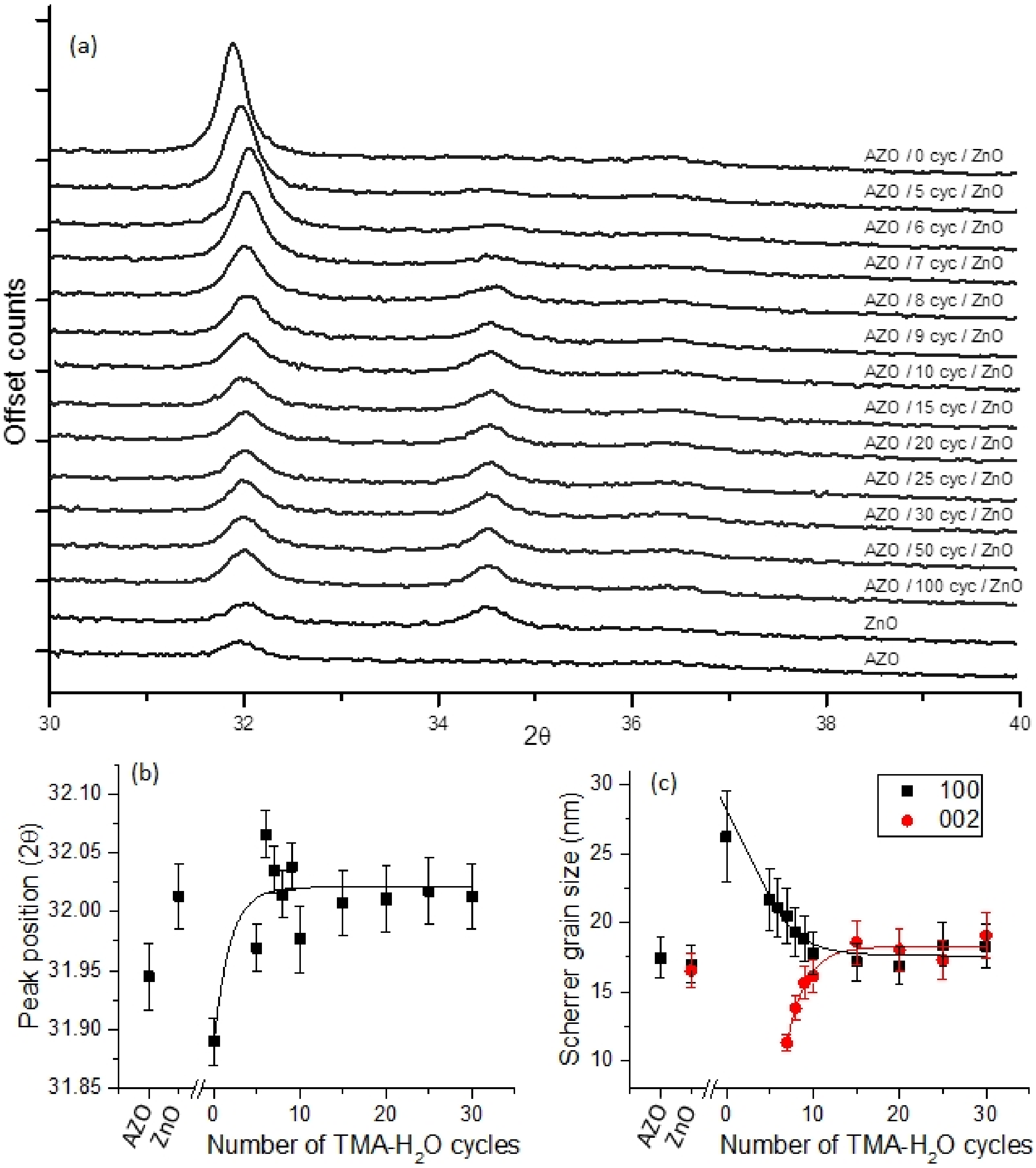

Figure 6.8: (a) XRD patterns for multilayer of AZO/Al_2O_3/ZnO with a varying number of TMA-H_2O cycles (cyc),with one TMA-H_2O cycle approximating to 0.11 nm Al_2O_3. Transition is seen from (100) planes where the peak is positioned at around $2\theta = 31.8$ °, to mixed (100)(002) planes where the (002) peak is positioned at around $2\theta = 34.5$ °. A weak (101) peak is also seen positioned at around $2\theta = 36.3$ ° but no other peaks were of sufficient magnitude for analysis. (b) The (100) peak position (line is guide to the eye). (c) The Scherrer grain sizes calculated from the (100) and (002) peaks (lines are guides to the eye). Instrument broadening was not corrected for in calculation.

the lamella type doping sequence. XRD only reveals information on out-of-plane lattice spacing whereas it is the in-plane crystal lattice with which the deposited layer aligns itself, so a smaller in-plane AZO lattice spacing would lead to strain increasing the out-of-plane ZnO spacing. Fig 6.9 shows a schematic of the possible AZO/ZnO strain situation.[196] The calculated out-of-plane strain is relatively small and considering the very similar AZO and ZnO crystal structures, it can be assumed that the lattice mismatch between AZO and ZnO is small enough that ZnO growth can initialise psuedomorphically on AZO. The ZnO layer is quite thick at 60 nm, so there may be stress-relaxing defects within ZnO crystals. This is a very simplified analogy to single crystal epitaxy which is not necessarily representative of the polycrystalline AZO/ZnO multilayer under consideration. One dissimilarity is the grain size of AZO is small, resulting in a high concentration of grain boundaries where there is an imperfect crystal lattice on which ZnO will grow. The strain on the ZnO lattice will probably be distinct for each ZnO grain as the defects present in grain boundaries should affect the strain at the edge of each grain. Also the surface of AZO is rough relative to polished single crystals.

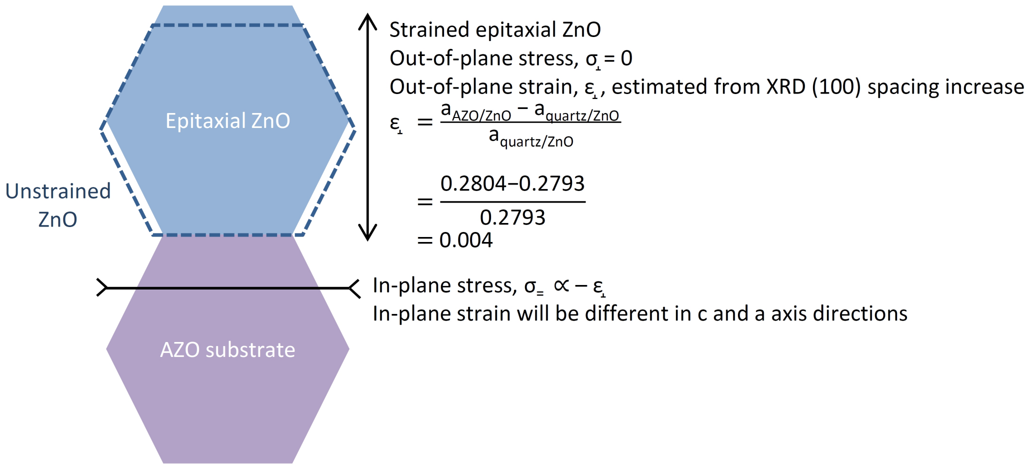

Figure 6.9: Schematic of the possible epitaxial relationship of ZnO deposited on AZO and the calculated strain. [001] crystal direction is into page.

Figure 6.8 (c) shows the out-of-plane size of [100] oriented crystals decreases with increasing Al_2O_3 interlayer thickness, in tandem with the appearance and increasing size of [002] oriented crystals. This supports the proposed theory that ZnO is growing epitaxially on at least some of the AZO crystals, resulting in a larger average out-of-plane size than in AZO or ZnO individually as the crystals straddle the AZO/ZnO layers. Epitaxy may not be occurring on all AZO crystal surfaces but in that case the AZO surface might still determine the orientation of a nucleating ZnO crystal. Note that instrument broadening was not corrected for in the Scherrer calculation so grain size values will be slightly underestimated, for example the AZO layer on quartz is 26 nm thick so the actual grain size will be between 20 nm (calculated size) and 26 nm. In addition, non-uniform strain may also be broadening the XRD peaks, however larger strain broadening would be expected in the case of ZnO growing epitaxially on AZO, resulting in a further underestimate of the grain size, so the trend in grain size is valid even with this possibility.

Figure 6.10(a) shows the UV-vis transmission and reflection spectra for the multilayers, revealing an increase in bandgap when ZnO is oriented with respect to the AZO underlayer. Changes in ZnO bandgap have been linked to lattice stress for epitaxial single crystals and to changes in film stress in polycrystalline ZnO with film thickness. These were both possible explanations for the shift in XRD peaks in Figure 6.8. Linear bandgap vs. stress and strain relations have been reported for epitaxial and biaxial stressed ZnO films. There are, however, large differences reported trends and most cases consider [002] oriented ZnO films so no direct comparison can be made.[197–201] There is not enough information from data obtained here to calculate in-plane stress, which is complicated by the polycrystalline and hexagonal structure of the ZnO, but the bandgap can be related to the out-of-plane strain. An approximately linear relationship between the out-of-plane strain and the bandgap relative to a reference ZnO sample is revealed (Figure 6.10(c)), supporting the hypothesis of strain-related bandgap changes.

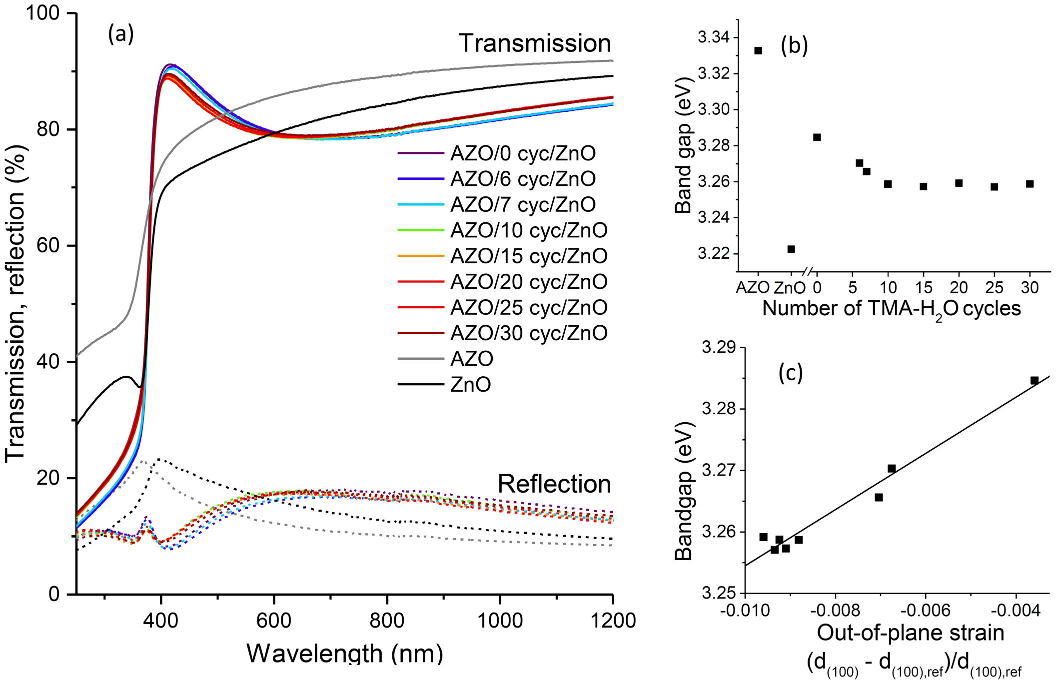

Figure 6.10: (a) UV-vis transmission (solid line) and reflection (dashed line) spectra of AZO/Al_2O_3/ZnO multilayers with varying number of TMA-H_2O cycles (cyc). (b) Calculated Tauc bandgap of the multilayers and (c) the bandgap relationship to the out-of-plane strain calculated from the reference (100) XRD plane spacing, 0.28143 nm, and the calculated (100) spacing in Figure 6.8(b)

As discussed in Section 6.2, it is possible to estimate the orientation of the surface ALD ZnO crystals from the SEM appearance. Crystals with [002] out-of-plane orientation, which will give rise to a (002) peak in XRD, are relatively small in diameter and symmetrical, almost appearing circular from SEM. These c-oriented crystals grow like long needles perpendicular to the substrate surface. [100] oriented crystals have anisotropic in-plane dimensions. From above they appear needle shaped with the long axis of the needle (ZnO [002] direction) oriented parallel to the substrate surface. Utilising this knowledge the transition in ZnO orientation was

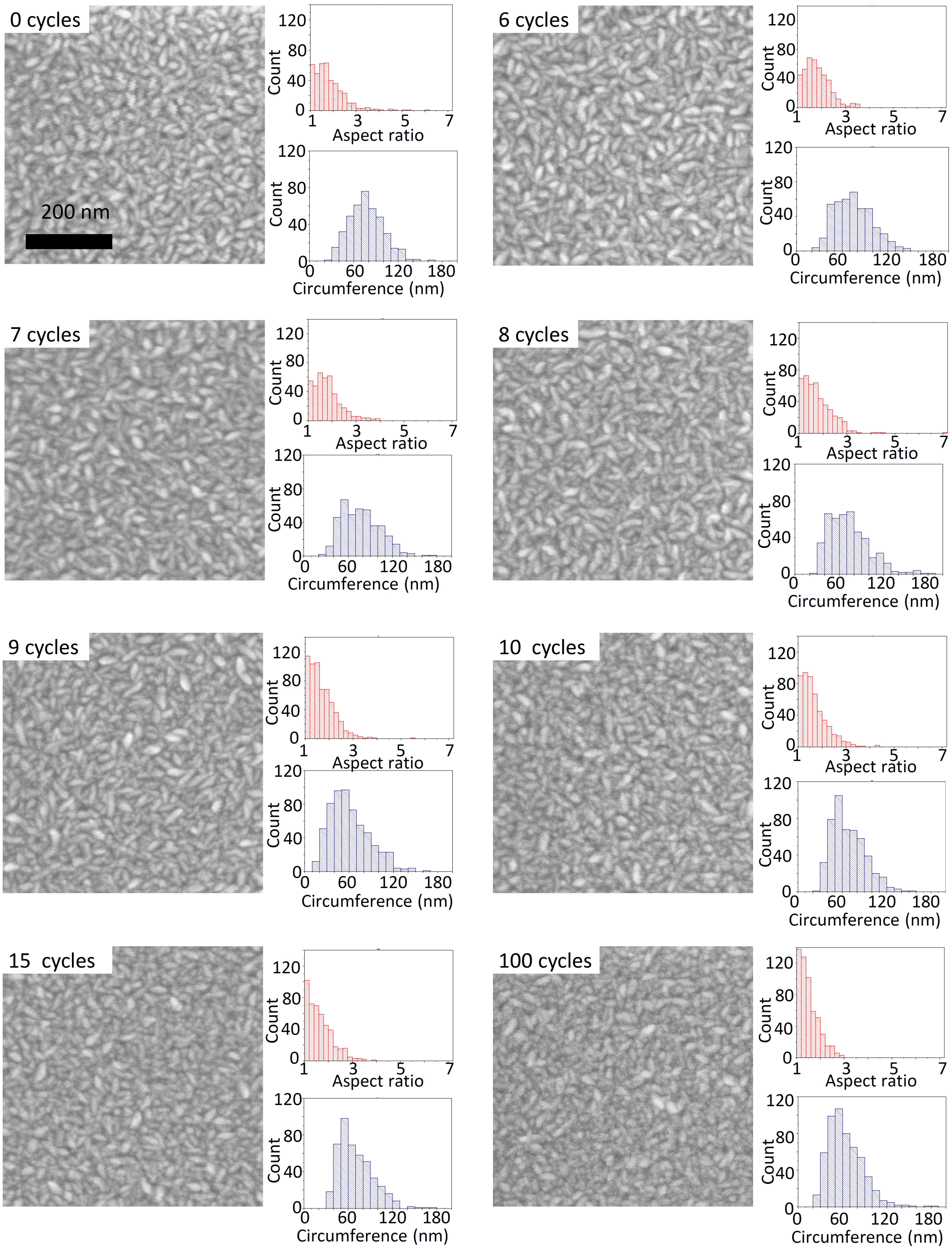

Figure 6.11: SEM images showing the transition in surface morphology for AZO/Al_2O_3/ZnO multilayers on quartz with number of TMA-H_2O cycles, along with the corresponding measured grain aspect ratio (length/width) and circumference (grain shape was approximated to be elliptical, and circumference was calculated using measured length and width) from a 400 nm x 500 nm area of the sample.

followed by SEM to compliment the XRD results. Figure 6.11 shows SEM images of the substrate surfaces accompanied by the respective aspect ratio and grain circumference statistics. Visually, it can be seen that the surface of the 0 cycle TMA-H_2O multilayer consists of needle-shaped [100] oriented grains and as the Al_2O_3 thickness increases there is an increasing number of smaller, circular [002] oriented grains. The aspect ratio and circumference measurements help to highlight this trend, revealing, for example, that an equivalent area of the 0 cycle sample contains a smaller total number of grains, as the grains have a higher circumference with a generally high aspect ratio, than the 10 cycle sample, which contains some large, high aspect ratio grains but also many grains which are small in circumference and approximately circular.

(a) Sample	Mobility ($cm^2 V^{-1} s^{-1}$)	Carrier concentration (cm^{-3})	Resistivity (Ω cm)
ZnO	1.23	6.64 x 10^{16}	76.1
AZO	0.46	5.15 x 10^{19}	0.261
AZO/0 cyc/ AZO	1.50	3.41 x 10^{19}	0.122
AZO/5 cyc/ AZO	1.57	3.14 x 10^{19}	0.126
AZO/10 cyc/ AZO	1.62	3.02 x 10^{19}	0.128
AZO/15 cyc/ AZO	1.59	3.16 x 10^{19}	0.124
AZO/20 cyc/ AZO	1.60	3.06 x 10^{19}	0.127
AZO/25 cyc/ AZO	Non-ohmic voltage-current behaviour		

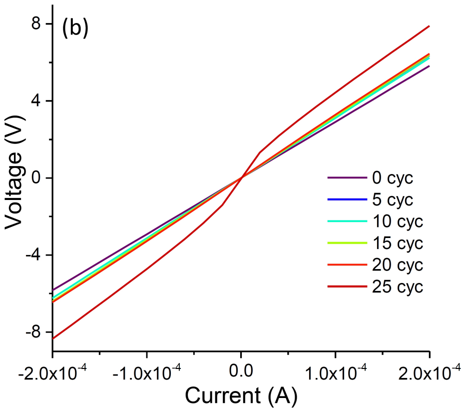

Figure 6.12: (a) Table of Van der Pauw and Hall measurements for AZO/Al_2O_3/ZnO with varying numbers of TMA-H_2O cycles (cyc). (b) The 2 point voltage-current behaviour for the multilayer samples

The electrical properties of lone ZnO layers were explored in Figure 6.6(f)-(h). For the multilayers, as might be expected, the Van der Pauw and Hall results are dominated by the conductivity of the AZO layer and there is little variation in properties for up to 20 cycles of TMA-H_2O (Figure 6.12). However, the carrier concentration in the multilayer is higher than that calculated when simply modelling the AZO/ZnO multilayer carrier concentration as the weighted average of the carrier concentrations of the two individual layers (Figure 6.13(a)). The weighted average gives the following result:

$$n_{total} = \frac{n_{AZO} \times d_{AZO} + n_{ZnO} \times d_{ZnO}}{d_{AZO} + d_{ZnO}}$$

$$= \frac{5.15 \times 10^{19} \times 25 + 6.64 \times 10^{16} \times 60}{25 + 60} = 1.52 \text{ x } 10^{19} \text{ cm}^{-3}$$

Where n is carrier concentration and d is layer thickness. The calculated value is considerably lower than the actual carrier concentration. As discussed previously, the carrier concentration of ZnO is higher when the crystals are more oriented by having a thicker layer or growth on an orienting substrate. The peak carrier concentration measured in these situations was around 4 x 10^{18} cm^{-3}, and growing ZnO on AZO does orient the ZnO layer more so it would not be unreasonable to use this carrier concentration to model the AZO/ZnO multilayer. Even with this value, calculated n_{total} is 1.80 x 10^{19} cm^{-3}, and the carrier concentration is also high for samples with non-oriented ZnO layers, which implies that the effective carrier concentration of the AZO layer is raised by being incorporated in the multilayer. The very simple weighted average model is not inconsistent with the data if n_{AZO} is calculated from measured n_{total} whilst taking into account the different estimated n and d layer values, giving n_{AZO} as $\approx$ 1.05 x 10^{20} cm^{-3} in the multilayer (Figure 6.13). The low thickness of the AZO layer (25 nm) means surface effects are likely to be limiting carrier concentration, as has been seen for thin 125 °C ZnO films, and so when ZnO is deposited on top of the AZO layer this surface effect is removed, resulting in a higher layer carrier concentration.

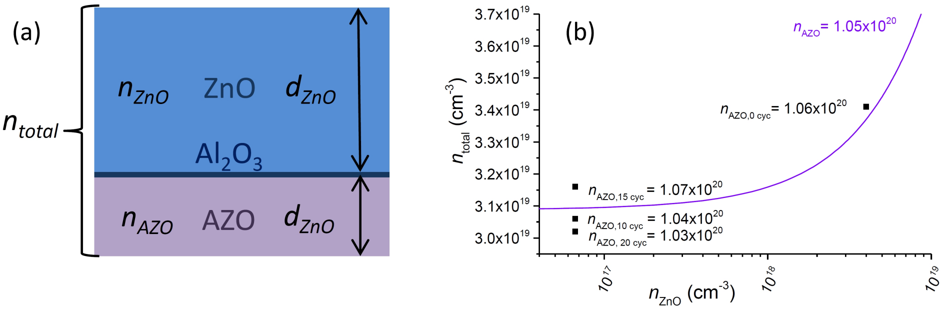

Figure 6.13: (a) Schematic of AZO/Al_2O_3/ZnO multilayers with the relevant layer thickness d and carrier concentration n labelled for the weighted sum model. (b) Graph showing the relationship between n_{ZnO} estimated from lone ZnO layers and measured n_{total} value for the multilayers. The data points are labelled with the corresponding n_{AZO} (in cm^{-3}) from the weighted sum model. The curve for the mean n_{AZO} = 1.05 x 10^{20} cm^{-3} is plotted. The 5 TMA-H_2O cycle (cyc) sample was omitted due to the difficulty of estimating n_{ZnO}.

The mobility of the multilayer is also greater than that of AZO or ZnO which could also be due to the removal of surface effects. Equally, oxygen and water diffusion along grain boundaries have been seen to reduce mobility in ZnO,[189] so the overlayers of ZnO (and Al_2O_3) on AZO may be offering some protection against this resulting in higher measured mobility for the multilayer compared to solo layers. Additionally, the multilayers with a continuous amorphous Al_2O_3 layer ($\geq$ 10 cycles) show slightly higher mobility than the 0 and 5 cycle multilayers which suggests there is extra protection against oxygen and water diffusion arising from the absence of grain boundaries passing through the entire film thickness in these layers, as has been seen for thin HfO_2 layers in transistors.[202]

For samples with a less than 20 cycle Al_2O_3 layer, current-voltage behaviour is ohmic, indicating that the Al_2O_3 layer is not significantly inhibiting conduction, but for 25 cycles or higher there is an s-shaped behaviour (Figure 6.12(b)). For these samples the insulating Al_2O_3 layer is presumed too thick for easy electron tunnelling, although reverse scans were not performed so it is unknown if there is also current hysteresis which could arise resistive switching behaviour.[159]

6.3.2 Multilayers on ITO for OPVs

Following on from the investigation of multilayers on quartz, this section explores multilayers deposited on pre-patterned glass/ITO substrates and their incorporation into an OPV as an electron transport layer (ETL).

Figure 6.14 shows SEM view comparing two different multilayers deposited on patterned substrates at the ITO-glass boundary. The AZO/ZnO multilayer shows randomly aligned, needle-like [100] oriented grains on the glass section, and areas of aligned grains on the ITO due an underlying ITO crystal. As is expected from the results in Section 6.3.1, if a 10 cycle layer of Al_2O_3 is added between AZO and ZnO then unaligned [100] and [002] grains are seen over the entire substrate.

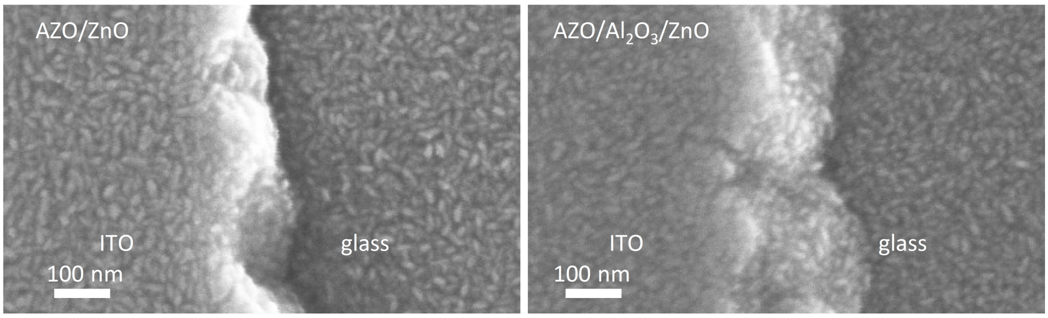

Figure 6.14: SEM images of AZO/ZnO and AZO/10 cycle TMA-H_2O/ZnO at the ITO-glass boundary of pre-patterend substrates.

To investigate the ITO/AZO/ZnO orientation relationship further, cross-sectional TEM was performed. Figure 6.15 shows the multilayer structure, demonstrating how lattice planes are aligned across the layer interfaces at certain locations, indicating an epitaxial type growth which supports the results discussed in Section 6.3.1.

A variety of multilayers were used as ETLs in OPVs to evaluate their performances. The active layer chosen for the OPV was a bulk heterojunction of poly[[4,8-bis[(2-ethylhexyl) oxy]benzo[1,2-b:4,5-b']dithiophene-2,6-diyl][3-fluoro-2- [(2-ethylhexyl) carbonyl]thieno[3,4-b]thiophenediyl]] : [6,6]-phenyl C71-butyric acid methyl ester (PTB7:$PC_{71}BM$), and an optimised sol-gel ZnO layer was used as a reference with which to compare. The total thickness of the ALD multilayers was between 60 - 75 nm, which was modelled to be the best thickness for an ITO/ZnO layer in terms of optical spacing within the cell structure. The results for a batch of OPVs are shown in Figure 6.16. The performance of the ITO/Al_2O_3/AZO/ZnO and ITO/AZO/ZnO cells are very similar, suggesting that the ZnO orientation does not have a particularly strong effect in this specific situation but again confirming that the 10 cycle Al_2O_3 layer does not significantly affect charge conduction. The ITO/AZO cell shows a slightly higher average J_{SC} than the AZO/ZnO containing cells whereas the ITO/ZnO cell has a lower J_{SC}, probably due to the difference in the conductivities of the ETLs as AZO has the highest and ZnO the lowest.

The ALD multilayer ETLs give worse PCEs than the sol-gel ZnO due to the lower V_{OC} and FF arising from the s-shaped current-voltage curve, which suggests there are charge transfer and recombination issues at the ETL/active layer interface. An important factor in the performance of ETLs is the work function, as an ideal

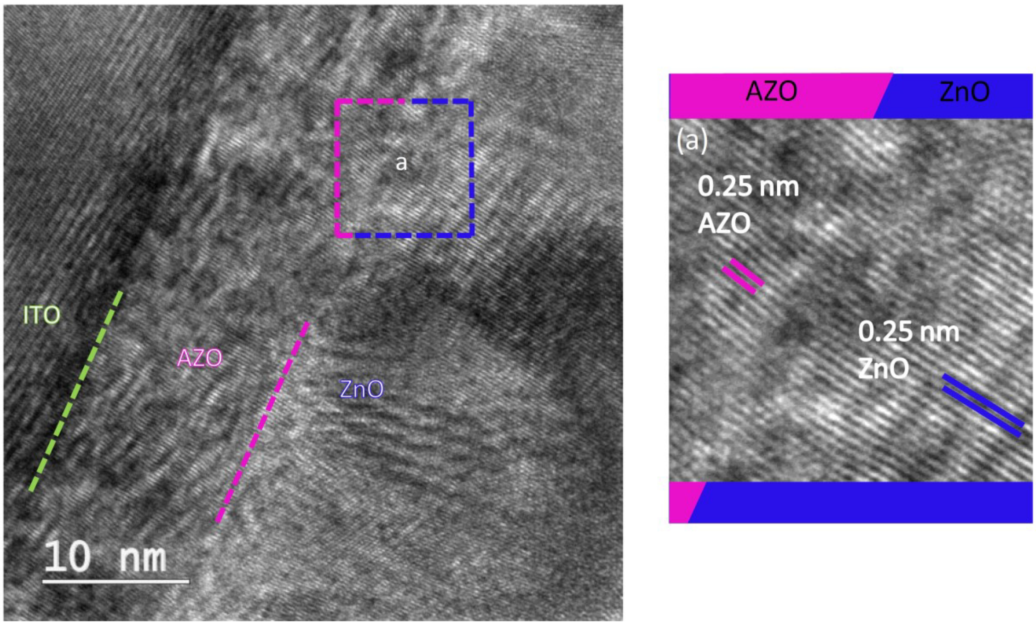

Figure 6.15: Cross-sectional HRTEM image of an ITO/AZO/ZnO multilayer. Area (a) is AZO/ZnO boundary where AZO and ZnO fringes are aligned, attributed to aligned (002) planes.

ETL would have a work function close to the lowest unoccupied molecular orbital (LUMO) of the electron acceptor material, enabling facile and electron-selective charge transfer. In this case, the PCBM electron acceptor has a -3.7 eV LUMO. The Kelvin probe measurements were taken to investigate the ALD multilayer work functions (Figure 6.17). ITO/AZO has a larger work function than multilayers terminating with ZnO, indicating that Al doping has a strong effect on the material's work function. The used here AZO has a very high dopant concentration (10 atomic % Al by EDX); varying the Al doping can be used to tailor the work function (studied in Section 7.4). There are only small variations in work function for the ITO/.../ZnO multilayers, with values around 4.5 eV, within a 0.09 eV range. None of the work functions are favourable for a PTB7:$PC_{71}BM$ OPV, explaining the consistently s-shape current-voltage curves, low V_{oc} and FF of all the ALD samples compared to the sol-gel ZnO reference (work function = 4.36 eV).[8] To obtain better PCE, either the work function of these ALD multilayers could be adjusted by e.g. surface functionalistion or the ETLs could be employed in cells with a more compatible active layer material.

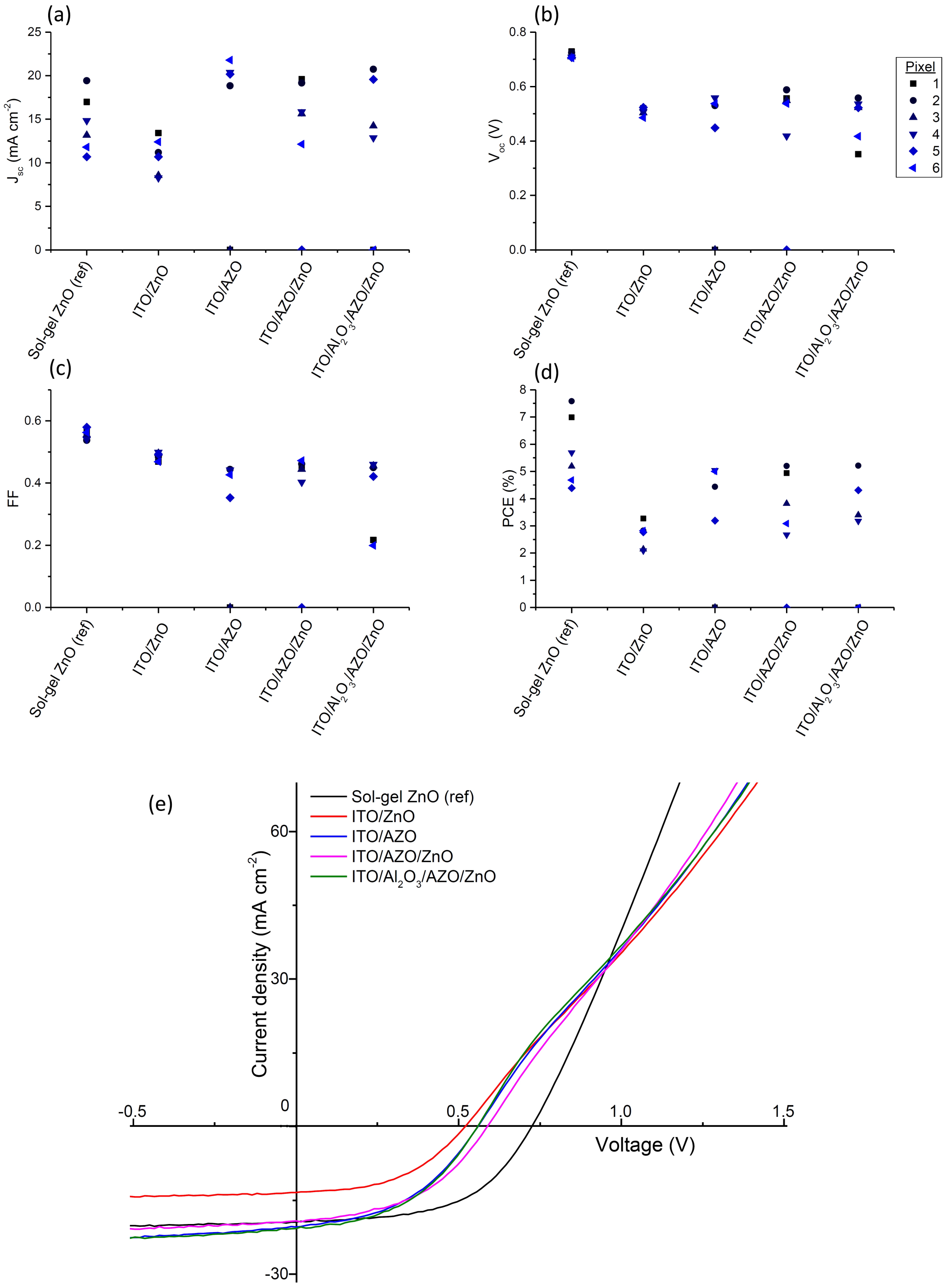

Figure 6.16: The (a) short circuit current density (J_{SC}), (b) open circuit voltage (V_{OC}), (c) fill factor (FF) and peak power conversion efficiency (PCE) are shown for a batch of PTB7:PC_{71}BM solar cells with different electron transport layers. Optimised sol-gel ZnO is used as a reference for the ALD multilayers. Each cell had six MoO_x electrodes deposited on top, which are referred to here as pixels, and are labelled 1-6 in graphs (a)-(d). The current-voltage behaviours of the best performing pixel of each cell are shown in (e)

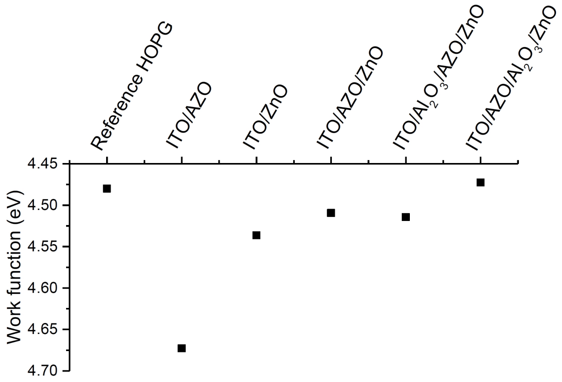

Figure 6.17: Work function of multilayers deposited on ITO, calculated from Kelvin probe measurements relative to a highly oriented pyrolytic graphite (HOPG) reference sample with a 4.48 eV work function.

6.4 Conclusions

The properties, particularly crystal orientation, of ALD ZnO deposited at 100 °C on a variety of substrates and ALD multilayers was investigated. The following results were found:

- AZO has a different crystal orientation to ZnO due to the Al doping, and both appear to have random in-plane crystal alignments when deposited on quartz and glass

- ZnO and AZO grown on ITO films are oriented with respect to the underlying ITO crystals.

- (100) and (001) cut sapphire substrates orient ZnO in the [100] and [002] directions respectively.

- The mobility of ZnO deposited at 100 °C is inherently low, around 1 - 3 $cm^2(Vs)^{-1}$, likely due to defects within the crystal.

- The carrier concentration of ZnO has an approximate bulk value of 4 x 10^{18} cm^{-3}, reached through either deposition on an orienting substrate or after a relatively high thickness ($\approx$ 145 nm). Defects and traps within poorly aligned grain boundaries are the proposed cause of the otherwise low carrier concentration.

- Deposition of ZnO on [100] AZO causes the generally mixed [100][002] film to orient to the more favourable [100] direction, through at least partially epitaxial growth, resulting in strain and bandgap changes.

- Insertion of a layer of Al_2O_3 of >10 cycles prevents subsequently deposited ZnO from orienting with respect to an underlying crystal substrate, without significantly inhibiting conduction until layers of >20 cycles.

- The large work function of the ALD ETLs was the performance-limiting factor in PTB7:$PC_{71}BM$ OPVs.

- The investigated ALD multilayer concept can be applied to a variety of devices to elucidate performance dependence on ZnO orientation

Chapter 7

Stability of perovskite on ALD layers

7.1 Introduction

One of the areas of solar cell research that has recently arisen is that of so-called, organic-inorganic perovskite solar cells. The new use of these materials in solar cells is of interest because they are compatible with inexpensive, print processing and flexible substrates,[203, 204] and the efficiencies have surpassed those of rival materials for this application area in just a few years of research (Figure 7.1 (a)).[205] The perovskite layers are employed as light absorbing semiconductors in the solar cells, and there are multiple possible elemental compositions for these materials, offering different beneficial aspects e.g. stability, efficiency and bandgap.[206] The perovskite used in this research is $CH_3NH_3PbI_3$, but the general organic-inorganic perovskite crystal structure is of ABX_3 form, where 'A' is an organic cation ($CH_3NH_3{}^+$), 'B' is a metal cation (Pb^{2+}), and X is a halide anion to which both are bonded (I^-). The 'B' atom sits centrally in a 'X' atom octahedron, and eight of these octrahedrons surround an 'A' atom, as shown in Figure 7.1(b).

The $CH_3NH_3PbI_3$ composition has produced the highest efficiency solar cells to date, but there are challenges to be overcome when using $CH_3NH_3PbI_3$ as often devices exhibit hysteresis and instability under certain conditions.[206–208] Studies have revealed that $CH_3NH_3PbI_3$ can be degraded irreversibly on exposure to water, but also that intermediate, reversible, hydrated $CH_3NH_3PbI_3$ phases are formed at lower humidities[16] and that the presence of a humid atmosphere whilst annealing perovskite layers for solar cells can improve their performance due to grain size increase and reduction of pin holes.[209] $CH_3NH_3PbI_3$ is also seen to degrade under combined light and O_2 exposure, attributed to the formation of $O_2{}^-$.[210] Elevated temperatures are generally (but not always)[211] needed to form good quality $CH_3NH_3PbI_3$ from reactant solution,[212] and there are also reports that annealing at e.g. temperatures of 150°C for an hour can be beneficial as small grains of PbI_2 form at grain boundaries, reducing solar cell recombination. Prolonged or higher temperature heating, however, leads to complete degradation.[213] Considering that solar cells can reach temperatures of 85 °C in operation, studying the degradation of $CH_3NH_3PbI_3$ at temperatures between 100 -170 °C can both give information on how annealing perovskite layers can affect device performance but also can be used as an approximate measure of how stable a perovskite solar cell might be in

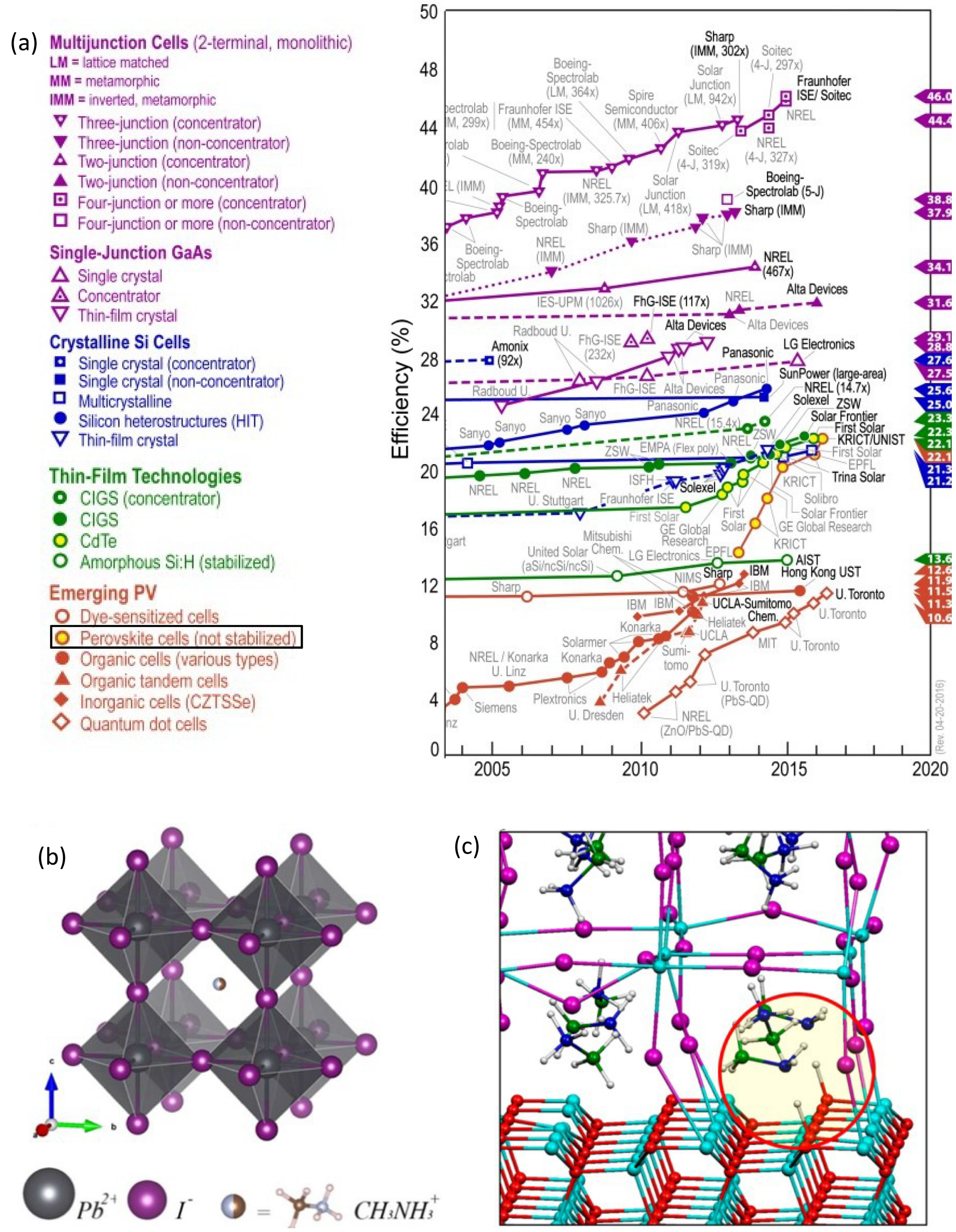

Figure 7.1: (a) Graph of the record research solar cell efficiencies, with the perovskite symbol outlined for easy identification in the key. Adapted from graph released by the National Renewable Energy Laboratory, www.nrel.gov/ncpv/images/efficiency_chart.jpg. (b) Crystal structure of $CH_3NH_3PbI_3$. Reproduced with permission from reference,[14] ©2015 American Chemical Society. (c) Computer simulation of $ZnO/CH_3NH_3PbI_3$ interface revealing the deprotonatation of methylammonium. Reproduced with permission from reference[15] ©2015 American Chemical Society

the long-term. Studying $CH_3NH_3PbI_3$ degradation with temperature is the focus of this chapter.

Devices employing a $CH_3NH_3PbI_3$ absorbing layer typically require $CH_3NH_3PbI_3$ to be sandwiched between selective electron and hole transport layers (ETL and HTL) with which a transparent and a metal electrode are in contact. ZnO is a candidate material for ETLs: it has a wide bandgap and reasonably good conduction band alignment with $CH_3NH_3PbI_3$ so can selectively conduct electrons from $CH_3NH_3PbI_3$ to a conductive electrode. ZnO is more stable itself than organic alternatives and (if a continuous layer is used) could offer some protection against water and oxygen infiltration into the active layer.[214] The electron mobility of ZnO is higher than frequently-used TiO_2, which can be beneficial for this cell type as the lifetime of an electron is lower than that of holes in $CH_3NH_3PbI_3$, so nanostructured ETLs which penetrate into the active layer can be used to help collect electrons, raising efficiencies.[215] There are multiple reports of perovskite solar cells with reasonable power conversion efficiencies (>10 %) which use ZnO ELTs.[204,216,217] However, ZnO does have some disadvantages as an ETL, for example ZnO surfaces are complex and can contain traps[77] and the charge transfer properties in these and other solar cell types have sometimes been reported as poorer than for e.g. TiO_2.[76,218] Also, specifically for perovskite solar cells, contact between ZnO and $CH_3NH_3PbI_3$ has been seen to cause a large increase in instability of the $CH_3NH_3PbI_3$. $CH_3NH_3PbI_3$ deposited on ZnO degraded more rapidly in the presence of water vapour or heat than on reference samples.[15,216,219,220] Modelling revealed that at a $ZnO/CH_3NH_3PbI_3$ interface some of the $CH_3NH_3^+$ ions became deprotonated through an acid-base reaction with ZnO, resulting in an O–H terminated ZnO surface (Figure 7.1(c)). This was thought to be initiation step of the $CH_3NH_3PbI_3$ degradation, and the deprotonation was not seen to occur for $TiO_2/CH_3NH_3PbI_3$ interfaces. The same study reported annealing their sol-gel ZnO before $CH_3NH_3PbI_3$ deposition increased the stability, which was attributed to a decrease in organic residue and hydroxyl components on the ZnO surface, however annealing can have other effects that may have also contributed, including changes in ZnO stoichiometry and crystallinity. As shown in Chapter 6, through substrate choice, doping and multilayers ALD can be used to control ZnO orientation without deposition parameter changes, which allows the separation of this factor from the other possible contributions. This chapter presents the study of the factors affecting $CH_3NH_3PbI_3$ decomposition on ZnO and AZO at elevated temperatures, with all ALD layers deposited at 100 °C for consistency.

7.2 Zinc oxide/perovskite decomposition on heating

Two main techniques were chosen for studying the decomposition of $CH_3NH_3PbI_3$: photography and X-ray diffraction (XRD). From Figure 7.2(a) it can be seen that $CH_3NH_3PbI_3$ layers appear dark brown/black due to the small bandgap ($\approx$ 1.5 eV) and good absorbance over visible wavelengths,[221] whereas as the decomposed layer, consisting of PbI_2, appears yellow. This enables the decomposition process to be followed through colour change. Figure 7.2(b) shows a series of photographs following the decomposition of $CH_3NH_3PbI_3$ on glass/ITO compared to glass/ITO/ALD ZnO whilst heated at 100 °C on a hotplate in a N_2 glove box. The glass/ITO/ZnO/$CH_3NH_3PbI_3$ multilayer structure is equivalent to the anode side of a $CH_3NH_3PbI_3$ solar cell (as is used in Section 7.4). It is clear that $CH_3NH_3PbI_3$

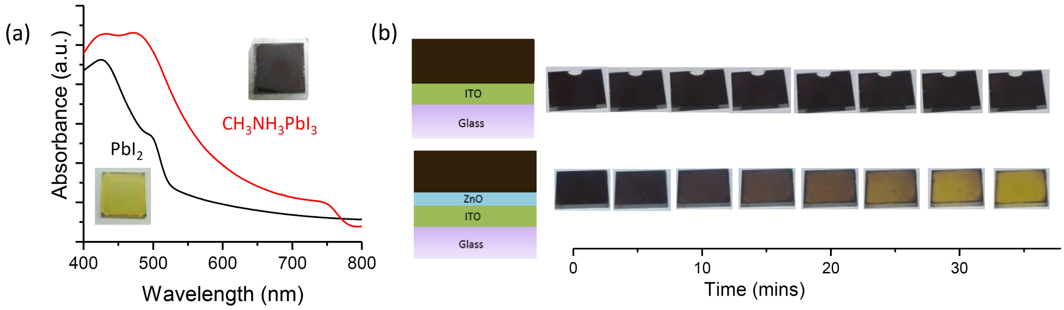

Figure 7.2: (a) Absorbance of an as-deposited $CH_3NH_3PbI_3$ film and a decomposed film (PbI_2). (b) Sequential photographs of samples heated on a hotplate at 100 °C within a N_2 glove box. The samples consist of glass/ITO/ZnO/$CH_3NH_3PbI_3$ and glass/ITO/$CH_3NH_3PbI_3$ layers, represented by the adjacent schematics. These schematics are used in the rest of this chapter with the same colour representations: substrate = purple, ITO = green, ZnO = blue, perovskite = brown.

was degraded more rapidly on ZnO compared to ITO, in agreement with the literature on the instability of ZnO/$CH_3NH_3PbI_3$ layers.

This degradation of $CH_3NH_3PbI_3$ can also be followed by XRD; a temperature-controlled XRD system which had a vacuum chamber, heated stage and a controlled 0.7 × 0.7 mm measurement area (using the 'Autoslits' program, Section 3.1.4) was used to follow the degradation process in-situ. Figure 7.4(a) shows the diffraction patterns of the three phases seen during the degradation experiment. As described earlier, $CH_3NH_3PbI_3$ has a perovskite crystal structure which, at room temperature, is tetragonal. At 54 °C the $CH_3NH_3PbI_3$ transforms from tetragonal to cubic due to the increase in energy, as the ions lack the required relative sizes to form a cubic perovskite structure at lower temperatures.[14] This transformation is of some concern for solar cells as they may fluctuate across this temperature threshold during operation. $CH_3NH_3PbI_3$ also has a high coefficient of thermal expansion compared to some other solar cell materials e.g. 6 times higher than glass,[14] which could lead to some unusual stress-related temperature effects in the solar cells. A change in the XRD peaks present at 40 °C and 135 °C was seen for a quartz/ZnO/$CH_3NH_3PbI_3$ sample, shown in Figure 7.4(a), corresponding to the tetragonal to cubic transformation, along with a peak shift to smaller angles due to the thermal expansion. The quartz/ZnO/$CH_3NH_3PbI_3$ was held at 135 °C under vacuum for 6 hours, and the final crystal structure seen was predominantly that of PbI_2. Figure 7.4(b) shows the sequential XRD patterns for this in-situ, gradual degradation of $CH_3NH_3PbI_3$ into PbI_2. Note that there are no ZnO XRD peaks labelled on the patterns despite the initial ZnO/$CH_3NH_3PbI_3$ bilayer; this is due to the ZnO peaks being too small to be visible at these rapid 2θ scan rates (thin film with weaker out-of-plane orientation).

As was expected, the degradation of $CH_3NH_3PbI_3$ on ALD ZnO occurred more rapidly at higher temperatures due to the increased energy available for the reactions. This was revealed when the degradation of $CH_3NH_3PbI_3$ was monitored by in-situ XRD at different temperatures, as shown in Figure 7.4 where the cubic $CH_3NH_3PbI_3$ (100) peak area was used as measure of the perovskite degradation progress.

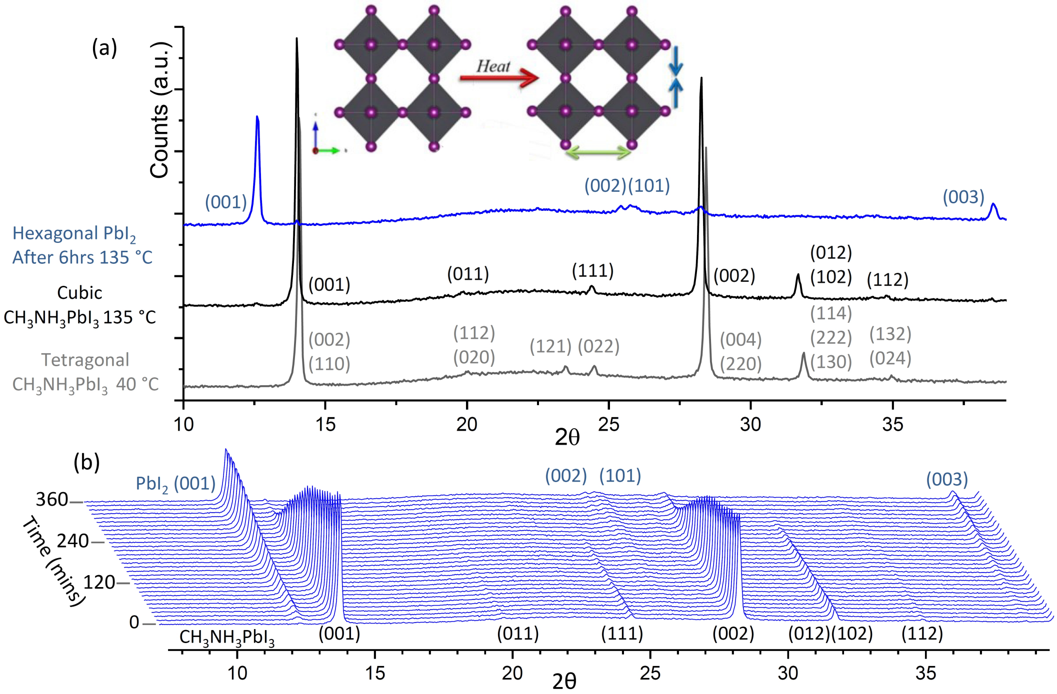

Figure 7.3: (a) XRD patterns illustrating the three main crystal structures between which $CH_3NH_3PbI_3$ transforms. Inset diagram of crystal transformation from tetragonal to cubic with temperature is reproduced with permission from reference,[14] ©2015 American Chemical Society. (b) The XRD pattern following the decomposition of $CH_3NH_3PbI_3$ deposited on top of ALD ZnO during heating at 135 °C under vacuum.

The degradation of $CH_3NH_3PbI_3$ was seen to depend on the underlying ZnO thickness. Figure 7.5 shows the sequential photographs of $CH_3NH_3PbI_3$ layers deposited on different thickness ALD ZnO layers and heated to 100 °C and 160 °C. The $CH_3NH_3PbI_3$ on the 240 and 360 cycle samples decomposed at approximately equal rates. There are varying decomposition rates between areas of the substrates; this is due to different ZnO crystal alignment which depends on the underlying substrate on which the ZnO is grown. The faster degradation occurred in two strips on opposite edges, corresponding to the glass/ZnO areas of the substrate, whereas slower degradation occurred on the glass/ITO/ZnO area (explored further in Section 7.3). The degradation rate on the 60 cycle ZnO is very different to that on the 240 and 360 cycle samples. After 10 mins the 60 cycle sample had decomposed slightly, but no significant change was seen after that point up to 60 minutes. When the film was then heated to 160 °C the degradation rate approximately followed that of the ITO/$CH_3NH_3PbI_3$ reference, where perovskite on ITO degraded faster than on glass. In comparison, a 240 cycle sample completely degraded within 2 minutes at 160 °C. These results reveal that at ZnO and $CH_3NH_3PbI_3$ react but that a certain amount of ZnO is needed to completely degrade the $CH_3NH_3PbI_3$ layer, so the ZnO must be consumed in the reaction. When the ZnO thickness is beyond the critical value then the $CH_3NH_3PbI_3$ decomposition continues to completion, without significant rate dependence on thickness. Below the critical thickness the reaction proceeds until the ZnO is fully depleted, followed by degradation at the rate determined by the newly exposed interface material.

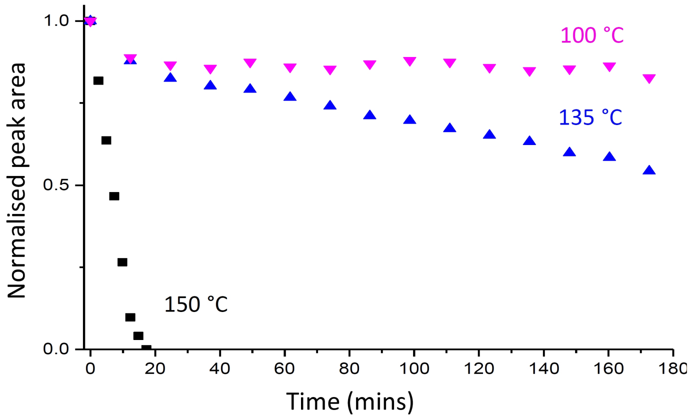

Figure 7.4: Graph showing the normalised (100) $CH_3NH_3PbI_3$ peak area for quartz/ZnO/$CH_3NH_3PbI_3$ films heated to different temperatures.

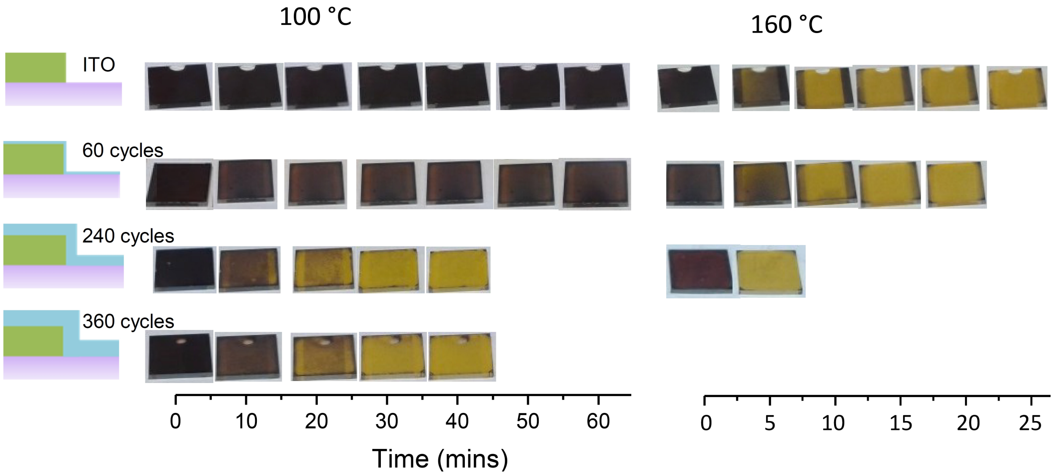

Figure 7.5: Photographs of ZnO/$CH_3NH_3PbI_3$ films with different ZnO thickness (number of ALD cycles) heated to 100 °C in a glove box. 60 cycles = 10 nm ZnO, 240 cycles = 40 nm, 360 cycles = 60 nm. The ITO and 60 cycle samples photographed at 100 and 160 °C are the same samples (following the insignificant degradation after heating at 100 °C for 60 mins, they were heated to 160 °C).

To investigate the effect of the heating on both ZnO and $CH_3NH_3PbI_3$ simultaneously, a temperature-controlled XRD study was carried out. Instead of depositing ZnO on quartz, where there are no easily visible ZnO XRD peaks, ZnO was deposited on $(10\bar{1}0)$ sapphire resulting in a strong (100) ZnO peak (as was explored in Section 6.2). The in-situ XRD patterns are shown in Figure 7.6(a) and the areas of the (100) $CH_3NH_3PbI_3$ and (100) ZnO peaks are plotted in Figure 7.6(b). It is clear that both $CH_3NH_3PbI_3$ and ZnO have decomposed. The (100) $CH_3NH_3PbI_3$ peak almost completely disappeared, and the remaining, extremely small $CH_3NH_3PbI_3$ peaks are thought to be from film defects e.g. particles of $CH_3NH_3PbI_3$ which are not representative of the bulk film. The ZnO (100) peak area, on the other hand, decreased until plateauing at 67 % of the original value. The ZnO layer was 40 nm thick (240 cycles), so a decrease of 33 % is very approximately equivalent to the loss of 13 nm of ZnO. This result agrees with the previous findings, where a 10 nm ZnO layer was insufficiently thick to completely decompose the $CH_3NH_3PbI_3$ layer. The

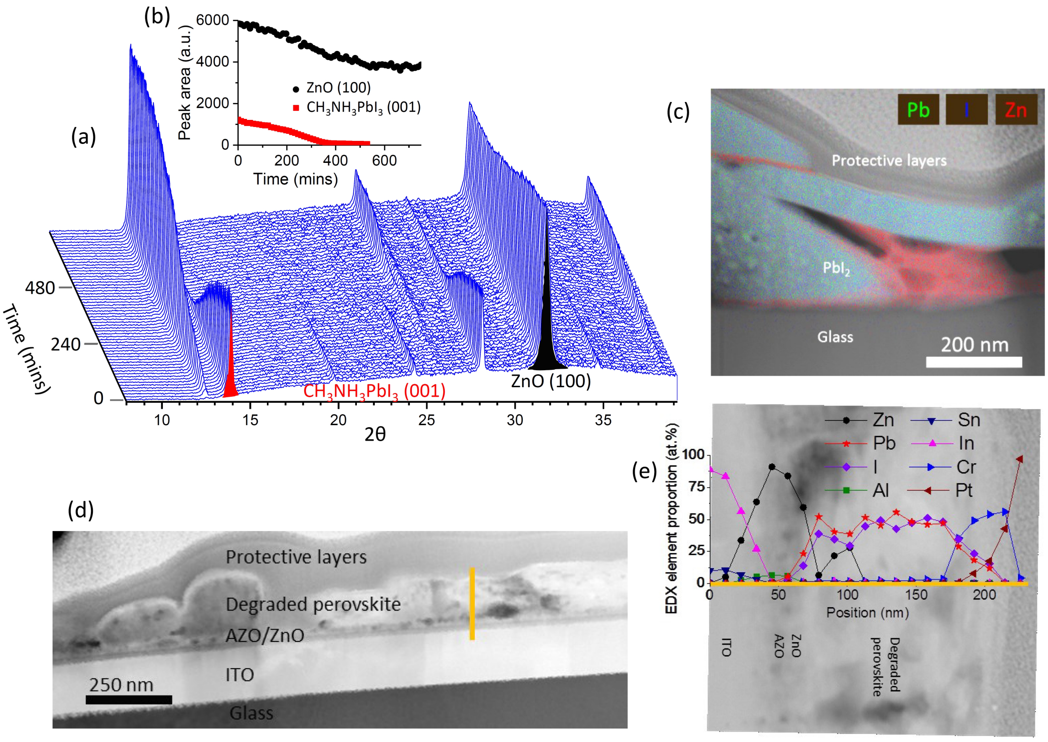

Figure 7.6: (a) XRD pattern following the decomposition of $(10\bar{1}0)$ sapphire/(100)ZnO/$CH_3NH_3PbI_3$ whilst annealing at 135 °C under vacuum. The (100) $CH_3NH_3PbI_3$ peak and (100) ZnO peak areas are plotted in (b). (c) Dark field STEM image of decomposed ZnO/$CH_3NH_3PbI_3$ multilayer after annealing at 100 °C in a glove box, with EDX colour map overlay. (d) Dark field STEM image of decomposed AZO/ZnO/$CH_3NH_3PbI_3$ multilayer after annealing at 150 °C under vacuum. EDX line scan across the film is shown in (e).

thickness of the $CH_3NH_3PbI_3$ layer was ≈ 250 nm, which suggests that complete decomposition might require an approximate $CH_3NH_3PbI_3$:ZnO thickness ratio of around 19:1.

The decomposition of $CH_3NH_3PbI_3$ occurs differently in the glove box to in vacuum (discussed later in this section), so cross-sectional TEM samples were prepared for samples annealed until complete degradation in vacuum and in the glove box. Figure 7.6(c) shows an area of the decomposed, 100 °C, glove box multilayer. Large PbI_2 crystals were seen, and there was no longer a 40 nm crystalline film of ZnO present. Instead, there were areas of the substrate where only an ultrathin film of Zn containing material existed between the glass substrate and the PbI_2 crystals. In other areas there were agglomerations of amorphous-appearing Zn-containing material. Figure 7.6(d),(e) shows a sample, originally of an ITO/AZO/ZnO/$CH_3NH_3PbI_3$ structure which was heated until degradation at 150 °C under vacuum. The appearance is quite different from glove box sample: the ZnO layer had decreased in thickness due to being consumed in the degradation reaction but there was still a crystalline portion of ZnO remaining on top of the AZO. At some locations on the sample the presence of Zn could be seen within the degraded perovskite layer as shown by the EDX line scan in Figure 7.6(e).

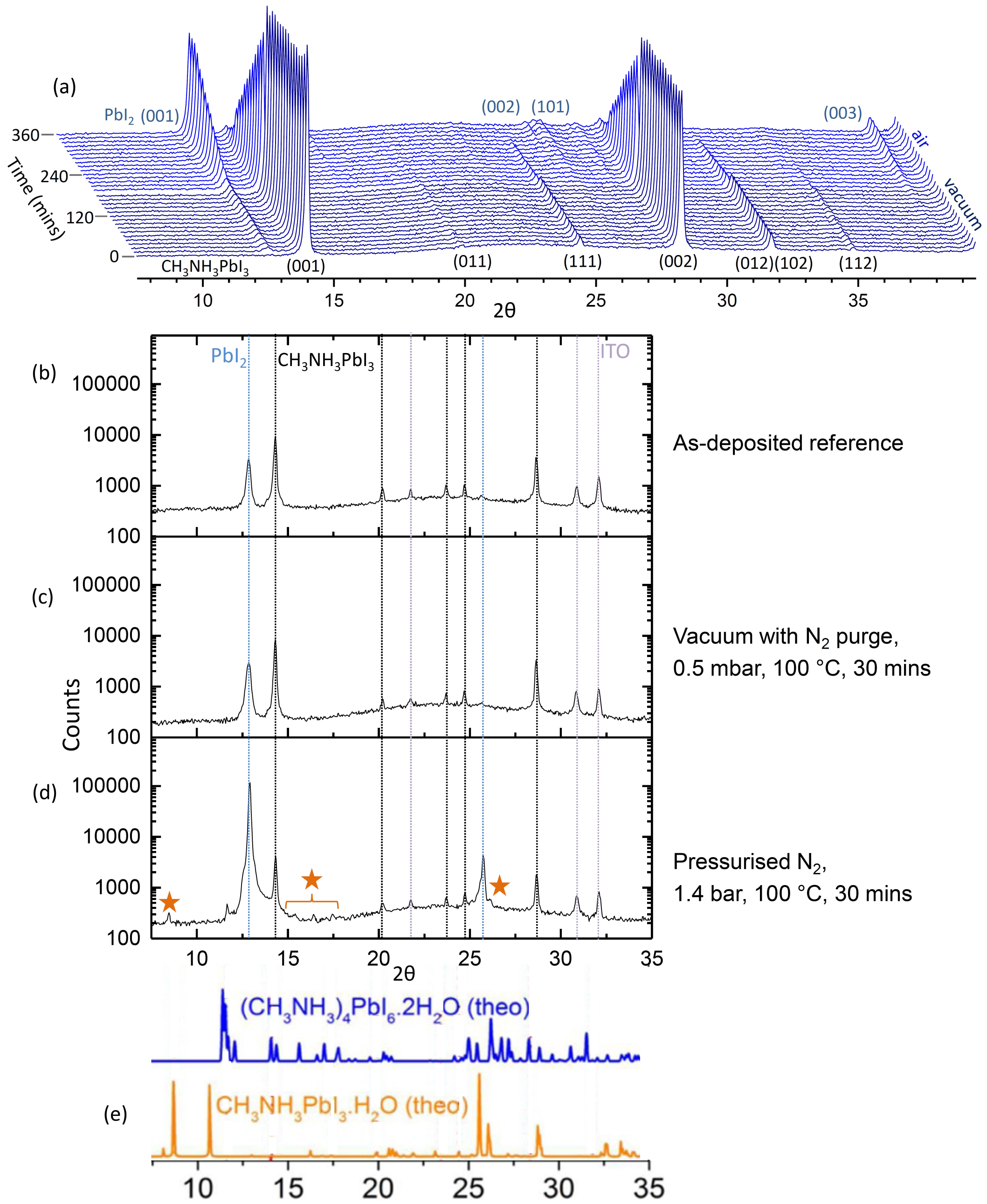

Figure 7.7: (a) XRD pattern of ZnO/$CH_3NH_3PbI_3$ heated at 100 °C under vacuum and then under air. (b)-(d) The XRD patterns comparing three ZnO/$CH_3NH_3PbI_3$ samples with different heat treatments. (e) Theoretical XRD patterns of hydrated $CH_3NH_3PbI_3$. Adapted with permission from reference[16] ©2015 American Chemical Society

As mentioned above, degradation of $CH_3NH_3PbI_3$ occurs differently under vacuum from in the glove box, indicated by the disparate times needed for complete decomposition seen in the preceding results. For example, the degradation of $CH_3NH_3PbI_3$ on 40 nm ZnO took $\approx$ 5 hours at 135 °C under vacuum, whereas the same thickness of ZnO and $CH_3NH_3PbI_3$ took $\approx$ 30 minutes at 100 °C in the glove box. This vast difference in rate suggested that either the atmosphere and/or pressure under which $ZnO/CH_3NH_3PbI_3$ effects the degradation reaction. A temperature controlled XRD measurement was carried out to investigate this further (Figure 7.7(a)). Under vacuum at 100 °C very little degradation of a quartz/$ZnO/CH_3NH_3PbI_3$ sample was seen. After 3 hours the sample was cooled, air was let into the chamber, then the sample was heated back up to 100 °C again (took <15 minutes). The sample immediately showed much more rapid degradation and was fully degraded within 160 minutes.

From the photography and temperature controlled XRD observations it was suspected that the pressure was the dominant rate determining factor, as the degradation rate was fastest in the N_2 glovebox (2 mbar above atmosphere), slower in air (1 bar) and considerably slower under vacuum (10^{-5} bar). However, to be confident of this, other factors that might affect decomposition rate must be considered and eliminated. There was likely to be a difference in temperature between the hot plate in the glove box and the heated stage in the temperature controlled XRD equipment. The temperature of the hot plate was measured with an infra-red heat gun and the substrate temperatures were checked for both systems using colour changing indicators (Section 4.4.3) which revealed that the temperature was within the expected range of 6 °C precision. Even so, the temperatures were not likely to be identical, so direct comparisons should only be made where there is a very large, indisputable difference in reaction rate. Another factor that could have affected the decomposition rate is the difference in atmosphere. The samples in vacuum and the glove box can be considered to be under inert atmosphere; however, the sample in air is exposed to H_2O and O_2 which are known to increase degradation rate in some situations. Additionally the sample in the glove box was exposed to normal room lighting, whereas those in the XRD were in the dark.

An experiment was designed to reduce the amount of extra variables. ITO/ZnO/$CH_3NH_3PbI_3$ samples were prepared and the ALD system was used to heat them in the dark under two different pressures of inert N_2 atmosphere. The two samples were separately put into the reaction chamber and both underwent 7 minutes of the chamber being evacuated and purged with N_2 (7 minutes being approximately the time taken for the sample to equilibrate at 100 °C). The low pressure sample was then kept under the flowing 0.5 mbar N_2 for 30 minutes, whilst for the high pressure sample the chamber was filled with N_2 pressurised to 1.4 bar for the 30 minutes' heating. XRD patterns of these two samples were taken immediately after removal from the ALD system, and a reference as-deposited sample was also measured. Figure 7.7(b)-(d) shows the XRD patterns of the three samples. It can be seen that the sample under 0.5 mbar did not significantly degrade but the sample under pressurised N_2 underwent rapid degradation. In addition to the ITO, $CH_3NH_3PbI_3$ and PbI_2 peaks a few extra, very small peaks are distinguishable for the pressurised N_2 sample. These may be due to intermediate compounds formed before complete degradation to PbI_2. One possibility is that they might be hydrated perovskite as they somewhat match the theoretical and experimental peaks from the literature[16] (Figure 7.7). A possible mechanism is that H_2O is formed at some stage in the acid-base reaction between ZnO and $CH_3NH_3PbI_3$, which would be removed from the film by a vacuum but would remain under high pressure, increasing the degradation rate of the $CH_3NH_3PbI_3$. This may also explain why some crystalline ZnO remained in the TEM of the vacuum sample in Figure 7.6 whilst the Zn in the glove box sample appeared as an amorphous, unknown compound, maybe as a result of ZnO dissolution. Generally annealing perovskite under vacuum has also been reported as beneficial due to the removal of by-product from the perovskite layer, so this affect may also be contributing.[222, 223]

7.3 Stability dependence on zinc oxide orientation

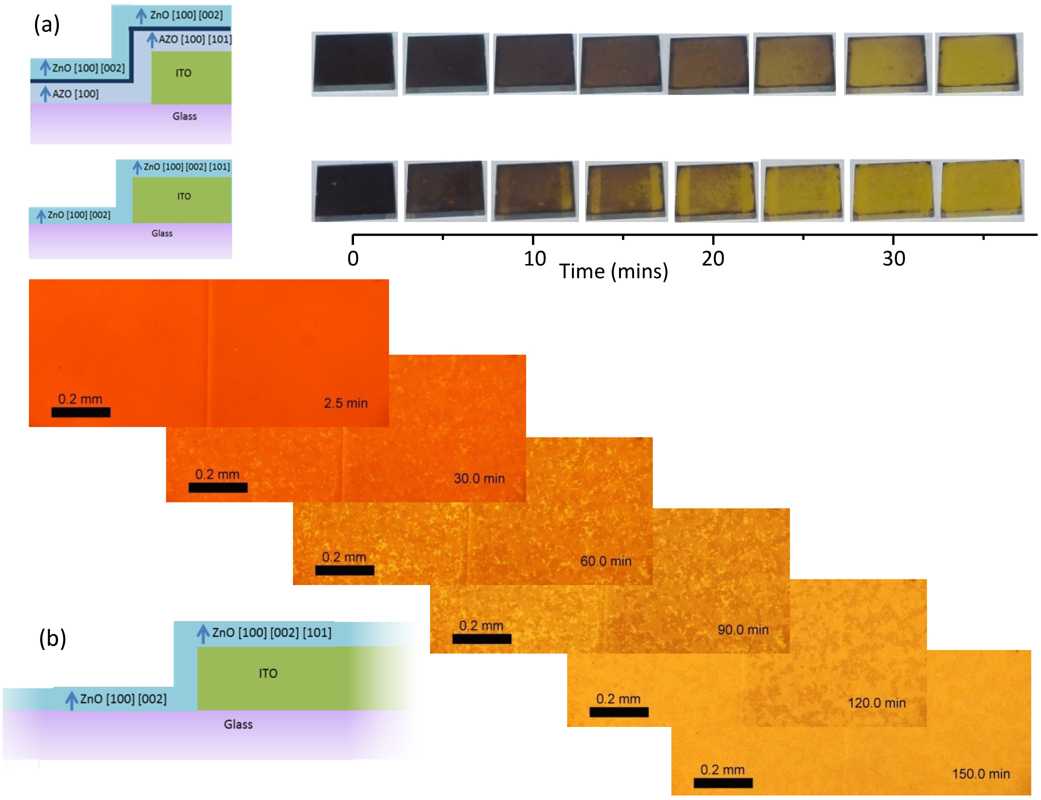

Figure 7.8: (a) Photographs following the decomposition of $CH_3NH_3PbI_3$ on ZnO with uniform crystal structure and ZnO with different crystal orientation on glass and ITO. Heating is at 100 °C in a glove box. (b) Micrographs of the decomposition of ZnO/$CH_3NH_3PbI_3$ at 100 °C at the boundary between ZnO on glass and ZnO on ITO.

It was observed in the previous section that the degradation of ZnO/$CH_3NH_3PbI_3$ sometimes occurred at different rates on different areas of a substrate. From the studies in Section 6.2 it is known that ZnO deposited on pre-patterned ITO has a different crystal alignment on the glass edge areas to on ITO. It was suspected that this difference in ZnO orientation was responsible for the difference in degradation rate. Figure 7.8 shows that for substrates with all else equal the different degradation rates are only observed when there are areas of ZnO of different orientations.

Studying this effect further with optical microscopy revealed that patches of the $CH_3NH_3PbI_3$ film, possibly particularly susceptible areas, degraded quicker than other areas but the bulk of the perovskite on the glass/ZnO area degraded more rapidly than that on the glass/ITO/ZnO.

To further investigate the effect of the crystal orientation, ZnO was deposited on sapphire substrates. As was discussed in Section 6.2, ZnO is preferentially [100] oriented on $(10\bar{1}0)$ sapphire, mixed [100][002] oriented on quartz and [002] oriented on (0001) sapphire (Figure 7.9(a)). $CH_3NH_3PbI_3$ was deposited on top of the ZnO layers and degradation was followed by temperature controlled XRD. Figure 7.9(c)-(e) shows the XRD patterns of the substrates, which show clear differences in the degradation rates and Figure 7.9(b) directly compares the normalised (100) $CH_3NH_3PbI_3$ peak area as a measure of degradation progression. The $CH_3NH_3PbI_3$ degrades most rapidly on the [002] oriented ZnO, followed by the mixed [100][002] ZnO and the slowest rate was on [100] oriented ZnO. The faster degradation on the [002] orientation could be linked to the polar nature of that orientation; in the literature, adsorption selectivity[185] and differences in photocatalytic activity[186] have been reported for different ZnO orientations. There may also be effects due to the grain size etc. so further studies and computer modelling are needed to elucidate this.

7.4 Stability with aluminium doped zinc oxide

Al doped ZnO is a possible alternative to ZnO as an ETL and had been reported to produce improved efficiencies in solar cells, possibly due to a better band alignment with $CH_3NH_3PbI_3$.[91, 224, 225] It was chosen that the deposition temperature would be kept to the 100 °C used for the earlier ZnO films in order to minimise deposition variables. As was true for AZO deposited at higher temperatures (Section 5.3), changing the doping ratio of the films is an effective way of tuning the AZO properties. The doping used a DEZ-H_2O:TMA-H_2O precursor release sequence. Using EDX, the composition of the deposited films was measured (Figure 7.10); the doping amount was similar equivalent cycle ratios in literature.[30] The switch between mixed [100][002] orientation and [100] preferential orientation is observed for these AZO films when doped, due to the disruption of the polar ZnO surfaces by Al as described in Section 5.3. The bandgap widens with increasing doping; however the bandgap does decrease between the 5 % and 8 % dopings. This could be linked to the changes in the crystal structure as the (100) peak is smaller than for others with heavier doping. For the 5 % doping the TMA-H_2O cycles are separated by a large number of DEZ-H_2O cycles, so the (100) orientation did not develop as fully, resulting in a different strain of the film. The work functions of the films reduced Al doping of <8 %, but increased dramatically with heavier doping. This is in agreement with a study by Dong et al. where intermediate Al doping raised the conduction band closer to that of perovskite, reducing recombination, whereas heavy doping lowered it.[91] Increasing work function with heavier Al doping has also reported elsewhere.[89] The electrical properties are shown in Figure 7.10(e); the doping increased the carrier concentration to the order of 10^{19} cm^{-3}. The mobility increased up to 8 % doping and then decreased. In the AZO films deposited at 150 °C the mobility decreased with doping, however, ALD ZnO deposited at low temperatures has a different limiting factor (possibly the high H content), so if

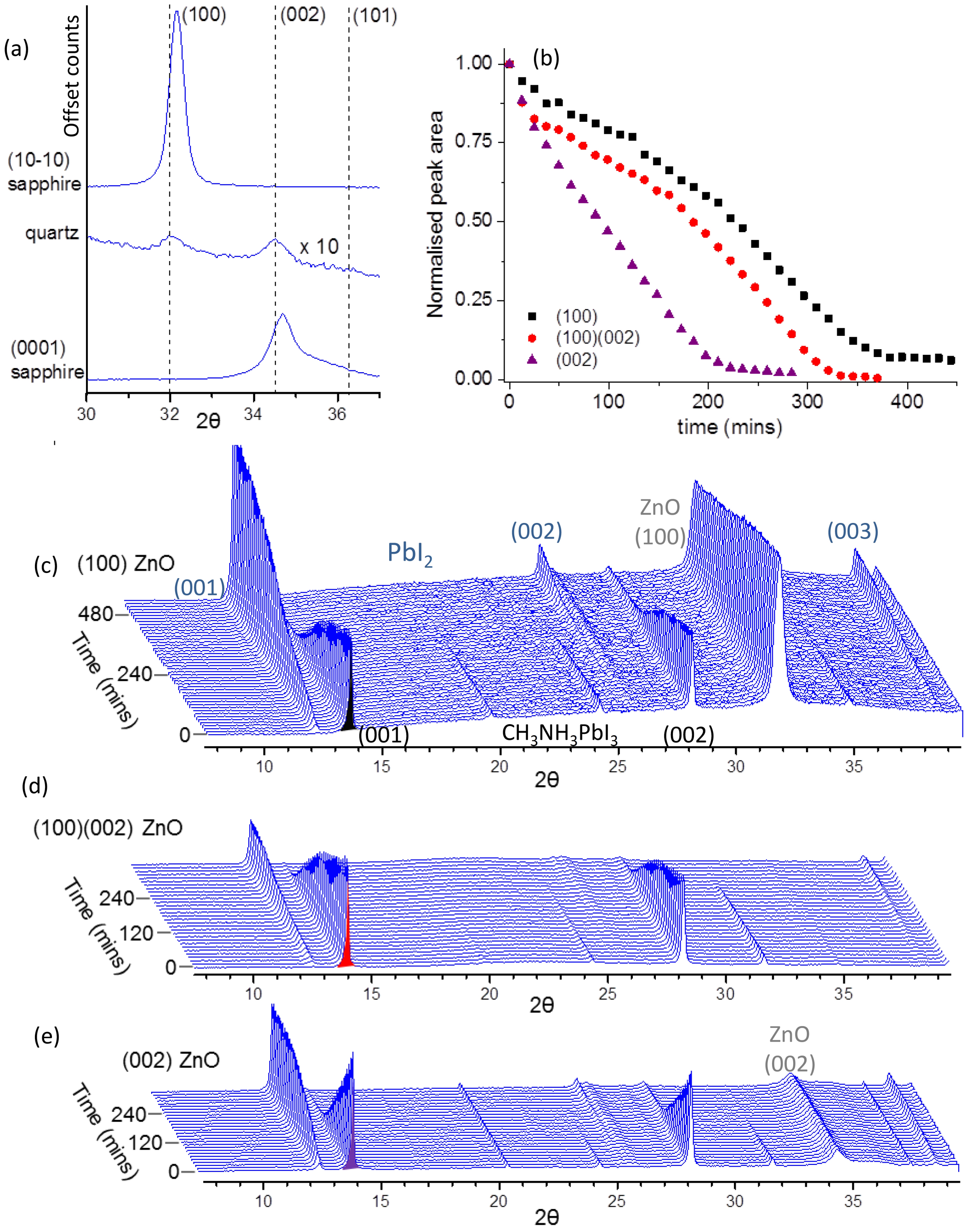

Figure 7.9: (a) XRD pattern of ZnO on (10$\bar{1}$0) sapphire, quartz and (0001) sapphire. (c)-(e) XRD patterns of the ZnO/$CH_3NH_3PbI_3$ 135 °C samples. The normalised peak areas of (100) $CH_3NH_3PbI_3$ with time for each substrates are shown in graph (b).

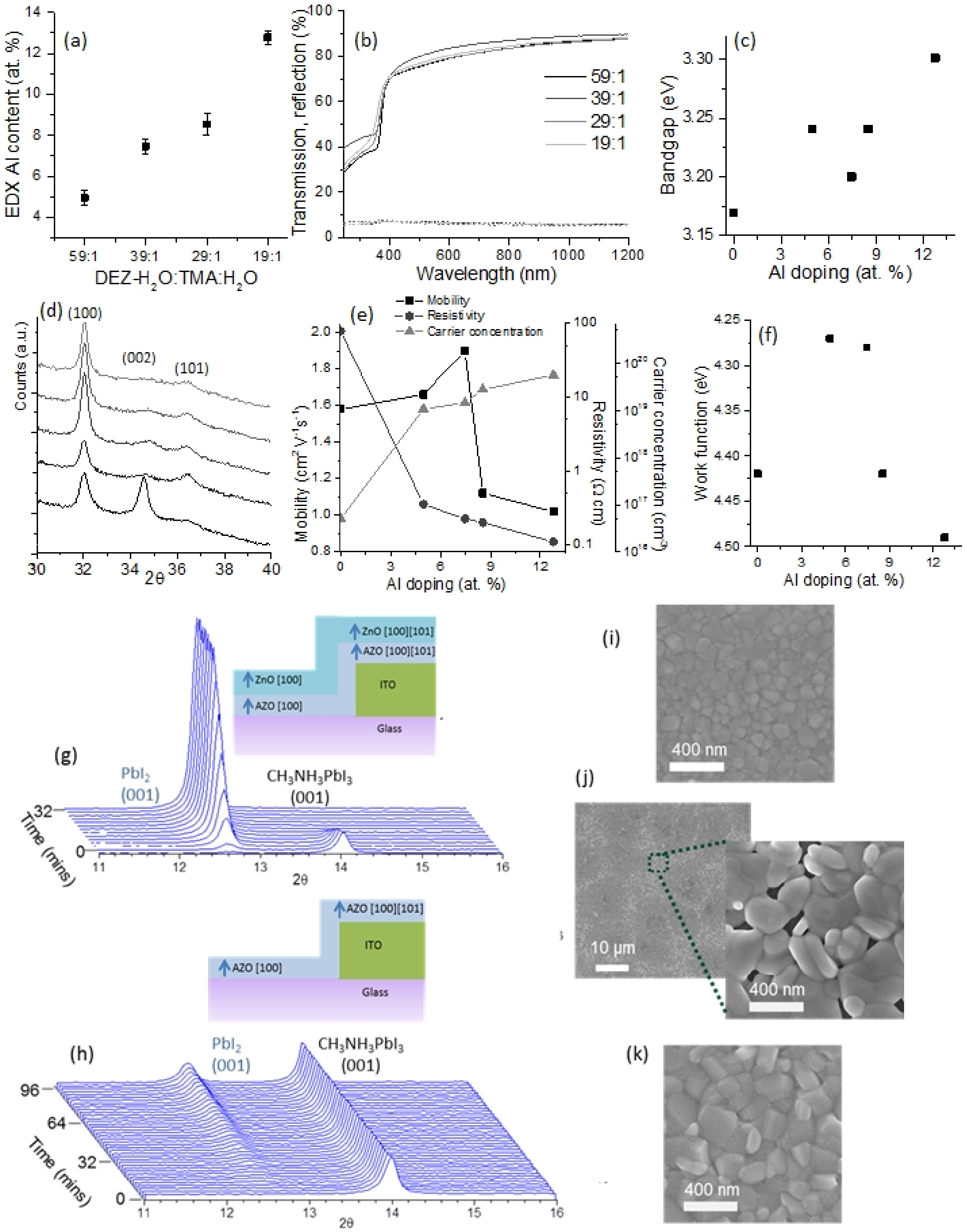

Figure 7.10: (a) EDX Al content with doping cycles. (b) Transmission and reflection of AZO and (c) the respective bandgaps. (d) XRD, (e) electrical properties and (f) work function of the AZO films. (g) and (h) show XRD patterns of $CH_3NH_3PbI_3$ films deposited on ZnO and AZO samples, heated at 150 °C under vacuum. (i) shows SEM of the as deposited $CH_3NH_3PbI_3$, and (j) and (k) show SEM of the ZnO/$CH_3NH_3PbI_3$ and AZO/$CH_3NH_3PbI_3$ films following the heated XRD studies.

the TMA-H_2O cycles help eliminate some of the sources of low mobility then there will be an increase. Also, the carrier concentration could be improving mobility for conduction across grain boundaries,[30] and furthermore the grain boundary misalignment may be improved due to the strong [100] preferential orientation. For heavier doping, the mobility reduced, probably due to scattering from the ionised dopant atoms and the interruptions in the crystal structure caused by Al rich layers.

The stability of $CH_3NH_3PbI_3$ on AZO and ZnO under vacuum was studied by XRD. It was found that degradation of the $CH_3NH_3PbI_3$ on AZO occurred in a different manner to that on ZnO and was quite similar to that on TiO_2 from the literature,[226] indicating that the interface was more stable than that of ZnO/$CH_3NH_3PbI_3$. During the vacuum annealing of AZO/$CH_3NH_3PbI_3$, in-plane $CH_3NH_3PbI_3$ grain growth occurred, as shown by the larger grains in SEM (Figure 7.10 (k) compared with as-deposited film in (i)). Note no sharpening of XRD peaks occurred (Figure 7.10(h)) because out-of-plane grain size was already approximately equal to the film thickness. PbI_2 crystals formed along the $CH_3NH_3PbI_3$ grain boundaries (the smaller, lighter grains in the SEM image); this was reported by Chen et al.[226] for $CH_3NH_3PbI_3$ on TiO_2, and the presence of PbI_2 reduced recombination in solar cells. The degradation on ZnO, however, occurred very rapidly and rounded grains of PbI_2 were formed with large gaps between the different grains. The discontinuity of the film probably arose due to the reduced material volume (increased density) as CH_3NH_2 was lost from the crystal structure.

Under glove box annealing, the $CH_3NH_3PbI_3$ on AZO films also showed a higher stability than ZnO, and the higher the doping, the higher the stability (Figure 7.11(a)). This increased stability with AZO compared to ZnO has also been seen in the literature and was attributed to the lower isoelectric point of AZO compared to ZnO (i.e. AZO is less basic).[85,219,227] Because of the delta-doping method of depositing AZO, the final ALD cycle was one of TMA-H_2O. This surface layer is likely to affect the multilayer stability and so the effect of TMA-H_2O overlayers on ZnO was studied (Figure 7.11(b)). Even one cycle of TMA-H_2O increased stability, but not to the same extent as a layer of AZO, demonstrating that the doping within the ZnO also contributed to stability. The thicker Al_2O_3 layers increased stability greatly, and the 30 cycle layers were stable for a considerably longer time than AZO or on ITO. However, 30 cycle layers are thick too thick (≈ 3.3 nm) to be able to allow enough current flow for use in a device. This is in agreement another report, that a 0.4 nm Al_2O_3 layer on ALD ZnO enhanced stability and additionally performed well in a device.[193]

An initial batch of perovskite solar cells was fabricated with AZO ELTs. The results were not reproducible but a working solar cell was produced with an 8 atomic % Al AZO ETL. The open circuit voltage, V_{OC}, was adequate but the FF was quite low and there was a large hysteresis. This was probably because the perovskite was not annealed for a usual length of time (order of minutes); instead it was annealed for 20 s at 110 °C, as had been used earlier, leading to more ion migration.[208] This result is encouraging and further optimisation will may potentially produce promising devices.

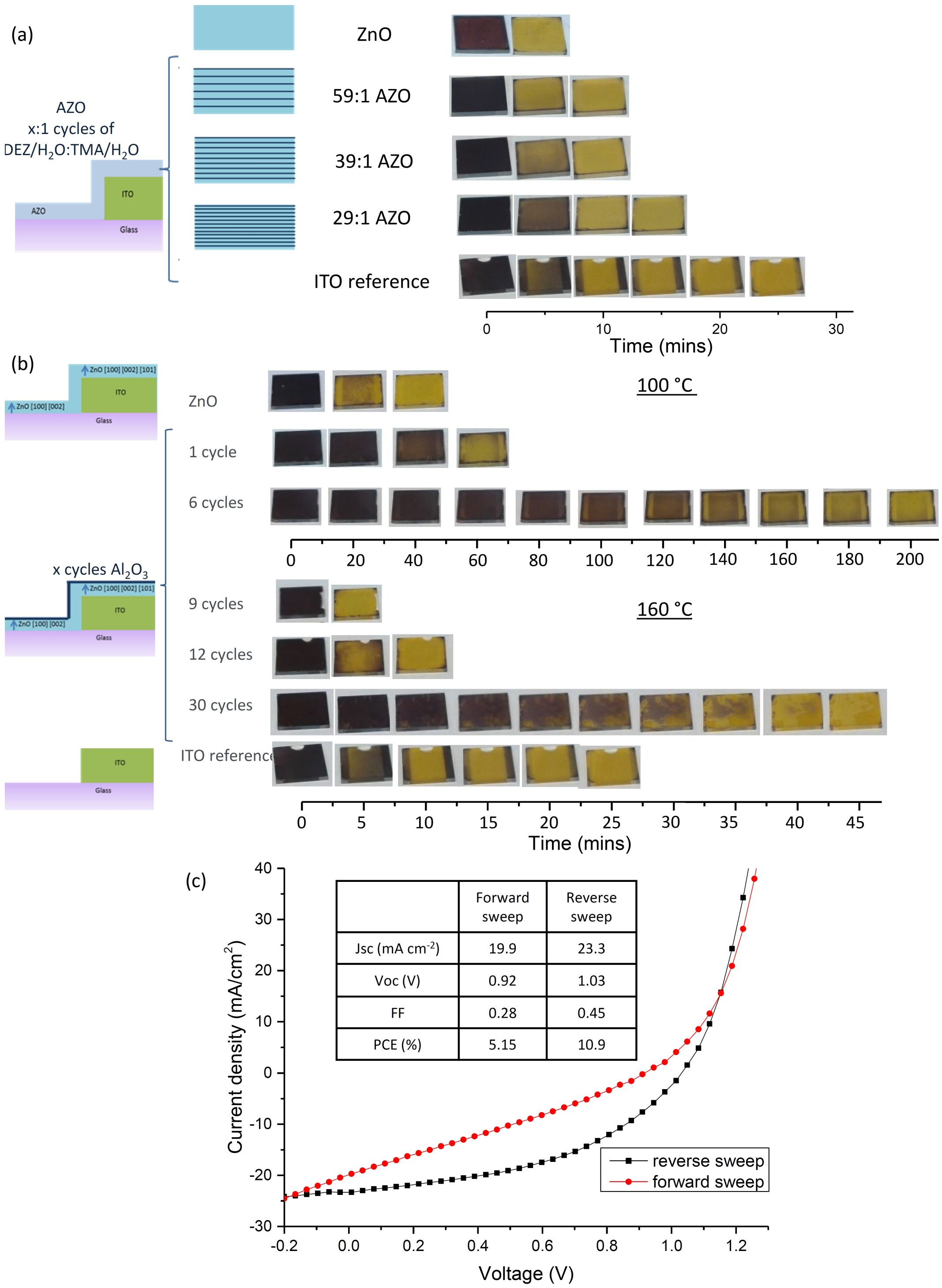

	Forward sweep	Reverse sweep
Jsc (mA cm^{-2})	19.9	23.3
Voc (V)	0.92	1.03
FF	0.28	0.45
PCE (%)	5.15	10.9

Figure 7.11: (a) Photographs of AZO/$CH_3NH_3PbI_3$ multilayers with varying ratios of ZnO-H_2O:Al_2O_3 cycles. Samples were heated to 160 °C in a glove box. (b) Photographs of ZnO/Al_2O_3/$CH_3NH_3PbI_3$ multilayers with Al_2O_3 deposited with varying numbers of TMA-H_2O ALD cycles. Samples were heated to 100 and 160 °C in a glove box. (c) Current-voltage sweep graph and table of short circuit current density (J_{SC}), open circuit voltage (V_{OC}), fill factor (FF), and power conversion efficiency (PCE) results for a perovskite solar cell with an AZO ETL.

7.5 Conclusions

The dependence of $CH_3NH_3PbI_3$ degradation on ZnO and AZO underlayers was studied using temperature controlled XRD and through colour change. The following results were found:

- $CH_3NH_3PbI_3$ decomposed into PbI_2 at a much quicker rate when deposited on ZnO to on glass/ITO, and the rate increased at higher temperatures.
- Both the $CH_3NH_3PbI_3$ and ZnO layers degraded on heating and a dependence on atmosphere was seen, with higher stability observed when annealing under vacuum compared to inert gas.
- Degradation rate was affected by the crystal orientation of ZnO, occurring more rapidly on [002] out-of-plane orientations. Computer modelling may help to explain this effect.
- AZO/$CH_3NH_3PbI_3$ layers showed improved stability with increased Al atomic %. Overcoating ZnO with Al_2O_3 also increased stability
- A preliminary AZO/$CH_3NH_3PbI_3$ solar cell showed a hysteretic performance but through optimisation of the solar cells, good performances look promising.

Chapter 8

Deposition onto Complex Structures

There are many applications for which ALD is useful but one of the key abilities of ALD, which no other deposition technique is able to match, is the ability to conformally coat complex 3D surfaces. ALD has been invaluable in coating nanostructured substrates such as the porous films for dye sensitised solar cells[70] and high aspect ratio trenches for improved integrated circuits.[228] Having successfully deposited ZnO and Al_2O_3 on a variety of planar structures in the preceding chapters, a complementary study into coating complex 3D surfaces is reported here.

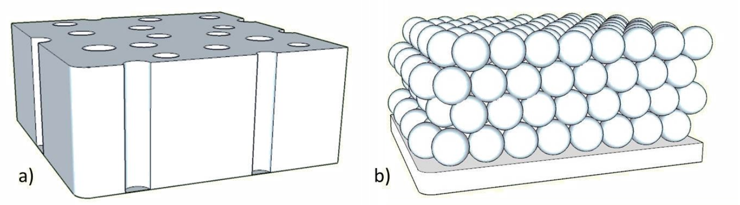

Figure 8.1: Schematic of a) a track-etched membrane and b) a nanoparticle film on top of a planar substrate, not to scale. The typical membranes used in this study are 10 μm thick with 200 nm diameter pores, and the nanoparticle films are around 250 nm thick, consisting of nanoparticles of approximately 10 nm diameter.

For some 3D surfaces identical ALD conditions can be used as in coating planar substrates, but for other higher aspect ratio substrates adjustments in timings need to be made to allow for the diffusion of precursors through the entire structure. In this chapter increasingly challenging substrates are coated: firstly track-etched membranes and then nanoparticle films. Schematics and dimensions of these structures are shown in Figure 8.1. The growth of ALD material on these substrates was studied, and nanoparticle films were employed as photocathode layers.

8.1 ALD on Track-Etched Membranes

Track-etched polycarbonate (PC) membranes are commercially available, high aspect ratio substrates, ideal for both ALD conformality investigations and applications.[229–231] The pores in the membranes are manufactured by bombarding the PC

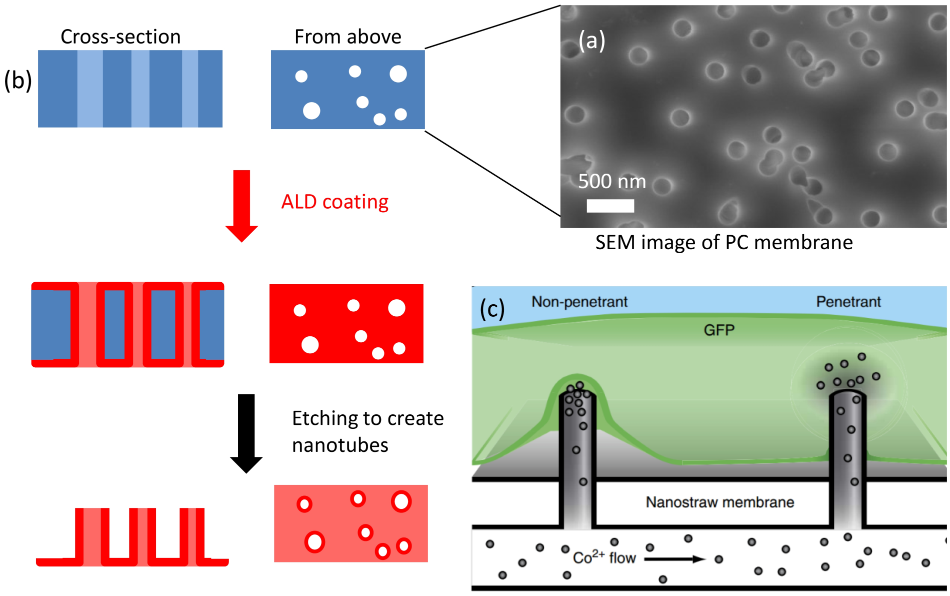

Figure 8.2: (a) SEM image of a track-etched PC membrane (coated with 2 nm Cr to prevent charging during imaging). (b) The process of coating the porous membrane with ALD Al_2O_3, then etching the top Al_2O_3 and the PC to leave a free-standing array of nanotubes. (c) Image showing how the nanotubes can be used to penetrate living cells, allowing direct delivery of chemicals. Reproduced with permission from reference[17] ©2014 Nature Publishing Group

with ions and then chemically etching the pores to a specific size. Here the track-etched PC membranes (Whatman® Nuclepore Track-Etched Membranes) are used as a template for the growth of nanotubes. This technique for creating nanotubes has been used in the literature for filtration[232] and ion conductance measurements,[233] and for delivery of chemicals directly into living cells as shown in Figure 8.2.[17,234]

Al_2O_3 was chosen as the first material to be studied due to the amorphous, smooth nature of the deposited layer, which makes thickness measurements easier than for the crystalline ZnO. Better quality Al_2O_3 layers (e.g. less H contamination) are deposited at higher temperatures however there is a temperature limit for the use of the membranes as PC undergoes glass transition and melting at high temperatures. The manufacturer's specification for the maximum temperature is 121 °C, so the deposition temperature selected for the study was 115 °C to allow a small amount of leeway. The first step of the investigation was to use the same deposition conditions used for Al_2O_3 ALD on planar substrates from Section 5.1 to see if this was sufficient to produce a uniform thickness layer throughout the membrane pores (TMA and H_2O precursors, 50 ms release, 20 s purge). Figure 8.3 shows uniform thickness coating was achieved through the entire porous membrane with these deposition parameters, so no lengthened exposure or purging time was necessary. Note that the diameter of the pores at the surface is smaller than the diameter within the membrane, which is a common result of non-uniform etching in the manufacturing process.[235,236]

To be able to grow specific sizes of nanotubes it is necessary to determine the GPC of Al_2O_3 on the membrane and whether there is a nucleation delay, as it cannot be assumed that ALD growth would occur at the same rate as on e.g. quartz. ALD

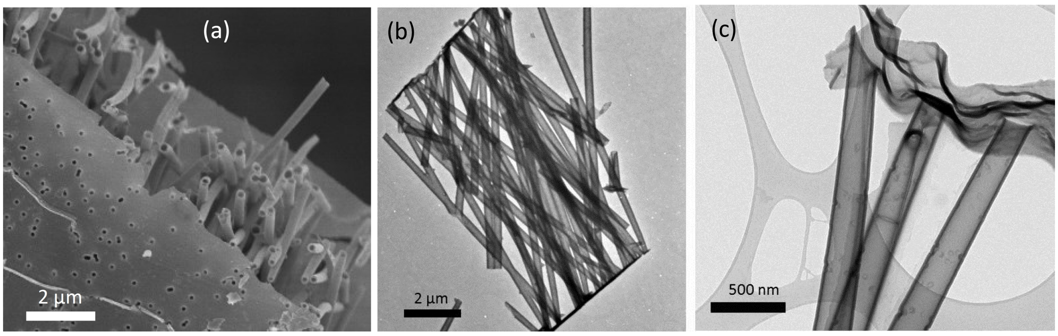

Figure 8.3: Images of Al_2O_3 nanotubes removed from the track-etched PC membrane by heating to 450°C. (a) Top-view SEM image of a fractured edge of the substrate showing the pores on the top surface and the Al_2O_3 nanotubes formed between the top and bottom surface. (b) TEM image showing the cross-sectional view of the nanotubes demonstrating that there is a continuous Al_2O_3 layer through the 10 μm membrane thickness. (c) TEM image showing the uniformity of the Al_2O_3 thickness.

growth on polymers using TMA-H_2O has been reported to depend on the reactivity of the polymer chemical groups with TMA, and often occurs through diffusion of TMA precursors into the polymer.[237] Depending on the hydrophobicity and the free volume in the polymer, the TMA could adsorb either onto the surface and into the near surface region, or into the bulk of the polymer. A certain amount of TMA is retained in the polymer after purging and then sub-surface Al_2O_3 clusters are formed when water is released. Eventually the subsurface clusters coalesce and a continuous layer of Al_2O_3 is formed at the surface and then growth proceeds on that Al_2O_3 surface, with no further diffusion of precursors into the polymer.[111] For deposition on PC specifically, there are a mix of reports on ALD growth behaviour. A slightly lower thickness of TiO_2 grew on PC compared to on Al_2O_3 for the same number of cycles,[238] and nearly the same thickness of TiO_2 and SiO_2 (and Al_2O_3 once parameters were optimised) was grown on track-etched PC as on Si/native SiO_x.[233] It is possible that their track-etching of the PC in NaOH produced a more carboxylated PC surface.[230] This has been reported as beneficial for ALD growth e.g. H_2O plasma raised the amount of surface hydroxyl groups on PC, improving ALD TiO_2 adhesion.[239]

The PC membranes used in this study had been pre-treated with polyvinylpyrrolidone (PVP) by the manufacturer to make them hydrophilic for general applications, so the effect of the PVP surface layer also has to be considered. PVP has been used as a printed, growth-inhibiting layer to pattern spatial ALD Al_2O_3, ZnO and AZO layers for TFTs.[95,117,240] Inhibition of over 200 nm was achieved but the inhibition thickness of the PVP layer was generally low at low temperatures and also reduced with increasing precursor exposure. The exposure times in conventional ALD are relatively long compared to spatial ALD so it is expected there will be much less inhibition of the Al_2O_3 growth here. Triani et al.[229] reported a growth rate similar to on Si when coating TiO_2 on “hydrophilic polycarbonate” (not specified but likely the hydrophilicity was due to PVP treatment), suggesting little PVP inhibition.

Measuring the internal channel sizes of the nanotubes by SEM was chosen as the method for GPC analysis: the difference in pore inner diameter between an uncoated and ALD coated membrane is equal to twice the coating thickness. Figure

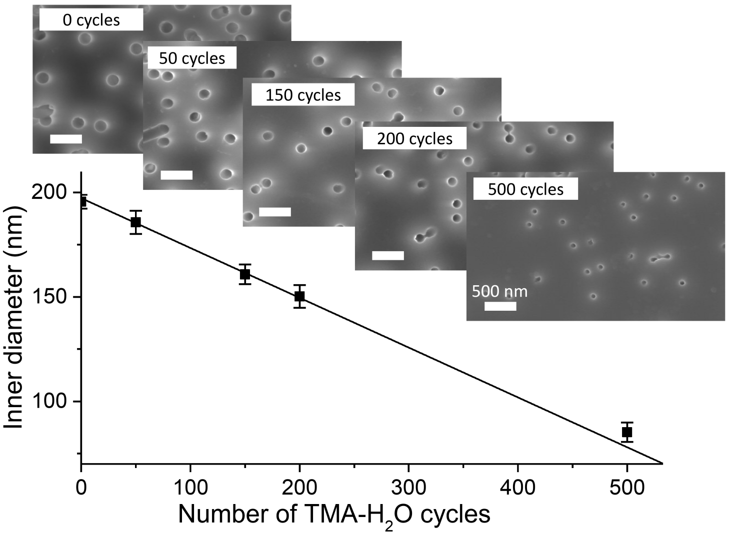

Figure 8.4: SEM images of the membrane pore sizes with different numbers of ALD cycles (not annealed, as deposited). The samples were all coated with 2 nm Cr to prevent charging. Graph shows the inner diameter measurement results, 100 pores were measured per data point. The gradient of the best fit line for the 0 - 200 cycle data points is -0.239 nm/cycle, so GPC = 0.119 nm/cycle.

8.4 shows a selection of SEM images and the results of the pore inner diameter measurements. The growth was found to be linear with a GPC of 0.119 nm/cycle with no nucleation delay, which is a slightly higher than measured on Si/SiO_2 by spectral reflectance (0.105 nm/cycle, Section 5.1). Using the pore diameter as a measure of Al_2O_3 thickness is only reliable so long as the pore is relatively large compared to the coating thickness, because effects such as the less well-defined pore edge, the steric hinderance of precursors and the diffusion through the higher aspect ratio tube will have an increasingly large influence with reducing radius. The deviation from the best fit line at 500 cycles in Figure 8.4 is a reflection of this.

Following the successful deposition of Al_2O_3 on track-etched PC membranes the deposition of ZnO and AZO was attempted. At 115 °C, ZnO was deposited on the PC membrane (Figure 8.5 (a)(b)) but there was an approximately 60 cycle nucleation delay. The nucleation delay increased to around 150 cycles for ZnO deposited at 100 °C, and when 360 cycle AZO layers were deposited at the same temperature there was a thickness increase with doping, the opposite trend to thickness on glass. It is clear that the nucleation of growth on the surface PVP is much more rapid with TMA-H_2O than DEZ-H_2O. The increase in the number of TMA-H_2O cycles with Al doping led to an increased final thickness of AZO because, even though the steady-state GPC is lower with higher doping cycle ratios, the film growth initiated earlier. This matches with the spatial ALD studies of PVP inhibition in which ZnO growth was more inhibited than Al_2O_3 (although a different Al precusor, dimethylaluminum isopropoxide, was used).[95]

Not only is the thickness of AZO layers deposited at 100 °C different on PC membranes to glass, but the crystallinity is also different. This is expected due to the likely higher amount of Al incorporated into the AZO films, especially at the interface where growth initiated. Figure 8.6(b),(c) show the difference in ap-

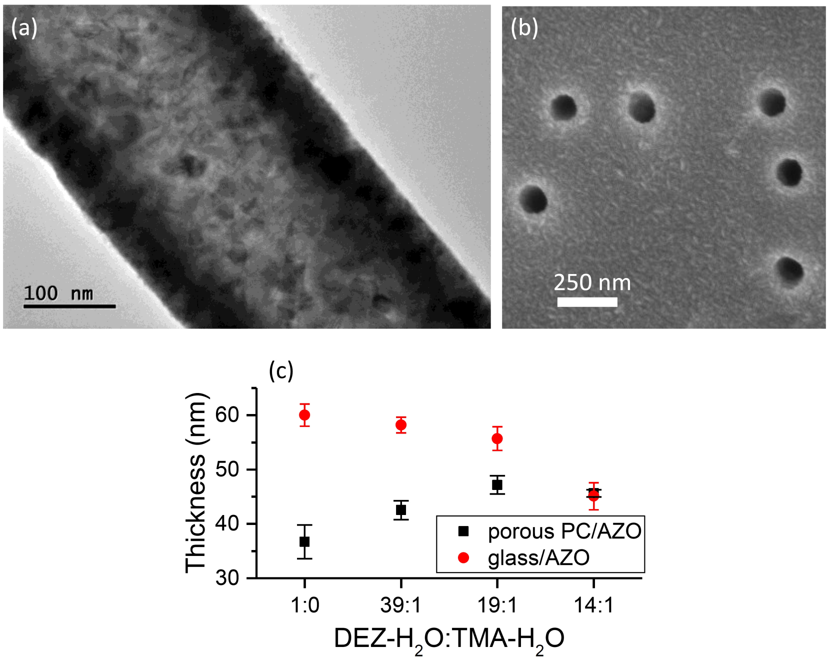

Figure 8.5: (a) TEM image of a 300 ALD cycle ZnO nanotube grown at 115 °C and subsequently removed from the PC membrane (annealed at 450°C). Contrast is seen between the differently oriented ZnO crystals, although it might not be representative of the as-deposited crystallinity. (b) SEM image of the 115 °C, 300 cycle ZnO coated PC membrane (not annealed, as deposited), showing the conformal, crystalline ZnO layer which, at this thickness, is similar in appearance to ZnO on glass. (c) The thickness of 360 cycle ZnO and AZO layers with varying DEZ-H_2O:TMA-H_2O cycle ratios. Films were deposited on glass (measured by cross-sectional SEM) and on porous PC membrane (measured using pore sizes in SEM) at 100 °C.

pearance of AZO (19:1 doping ratio) deposited on glass and PC membrane. Clear needle shaped grains with high length/width ratio can be seen on glass. Needle-like grains can also be seen on PC membrane but with a reduced length/width ratio and generally smaller size. The XRD patterns are very distinct for the two different substrates, which is a culmination of a number of different factors. Firstly, XRD of glass produces an amorphous halo centred at $2\theta \approx 25°$ and glass has a relatively high density causing a large amount of X-ray scattering, resulting in the high and sloping background for the glass/AZO pattern. PC produces an amorphous halo at $2\theta \approx 16°C^{241}$ due to the larger nearest-neighbour separation, so within the 25 - 70° 2θ range measured here the porous PC/AZO background is relatively low and flat. To hold the PC membrane rigid and in-place for the XRD measurement it was stuck onto a glass slide using silver paste, so there are Ag diffraction peaks in the XRD pattern from the paste.

The preferential out-of-plane orientation of AZO on glass is [100], which is clearly demonstrated by XRD. From the XRD pattern of the porous PC/AZO sample it is not possible to identify the exact out-of-plane orientation as the XRD signals are from both the coating on top and within the pores. This variation of growth surface alignment with respect to the X-ray beam has enabled additional peaks to be analysed compared to planar substrates. The orientation of AZO on PC membrane is likely to also be [100] out-of-plane, judging from SEM (Figure 8.6(c)) and from

[100] orientations being consistently favourable at 100 °C. (002) and (101) peaks of similar height to the (100) are seen; they are visibly broader and of a different shape than the (100) peak and so are attributed mainly to AZO within the pores. The peak area ratio of (100):(002):(101) is 1.05:1.40:1, which is different from the powder diffraction reference of 0.57:0.44:1 so the AZO still has a preferential orientation relative to the horizontal even with the signals from AZO in the pores. This suggests that the AZO within the pores is preferentially [002] aligned along the axis of the pores, which does reasonable considering [002] corresponds with the long axis of the needle shaped AZO grains (but this needs to be confirmed by TEM).

The (100) peak on the porous PC membrane has quite concave sides but (002) and (101) have fairly straight sides and are more "Gaussian" in appearance. The FWHM values of the peaks are: (100) = 0.48°, (002) = 0.81°, (101) = 0.67°. The reason for these different shapes and widths is suspected to be due to differences in strain behaviour. The thermal expansion coefficient of PC[242] is 65 x 10^{-6} K^{-1} compared to 4 x 10^{-6} K^{-1} for ZnO,[197] so it is expected that thermal contraction mismatch will contribute to stress in the AZO film on cooling from the 100 °C deposition temperature.[243] The (100) AZO peak on the membrane is shifted compared to that on glass, which could be in part due to the difference in thermal contraction mismatch stress of AZO on the top surfaces of these materials (Al dopant distribution etc. will probably also contribute). The thermal stress on the surface should be a fairly uniform biaxial stress resulting a uniform strain and sharp diffraction peaks. The stress in the pores of the membrane, however, depends on the direction of alignment of the nanotube relative to the PC membrane thickness. From the images in Figure 8.3 it is clear that many nanotubes are not oriented perpendicular to the surface. There is a range of varying alignments so it is expected that the axial stress experienced by each individual nanotube will be different, resulting in an overall strain distribution and therefore broadening of the (002) and (101) XRD peaks. Further detailed investigation by e.g. stress modelling, TEM and temperature controlled XRD would be needed to confirm this hypothesis.

The general height of the diffraction peaks is smaller for porous PC/AZO than glass/AZO, which could in part be due to the reduced crystallinity of the AZO layer on the PC membrane. However, there are a number of contributions possibly affecting the peak height, as listed below.

Factors **decreasing** AZO peak height on PC membrane relative to glass:

- AZO on the PC membrane may be less crystalline due to delayed nucleation and higher Al content.
- The preferential out-of-plane orientation of AZO may be different on PC membrane to on glass.
- AZO coating is thinner on the PC membrane.
- The area of the PC membrane was smaller than that of the glass/AZO sample. If the X-ray beam was larger than the PC membrane area then the measurement areas would have been different.
- The stuck-down PC membrane was not as precisely flat as glass so the height variation might have caused peak broadening.

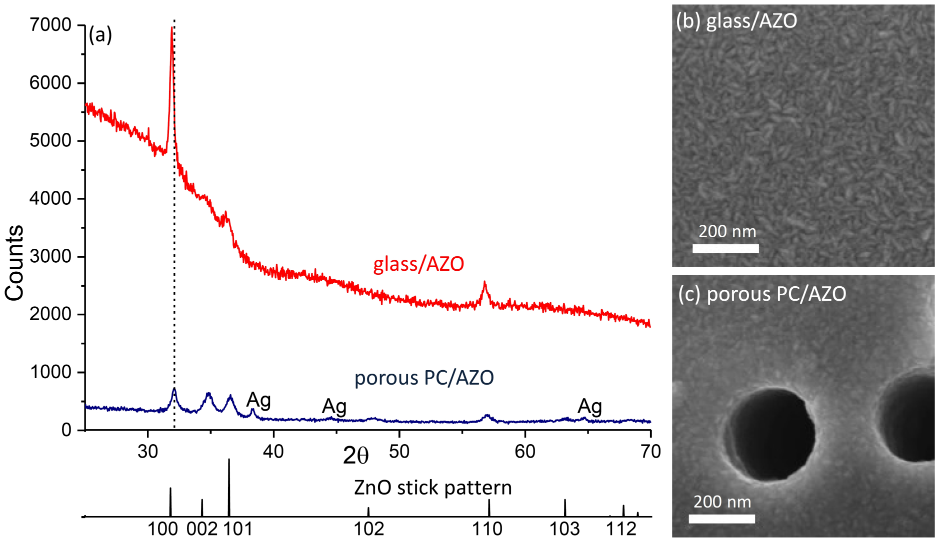

Figure 8.6: (a) XRD pattern of AZO deposited on glass and on porous PC membrane. The doping ratio was 19:1 ZnO-H_2O:TMA-H_2O, at 100 °C. Note that the patterns have not been offset. The stick pattern for powder ZnO is given below, and the dashed line at the (100) peaks demonstrates the shift in peak centre between the samples. (b) and (c) show SEM of 19:1 doped AZO on glass and porous PC membrane, from the same deposition batch. Note a large pore size membrane was used in this case (420 nm).

Factors **increasing** peak height on PC membrane relative to glass:

- For the porous PC membrane, X-ray signals come from the AZO within the pores as well as from the surface.

In addition to the deposition of a single material on the PC membrane, multilayers were also shown to be possible, which could be useful for fabricating devices e.g. high surface area gas sensors in the future. Figure 8.7 shows a porous PC membrane coated with a ZnO/Al_2O_3 bilayer. From the STEM EDX map it can be seen that both layers remain distinct.

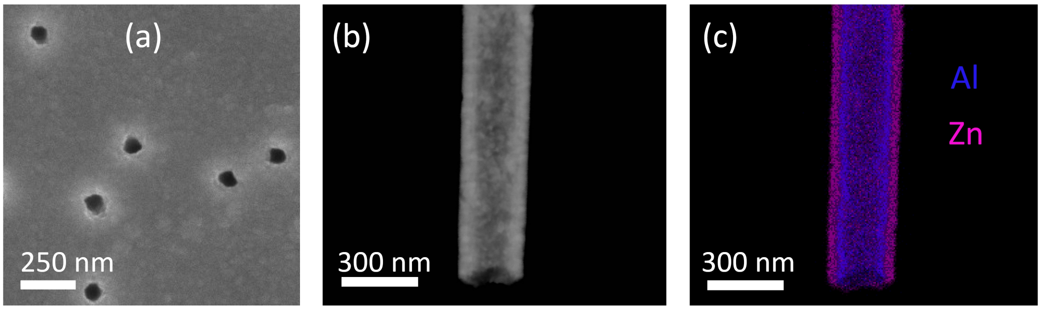

Figure 8.7: a) SEM image of a track-etched PC membrane coated with ZnO and then Al_2O_3. d) Dark field STEM image of the ZnO/Al_2O_3 bilayer nanorod removed from the substrate and e) the corresponding EDX elemental map

8.2 ALD on nanoparticle films

In this section, initial results on ALD coating of films of nanoparticles are presented. The nanoparticles in question are spheres of Cu_2ZnSnS_4 (CZTS), which is a key material of interest in solar energy research. CZTS has a bandgap of $\approx$ 1.5 eV and is commonly used as a p-type, light absorbing layer.[244] The elements of which CZTS is composed are all earth-abundant and non-toxic compared to rival materials such as $CuIn_{(1-x)}Ga_xSe$ and CdTe.[245] There are many ways of forming a CZTS layer[246] including vacuum based techniques such as sputtering[247] and evaporating[248] (and even ALD),[249] or solution based techniques such as electrodeposition and sulphurisation[250–253] or nanoparticle synthesis followed by film formation and annealing.[9, 245] The CZTS used here was made using hot-injection into oleylamine to form $\approx$ 10 nm diameter nanoparticles, compatible with printing and low temperature film formation.

The application for the CZTS films considered here was as the absorbing layer in photocathodes. ALD coatings have been used to improve a variety of photoelectrodes.[254, 255] Passivation of surface states by <2 nm Al_2O_3[57] improved hematite photoanode PEC performance, and charge transfer has also been improved by ALD of ultrathin cobalt-based layers on these and $BiVO_4$ photoanodes.[256, 257] The stability of $BiVO_4$ has also been increased with a ALD TiO_2 overlayer,[258] and ALD AZO/TiO_2 bilayers on Cu_2O photocathodes have been used to protect from photocorrosion by the electrolyte whilst simultaneously forming a p-n junction for the facilitation of charge extraction.[259, 260] The same multilayer protection method was used on CZTS where electrodes of Mo/CZTS/CdS/AZO/TiO_2/Pt showed high photocurrent and significantly improved stability.[250] From this literature, ALD on CZTS nanoparticles for photoelectrochemical (PCE) testing was an interesting area for investigation.

The CZTS was incorporated into a photocathode to assess photoelectrochemical performance (testing described in Section 3.2.3). A fluorine doped tin oxide (FTO) electrode was coated with a CZTS nanoparticle film by repeated dip coating followed by ligand exchange (replacement of the long oleylamine ligands on the synthesised nanoparticles with shorter ethylenediamine ligands).[9] Exchanging ligands results in more closely packed nanoparticles so the film is less likely to crack on annealing and also allows better electrical conduction between nanoparticles.[245, 261] Normally CZTS nanoparticle films are annealed, removing the short ligands, so that a thin, continuous film of CZTS is formed but in this case the initial investigation was into the non-annealed nanoparticle film and how it could be improved using ALD coating.

The ability of ALD to infiltrate such porous structures has led to improvements over a wide range of devices. ALD has been frequently used to deposit ultrathin layers on mesoporous titania films, a common substrate for dye sensitised solar cells and catalysis.[61, 64, 262] These substrates were porous in order to produce a high surface area, but another type of highly porous structures are quantum dot thin films. Low deposition temperatures are especially important in coating these films due to grain sintering and loss of confinement, and both ZnO and Al_2O_3 have been successfully deposited by ALD for this purpose in the literature. Al_2O_3 coating improved the stability of PbS quantum dots[263] and created channels for electron

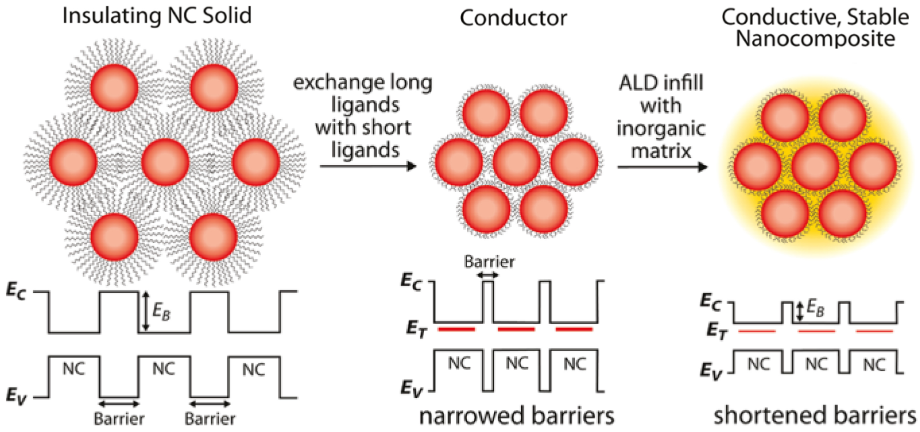

Figure 8.8: Schematic of ligand exchange and ALD coating on nanoparticles and how this can affect charge carrier transport. Reproduced with permission from reference[18] ©2011 American Chemical Society.

transport.[264] ZnO improved the photosensitivity of CdSe quantum dot films[265] and an Al_2O_3/ZnO bilayer improved the performance of PbSe transistors,[18] both effects due to the increase in mobility by lowering the interparticle tunnelling barrier (Figure 8.8). For these CZTS nanoparticle photocathodes Al_2O_3 was chosen as the first material to deposit due to the higher stability compared to ZnO and the ease of analysis as Al is not present in CZTS but Zn is.

The initial investigation was a series of different thickness ALD coatings on FTO/CZTS substrates at 85 °C without any post deposition annealing. The performance of the photocathodes with 1, 5 and 14 cycles of TMA-H_2O was compared with an uncoated sample. Figure 8.9(a) shows the current behaviour under prolonged chopped illumination of increasing wavelengths, and Figure 8.9(b) shows the baseline-subtracted photocurrent measured for each photocathode on first light exposure. It can be seen that the uncoated sample generates the highest initial photocurrent, however the signal is considerably noisy and the dark current rapidly increases during the chopped illumination, indicating swift degradation of the photocathode. Coating of even one cycle of ALD reduced the photocurrent magnitude, possibly due to creation of an insulating tunnelling layer and reduction in surface area, especially as the Al_2O_3 layer deposited was thicker than expected (see below), but other affects may have also contributed such as reaction of TMA with the surface of CZTS affecting the bonding and surface states.[100,136,264,266,267] Photocathode stability increases with the number of ALD coating cycles, but only the 14 cycle sample was sufficiently stable to still show a measurable photocurrent and a constant dark current beyond 600 s.

From SEM characterisation (Figure 8.10) it was concluded that the main degradation mechanism of the films was probably detachment of areas of the CZTS nanoparticle films from the FTO electrode layer. The improvement in stability of the photocathode with the ALD Al_2O_3 was attributed to the formation of a continuous overlayer of Al_2O_3 on top of the CZTS nanoparticles which kept the CZTS attached to the FTO. ALD Al_2O_3 does not form a continuous layer after one cycle but requires repeated cycles, for example 10 cycles of Al_2O_3 were needed to block the

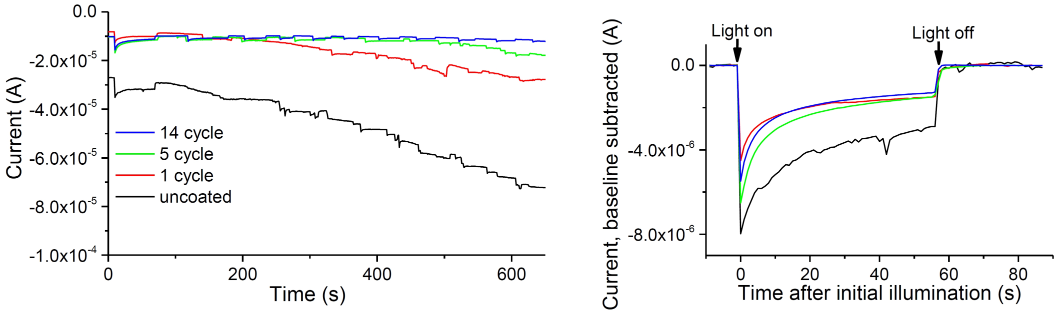

Figure 8.9: (a) The current of the CZTS nanoparticle photocathodes coated with different numbers of TMA-H_2O cycles (85 °C deposition, 0.1 s release, 15 s hold, 90 s purge). (b) Baseline-subtracted photocurrent peak for the first light exposure.

influence of the underlying layer in Chapter 6. The increasing number of ALD cycles increased the attachment until, by 14 cycles, a continuous film was present. Figure 8.10(b) shows an area of the photocathode where a patch of Al_2O_3 has flaked off; the difference between the appearance of the uncovered CZTS nanoparticles and the smoother top surface covered by Al_2O_3 suggests that the Al_2O_3 layer is thicker than expected for 14 cycles and exists mostly on top of the CZTS rather than infiltrating. This could be due to a CVD component to the growth as Al_2O_3 deposition has not been calibrated at this temperature, and the settings were guided by reports from the literature.[61,64,264,268,269] Also the CZTS layer may have adsorbed e.g. H_2O from the brief 5 minute air exposure which was then not properly purged away due to the low temperature used.

From these preliminary results it could be seen that the Al_2O_3 coatings present some promising aspects for investigation. Nonetheless, the 14 ALD cycles film, the only film stable enough for measurement, showed an incident photon to current efficiency (IPCE) of less than 0.6 %. This is low relative to literature values (often over 2 %).[9,270] In the interest of increasing the IPCE of the photocathodes a number of changes to the fabrication method were made.

It was decided that a higher ALD deposition temperature would be used, one for which growth had already been calibrated for this system. Low temperatures are usually used for the ALD coating of nanoparticles to minimise grain growth and sintering, especially when quantum confinement is required.[264] However, in the case of these CZTS nanoparticles there are less stringent requirements: a CZTS structure with smaller nanoparticle size has a greater surface area for interaction with electrolyte but no quantum confinement is required. At lower temperatures during the purge steps it is more difficult to completely remove adsorbed molecules e.g. H_2O from air exposure and remnant H_2O and DEZ after precursors release, resulting in CVD reactions. While the purge and hold times used here were acceptable for other research groups at similar temperatures, purging ability is limited in part by the capacity of the vacuum pump and the N_2 flow rate (our maximum is 60 sccm). Purge times could be lengthened to increase the precursor removal ability but a higher deposition temperature was likely to be more successful, so a 110 °C growth temperature was selected. Additionally, Al_2O_3 layers tend to be of higher quality when deposited at higher temperatures.

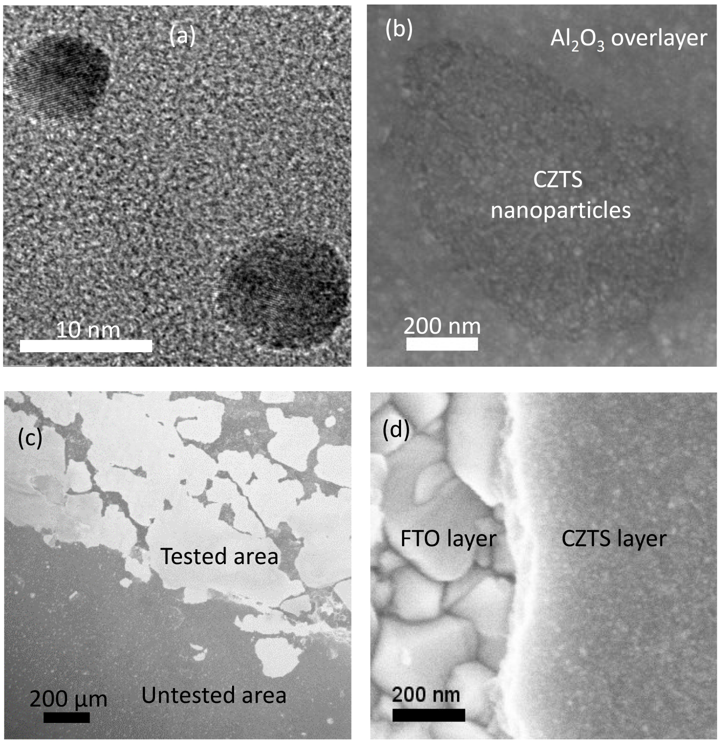

Figure 8.10: (a) TEM image of two individual CZTS nanoparticles, measuring around 8 and 11 nm in diameter. (b) Top view SEM of the CZTS nanoparticle film of the 14 ALD cycle photocathode. In the central area the Al_2O_3 overlayer has flaked off. (c) Large area SEM view of the boundary between the tested and untested (i.e. not submerged in electrolyte) areas of the uncoated CZTS photocathode. The bright areas correspond to locations where CZTS film has detached, exposing the FTO underneath, as seen at higher magnification in (d).

Generally CZTS nanoparticles are used as a route to thin film CZTS formation, so an annealing step is carried out after coating the nanoparticles on a substrate. This removes the organic ligands attached to the nanoparticles and induces grain growth which improves carrier mobility. It also attaches the nanoparticles together more firmly, which, due to detachment being a key degradation route here, could be very beneficial. There is a report of non-annealed CZTS nanoparticle films being used in a photocathode, degradation by film detachment was not an apparent issue however annealing still improved their IPCE,[9] so a study of annealed and non-annealed photocathodes was included in the subsequent experiments.

With the higher ALD temperture of 110 °C and a coating of 14 ALD cycles, the extent to which the ALD coating had penetrated into the CZTS layer was examined by EDX in STEM and depth profiling by ToF-SIMS. Both techniques revealed that least some Al had been deposited through the entire layer thickness (Figure 8.11) but the information from each technique was different due to the contrasting methods, including the different measurement areas and sensitivities to the elements, as discussed below.

Both Al and O can be detected to some extent by EDX. The sensitivity of EDX to O is very low and it cannot be used reliably to quantify atomic percentage. Also,

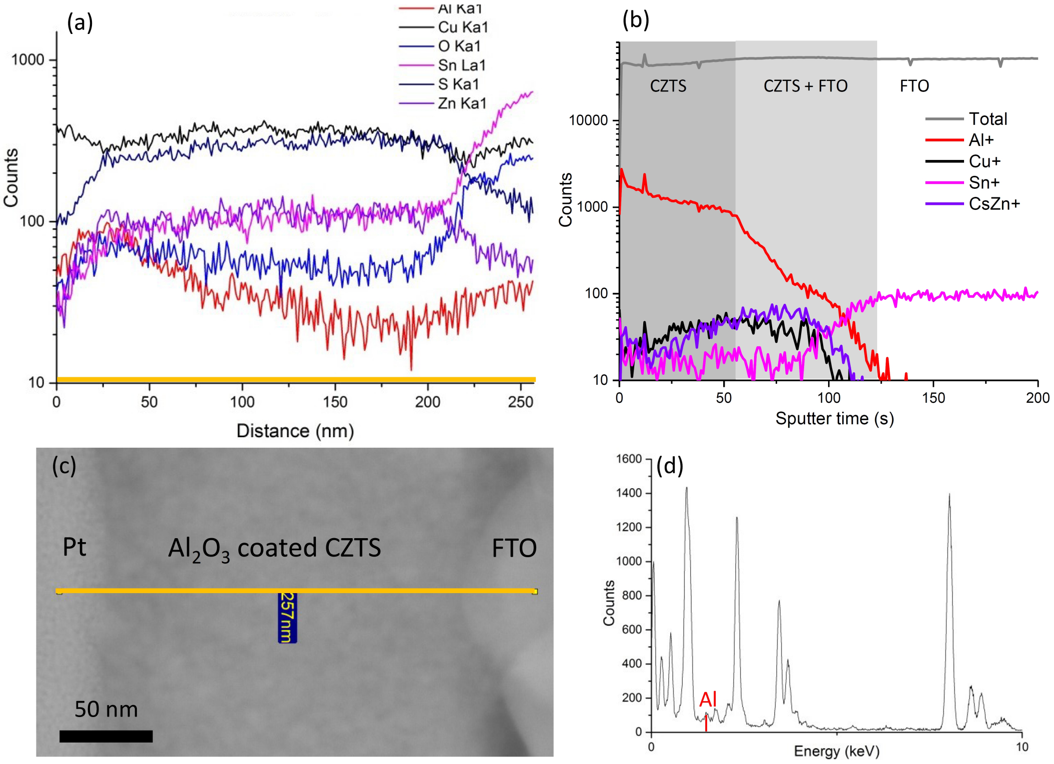

Figure 8.11: (a) The EDX line scan of the area of the dark field STEM image indicated in (c), with counts plotted for Al, Cu, O, Sn, S and Zn. A contribution to the Cu signal also comes from the copper lamella support. (d) shows the EDX spectrum of CZTS adjacent to the interface with FTO, indicating the presence of Al. (b) A depth profile using ToF-SIMS, with counts for Al^+, Cu^+, Sn^+ and $CsZn^+$. Zn^+ had much too low a yield for analysis.

detecting O within the CZTS layer is not an effective way to analyse the Al_2O_3 coating depth because O could also be present from other sources e.g. oxidation of the CZTS and O in the FTO layer. However, the presence of Al can only be from ALD. Al also has a low atomic mass so gives only a weak signal in EDX. This and the small number of ALD cycles (14 cycles, very approximately a 1.5 nm coating) resulted in the relatively low amount of Al counts in EDX compared to elements such as S, Zn Sn and Cu (note the Cu signal also has a contribution from the support). Even though the Al signal is noisy in the EDX line scan, especially at the bottom of the film, a point EDX spectrum in the CZTS adjacent to the FTO had a clear Al peak (Figure 8.11(d)) confirming that the ALD coating reached the bottom of the nanoparticle layer.

In ToF-SIMS only ions of positive or negative charge can be detected at once. As in EDX, Al was chosen as the indicator of the ALD coating presence, so positive ions were monitored. Al^+ has a higher sputter yield with the 25 keV Bi^+ analytical beam than Cu^+, Sn^+ and $CsZn^+$ resulting in much higher Al^+ counts. The variation in the Al content was therefore able to be seen much more precisely than with EDX. In STEM, however, the EDX line scan can be matched with the image so boundaries between materials can be easily identified, whereas in SIMS this is not directly possible and boundaries are identified by the transition points of counts from specific ions. The ToF-SIMS showed the Al content within the CZTS layer gradually decreased until about 60 s sputtering time, then began to drop more rapidly until no Al was seen within the FTO layer. Because the FTO layer is rough and the sampling area is relatively large (100 × 100 μm), and also because the Sn^+ signal is relatively weak, it is difficult to know whether the beginning of the swift Al content decline corresponds with first encounter of an FTO crystal. It does appear that the decline could be before the sputtering reached the FTO. Overall, by both EDX and SIMS, Al was confirmed to be present at all the way through the CZTS film indicating successful infilling. However, repeat samples with different hold times are needed to determine whether the infilling was completely uniform as both measurements showed a gradient in the amount of Al, although that could just be due to the nature of the techniques.

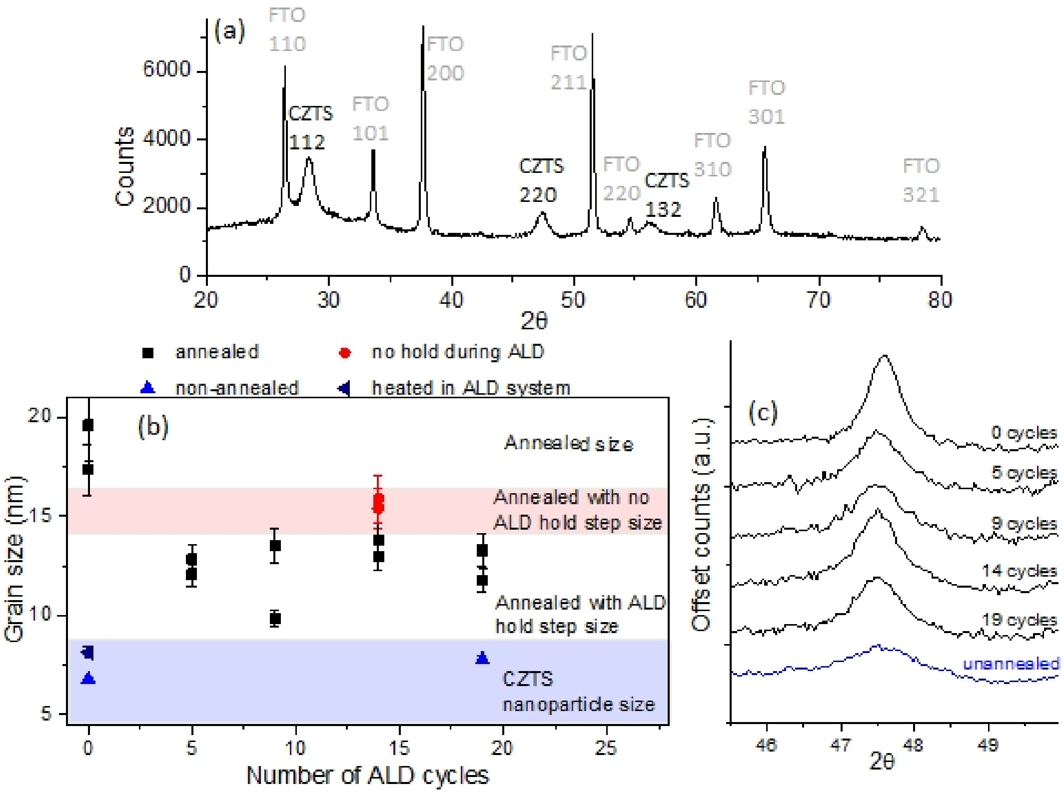

Figure 8.12: (a) XRD pattern of glass/FTO/CZTS photocathode. (b) The grain sizes for a range of CZTS nanoparticle films calculated using the Scherrer equation from the 220 and 112 CZTS diffraction peaks. The samples studied had four different ranges of grain sizes, indicated on the graph. (c) The offset (220) diffraction peaks for the annealed samples with different numbers of TMA-H_2O cycles, compared to an unannealed sample.

The effect of annealing on FTO/CZTS photocathodes was studied by XRD and changes in grain size were revealed (Figure 8.12). The smallest grain size range was below 9 nm, which corresponds to approximately the sizes of CZTS nanoparticle seen by TEM in Figure 8.10(a) (note instrument broadening was not corrected for in the Scherrer calculation, resulting in underestimated sizes). The samples with grain sizes in this range were as-deposited (non-annealed) CZTS, non-annealed CZTS with a 19 cycle Al_2O_3 coating and CZTS heated under deposition conditions for the same length of time as the 19 cycle coating process (heated in ALD system). It is clear that the ALD deposition at 110 °C itself does not significantly change the grain size of the CZTS, suggesting the that the film remains in nanoparticle state after ALD coating.

The ALD coated and then annealed CZTS films all had a larger grain size, in the range of 9 - 14 nm, showing that grain growth has occurred, probably through the coalescence of nanoparticles. This grain size is smaller than that of annealed, uncoated CZTS film (17 - 20 nm) and that of annealed, 14 cycle coated CZTS (15 - 16 nm) where no hold step was used during deposition i.e. there was no lengthened exposure of to the precursor to allow diffusion through the pores. The uncoated CZTS nanoparticles can easily coalesce so have the largest grain size, and the smaller sizes for coated samples indicates the Al_2O_3 reduces the coalescence of CZTS nanoparticles as has been seen for other nanoparticle films.[263, 271] When no hold step is used it is likely that the ALD coating is only present near the film surface, reducing the CZTS coalescence there but not further within the film, resulting in a grain size close to that of uncoated annealed CZTS. For the ALD coatings where a hold step was used Al_2O_3, as shown by EDX and ToF-SIMS, has coated the CZTS nanoparticles throughout the film thickness. The Al_2O_3 does not entirely block the coalescence of the CZTS which could indicate the Al_2O_3 layer is not thick enough deep in the film, or that the general Al_2O_3 thickness is not high enough to completely block growth, but considering that there is no obvious trend in size with number of ALD cycles it is possible that Al_2O_3 coating of the CZTS films would never be able to fully inhibit growth. Explanations for this could be that the pore size is limiting the coating thickness on the nanoparticles so that the coating has reached its maximum thickness for ≥ 5 cycle depositions, or that ALD is prevented at the locations where neighbouring CZTS particles touch so CZTS will always be somewhat interconnected, or Al_2O_3 as a material might not completely block CZTS coalescence as some diffusion etc. may occur. A particle coating ALD reactor could be used to overcome the first two aspects if complete grain growth inhibition was desired.

Figure 8.13(a) shows the IPCE of three different photocathodes. It was seen that the annealed, uncoated sample had the highest IPCE and did not suffer from the severe degradation through detachment of CZTS that the non-annealed version experienced. Of the two ALD coated samples, the annealed one also had the higher IPCE. The differing magnitude and shapes of the IPCE curves indicate different processes are dominating. The very low IPCE of the unannealed sample suggests the high resistivity of the nanoparticle layer combined with resistance of the Al_2O_3 coating is the limiting factor. The IPCE of the uncoated sample follows the trend of the CZTS absorbance with wavelength (Figure 8.13(b)), which suggests the sample has a fairly constant absorbed photon conversion efficiency with wavelength (the absorption spectrum was not taken before the measurement though, so this cannot be accurately calculated). This means photons absorbed throughout the film are contributing holes to the photocurrent. Conversely, the 19 cycles, annealed sample shows a constant IPCE ≈ 1 % for wavelengths beyond 440 nm, and the IPCE was nearly equal with the uncoated sample at 800 nm. The photocurrent tests were carried out with front illumination so the intensity of the light within the CZTS layer decreased closer to the FTO electrode as shown in Figure 8.13(c). Shorter wavelengths of light are absorbed more at the front surface of the CZTS whereas longer wavelengths are absorbed fairly uniformly throughout the CZTS layer and 19 cycle, annealed CZTS sample is expected to be more resistive than it its uncoated counterpart due to the smaller amount of nanoparticle coalescence. It is hypothesised that

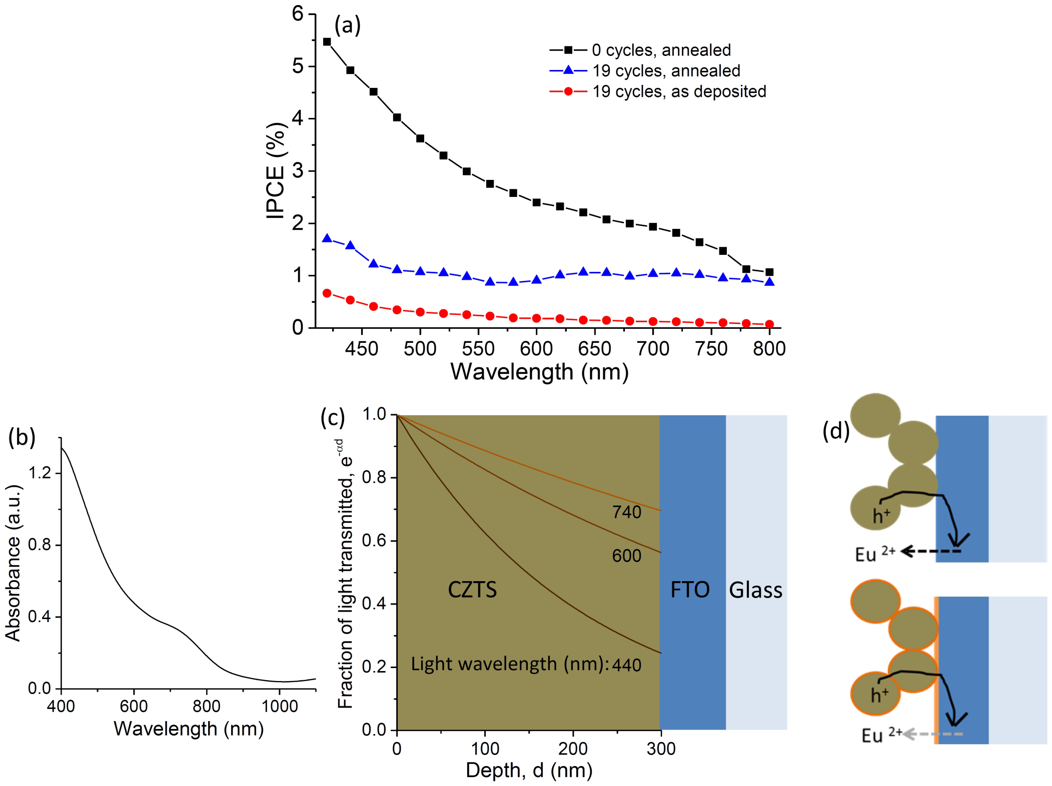

Figure 8.13: (a) Incident photon conversion efficiency (IPCE) of front illuminated glass/FTO/CZTS photocathodes at -0.35 V bias with/without 19 TMA-H_2O ALD cycles (110 °C, 0.1 s release, 5 s hold, 60 s purge) and post-deposition annealing (of 20 minutes at 350 °C.). (b) Absorbance of a typical glass/FTO/CZTS sample. (c) Approximation of the fraction of light within the CZTS layer relative to incident light of different wavelengths. (d) Schematic of CZTS nanoparticles on FTO with/without Al_2O_3 to block recombination of photogenerated holes through the electrolyte in contact with FTO.

the resistivity of the 19 cycle, annealed sample means carriers photogenerated near the surface will not significantly contribute to the photocurrent and will recombine, whereas those absorbed near the FTO will, resulting an equal IPCE for all wavelengths.[251] The Al_2O_3 coating may also be reducing recombination of holes with the electrolyte if there is electrolyte contact with the FTO (Figure 8.13(d)), which has been an issue with other CZTS photocathodes.[9] To investigate these hypotheses further a wider range of coated/annealed photoelectrodes needs to be fabricated, and additional resistivity, absorbance and front and back illuminated IPCE measurements performed.

8.3 Conclusions

Deposition onto complex structures was achieved using the ALD system, and some preliminary material and device investigations were carried out. Future investigations are needed to fully understand the results; the key findings so far are:

- Saturated, uniform deposition on 10 μm thick track-etched membranes with 200 nm pores was possible using standard ALD deposition conditions.

- Al_2O_3 had a linear 0.119 nm/cycle growth rate on the PVP-treated PC at 115 °C, whereas ZnO showed substrate inhibited growth, and AZO deposited at 100 °C had a higher growth rate with increasing doping for ratios up to 19:1 because of the better nucleation of TMA compared to DEZ.

- Non-annealed CZTS nanoparticle photocathodes degraded rapidly via layer detachment, which could be prevented by a continuous overlayer of Al_2O_3 at the expense of photocurrent magnitude.

- A hold step to lengthen precursor exposure was necessary to coat through the 250 nm thickness of CZTS nanoparticle film. With a 15 s hold Al was detected at the bottom of the film but more studies are necessary to assess uniformity.

- Al_2O_3 coating reduced the grain growth of CZTS under annealing.

- Annealed, uncoated CZTS had the highest IPCE. The annealed, Al_2O_3 coated (19 ALD cycle) CZTS had the next highest IPCE, which was approximately constant with wavelength, suggesting prohibitive resistivity.

Chapter 9

Conclusions and future work

- ALD, a deposition technique that cannot be rivalled in repeatability, uniformity and conformality over complex surfaces, shows great potential for deposition of thin films for layers in optoelectronic devices. The low deposition temperatures are possible and the technique is scalable for manufacturing.

- Using only TMA, DEZ H_2O precursors, deposition of materials with a wide range of properties is possible. The Al_2O_3 (amorphous, insulating), ZnO (crystalline, semiconducting) and AZO (crystalline, conducting) layers which can be deposited have many different applications in optoelectronic devices.

- A custom ALD system was designed and constructed for conventional, thermal ALD on substrates for optoelectronics. The ALD system successfully deposited Al_2O_3, ZnO and AZO layers with GPC and material properties in agreement with literature values. The system can therefore be reliably used in the future for more device applications and the deposition of other ALD materials.

- The dependence of material properties on deposition variables was studied. The conductivity of ZnO was seen to increase with temperature and doping, and the out-of-plane orientation was seen to be increasingly [100] at lower temperature and with higher Al doping. At purge times < 10 s there was apparently a CVD contribution to ZnO growth, and the carrier concentration and mobility were reduced, with ZnO channel TFTs showing larger hysteresis.

- Substrate crystallinity was seen to affect the orientation of ALD ZnO. Deposition on quartz, ITO, glass and sapphire substrates was investigated and the resulting optical, electrical and structural properties were linked.

- AZO films showed [100] preferential out-of-plane crystal orientations, and deposition of ZnO on top caused the usually mixed [100][002] ZnO to orient in that same direction. Insertion of a layer of Al_2O_3 of >10 cycles between the AZO and ZnO prevented orientation alignment effect without significantly inhibiting conduction. This method can be used to investigate device performance dependence on ZnO orientation, for example to study whether charge transfer behaviour is affected by orientation, in addition to stability. The same method could potentially be expanded to other crystalline materials.

- The dependence of ZnO/$CH_3NH_3PbI_3$ degradation was studied to improve understanding for perovskite solar cell applications. Both the $CH_3NH_3PbI_3$ and ZnO layers degraded on heating, and stability was higher when annealing under vacuum.

- The ZnO/$CH_3NH_3PbI_3$ degradation rate was highest on [002] oriented ZnO; computer modelling may help to explain this effect. Al doping of ZnO and overcoating with Al_2O_3 both increased stability, and the preliminary AZO/$CH_3NH_3PbI_3$ solar cell result was promising. Different organic-inorganic perovskite materials could be investigated in combination with the ALD layers in the future, as there are more stable alternatives to $CH_3NH_3PbI_3$ which might be more suitable to use with ZnO ETLs.

- Saturated, uniform deposition on 10 μm thick track-etched membranes with 200 nm pores was possible using standard ALD deposition conditions, whereas a hold step was needed to lengthen precursor exposure to coat through the thickness of a CZTS nanoparticle film. The dependence of precursor infiltration into nanoparticle films on hold times should be investigated further.

- Different growth behaviours were seen on PVP-treated PC track-etched membranes for ZnO (substrate inhibited growth) and Al_2O_3 (linear) deposition.

- Non-annealed CZTS nanoparticle photocathodes degraded rapidly via layer detachment, and annealed, uncoated CZTS photocathodes showed the highest IPCE in this study. Al_2O_3 coating of CZTS nanoparticles was shown to control their grain growth during annealing. Future investigations into combinations of ALD coatings and annealing could help understand and optimise CZTS photocathode performance further.

- There are many other optoelectronic applications in which these ALD ZnO and Al_2O_3 layers could be employed. Ultrathin Al_2O_3 layers are useful for stability improvements, as long as thickness is kept low enough for sufficient current to flow. ALD ZnO could find further applications particularly as an electron transport layer in solar cells, and doping ZnO with different elements should be a good tool for tuning the work function, stability etc. to the requirements of the specific device.

Bibliography

[1] Miikkulainen, V., Leskela, M., Ritala, M., Puurunen, R. L., Leskelä, M., Ritala, M., and Puurunen, R. L. *Journal of Applied Physics* **113**(2), 021301 (2013).

[2] Lu, W., Dong, Y., Li, C., Xia, Y., Liu, B., Xie, J., Li, N., and Zhang, Y. *Applied Surface Science* **303**, 111–117 (2014).

[3] Poodt, P., Cameron, D. C., Dickey, E., George, S. M., Kuznetsov, V., Parsons, G. N., Roozeboom, F., Sundaram, G., and Vermeer, A. *Journal of Vacuum Science & Technology A* **30**, 010802 (2012).

[4] Puurunen, R. L. *Journal of Applied Physics* **97**(12), 121301 (2005).

[5] Puurunen, R. L. and Vandervorst, W. *Journal of Applied Physics* **96**, 7686–7695 (2004).

[6] Williams, D. B. and Carter, C. B. *Transmission electron microscopy: A textbook for materials science.* Springer US, (1996).

[7] Fortunato, E., Barquinha, P., and Martins, R. *Advanced materials (Deerfield Beach, Fla.)* **24**(22), 2945–86 jun (2012).

[8] Zhang, J., Faria, J. C. D., Morbidoni, M., Porte, Y., Burgess, C. H., Harrabi, K., and McLachlan, M. A. *Advanced Electronic Materials* **2**(6), 1600008 (2016).

[9] Riha, S. C., Fredrick, S. J., Sambur, J. B., Liu, Y., Prieto, A. L., and Parkinson, B. a. *ACS Applied Materials and Interfaces* **3**(1), 58–66 (2011).

[10] White, J. L., Baruch, M. F., Pander, J. E., Hu, Y., Fortmeyer, I. C., Park, J. E., Zhang, T., Liao, K., Gu, J., Yan, Y., Shaw, T. W., Abelev, E., and Bocarsly, A. B. *Chemical Reviews* **115**(23), 12888–12935 (2015).

[11] Suryawanshi, M. P., Shin, S. W., Ghorpade, U. V., Gurav, K. V., Hong, C. W., and Moholkar, a. V. *Electrochimica Acta* **150**, 136–145 (2014).

[12] Tynell, T. and Karppinen, M. *Semiconductor Science and Technology* **29**(4), 043001 apr (2014).

[13] Taghavi, M., Mattoli, V., Mazzolai, B., Filippeschi, C., and Beccai, L. *Nanoscale* **5**(8), 3505–13 (2013).

[14] Jacobsson, T. J., Schwan, L. J., Ottosson, M., Hagfeldt, A., and Edvinsson, T. *Inorganic Chemistry* **54**(22), 10678–10685 (2015).

[15] Yang, J., Siempelkamp, B. D., Mosconi, E., De Angelis, F., and Kelly, T. L. *Chemistry of Materials* **27**(12), 4229–4236 (2015).

[16] Leguy, A., Hu, Y., Campoy-Quiles, M., Alonso, M. I., Weber, O. J., Azarhoosh, P., van Schilfgaarde, M., Weller, M. T., Bein, T., Nelson, J., Docampo, P., and Barnes, P. R. *Chemistry of Materials* **27**, 3397–3407 (2015).

[17] Xu, A. M., Aalipour, A., Leal-Ortiz, S., Mekhdjian, A. H., Xie, X., Dunn, A. R., Garner, C. C., and Melosh, N. a. *Nature communications* **5**, 3613 (2014).

[18] Liu, Y., Gibbs, M., Perkins, C. L., Tolentino, J., Zarghami, M. H., Bustamante, J., and Law, M. *Nano letters* **11**(12), 5349–5355 dec (2011).

[19] Parsons, G. N., Elam, J. W., George, S. M., Haukka, S., Jeon, H., Kessels, W. M. M., Leskela, M., Poodt, P., Ritala, M., and Rossnagel, S. M. *Journal of Vacuum Science & Technology A* **31**(5), 050818 (2013).

[20] Puurunen, R. L. *Chemical Vapor Deposition* **20**(10-11-12), 332–344 (2014).

[21] Malygin, B. A. A., Drozd, V. E., Malkov, A. A., and Smirnov, V. M. *Chemical Vapor Deposition* **21**, 216–240 (2015).

[22] Poodt, P., Lankhorst, A., Roozeboom, F., Spee, K., Maas, D., and Vermeer, A. *Adv Mater* **22**(32), 3564–3567 (2010).

[23] van Delft, J. A., Garcia-Alonso, D., and Kessels, W. M. M. *Semiconductor Science and Technology* **27**(7), 074002 (2012).

[24] Ritala, M. and Niinistö, J. *ECS Transactions* **25**(8), 641–652 (2009).

[25] Karttunen, A. J., Tynell, T., and Karppinen, M. *The Journal of Physical Chemistry C* **119**, 150518123734004 (2015).

[26] Elam, J. W., Groner, M. D., and George, S. M. *Review of Scientific Instruments* **73**(8), 2981 (2002).

[27] Hoye, R. L. Z., Muñoz-Rojas, D., Nelson, S. F., Illiberi, A., Poodt, P., Roozeboom, F., and MacManus-Driscoll, J. L. *APL Materials* **3**(4), 040701 (2015).

[28] Lim, S. J., Kim, J.-M., Kim, D., Kwon, S., Park, J.-S., and Kim, H. *Journal of The Electrochemical Society* **157**(2), H214–H218 (2010).

[29] Lee, D.-J., Kwon, J.-Y., Kim, S.-H., Kim, H.-M., and Kim, K.-B. *Journal of The Electrochemical Society* **158**(5), D277–D281 (2011).

[30] Wu, Y., Hermkens, P. M., van de Loo, B. W. H., Knoops, H. C. M., Potts, S. E., Verheijen, M. a., Roozeboom, F., and Kessels, W. M. M. *Journal of Applied Physics* **114**(2), 024308 (2013).

[31] Wu, Y., Potts, S. E., Hermkens, P. M., Knoops, H. C. M., Roozeboom, F., and Kessels, W. M. M. *Chemistry of Materials* **25**(22), 4619–4622 (2013).

[32] Park, H. K. and Heo, J. *Applied Surface Science* **309**, 133–137 (2014).

[33] Pollock, E. B. and Lad, R. J. *J. Vac. Sci. Technol., A* **32**(May), 041516 (2014).

[34] Yanguas-Gil, A., Peterson, K. E., and Elam, J. W. *Chemistry of Materials* **23**(19), 4295–4297 (2011).

[35] Na, J. S., Peng, Q., Scarel, G., and Parsons, G. N. *Chemistry of Materials* **21**(23), 5585–5593 (2009).

[36] Dong, L., Sun, Q. Q., Shi, Y., Guo, H. W., Liu, H., Wang, C., Ding, S. J., and Zhang, D. W. *Thin Solid Films* **517**(15), 4355–4359 (2009).

[37] Kim, S. H., Pyeon, J. J., Lee, W. C., Jeong, D. S., Baek, S.-H., Kim, J.-S., and Kim, S. K. *The Journal of Physical Chemistry C* **119**, 2347023477 (2015).

[38] Na, J.-s., Scarel, G., Parsons, G. N., and Carolina, N. *Journal of Physical Chemistry C* **114**, 383–388 (2010).

[39] Riha, S. C., Libera, J. a., Elam, J. W., and Martinson, A. B. F. *The Review of scientific instruments* **83**(9), 094101 sep (2012).

[40] Langereis, E., Heil, S. B. S., Knoops, H. C. M., Keuning, W., van de Sanden, M. C. M., and Kessels, W. M. M. *Journal of Physics D: Applied Physics* **42**(7), 073001 apr (2009).

[41] Larrabee, T. J., Mallouk, T. E., and Allara, D. L. *Review of Scientific Instruments* **84**, 014102 (2013).

[42] Klug, J. A., Weimer, M. S., Emery, J. D., Yanguas-gil, A., Seifert, S., Christian, M., Martinson, A. B. F., Elam, J. W., Hock, A. S., and Proslier, T. *Review of Scientific Instruments* **86**, 113901 (2015).

[43] Dasgupta, N. P., Neubert, S., Lee, W., Trejo, O., Lee, J. R., and Prinz, F. B. *Chemistry of Materials* **22**(16), 4769–4775 (2010).

[44] Granneman, E., Fischer, P., Pierreux, D., Terhorst, H., and Zagwijn, P. *Surface & Coatings Technology* **201**, 8899–8907 (2007).

[45] Munoz-Rojas, D. and MacManus-Driscoll, J. *Materials Horizons* , 314–320 (2014).

[46] Ritala, M. and Niinistö, J. *Chemical Vapour Deposition: Precursors and Processes.* Royal Society of Chemistry, (2009).

[47] Wank, J. R., George, S. M., and Weimer, A. W. *Journal of the American Ceramic Society* **87**(4), 762–765 (2004).

[48] Martin, P. M. *Handbook of deposition technologies for films and coatings science, applications and technology.* Elsevier, 3rd edition, (2010).

[49] Dingemans, G. and Kessels, W. M. M. *Journal of Vacuum Science & Technology A: Vacuum, Surfaces, and Films* **30**(2012), 040802 (2012).

[50] Bae, D., Kwon, S., Oh, J., Kim, W. K., and Park, H. *Renewable Energy* **55**, 62–68 (2013).

[51] Choi, D.-w., Kim, S.-J., Lee, J. H., Chung, K.-B., and Park, J.-S. *Current Applied Physics* **12**, S19–S23 sep (2012).

[52] Groner, M. D., Fabreguette, F. H., Elam, J. W., and George, S. M. *Chemistry of Materials* **16**(4), 639–645 (2004).

[53] Robertson, J. *the European Physical Journal Applied Physics* **291**, 265–291 (2004).

[54] van Hemmen, J. L., Heil, S. B. S., Klootwijk, J. H., Roozeboom, F., Hodson, C. J., van de Sanden, M. C. M., and Kessels, W. M. M. *Journal of The Electrochemical Society* **154**(7), G165–9 (2007).

[55] Elam, J. W., Routkevitch, D., and George, S. M. *Journal of The Electrochemical Society* **150**(6), G339–G347 (2003).

[56] Jeong, K. S., Kwon, H. M., Lee, H. D., and Lee, G. W. *Physica Status Solidi (a)* **211**(8), 1850–1856 (2014).

[57] Le Formal, F., Tétreault, N., Cornuz, M., Moehl, T., Grätzel, M., and Sivula, K. *Chemical Science* **2**(4), 737 (2011).

[58] Zardetto, V., Di Giacomo, F., Mohammed, M. A., Lucarelli, G., Razza, S., D'Epifanio, A., Licoccia, S., Kessels, W. M. M., Di Carlo, A., Brown, T. M., and Creatore, M. *ECS Transactions* **69**(7), 15–22 (2015).

[59] Qi, L., Zhang, C., and Chen, Q. *Thin Solid Films* **567**, 1–7 (2014).

[60] Wei, H., Shi, J., Xu, X., Xiao, J., Luo, J., Dong, J., Lv, S., Zhu, L., Wu, H., Li, D., Luo, Y., Meng, Q., and Chen, Q. *Physical Chemistry Chemical Physics* **17**(7), 4937–4944 (2015).

[61] Roelofs, K. E., Brennan, T. P., Dominguez, J. C., Bailie, C. D., Margulis, G. Y., Hoke, E. T., Mcgehee, M. D., and Bent, S. F. *Journal of Physical Chemistry C* **117**, 5584–5592 (2013).

[62] Brennan, T. P., Bakke, J. R., Ding, I.-K., Hardin, B. E., Nguyen, W. H., Mondal, R., Bailie, C. D., Margulis, G. Y., Hoke, E. T., Sellinger, A., McGehee, M. D., and Bent, S. F. *Physical Chemistry Chemical Physics* **14**, 12130–40 sep (2012).

[63] Lin, C., Tsai, F.-Y., Lee, M.-H., Lee, C.-H., Tien, T.-C., Wang, L.-P., and Tsai, S.-Y. *Journal of Materials Chemistry* **19**(19), 2999 (2009).

[64] Kim, D. H., Losego, M. D., Hanson, K., Alibabaei, L., Lee, K., Meyer, T. J., and Parsons, G. N. *Physical chemistry chemical physics* **16**, 8615–22 (2014).

[65] Dong, X., Fang, X., Lv, M., Lin, B., Zhang, S., Ding, J., and Yuan, N. *J. Mater. Chem. A* **3**(10), 5360–5367 (2015).

[66] Janotti, A. and Van de Walle, C. G. *Reports on Progress in Physics* **72**(12), 126501 dec (2009).

[67] Guziewicz, E., Godlewski, M., Wachnicki, L., Krajewski, T. A., Luka, G., Gieraltowska, S., Jakiela, R., Stonert, A., Lisowski, W., Krawczyk, M., Sobczak, J. W., and Jablonski, A. *Semiconductor Science and Technology* **27**(7), 074011 (2012).

[68] Jeon, S., Bang, S., Lee, S., Kwon, S., Jeong, W., Jeon, H., Chang, H. J., and Park, H.-H. *Journal of The Electrochemical Society* **155**(10), H738–H743 (2008).

[69] Niu, W., Li, X., Karuturi, S. K., Fam, D. W., Fan, H., Shrestha, S., Wong, L. H., and Tok, A. I. Y. *Nanotechnology* **26**(6), 064001 (2015).

[70] Bakke, J. R., Pickrahn, K. L., Brennan, T. P., and Bent, S. F. *Nanoscale* **3**(9), 3482–3508 sep (2011).

[71] Johnson, R. W., Hultqvist, A., and Bent, S. F. *Materials Today* **17**(5), 236–246 (2014).

[72] Hoye, R. L. Z., Musselman, K. P., and Macmanus-Driscoll, J. L. *APL Materials* **1**(6), 060701 (2013).

[73] Levy, D. H. and Nelson, S. F. *Journal of Vacuum Science & Technology A: Vacuum, Surfaces, and Films* **30**(1), 018501 (2012).

[74] Luka, G., Godlewski, M., Guziewicz, E., Stakhira, P., Cherpak, V., and Volynyuk, D. *Semiconductor Science and Technology* **27**(7), 074006 (2012).

[75] Saadat, M., Moradi, M., and Zahedifar, M. *Journal of Materials Science: Materials in Electronics* (2015).

[76] Gershon, T. *Materials Science and Technology* **27**(9), 1357–1371 (2011).

[77] Hewlett, R. M. and Mclachlan, M. A. *Advanced Materials* **28**, 3893–3921 (2016).

[78] Burgess, C. H. *Materials Science and Technology* (June) (2016).

[79] Lim, S. J., Kwon, S.-J. J., Kim, H., and Park, J.-S. S. *Applied Physics Letters* **91**(18), 183517 (2007).

[80] Ehrler, B., Musselman, K. P., Böhm, M. L., Morgenstern, F. S. F., Vaynzof, Y., Walker, B. J., Macmanus-Driscoll, J. L., and Greenham, N. C. *ACS nano* **7**(5), 4210–20 (2013).

[81] Musselman, K. P., Albert-Seifried, S., Hoye, R. L. Z., Sadhanala, A., Munoz-Rojas, D., Macmanus-Driscoll, J. L., and Friend, R. H. *Advanced Functional Materials* **24**(23), 3562–3570 (2014).

[82] Luka, G., Krajewski, T. a., Witkowski, B. S., Wisz, G., Virt, I. S., Guziewicz, E., and Godlewski, M. *Journal of Materials Science: Materials in Electronics* **22**(12), 1810–1815 apr (2011).

[83] Kim, J. Y., Choi, Y.-j., Park, H.-h., Golledge, S., and Johnson, D. C. *Journal of Vacuum Science & Technology A* **28**, 3–7 (2010).

[84] Qian, X., Cao, Y., Guo, B., Zhai, H., and Li, A. *Chemical Vapor Deposition* **19**(4-6), 180–185 (2013).

[85] Elam, J. W. and George, S. M. *Chem. Mater.* **15**, 1020–1028 (2003).

[86] Banerjee, P., Lee, W.-J., Bae, K.-R., Lee, S. B., and Rubloff, G. W. *Journal of Applied Physics* **108**(4), 043504 (2010).

[87] Maeng, W. J., Lee, J. H. J.-w., Lee, J. H. J.-w., Chung, K.-B., and Park, J.-S. *Journal of Physics D: Applied Physics* **44**(44), 445305 nov (2011).

[88] Illiberi, a., Scherpenborg, R., Wu, Y., Roozeboom, F., and Poodt, P. *ACS applied materials & interfaces* **5**(24), 13124–8 dec (2013).

[89] Choi, Y.-J., Gong, S. C., Park, C.-S., Lee, H.-S., Jang, J. G., Chang, H. J., Yeom, G. Y., and Park, H.-H. *ACS applied materials & interfaces* **5**(9), 3650–5 may (2013).

[90] Cheun, H., Fuentes-Hernandez, C., Shim, J., Fang, Y., Cai, Y., Li, H., Sigdel, A. K., Meyer, J., Maibach, J., Dindar, A., Zhou, Y., Berry, J. J., Bredas, J.-L., Kahn, A., Sandhage, K. H., and Kippelen, B. *Advanced Functional Materials* **22**(7), 1531–1538 (2012).

[91] Dong, J., Zhao, Y., Shi, J., Wei, H., Xiao, J., Xu, X., Luo, J., Xu, J., Li, D., Luo, Y., and Meng, Q. *Chemical communications (Cambridge, England)* **50**(87), 13381–4 (2014).

[92] Nalwa, H. S. *Handbook of Thin Film Materials, Volume 1: Deposition and Processing of Thin Films.* Academic Press, San Diego, (2002).

[93] Hu, J. and Gordon, R. G. *Journal of Applied Physics* **71**, 880–890 (1992).

[94] Wind, R. a. and George, S. M. *Journal of Physical Chemistry A* **114**(3), 1281–9 jan (2010).

[95] Ellinger, C. R. and Nelson, S. F. *Chemistry of Materials* **26**(4), 1514–1522 (2014).

[96] Haynes, W. M., editor. *CRC Handbook of Chemistry and Physics.* Taylor & Francis, Boca Raton, 94 edition, (2013).

[97] Profijt, H. B., Potts, S. E., van de Sanden, M. C. M., and Kessels, W. M. M. *Journal of Vacuum Science & Technology A: Vacuum, Surfaces, and Films* **29**(5), 50801 (2011).

[98] Kim, D., Kang, H., Kim, J.-M., and Kim, H. *Applied Surface Science* **257**(8), 3776–3779 (2011).

[99] Jin, M. J., Jo, J., Neupane, G. P., Kim, J., An, K. S., and Yoo, J. W. *AIP Advances* **3**(2013), 0–12 (2013).

[100] Lee, S. W., Lee, Y. S., Heo, J., Siah, S. C., Chua, D., Brandt, R. E., Kim, S. B., Mailoa, J. P., Buonassisi, T., and Gordon, R. G. *Advanced Energy Materials* **4**(11), 1–7 (2014).

[101] Hoye, R. L. Z., Chua, M. R., Musselman, K. P., Li, G., Lai, M.-l., Tan, Z.-k., Greenham, N. C., Macmanus-driscoll, J. L., Friend, R. H., and Credgington, D. *Advanced Materials* **27**(8), 1414–1419 (2015).

[102] Nelson, S. F., Levy, D. H., Tutt, L. W., and Burberry, M. *Journal of Vacuum Science & Technology A* **30**(1), 01A154 (2012).

[103] Nandakumar, N., Dielissen, B., Garcia-alonso, D., Liu, Z., Roger, G., Kessels, W. M. M. E., Aberle, A. G., and Hoex, B. *IEEE Journal of Photovoltaics* **5**(5), 1462–1469 (2015).

[104] Chang, C.-Y. and Tsai, F.-Y. *Journal of Materials Chemistry* **21**(15), 5710–5715 (2011).

[105] Bayer, T. J. M., Wachau, A., Fuchs, A., Deuermeier, J., and Klein, A. *Chemistry of Materials* **24**, 4503–4510 (2012).

[106] Deuermeier, J., Bayer, T. J. M., Yanagi, H., Kiazadeh, A., Martins, R., Klein, A., and Fortunato, E. *Materials Research Express* **3**(4), 046404 (2016).

[107] Delabie, A., Sioncke, S., Rip, J., Van Elshocht, S., Pourtois, G., Mueller, M., Beckhoff, B., and Pierloot, K. *Journal of Vacuum Science & Technology A: Vacuum, Surfaces, and Films* **30**(1), 01A127 (2012).

[108] Ahn, C. H., Woo, C. H., Hwang, S., Lee, J. Y., Cho, H. K., Cho, H. J., and Yeom, G. Y. *Surface and Interface Analysis* **42**(6-7), 955–958 (2010).

[109] Fong, D. D., Eastman, J. A., Kim, S. K., Fister, T. T., Highland, M. J., Baldo, P. M., and Fuoss, P. H. *Applied Physics Letters* **97**(19), 2–5 (2010).

[110] Parsons, G. N., Atanasov, S. E., Dandley, E. C., Devine, C. K., Gong, B., Jur, J. S., Lee, K., Oldham, C. J., Peng, Q., Spagnola, J. C., and Williams, P. S. *Coordination Chemistry Reviews* **257**(23-24), 3323–3331 (2013).

[111] Wilson, C. A., Grubbs, R. K., and George, S. M. *Chem. Mater.* **17**(5), 5625–5634 (2005).

[112] Obuchovsky, S., Shamieh, B., Deckman, I., Ankonina, G., and Frey, G. L. *Solar Energy Materials and Solar Cells* **143**, 280–283 (2015).

[113] Obuchovsky, S., Deckman, I., Moshonov, M., Segal Peretz, T., Ankonina, G., Savenije, T. J., Frey, G. L., Peretz, T. S., Ankonina, G., Segal Peretz, T., Ankonina, G., Savenije, T. J., and Frey, G. L. *J. Mater. Chem. C* **2**(42), 8903–8910 sep (2014).

[114] Wei, H., Shi, J., Xu, X., Xiao, J., Luo, J., Dong, J., Lv, S., Zhu, L., Wu, H., Li, D., Luo, Y., Meng, Q., and Chen, Q. *Phys. Chem. Chem. Phys.* **17**, 4937–4944 (2015).

[115] Choudhury, D., Rajaraman, G., and Sarkar, S. *Nanoscale* **8**, 7459–7465 (2016).

[116] Mackus, A., Bol, A., and Kessels, W. *Nanoscale* **6**(2011), 10941–10960 (2014).

[117] Levy, D. H., Ellinger, C. R., and Nelson, S. F. *Applied Physics Letters* **103**(4) (2013).

[118] Chen, M.-J., Yang, J.-R., and Shiojiri, M. *Semiconductor Science and Technology* **27**(7), 074005 (2012).

[119] Wachnicki, Ł., Krajewski, T., Łuka, G., Witkowski, B., Kowalski, B., Kopalko, K., Domagala, J. Z., Guziewicz, M., Godlewski, M., and Guziewicz, E. *Thin Solid Films* **518**, 4556–4559 (2010).

[120] Na, J.-s., Gong, B., Scarel, G., and Parsons, G. N. *ACS Nano* **3**(10), 3191–3199 (2009).

[121] Kim, K.-d., Lim, D. C., Hu, J., Kwon, J.-d., Jeong, M.-g., Seo, H. O., Lee, J. Y., Jang, K.-y., Lim, J.-h., Lee, K. H., Jeong, Y., Kim, Y. D., and Cho, S. *ACS Appl. Mater. Interfaces* **5**, 87188723 (2013).

[122] Singh, T., Lehnen, T., Leuning, T., Sahu, D., and Mathur, S. *Applied Surface Science* **289**, 27–32 (2014).

[123] Cheun, H., Fuentes-Hernandez, C., Zhou, Y., Potscavage, W. J., Kim, S.-J. J., Shim, J., Dindar, A., and Kippelen, B. *Journal of Physical Chemistry C* **114**(48), 20713–20718 dec (2010).

[124] Platzer-Björkman, C., Törndahl, T., Hultqvist, a., Kessler, J., and Edoff, M. *Thin Solid Films* **515**(15), 6024–6027 (2007).

[125] Wang, J.-C., Weng, W.-T., Tsai, M.-Y., Lee, M.-K., Horng, S.-F., Perng, T.-P., Kei, C.-C., Yu, C.-C., and Meng, H.-F. *Journal of Materials Chemistry* **20**(5), 862–866 (2010).

[126] Shimizu, A., Chaisitsak, S., Sugiyama, T., Yamada, A., and Konagai, M. *Thin Solid Films* **361**, 193–197 (2000).

[127] Lee, K.-M., Chang, S. H., Wang, K.-H., Chang, C.-M., Cheng, H.-M., Kei, C.-C., Tseng, Z.-L., and Wu, C.-G. *Solar Energy* **120**, 117–122 (2015).

[128] Gilot, J., Barbu, I., Wienk, M. M., and Janssen, R. A. J. *Applied Physics Letters* **91**(11), 1–4 (2007).

[129] Hoye, R. L. Z., Heffernan, S., Ievskaya, Y., Sadhanala, A., Flewitt, A., Friend, R. H., MacManus-Driscoll, J. L., and Musselman, K. P. *ACS applied materials & interfaces* **6**(24), 22192–8 (2014).

[130] Kemp, K. W., Labelle, A. J., Thon, S. M., Ip, A. H., Kramer, I. J., Hoogland, S., and Sargent, E. H. *Advanced Energy Materials* **3**(7), 917–922 (2013).

[131] Kim, K. D., Lim, D. C., Jeong, M. G., Seo, H. O., Lee, J. Y., Song, Y., Cho, S., Lim, J. H., and Kim, Y. D. *Bulletin of the Korean Chemical Society* **35**(2), 353–356 (2014).

[132] Boichot, R., Tian, L., Richard, M. I., Crisci, A., Chaker, A., Cantelli, V., Coindeau, S., Lay, S., Ouled, T., Guichet, C., Chu, M. H., Aubert, N., Ciatto, G., Blanquet, E., Thomas, O., Deschanvres, J. L., Fong, D. D., and Renevier, H. *Chemistry of Materials* **28**(2), 592–600 (2016).

[133] Kang, Y.-J., Kim, C. S., Kwack, W.-S., Ryu, S. Y., Song, M., Kim, D.-H., Hong, S. W., Jo, S., Kwon, S.-H., and Kang, J.-W. *ECS Solid State Letters* **1**(1), Q1–Q3 jan (2012).

[134] Park, S.-Y., Seo, H. O., Kim, K.-D., Lee, J. E., Kwon, J.-D., Kim, Y. D., and Lim, D. C. *physica status solidi RRL* **6**(5), 196–198 may (2012).

[135] Lucero, A. T., Byun, Y.-c., Qin, X., Cheng, L., Kim, H., Wallace, R. M., and Kim, J. *Electron. Mater. Lett.* **11**(5), 769–774 (2015).

[136] Azevedo, J., Tilley, S. D., Schreier, M., Stefik, M., Sousa, C., Araújo, J. P., Mendes, A., Grätzel, M., and Mayer, M. T. *Nano Energy* **24**, 10–16 (2016).

[137] George, S. M. *Chemical Reviews* **110**(1), 111–131 (2010).

[138] Chang, C.-Y., Lee, K.-T., Huang, W.-K., Siao, H.-Y., and Chang, Y.-C. *Chemistry of Materials* **27**(14), 5122–5130 (2015).

[139] Pung, S.-Y., Choy, K.-L., Hou, X., and Shan, C. *Nanotechnology* **19**(43), 435609 (2008).

[140] Malm, J., Sahramo, E., Perälä, J., Sajavaara, T., and Karppinen, M. *Thin Solid Films* **519**(16), 5319–5322 jun (2011).

[141] Lin, Y.-Y., Chang, Y.-N., Tseng, M.-H., Wang, C.-C., and Tsai, F.-Y. *Nanotechnology* **26**(2), 024005 (2015).

[142] Platzer-Bjorkman, C., Lu, J., Kessler, J., and Stolt, L. *Thin Solid Films* **431**(03), 321–325 (2003).

[143] Torndahl, T., Coronel, E., Hultqvist, A., Platzer-Bjorkman, C., Leifer, K., and Edoff, M. *Progress in Photovoltaics: Research and Applications* **17**(1), 115–125 (2009).

[144] Alkis, S., Tekcan, B., Nayfeh, A., and Okyay, A. K. *Journal of Optics* **15**(10), 105002 (2013).

[145] Brittman, S., Yoo, Y., Dasgupta, N. P., Kim, S. I., Kim, B., and Yang, P. *Nano Letters* **14**(8), 4665–4670 (2014).

[146] Pietruszka, R., Luka, G., Kopalko, K., Zielony, E., Bieganski, P., Placzek-Popko, E., and Godlewski, M. *Materials Science in Semiconductor Processing* **25**, 190–196 (2014).

[147] Vasilopoulou, M., Konofaos, N., Davazoglou, D., Argitis, P., Stathopoulos, N. a., Savaidis, S. P., and Iliadis, A. a. *Solid State Electronics* **101**, 50–56 (2014).

[148] Bang, S., Lee, S., Park, J., Park, S., Jeong, W., and Jeon, H. *Journal of Physics D: Applied Physics* **42**(23), 235102 (2009).

[149] Oruc, F. B., Aygun, L. E., Donmez, I., Biyikli, N., Okyay, A. K., and Yu, H. Y. *Journal of Vacuum Science & Technology A* **33**, 01A105 (2015).

[150] Gong, S. C., Bang, S., Jeon, H., Park, H.-H., Chang, Y. C., and Chang, H. J. *Metals and Materials International* **16**(6), 953–958 dec (2010).

[151] Oh, B.-Y., Kim, Y.-H., Lee, H.-J., Kim, B.-Y., Park, H.-G., Han, J.-W., Heo, G.-S., Kim, T.-W., Kim, K.-Y., and Seo, D.-S. *Semicond. Sci. Technol.* **26**(8), 85007 (2011).

[152] Manifacier, J. C. *Journal of Physics E: Scientific Instruments* **9**, 1002–1004 (1976).

[153] Aristidou, N., Sanchez-Molina, I., Chotchuangchutchaval, T., Brown, M., Martinez, L., Rath, T., and Haque, S. A. *Angewandte Chemie - International Edition* **54**(28), 8208–8212 (2015).

[154] Fearn, S. *An Introduction to Time-of-Flight Secondary Ion Mass Spectrometry (ToF-SIMS) and its Application to Materials Science.* (2015).

[155] Jeon, N. J., Noh, J. H., Kim, Y. C., Yang, W. S., Ryu, S., and Seok, S. I. *Nature materials* **13**, 897 903 (2014).

[156] Colombara, D., Dale, P. J., Kissling, G. P., Peter, L. M., and Tombolato, S. *The Journal of Physical Chemistry C* , acs.jpcc.5b12531 (2016).

[157] Lubitz, M., Iv, P. A. M., Antic, A., Rosin, J. T., and Fahlman, B. D. (2014).

[158] Selvaraj, S. K., Jursich, G., Takoudis, C. G., Selvaraj, S. K., Jursich, G., and Takoudis, C. G. **095109**(2013) (2014).

[159] Ponraj, J. S., Attolini, G., and Bosi, M. *Critical Reviews in Solid State and Materials Sciences* **38**(3), 203–233 jan (2013).

[160] Kimes, W. A., Moore, E. F., Maslar, J. E., Kimes, W. A., Moore, E. F., and Maslar, J. E. **083106**(2012) (2015).

[161] Holmqvist, a., Magnusson, F., and Stenström, S. *Chemical Engineering Science* **117**, 301–317 (2014).

[162] Maydannik, P., Kääriäinen, T., and Cameron, D. *Chemical Engineering Journal* **171**(1), 345–349 jun (2011).

[163] Saha, D., Das, A. K., Ajimsha, R. S., Misra, P., and Kukreja, L. M. *Journal of Applied Physics* **114**(4) (2013).

[164] Dasgupta, N. P., Trejo, O., and Prinz, F. B. *Journal of Vacuum Science & Technology A: Vacuum, Surfaces, and Films* **30**(1), 01A110 (2012).

[165] Sinha, A., Hess, D. W., and Henderson, C. L. *Journal of Vacuum Science & Technology B: Microelectronics and Nanometer Structures* **24**(6), 2523 (2006).

[166] Snyder, M. Q., Trebukhova, S. a., Ravdel, B., Wheeler, M. C., DiCarlo, J., Tripp, C. P., and DeSisto, W. J. *Journal of Power Sources* **165**(1), 379–385 (2007).

[167] Selvaraj, S. K. and Takoudis, C. G. *Journal of Vacuum Science & Technology A: Vacuum, Surfaces, and Films* **33**(1), 013201 (2015).

[168] Hausmann, D. M. and Gordon, R. G. *Journal of Crystal Growth* **249**(1-2), 251–261 feb (2003).

[169] Kowalik, I. A., Guziewicz, E., Kopalko, K., Yatsunenko, S., Wójcik-Głodowska, A., Godlewski, M., Dłuzewski, P., Łusakowska, E., and Paszkowicz, W. *Journal of Crystal Growth* **311**(4), 1096–1101 (2009).

[170] Puurunen, R. L. In *16th International Conference on Atomic Layer Deposition*, O091, (2016).

[171] Tallarida, M., Kukli, K., Michling, M., Ritala, M., Leskelä, M., and Schmeisser, D. *Chemistry of Materials* **23**(13), 3159–3168 (2011).

[172] Tabe, M. *Applied Physics Letters* **45**(10), 1073–1075 (1984).

[173] Makino, H., Kishimoto, S., Yamada, T., Miyake, A., Yamamoto, N., and Yamamoto, T. *Physica Status Solidi (A) Applications and Materials Science* **205**(8), 1971–1974 (2008).

[174] Lee, D.-J., Kim, H.-M., Kwon, J.-Y., Choi, H., Kim, S.-H., and Kim, K.-B. *Advanced Functional Materials* **21**(3), 448–455 feb (2011).

[175] Viezbicke, B. D., Patel, S., Davis, B. E., and Birnie, D. P. *Physica Status Solidi (B)* **11**(8), n/a–n/a (2015).

[176] Kim, C. E., Moon, P., Kim, S., Myoung, J. M., Jang, H. W., Bang, J., and Yun, I. *Thin Solid Films* **518**(22), 6304–6307 (2010).

[177] Sarkar, A., Ghosh, S., Chaudhuri, S., and Pal, A. K. *Thin Solid Films* **204**(2), 255–264 (1991).

[178] Kwon, S., Bang, S., Lee, S., Jeon, S., Jeong, W., Kim, H., Gong, S. C., Chang, H. J., Park, H.-h., and Jeon, H. *Semiconductor Science and Technology* **24**(3), 035015 (2009).

[179] Kajikawa, Y. *Journal of Crystal Growth* **289**(1), 387–394 (2006).

[180] Park, H. K., Yang, B. S., Park, S., Kim, M. S., Shin, J. C., and Heo, J. *Journal of Alloys and Compounds* **605**, 124–130 (2014).

[181] Egginger, M., Bauer, S., Schwödiauer, R., Neugebauer, H., and Sariciftci, N. S. *Monatshefte fur Chemie* **140**(7), 735–750 (2009).

[182] Fakhri, M., Johann, H., Gorrn, P., and Riedl, T. *ACS Applied Materials and Interfaces* **4**(9), 4453–4456 (2012).

[183] Leow, C., Harada, T., Ohnishi, T., and Matsumura, M. *RSC Adv.* **5**(29), 22647–22653 (2015).

[184] MacLeod, B. A., Tremolet de Villers, B. J., Schulz, P., Ndione, P. F., Kim, H., Giordano, A. J., Zhu, K., Marder, S. R., Graham, S., Berry, J. J., Kahn, A., and Olson, D. C. *Energy Environ. Sci.* **8**(2), 592–601 (2015).

[185] Nicholas, N. J., Franks, G. V., and Ducker, W. a. *Langmuir : the ACS journal of surfaces and colloids* **28**(18), 7189–96 may (2012).

[186] Li, G., Yi, Z., Wang, H., Jia, C., and Zhang, W. *Applied Catalysis B: Environmental* **158-159**, 280–285 (2014).

[187] Jacobi, K., Zwicker, G., and Gutmann, A. *Surface Science* **141**(1), 109–125 (1984).

[188] Matsui, H. and Tabata, H. *Journal of Applied Physics* **99**(12), 124307 (2006).

[189] Illiberi, A., Scherpenborg, R., Theelen, M., Poodt, P., and Roozeboom, F. *Journal of Vacuum Science & Technology A: Vacuum, Surfaces, and Films* **31**(2013), 061504 (2013).

[190] Ahn, C. H., Kim, S. H., Cho, S. W., Yun, M. G., and Cho, H. K. *physica status solidi (RRL) - Rapid Research Letters* **8**(4), 328–331 (2014).

[191] Chung, Y. J., Choi, W. J., Kang, S. G., Lee, C. W., Lee, J.-O., Kong, K.-J., and Lee, Y. K. *J. Mater. Chem. C* **2**(43), 9274–9282 (2014).

[192] Law, M., Greene, L. E., Radenovic, A., Kuykendall, T., Liphardt, J., and Yang, P. *The journal of physical chemistry. B* **110**(45), 22652–22663 (2006).

[193] Si, H., Liao, Q., Zhang, Z., Li, Y., Yang, X., Zhang, G., Kang, Z., and Zhang, Y. *Nano Energy* **22**, 223–231 (2016).

[194] Yi, C. H., Yasui, I., and Shigesato, Y. *Japanese Journal of Applied Physics* **34**(Part 1, No. 3), 1638–1642 (1995).

[195] Chen, Y., Bagnall, D. M., Koh, H.-j., Park, K.-t., Hiraga, K., Zhu, Z., and Yao, T. *Journal of Applied Physics* **84**(7), 3912 (1998).

[196] Yan, T., Lu, C.-Y. J., Chang, L., Chou, M. M. C., Ploog, K. H., Chiang, C.-M., and Ye, N. *RSC Adv.* **5**(127), 104798–104805 (2015).

[197] Saron, K. M. A., Hashim, M. R., and Farrukh, M. A. *Applied Surface Science* **258**(13), 5200–5205 (2012).

[198] Ashrafi, A. B. M. A., Binh, N. T., Zhang, B. P., and Segawa, Y. *Applied Physics Letters* **84**(15), 2814–2816 (2004).

[199] Ghosh, R., Basak, D., and Fujihara, S. *Journal of Applied Physics* **96**(5), 2689–2692 (2004).

[200] Mohanty, B. C., Jo, Y. H., Yeon, D. H., Choi, I. J., and Cho, Y. S. *Applied Physics Letters* **95**(6), 2007–2010 (2009).

[201] Yan, Q., Rinke, P., Winkelnkemper, M., Qteish, a., Bimberg, D., Scheffler, M., and Van de Walle, C. G. *Semiconductor Science and Technology* **26**(1), 014037 (2010).

[202] Ahn, C. H., Yun, M. G., Lee, S. Y., and Cho, H. K. *IEEE Transactions on Electron Devices* **61**(1), 73–78 (2014).

[203] Williams, S. T., Rajagopal, A., Chueh, C. C., and Jen, A. K. Y. *Journal of Physical Chemistry Letters* **7**(5), 811–819 (2016).

[204] Ye, M., Hong, X., and Liu, X.-Y. *J. Mater. Chem. A* **4**, 6755–6771 (2016).

[205] Liu, X., Zhao, W., Cui, H., Xie, Y., Wang, Y., Xu, T., and Huang, F. *Inorg. Chem. Front.* **2**, 315–335 (2015).

[206] Leijtens, T., Eperon, G. E., Noel, N. K., Habisreutinger, S. N., Petrozza, A., and Snaith, H. J. *Advanced Energy Materials* **5**(20), 1–23 (2015).

[207] Berhe, T. A., Su, W.-N., Chen, C.-H., Pan, C.-J., Cheng, J.-H., Chen, H.-M., Tsai, M.-C., Chen, L.-Y., Dubale, A. A., and Hwang, B.-J. *Energy Environ. Sci.* **9**, Advance Article (2016).

[208] Tiep, N. H., Ku, Z., and Fan, H. J. *Advanced Energy Materials* **6**(3), 1–19 (2016).

[209] You, J., Yang, Y. M., Hong, Z., Song, T.-B., Meng, L., Liu, Y., Jiang, C., Zhou, H., Chang, W.-H., Li, G., and Yang, Y. *Applied Physics Letters* **105**(18), 183902 (2014).

[210] Bryant, D., Aristidou, N., Pont, S., Sanchez-Molina, I., Chotchunangatchaval, T., Wheeler, S., Durrant, J. R., and Haque, S. A. *Energy Environ. Sci.* **9**(5), pp 1655–1660 (2016).

[211] Dong, X., Hu, H., Lin, B., Ding, J., and Yuan, N. *Chem. Commun. (Cambridge, U. K.)* **50**(3), Ahead of Print (2014).

[212] Dualeh, A., Tétreault, N., Moehl, T., Gao, P., Nazeeruddin, M. K., and Grätzel, M. *Advanced Functional Materials* **24**(21), 3250–3258 (2014).

[213] Divitini, G., Cacovich, S., Matteocci, F., Cinà, L., Di Carlo, A., and Ducati, C. *Nature Energy* **1**(January), 15012 (2016).

[214] Stakhira, P. Y., Grygorchak, I. I., Cherpak, V. V., Ivastchyshyn, F. O., Volynyuk, D. Y., Luka, G., Godlewski, M., Guziewicz, E., Pakhomov, G. L., and Hotra, Z. Y. *Materials Science and Engineering B: Solid-State Materials for Advanced Technology* **172**(3), 272–275 (2010).

[215] Liu, H., Huang, Z., Wei, S., Zheng, L., Xiao, L., and Gong, Q. *Nanoscale* **8**(12), 6209–6221 (2016).

[216] Zhang, J. and Pauporté, T. *Journal of Physical Chemistry C* **119**(27), 14919–14928 (2015).

[217] Xu, X., Zhang, H., Shi, J., Dong, J., Luo, Y., Li, D., and Meng, Q. *J. Mater. Chem. A* **3**(38), 19288–19293 (2015).

[218] Dong, J., Xu, X., Shi, J.-J., Li, D.-M., Luo, Y.-H., Meng, Q.-B., and Chen, Q. *Chinese Physics Letters* **32**(7), 078401 (2015).

[219] Dkhissi, Y., Meyer, S., Chen, D., Weerasinghe, H. C., Spiccia, L., Cheng, Y. B., and Caruso, R. A. *ChemSusChem* **9**(7), 687–695 (2016).

[220] Kumar, S. and Dhar, A. *ACS Applied Materials and Interfaces* **8**(28), 18309–18320 (2016).

[221] Baikie, T., Fang, Y., Kadro, J. M., Schreyer, M., Wei, F., Mhaisalkar, S. G., Gratzel, M., and White, T. J. *Journal of Materials Chemistry A* **1**(18), 5628 (2013).

[222] Xie, F. X., Zhang, D., Su, H., Ren, X., Wong, K. S., and Gra, M. *ACS Nano* (1), 639–646 (2015).

[223] Manspeaker, C., Scruggs, P., Preiss, J., Lyashenko, D. A., and Zakhidov, A. A. *Journal of Physical Chemistry C* **120**(12), 6377–6382 (2016).

[224] Nicolaev, A., Mitran, T. L., Iftimie, S., and Nemnes, G. A. *Solar Energy Materials and Solar Cells* , 1–7 (2015).

[225] Tseng, Z.-L., Chiang, C.-H., and Wu, C.-G. *Scientific reports* **5**, 13211 (2015).

[226] Chen, Q., Zhou, H., Song, T.-b., Luo, S., and Hong, Z. *Nano Letters* **14**, 4158–4163 (2014).

[227] Zhao, X., Shen, H., Zhang, Y., Li, X., Zhao, X., Tai, M., Li, J., Li, J., Li, X., and Lin, H. *ACS Applied Materials and Interfaces* **8**(12), 7826–7833 (2016).

[228] Lankhorst, A. M., Paarhuis, B. D., Terhorst, H. J. C. M., Simons, P. J. P. M., and Kleijn, C. R. *Surface and Coatings Technology* **201**(22-23), 8842–8848 (2007).

[229] Triani, G., Evans, P. J., Attard, D. J., Prince, K. E., Bartlett, J., Tan, S., and Burford, R. P. *Journal of Materials Chemistry* **16**(14), 1355 (2006).

[230] Sobel, N., Hess, C., Lukas, M., Spende, A., Stuhn, B., Toimil-Molares, M. E., and Trautmann, C. *Beilstein Journal of Nanotechnology* **6**(1), 472–479 (2015).

[231] Shin, H., Jeong, D. K., Lee, J., Sung, M. M., and Kim, J. *Advanced Materials* **16**(14), 1197–1200 (2004).

[232] Li, F., Li, L., Liao, X., and Wang, Y. *Journal of Membrane Science* **385-386**, 1–9 dec (2011).

[233] Spende, A., Sobel, N., Lukas, M., and Zierold, R. *Nanotechnology* **26**(33), 335301 (2015).

[234] Vandersarl, J. J., Xu, A. M., and Melosh, N. A. *Nano Letters* **12**(8), 3881–3886 (2012).

[235] Motoyama, M., Chao, C.-C., An, J., Jung, H. J., Gür, T. M., and Prinz, F. B. *ACS nano* **8**(1), 340–51 jan (2014).

[236] Apel, P. Y., Blonskaya, I. V., Dmitriev, S. N., Orelovitch, O. L., Presz, A., and Sartowska, B. a. *Nanotechnology* **18**, 1–7 (2007).

[237] Spagnola, J. C., Gong, B., Arvidson, S. a., Jur, J. S., Khan, S. a., and Parsons, G. N. *Journal of Materials Chemistry* **20**(20), 4213 (2010).

[238] Szeghalmi, A., Helgert, M., Brunner, R., Heyroth, F., Gösele, U., and Knez, M. *Applied Optics* **48**(9), 1727–1732 (2009).

[239] Latella, B. A., Triani, G., Zhang, Z., Short, K. T., Bartlett, J. R., and Ignat, M. *Thin Solid Films* **515**(5), 3138–3145 (2007).

[240] Nelson, S. F., Ellinger, C. R., and Levy, D. H. *ACS Applied Materials & Interfaces* **7**, 2754–2759 (2015).

[241] Babal, A. S., Gupta, R., Singh, B. P., and Dhakate, S. R. *RSC Adv.* **5**(54), 43462–43472 (2015).

[242] Ghaddar, A., Gieraltowski, J., Gloaguen, F., Zuberek, R., Aleshkevych, P., Kazmierczak, J., Slawska-Waniewska, A., and Szymczak, H. *Acta Physica Polonica A* **116**(6), 1039–1043 (2009).

[243] Dubois, S., Colin, J., Duvail, J. L., and Piraux, L. *Physical Review B* **61**(21), 14315–14318 (2000).

[244] Gershon, T., Gokmen, T., Gunawan, O., Haight, R., Guha, S., and Shin, B. *MRS Communications* **4**(04), 159–170 nov (2014).

[245] Suehiro, S., Horita, K., Kumamoto, K., Yuasa, M., Tanaka, T., Fujita, K., Shimanoe, K., and Kida, T. *Journal of Physical Chemistry C* **118**, 804–810 (2014).

[246] Mitzi, D. B., Gunawan, O., Todorov, T. K., Barkhouse, D. A. R., and A, P. T. R. S. *Philosophical transsactions of Royal Society A* **371**(July), 20110432 (2013).

[247] Ito, K. and Nakazawa, T. *Japanese Journal of Applied Physics* **27**, 2094–2097 (1988).

[248] Wang, K., Gunawan, O., Todorov, T., Shin, B., Chey, S. J., Bojarczuk, N. A., Mitzi, D., and Guha, S. *Applied Physics Letters* **97**(14), 2014–2017 (2010).

[249] Thimsen, E., Riha, S. C., Baryshev, S. V., Martinson, A. B. F., Elam, J. W., and Pellin, M. J. *Chemistry of Materials* , 120809093129001 (2012).

[250] Rovelli, L., Tilley, S. D., and Sivula, K. *ACS Applied Materials and Interfaces* **5**, 8018–8024 (2013).

[251] Scragg, J. J., Dale, P. J., and Peter, L. M. *Electrochemistry Communications* **10**(4), 639–642 (2008).

[252] Guijarro, N., Prevot, M. S., and Sivula, K. *Journal of Physical Chemistry Letters* **5**, 3902–3908 (2014).

[253] Sarswat, P. K., Free, M. L., and Kumar, G. *Journal of Spectroscopy* **1**(1) (2013).

[254] Guijarro, N., Prévot, M. S., and Sivula, K. *Phys. Chem. Chem. Phys.* **17**, 15655–15674 (2015).

[255] Singh, T., Lehnen, T., Leuning, T., and Mathur, S. *Journal of Vacuum Science & Technology A: Vacuum, Surfaces, and Films* **33**(1), 010801 (2015).

[256] Riha, S. C., Klahr, B. M., Tyo, E. C., Seifert, S., Vajda, S., Pellin, M. J., Hamann, T. W., Brandon, A., and Martinson, F. *ACSNano* (3), 2396–2405 (2013).

[257] Lichterman, M. F., Shaner, M. R., Handler, S. G., Brunschwig, B. S., Gray, H. B., Lewis, N. S., and Spurgeon, J. M. *Journal of Physical Chemistry C* **4**, 4188–4191 (2013).

[258] Mcdowell, M. T., Lichterman, M. F., Spurgeon, J. M., Hu, S., Sharp, I. D., Brunschwig, B. S., and Lewis, N. S. *Journal of Physical Chemistry C* **118**, 19618–19624 (2014).

[259] Paracchino, A., Mathews, N., Hisatomi, T., Stefik, M., Tilley, S. D., and Grätzel, M. *Energy & Environmental Science* **5**(9), 8673 (2012).

[260] Paracchino, A., Laporte, V., Sivula, K., Grätzel, M., and Thimsen, E. *Nature materials* **10**(6), 456–61 jun (2011).

[261] Roelofs, K. E., Brennan, T. P., and Bent, S. F. *Journal of Physical Chemistry Letters* **5**, 348–360 (2014).

[262] Chandiran, A. K., Tetreault, N., Humphry-Baker, R., Kessler, F., Baranoff, E., Yi, C., Nazeeruddin, M. K., and Grätzel, M. *Nano letters* **12**(8), 3941–7 aug (2012).

[263] Ihly, R., Tolentino, J., Liu, Y., Gibbs, M., and Law, M. (10), 8175–8186 (2011).

[264] So, H.-M., Choi, H., Shim, H. C., Lee, S.-M., Jeong, S., and Chang, W. S. *Applied Physics Letters* **106**(9), 093507 (2015).

[265] Pourret, A., Guyot-Sionnest, P., and Elam, J. W. *Advanced Materials* **21**, 232–235 (2009).

[266] Riha, S. C., Jin, S., Baryshev, S. V., Thimsen, E., Wiederrecht, G. P., and Martinson, A. B. F. *ACS Applied Materials and Interfaces* **5**, 10302–10309 (2013).

[267] Trinh, H.-D., Chang, E. Y., Wong, Y.-Y., Yu, C.-C., Chang, C.-Y., Lin, Y.-C., Nguyen, H.-Q., and Tran, B.-T. *Japanese Journal of Applied Physics* **49**(11), 111201 nov (2010).

[268] Dafinone, M. I., Feng, G., Brugarolas, T., Tettey, K. E., and Lee, D. *ACS nano* **5**(6), 5078–87 jun (2011).

[269] Chandiran, A. K., Abdi-jalebi, M., Nazeeruddin, M. K., and Accepted, J. (3), 2261–2268 (2014).

[270] Wen, X., Luo, W., and Zou, Z. *Journal of Materials Chemistry A* , 15479–15485 (2013).

[271] Kong, J.-Z., Gao, M.-Y., Zhai, H.-F., Yan, Q.-Y., Li, A.-D., Li, H., and Wu, D. *Journal of Magnetism and Magnetic Materials* **343**, 1–5 oct (2013).

Appendix

ALD Handbook

Handbook introduction

This handbook should be used in combination with Chapter 4 of the thesis to ensure complete understanding of the ALD system. Chapter 4 details the key design decisions made and the general operations of the system. The purpose of this handbook is to add to this information by detailing specific assembly methods, wiring diagrams, and operation instructions so that every aspect of the system can be understood, operated and adapted by future users. Sections follow the vacuum system, temperature control, valve control and LabVIEW program with photos and manufacturers' part numbers where relevant.

ALD diagram

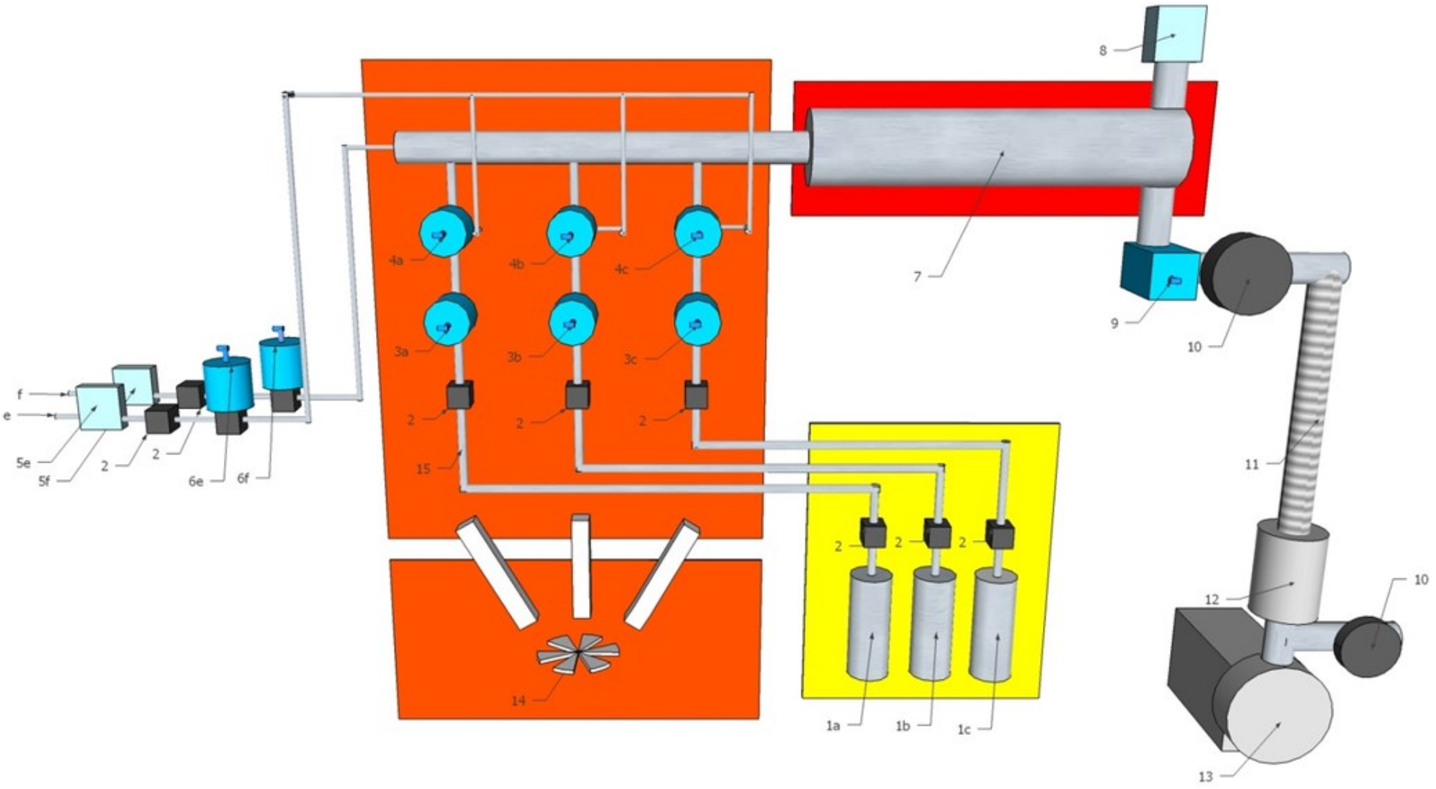

1 – Precursor flask (a TMA, b DEZ, c H_2O)

2 – Manual valve

3 – Pneumatic ALD valve (safety valve)

4 – Pneumatic ALD valve (release valve)

5 – Mass flow controller (e, f separate purified N_2 flows)

6 – Pneumatic diaphragm valve

7 – Reaction chamber

8 – Pirani vacuum gauge

9 – Pneumatic isolation valve

10 – Manual isolation valve

11 – Bellows

12 – Activated charcoal filter trap

13 – Scroll pump

14 – Fan to circulate heated air

15 – Place to attach heated precursor

Contents

A1: General advice

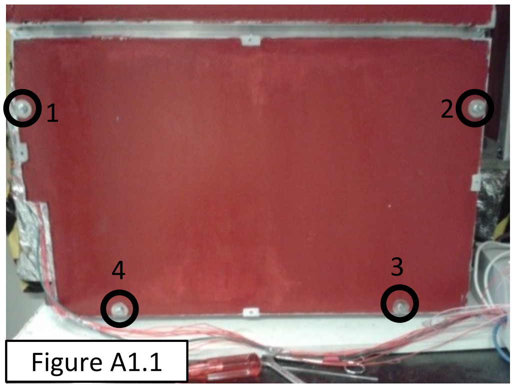

Figure A1.1

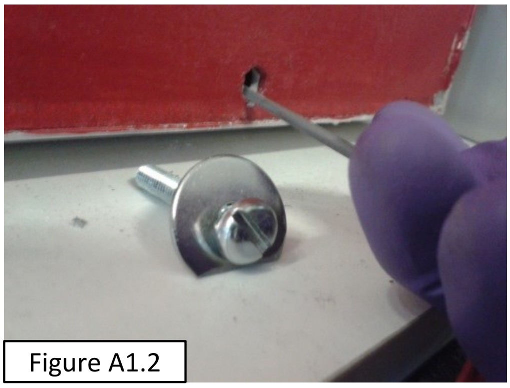

Figure A1.2

The oven, furnace and precursor box sections are all built off the back metal frame, which is the structural support for the whole system. Any moving of the ALD should be done by only holding the metal frame as the attached boxes, although robust enough for everyday use, will not be strong enough to take any significant weight. The ALD is constructed mostly with a combination metal brackets and edging which hold and protect Masterboard® faces of the boxes. The Masterboard is a calcium silicate/fibre composite, here it is arranged in a double layer with an air gap between, thus providing heat insulation on the heated areas of the ALD. It is also fire resistant for 30 mins, which is another useful function due to the fire risk associated with ALD. The material is fairly brittle and so should be handled carefully, and a risk assessment should be carried out if modifying the board due to the fibres and dust that can be produced. A layer of paint covering the exposed areas of Masterboard prevents dust in everyday use.

Holes have been drilled in the Masterboard boxes for tubing etc. to pass through. These holes are larger than the tube diameter to allow for flexibility when dis/assembling parts of the system and, in some cases, to allow room tightening the connections. The gaps around the tubes which pass through the holes need to be filled when using the ALD system as they are otherwise a significant heat loss route. Silicone rubber has been used to fill in these holes.

Figure A1.3

The edges of the door for the upper part of the oven and the front panel of the lower section of the oven are both designed to be easily and repeatedly opened. This means that silicone rubber cannot be used to seal the edges where the front panel sits against the sides of the box. Instead self adhesive EPDM rubber P strip is used to line edges, forming a seal against air and heat flow.

In the following sections the details on how to disassemble the system are included. Below is some general guidance:

- the system was handmade so all the panels, holes for screws, metal brackets etc. have been separately made and so they are not necessarily interchangeable and therefore make sure to keep track of where each part was positioned when disassembling the system.
- When screwing on a panel e.g. Figure A1.1, switch between the screws 1-4 gradually tightening each a few turns at a time rather than fully tightening one at a time. This will make the alignment of the panel easier.
- If it is difficult aligning holes for a screw to pass through, a thin rod of metal can be used to facilitate manoeuvring a panel so the holes come into alignment as shown in Figure A1.2.
- The KF flanges used in the vacuum system the wing nut should only be tightened to finger tight for a good vacuum seal. Using WD40 on the nut thread can make the tightening easier and reduce the chance of stripping the thread, which sometime occurs. If the thread does strip then the stripped metal should be carefully removed from the clamp's screw and then the clamp can be reused with a new wing nut. The KF flanges often become firmly closed and it can be a problem to remove them. If this happens an adjustable spanner can be used to loosen the wing nut and also to lever apart the flange halves as shown in Figure A1.3.
- For any modification of the tube or vacuum system the user should go on a Swagelok tube fitting course to learn how to safely carry out tube connections as this can be dangerous if done incorrectly. The tube sizes used in the ALD are in imperial units (inches) more of the components were compatible with those fittings.

A2: Electrical connections and laptop programs

The electrical components of the ALD are supplied power by four plug sockets. The selection of components connected to each multiplug were grouped with application and chosen to not exceed the plugs 13 A rating. The individual fuse rating for each component is written on the relevant plug and the ALD system, frame and shelving are all earthed. The electrical components are enclosed inside ABS boxes which must not be opened unless the electric supply has been turned off and unplugged due to risk of mains electric shock. All components need to be safety tested by a professional before switching on. The following components are connected to each plug:

Multiplug A:
Oven temperature controller and two finned heaters
Oven air circulation fan

Multiplug B
Reaction chamber temperature controller and two rope heaters.
End of chamber temperature controller and one rope heater
Line to pump temperature controller and two rope heaters

Multiplug C
Laptop power supply
Mass flow controller power supply
24 V power supply, which powers the 8 relay board, mac solenoid valves and pressure gauge

Plug D
Vacuum pump

The laptop is used to control the deposition using LabVIEW, as is demonstrated in Figure A2.2. The temperature of the system is controlled by the buttons and screen on the individual temperature controllers, they are not linked to the laptop.

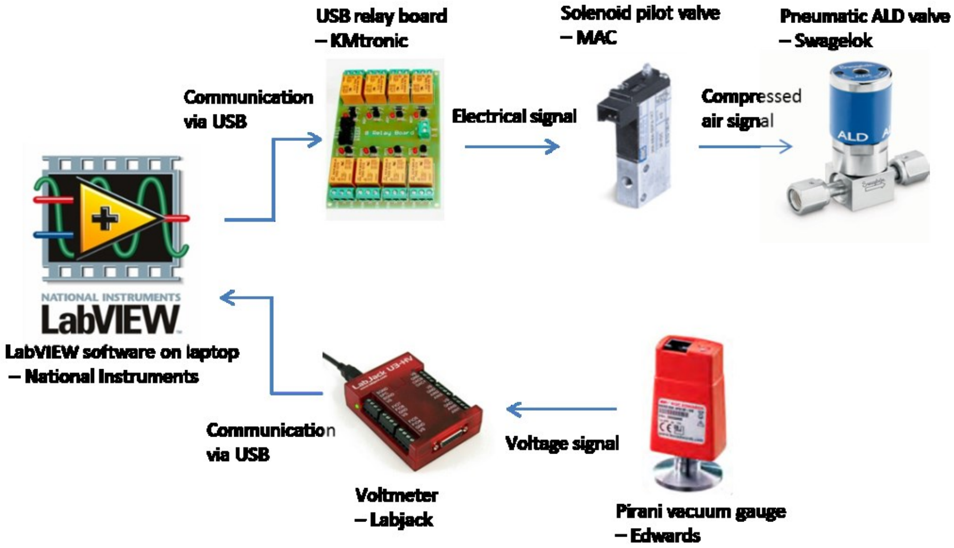

Figure A2.2 [images of components from respective manufacturer's websites]

Component	Seller	Part ID
White mains plug,13A	RS	490-015
IP65 grey ABS box,240x120x100mm	RS	501-143
Black silicone insulated mains cable	RS	744-0985
Red hook-up equipment wire,22awg	RS	177-1084

A3: Gas and precursor supplies

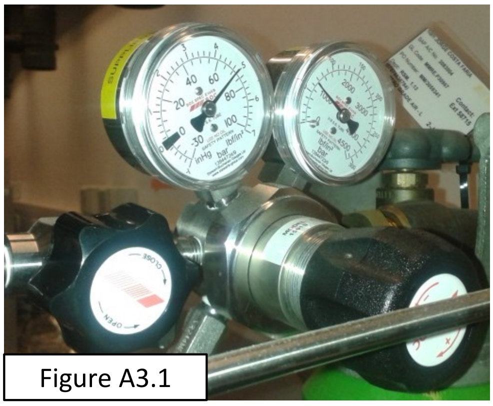
Figure A3.1

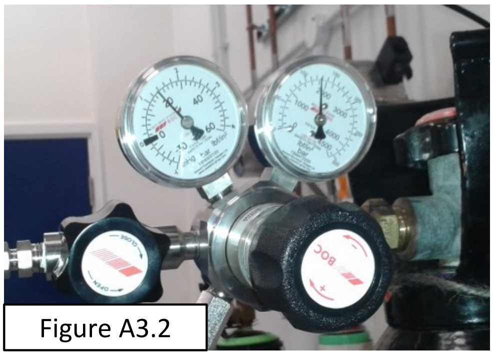
Figure A3.2

Table A3.1

Valve	Pressure requirement
MAC solenoid valve	Maximum 8.2 bar
ALD valves	3 .5 to 6 .2 bar
N_2 line diaphragm valves	4.2 to 8.2 bar
Furnace isolation valve	recommended 2.8 to 4.2 bar (max 7 bar)

Two gases and three precursors are connected to the ALD system at a time. The N_2 and compressed air cylinders are size L have a wheel opening valve for easy isolation, as can be seen in Figure A3.1 and A3.2. The regulators attached are single-stage which means the output pressure will change as the pressure inside the cylinder decreases. This does not present a problem as the consumption of gas is very low so the drift from the set pressure is slow, but the pressures should be checked and perhaps adjusted before each deposition. Any adjusting/reconnecting/handling of the gas cylinders should only be done by users who have been on the gas safety course as there are many hazards involved.

The N_2 used is high purity (N6.0 = 6 nines = 99.9999% pure) and the gas regulator is specially high purity compatible; this is a requirement in ALD. During deposition the N_2 gas pressure is set to 1.4 bar (Figure A3.2). If the N_2 gas cylinder is ever disconnected/replaced purging of the system should be carried out to remove any e.g. adsorbed H_2O which will be in the system after air exposure. Also you must bear in mind that the Entergris Gatekeeper further along the N_2 line should be isolated by the relevant ball valves before any change in the system due to its sensitivity. Firstly, the Gatekeeper is a purifier and can only remove a certain amount of impurities, and secondly, it will react extremely exothermically on prolonged air exposure and could catch fire. In general the N_2 gas cylinder is left open whilst the ALD system is depositing/on standby. Valves further along the ALD system are used to stop gas flow on standby.

Compressed air is chosen as the pneumatic control gas as it is cheap, inert and if a leak was to occur there would be no risk of oxygen depletion (a depletion calculation was carried out for the N_2 gas to ensure that the room is large enough that the average oxygen level is safe even on the accidental release of the entire N_2 bottle, and in addition the lab is equipped with oxygen depletion alarms). The pressure is set to 5 bar as this pressure is suitable for all the valves in the system (see Table A3.1)

Component	Seller	Part ID
N6.0 ultrahigh purity N_2 cylinder (size L)	BOC	296180-L
Compressed air cylinder (size L)	BOC	270028-L
High purity N_2 gas regulator with Swagelok adaptor	BOC	HP1500S.GG-BS3-1/4” Compression, material 851700, 0-2 bar outlet range
Compressed air regulator with Swagelok adaptor	BOC	HP1501S.GG-BS3-1/4” Compression, material 51700, 0-5 bar outlet range
Diethyl zinc (DEZ) packaged for use in ALD systems	Strem	93-3030 in 50 ml Swagelok cylinder (96-1070) for CVD/ALD
Trimethyl aluminium (TMA) packaged for use in deposition systems	Sigma Aldrich	663301-25G
Gatekeeper inert gas purifier	Entegris	CE35KFI4R
Nickel ¼” retained gaskets	Swagelok	NI-4-VCR-2-GR-VS

A3: Gas and precursor supplies cont.

The precursors are usually supplied in protective cans (see Figure A2.3) due to the danger if the precursor bottle was damaged. Inside the can the precursor is isolated in its stainless steel cylinder by a valve and a VCR cap (see Figure A2.4). Before changing any of the precursors carry out a risk assessment to understand the specific chemical as often ALD precursors are corrosive and pyrophoric. To load in a new precursor you must first make sure you have closed the manual valve on the precursor cylinder currently in the ALD system and that you have thoroughly purged any remaining precursor from the line leading to it. Purge the system by opening the relevant ALD safety and release valves and use N_2 flow under vacuum to purge the system for at least 30 minutes at temperature of around 100 °C. After this allow the system to cool. Next, the pressure inside the line needs to be equilibrated to atmospheric pressure. This can be done by opening the relevant pneumatic valves and both manual isolation valves so that the whole line is directly open to atmosphere. The VCR connection just above the precursor cylinder valve can be undone with a spanner and the old precursor bottle can then be removed. Even if you think the old precursor cylinder is empty make sure never to open the precursor cylinder in air due to the extremely dangerous pyrophoric nature of many precursors. The VCR cap which came originally with the old precursor bottle should be used to seal the bottle (with a new gasket) and the bottle should be stored safely in the protective can until safe disposal or reattachment to the system.

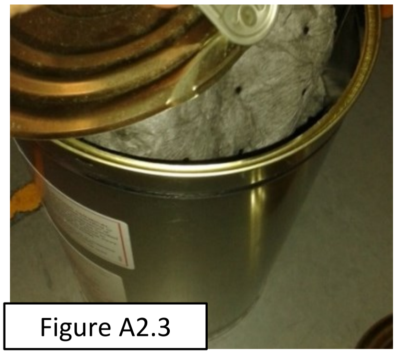

Figure A2.3

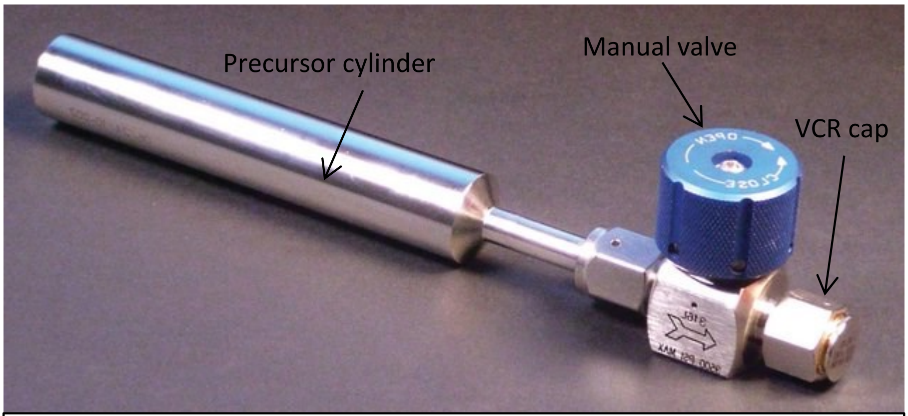

Figure A2.4 [from www.sigmaaldrich.com/catalog/product/aldrich/668729]

Before opening the new precursor bottle clamp it vertically in a fume hood and have a dry powder fire extinguisher to hand in case of emergencies. Check that the manual valve is closed and has not ever been opened (otherwise the tubing between the valve and VCR cap will contain precursor which will react when exposed to air); usually the precursor manual valves are provided tied or taped shut to avoid any accidental opening. The VCR cap can then be removed and the bottle can be taken from the fume hood and attached into the ALD system (using a new gasket). The line to the precursor bottle should then be put under vacuum and purged thoroughly again to remove the molecules which adsorbed on air exposure. Preliminary checks should be carried out to see if the line holds vacuum (i.e. does not leak) since a new connection has been made. These can be done by evacuating the line and then closing the pneumatic valves for a length of time. Reopen the ALD pneumatic valves whilst monitoring the chamber pressure, if there is a sharp increase in pressure this shows that the connection is leaking. Helium leak testing on the connection will reveal slower leaks. Only once the purging is complete, the connection has been fully leak tested and the ALD valves are closed can you open the precursor bottle. As described in Chapter 4, the precursor should then be degassed.

N1: Nitrogen flow system

Figure N1.1

The ultrahigh purity N_2 from the gas cylinder travels through a series of components before entering the oven section of the ALD system. Figure N1.1 shows a photo of this section of the system and Figure N1.2 shows the schematic with each part explained. The components are screwed to a stainless steel sheet to minimise movement. The connection between components is by stainless steel tubing and Swagelok fittings. 1/4” tubing can be prepared by using a tube cutter, tube deburring tool and a tube bender, whilst the 1/8” and 1/16” tubes have to be cut with a hand saw, deburred with a file and bent by hand.

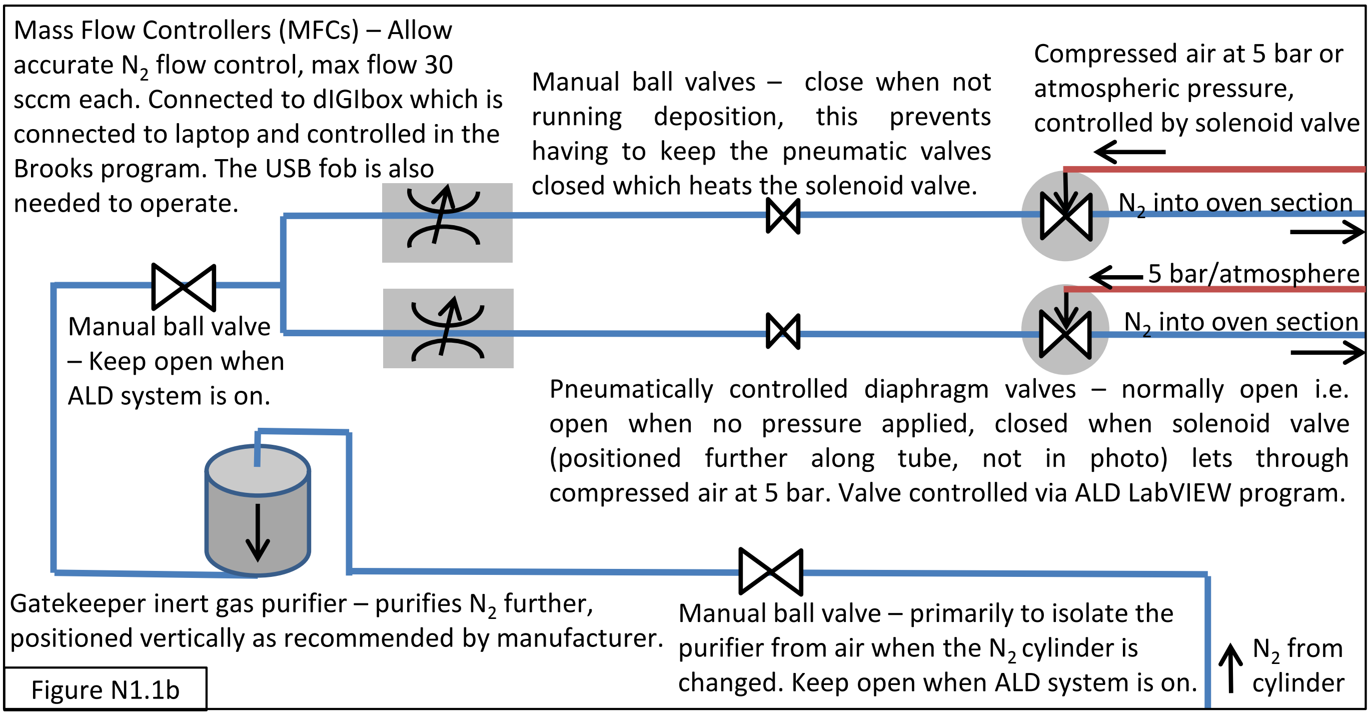
Mass Flow Controllers (MFCs) – Allow accurate N_2 flow control, max flow 30 sccm each. Connected to dIGIbox which is connected to laptop and controlled in the Brooks program. The USB fob is also needed to operate.

Manual ball valves – close when not running deposition, this prevents having to keep the pneumatic valves closed which heats the solenoid valve.

Compressed air at 5 bar or atmospheric pressure, controlled by solenoid valve

Manual ball valve – Keep open when ALD system is on.

Pneumatically controlled diaphragm valves – normally open i.e. open when no pressure applied, closed when solenoid valve (positioned further along tube, not in photo) lets through compressed air at 5 bar. Valve controlled via ALD LabVIEW program.

Gatekeeper inert gas purifier – purifies N_2 further, positioned vertically as recommended by manufacturer.

Manual ball valve – primarily to isolate the purifier from air when the N_2 cylinder is changed. Keep open when ALD system is on.

Figure N1.1b

Special care needs to be taken when carrying out any process which will affect the purifier therefore always check the manufactures instructions. Especially, do not allow any sudden, large gas flows through the purifier as this will damage it, and do not expose it to air as the catalyst may spontaneously combust.

Component	Seller	Part ID
Stainless steel tubing	Swagelok	1/4“ inner diameter: SS-T4-S-035-6ME; 1/8”: SS-T2-S-028-6ME; 1/16”: SS-T1-S-014-6ME
Manual ball valve	Swagelok	1/4“: SS-43GS4; 1/16”: SS-41GS1
Gatekeeper inert gas purifier	Entegris	CE35KFI4R
Brooks Mass flow controllers	M J Wilson	GF040CXXC-0013030C-T1PVS4-XXXXAX-00C
Brooks MFC power supply unit and RS485 communications	M J Wilson	dIGIbox 
Brooks smart interface software	M J Wilson	0260ABCAA
Pneumatically controlled diaphragm valve	Swagelok	6LVV-DPS4-0

N2: Oven vacuum system

The operation of the ALD valve assembly during deposition is described in detail in Chapter 4 along with schematic diagrams. To compliment that description, Figure N2.1 shows a photo of the assembly with the specific components identified and explained.

1/8” bulkhead unions – Connect the compressed air lines from the solenoid MAC valves on the outside of the oven section to the pneumatically controlled ALD valves inside. Bulkhead unions simplify connection because even though it would be possible to just pass a tube through a hole in the Masterboard sheet and therefore connect solenoid valves to ALD valves with a single tube (as is done with the three tubes leading out of the precursor box) it does make connection more awkward. Instead two separate tubes, one inside the oven box, one outside, are connected to either end of the bulkhead union which is clamped by nuts to metal support sheet to prevent the union rotating. A ratchet spanner with a pass-through socket is needed to tighten the nuts.

1/8” stainless steel tubing for connection of the pneumatic lines. The tubes have multiple bends because they need at least two bends in them otherwise the tubing is too inflexible, preventing connection from the ALD valve to the bulkhead union.

VCR cap on T-junction allowing the option of connecting a low vapour pressure precursor which needs heating here .

KF40 connection of valve assembly to reaction chamber. Flange is welded to the end of the reaction chamber tube. Can be easily disconnected if reaction chamber tube needs to be removed

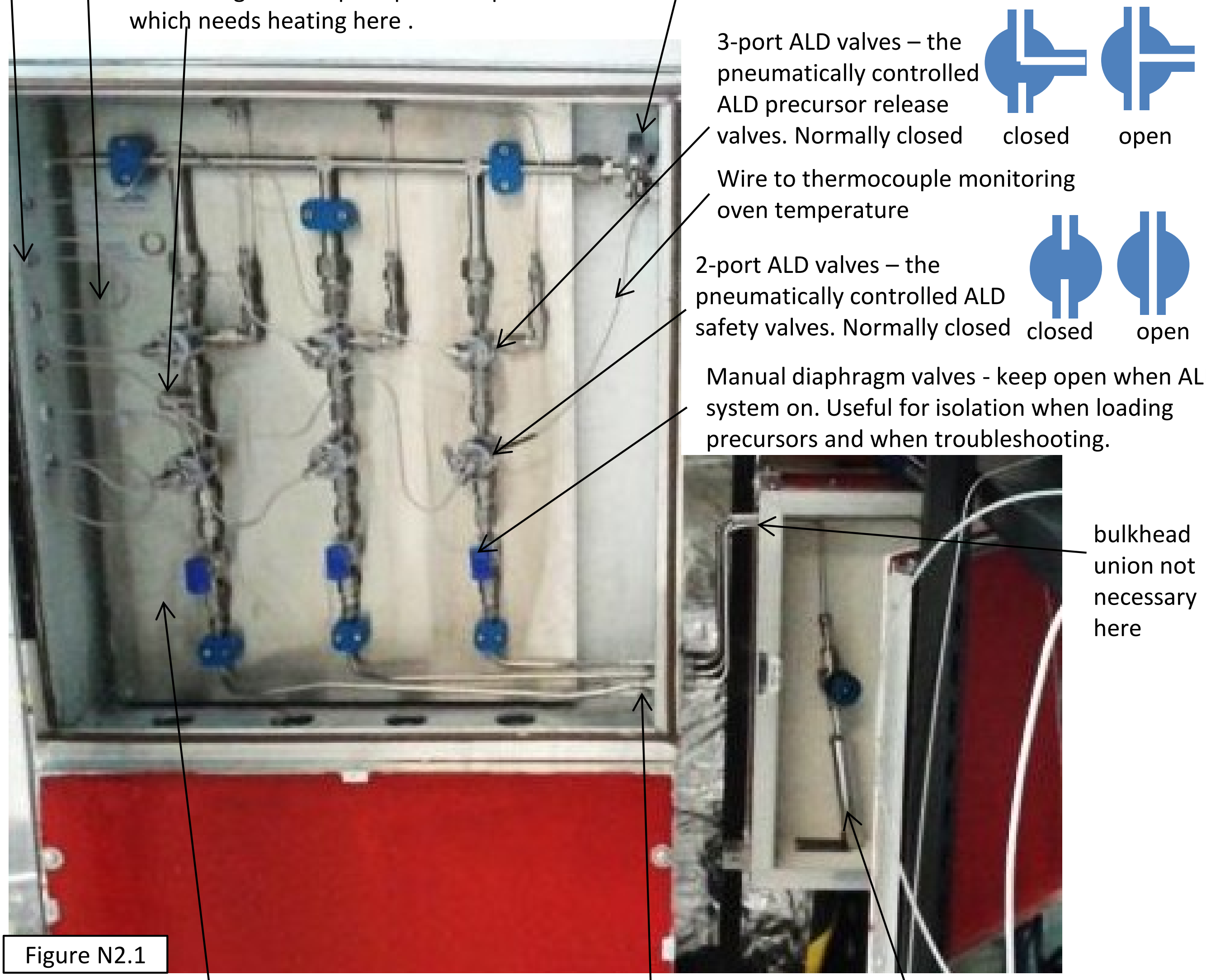

3-port ALD valves – the pneumatically controlled ALD precursor release valves. Normally closed

Wire to thermocouple monitoring oven temperature

2-port ALD valves – the pneumatically controlled ALD safety valves. Normally closed

Manual diaphragm valves - keep open when ALD system on. Useful for isolation when loading precursors and when troubleshooting.

bulkhead union not necessary here

Figure N2.1

Stainless steel back plate to which valve are screwed for support and easy assembly. Held in place by screws in the four corners

1/4” bulkhead unions – connection of lines from 3 precursors to valve assembly

Precursor cylinder (other two cylinders are to the right, behind the box door)

N2: Oven vacuum system cont.

When the N_2 is flowing during purging or deposition it flows into the oven section via two lines, with flow along each controlled by a mass flow controller and a pneumatic valve (as described in Section N1). In the LabVIEW program the pneumatic valves are referred to as "N_2 const." and "N_2 chrom.". Figure N2.2 shows the paths taken by the flows of N_2 from "N_2 const." and "N_2 chrom.", eventually joining together and flowing into the reaction chamber. The ALD release valves let small amounts of precursor into the relevant "N_2 const." flow stream at controlled intervals.

If there is a faulty ALD valve or a blockage the valve assembly on the stainless steel back plate may need to be removed from the oven box. In order to do this various tubes need to be disconnected, namely the connection of the tubes carrying N_2 from the MFCs to the assembly; the tubes carrying compressed air from bulkhead unions to ALD valves (disconnect both ends); the connections of the tubes carrying precursors from the bulkhead unions; the KF40 connection of the assembly to the reaction furnace tube. These connections are all circled in red in Figure N2.3. Once disconnected, the whole back plate can be removed by unscrewing it, shifting it slightly to the left and bringing it out right edge leading. Make sure to cover the ends of all disconnected tubes to prevent dust and contaminants entering during this process and be careful as the assembly is heavy (but still movable by a single person).

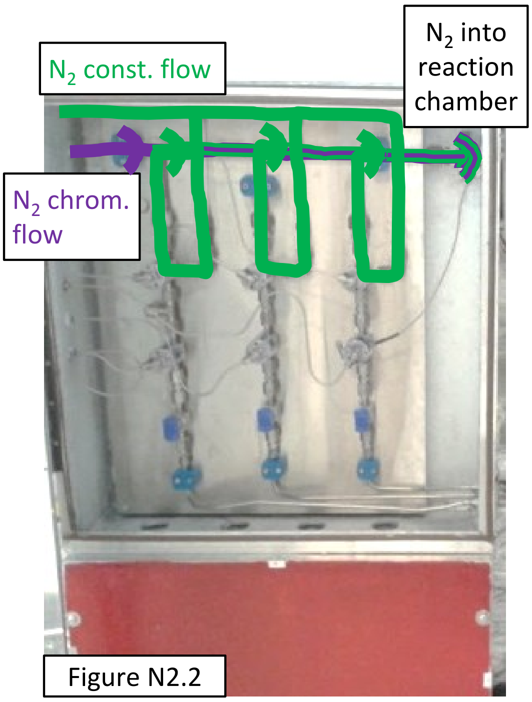

Figure N2.2

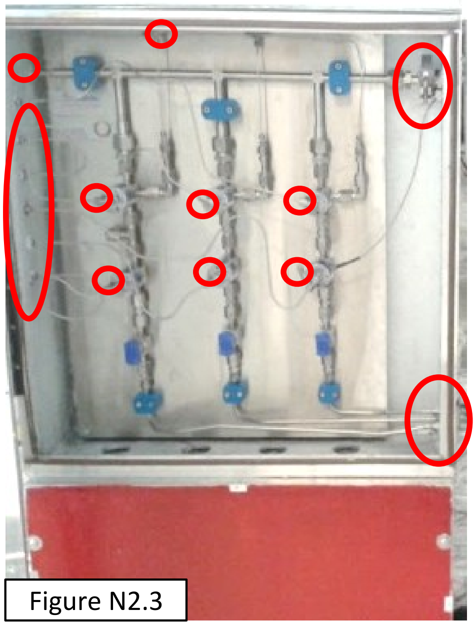

Figure N2.3

Component	Seller	Part ID
3 port, pneumatically controlled ALD diaphragm valve	Swagelok	6LVV-ALD3G333P-C
2 port, pneumatically controlled ALD diaphragm valve	Swagelok	6LVV-ALD3FR4-P-C
Manual diaphragm valve	Swagelok	6LVV-DPVFR4-P
Bulkhead unions	Swagelok	1/4": SS-400-61; 1/8": SS-200-61
NPT to Swagelok fittings for pneumatic connection to top of ALD valves. PTFE tape needed for fitting.	Swagelok	SS-200-2-2
KF40 cast aluminium clamp	Kurt J Lesker	QF40-150-C
Viton o-ring with centring ring for KF40 connection	Kurt J Lesker	QF40-150-SRV

N3: Reaction chamber and pressure monitoring system

The design of the reaction chamber the sample holders is described thoroughly in Chapter 4. To demonstrate how the chamber fits in the system Figure N3.1 shows the welded tube which forms the outer wall of the reaction chamber (shown in the photo before heating tape, insulation etc. is applied) and how it is connected to other components.

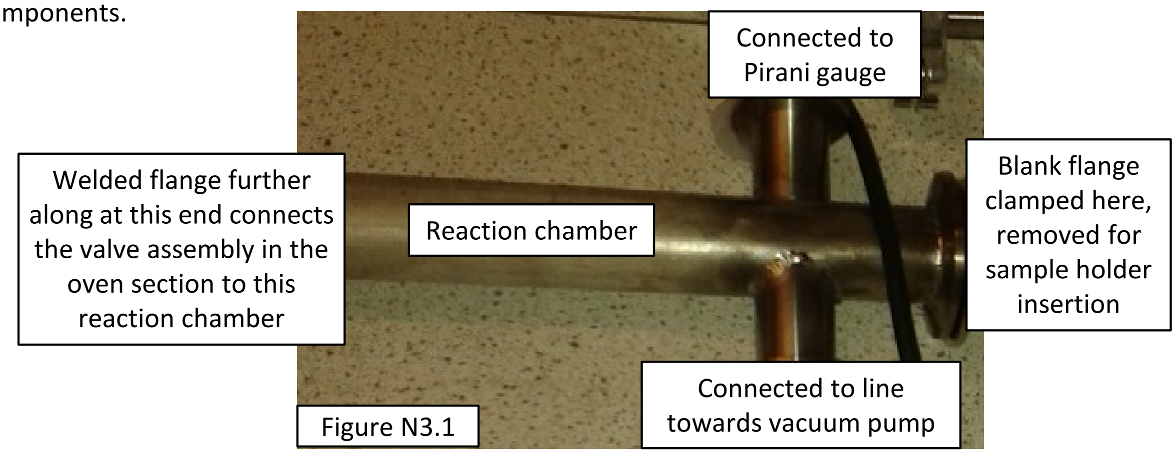

Figure N3.1

The pressure within the reaction chamber is monitored by a Pirani gauge (Figure N3.2) which consists of a heated filament from which the heat loss is monitored through electrical power. The thermal conductivity of the gas in the vacuum system is dependent on pressure. As described in Chapter 4 the heat loss of the filament also depends on the gas in the system, Figure N3.3 demonstrates this dependence for a selection of gases. Due to this dependence and the heating of the gas in the ALD system, the measured pressure during depositions is used only a guide and a method for detecting problems.

There are a number of options of how to monitor the pressure reading from the gauge in LabVIEW, the method chosen is to measure the output voltage (V) using a LabJack (Figure N3.4) and then to calculate the pressure in the program using the equation provided by the manufacturer: Pressure in mbar = $10^{(V-6)}$. A RJ45 8 way connector and cable connects to the gauge and is fed into an electrically insulated box (see Figure P1.1a,b) where wires are spliced and connected to relevant components: the supply positive and ground to the 24 V DC power supply; and the pressure measurement output signal and signal ground to ports AIN0 and GND of the LabJack respectively (Figure N3.4). There is a full wiring diagram in the manufacture's manual.

Figure N3.2

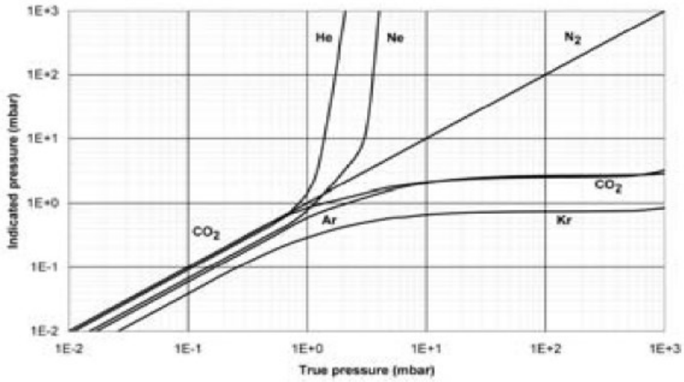

Figure N3.3 [from Edwards APG100 Active Pirani Gauge manual]

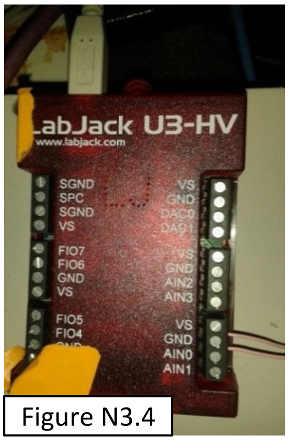

Figure N3.4

Component	Seller	Part ID
Active linear Pirani vacuum gauge with corrosion resistant filament, NW25 flange connector	Edwards	APG100-XLC
Cable	RS	
Labjack - USB data acquisition device	LabJack	U3-HV
Plasti-Grip butt splice - Connectors for cable wires to individual wires for signal distribution	RS	710-5323

N4: Line to pump system


Figure N4.1

The line to the pump consists of various components. There is a pneumatically controlled isolation valve (Figure N4.1) which can be used to hold precursor in the chamber for reactions were time is needed for precursor to diffuse within a structure. Several of the LabVIEW ALD programs have been designed to incorporate this hold step. The choice of program allows either a hold step with N_2 still flowing into the chamber and for this care must be taken to stop the pressure rising too high within the system. LabVIEW program 3 has a option for calculating the pressure rise after a set amount of hold time based on flows and the volume of the system. Alternatively both N_2 pneumatic valves can be closed during the hold step which avoids chamber pressure rising but also raises the risk of precursor condensation within the tubes inside the oven and there is a large pressure wave of N_2 when the N_2 valves are opened as gas will still flow through the MFCs. To improve on the design of the ALD a valve could be installed just before the reaction chamber so the chamber is isolated but at the same time the N_2 gas can flow through a bypass tube to the pump.

The pneumatically controlled isolation valve is normally closed however it would be preferable to have a normally open valve as that is the default state within the system. To avoid having the MAC solenoid valve switched on constantly for hours to open the valve (this was originally the case but it damaged the MAC valve), the tubes into the valve were reversed from the usual arrangement (described in section P2) so that when the MAC valve is off the pneumatic valve is pressurised and therefore open.

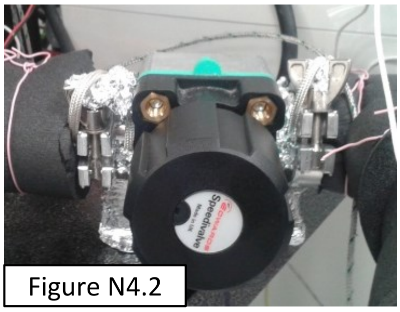
Figure N4.2

Next along the line to the pump is the manual isolation valve (Figure N4.2) which isolates the pump from the rest of the ALD system. This valve should be closed whenever the pump is switched on/off or the system vented. The manual valve can then be open slowly so that rapid pressure changes to the system are avoided, which would disturb substrates and could be damaging.

Flexible bellows pipe leads to the pump (see Figure N5.1), isolating the ALD system from vibrations from the pump. Too much bending of the pipe should be avoided to prevent leak creation. Just before the pump is also another manual valve at a T-junction which allows venting to atmosphere.

Component	Seller	Part ID
Pneumatic single acting cylinder, spring return pipeline valve, PV25PKA B	Edwards	C41311000
1" KF25 Speedivalve, SP25K, Fluoroelastomer Diaphram	Edwards	C33355000
KF 3/4" Speedivalve, SP16K, Nitrile Diaphragm	Edwards	C33205000
NW25 Flexible pipeline	Edwards	C10514287

N5: Trap and vacuum pump

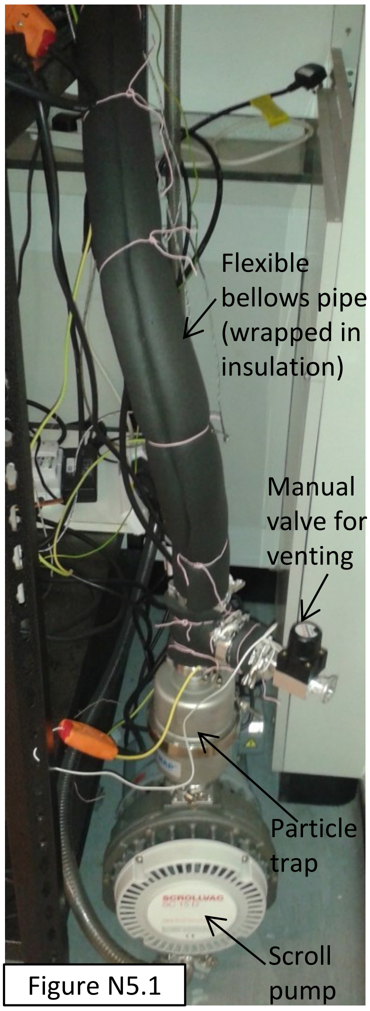

Figure N5.1

A particle trap is needed before the pump in ALD as some dust and particulates form when precursors react in the line to the pump which is at a lower temperature (65 °C) than the rest of the ALD system due to the sensitivity of the valves and the pump. The trap consists of an activated charcoal filter through which the system gas has to pass. The trap decreases the pumping rate due to the flow resistance it presents.

The choice of a scroll pump is described in Chapter 4. Generally for ALD the better the pumping capacity, the more effective and quicker the purging and other steps. This means the system could be improved by a larger pump but that is generally more expensive and recalibration of deposition should be carried out if switched. At the outlet of the pump reinforced PVC tubing leads to the ceiling extraction ports installed in the lab.

Component	Seller	Part ID
POSI-TRAP 4" Straight Thru Trap with NW 25 flanges with activated charcoal filter element	VACOM	MV-330025-AK
Replacement filter element	VACOM	MV-300945
Scroll pump	Oerlikon	SC15D
PVC Tubing with Embedded Spring	Kurt J Lesker	PT075

H1: Temperature controller system

The four temperature controllers for heating the oven, reaction chamber, end of chamber and line to pump are all wired similarly. Figure H1.1a shows the typical inside of the ABS box with the wiring diagram in Figure 1.1b. Cable glands are used around the wires entering and leaving the box to isolate and protect the electric components from any forces on the external cables. The three cord mains cable that enters the box is separated at the screw connector. Live and neutral are used to power the temperature controller and the relevant heater, with the heater live wire passing through the solid state relay (SSR). The SSR position is controlled by the temperature controller, which sends a logic signal of 0 v for open and 12 V for closed. A K-type thermocouple monitors the temperature at a representative location and the proportional–integral–derivative (PID) programing in the controller helps the system to reach a stable temperature through adjustment of the SSR close time lengths and frequencies. It was found that preheating before a deposition is best done using a heating program with a set ramp rate to try to gradually increase the temperature of the whole system, instead of heating rapidly up to the set point which causes fast, localised heating and the temperature controllers will tend to overshoot the set point due to the large thermal mass of the system. Table H1.1 shows the typical standby temperatures, ramp rates and deposition set point temperatures (and also states the earth point for the heaters). Keeping the system heated to a base level when not in use reduces heating time, purging time and thermal expansion stresses on the system.

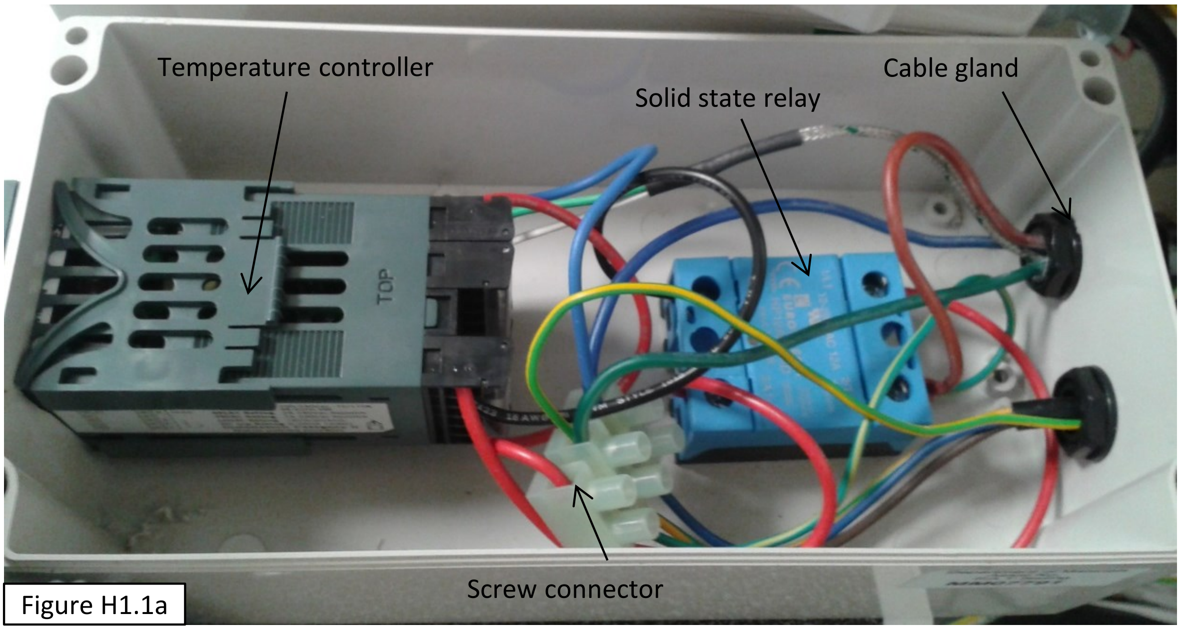

Figure H1.1a

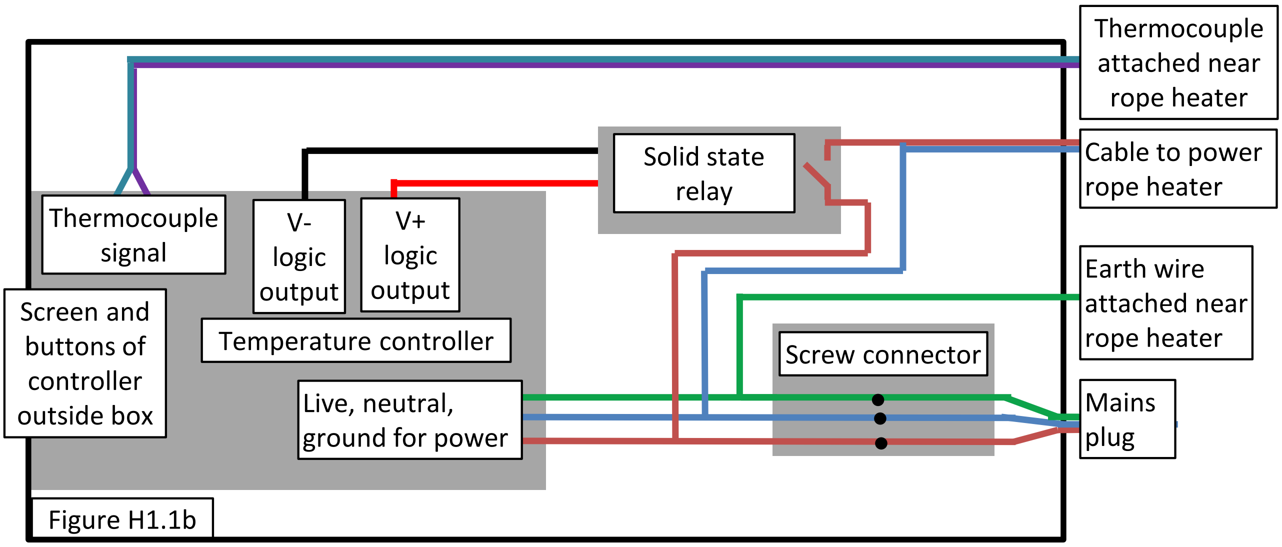

Figure H1.1b

H1: Temperature controller system cont.

Table H1.1

Temperature controller	Base temperature (°C)	Ramp rate (°C / min)	Deposition temperature (°C)	Earth point
Oven	65	0.6	95 / 100 / 100	Metal bracket to which the heating fin is screwed
Furnace	70	1.5	100 / 110-120 / 120-225	Metal frame, adjacent to where the furnace tube supporting arm is screwed and to the upright of the metal shelfing unit on which the laptop sits.
End of furnace	65	1.2	97 / 105 / 115	Clamped to the stainless steel flange attaching the pressure gauge to the furnace tube.
Line to pump	65	-	65	Clamped to the stainless steel T-shaped flange before the vacuum pump

The cable from the box to the heater is a three cord type, with only the live a neutral lines in use; earthing is done with a separate wire to allow flexibility of location. The power cable is connected to the temperature-resistant wire end of the rope heaters via a plug (heater side) and socket (mains side) shown in Figure H1.2. The wire ends of the rope heaters are too short to be directly wired to the ABS box.

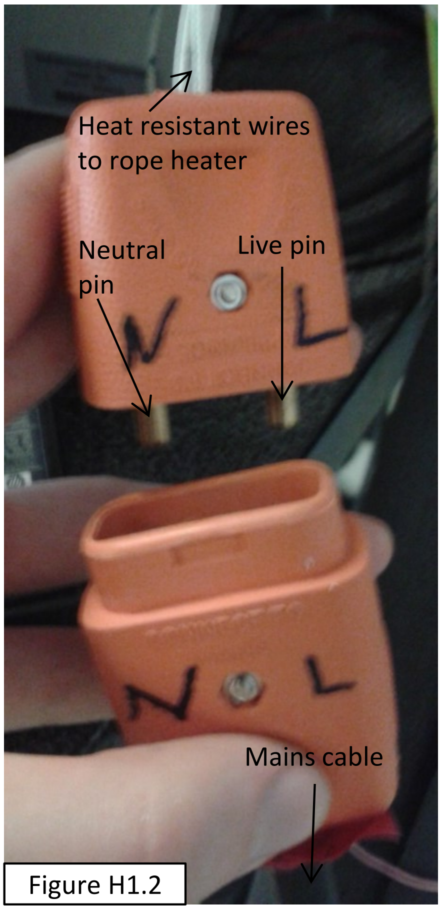

Figure H1.2

In the chamber heateer ABS box there is also an extra electrical circuit which was put in as the box was in a convenient location. This circuit contains the diode for the solenoid valve of the furnace hold valve (see section P2 for details).

Component	Seller	Part ID
RS -50 to +1100°C K Type Thermocouple 30-40mm	RS	621-2316
Temperature controller	Eurotherm	3216/CC/VH/LRXX/X/XXX/G/ENG/ENG/XXXXX/XXXXX/XXXXX/XXXXXX/K/3/J///////T
Solid state relay (25A/180V HOCKEY PUCK)	Eurotherm	HP25A/280/D
Orange 2 pin inline mains connector,10A 250V	RS	449-124
IP68 bellmouth cable gland	RS	458-3981

H2: Oven heating system

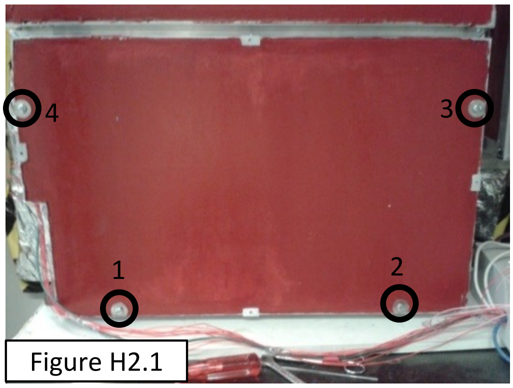

Figure H2.1

Access to the oven heater and fan is via the bottom compartment of the oven. The front cover can be removed by undoing screws labelled 1-4 in Figure H2.1. All the electrics must be switched off and unplugged before removing the cover as there is a risk of electric shock from the electrical connections inside.

Figure H2.2a shows the oven fan and two heaters; the corresponding wire diagram is shown in Figure H2.2b. All the components are compatible with temperatures above the 100 °C to which the oven is heated.

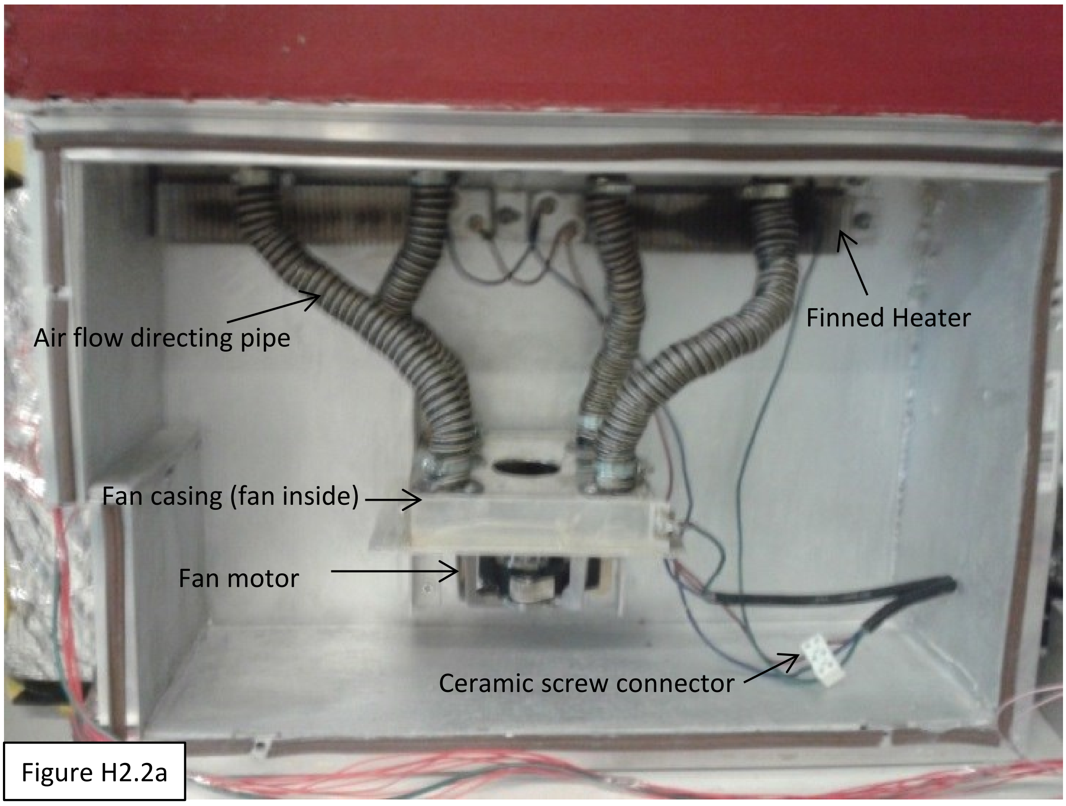

Figure H2.2a

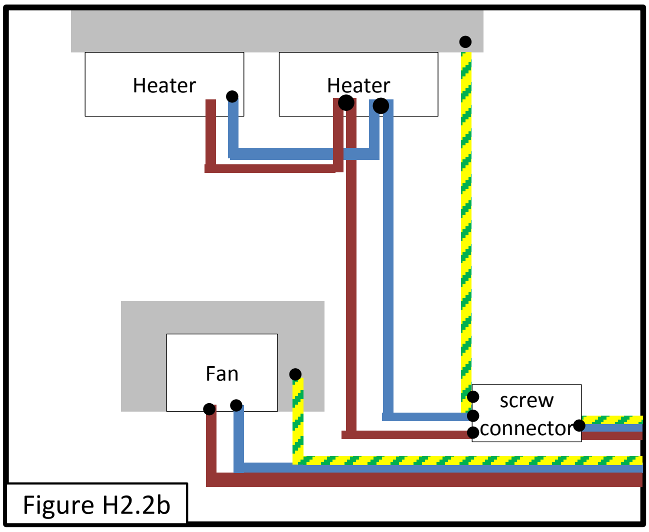

Figure H2.2b

H2: Oven heating system cont.

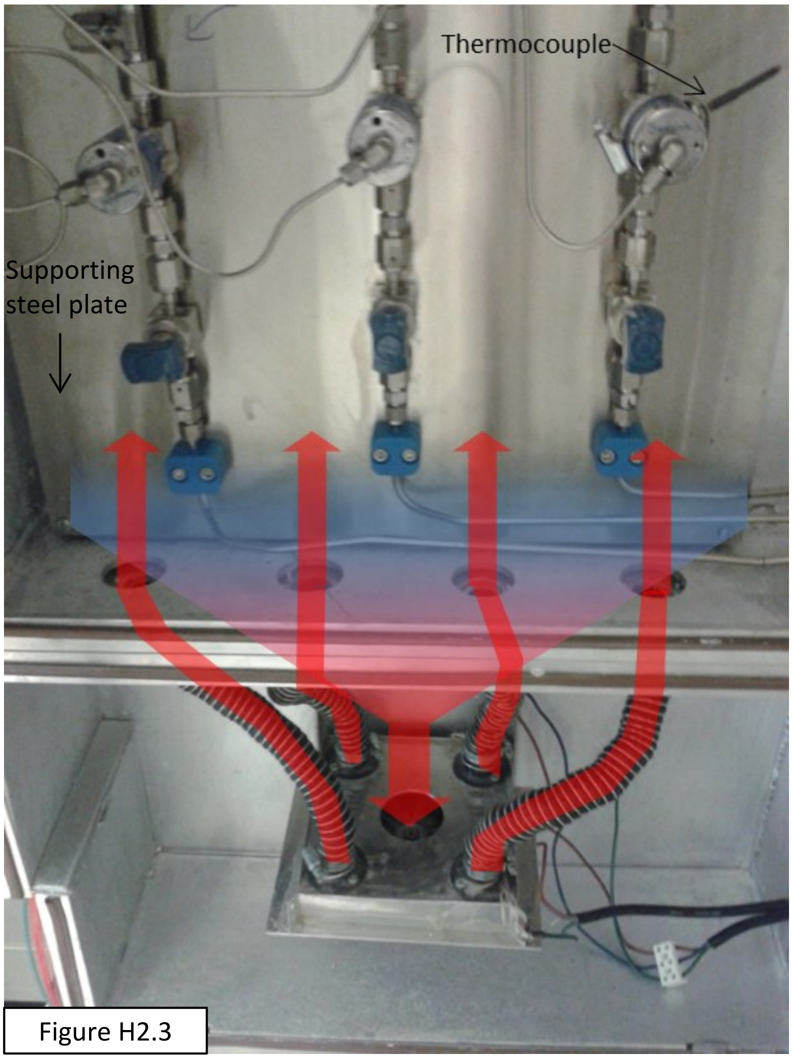

Figure H2.3

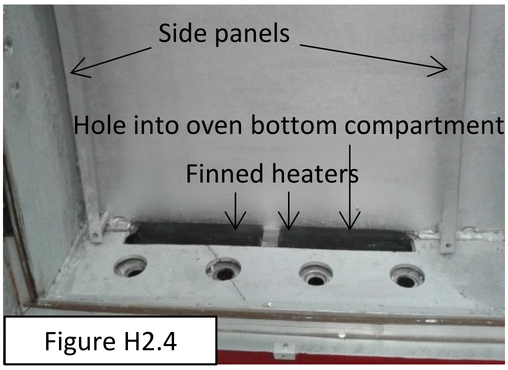

Figure H2.4

Figure H2.3 shows how the fan directs the air flow to ensure even heating of the vacuum system and valves inside the oven. The fan forces air up the four pipes at the corners of the fan casing. These pipes direct the hot air over the front of the supporting steel plate onto which the valves and vacuum tubes are secured. The air passes up to the top of the oven and then travels back down behind the supporting steel plate. This air will now be slightly cooler, especially during heat temperature ramping when the oven temperature has not equilibrated (air represented in blue in Figure H2.3). Through the hole behind the supporting plate (see Figure 2.4 for photo with supporting plate removed), this cool air will pass directly over the finned heaters, into the bottom compartment of the oven. The newly heated air will then enter the fan through the circular hole in the top of the casing to begin the circulation route again. The thermocouple monitoring the temperature to feedback to the finned heaters' temperature controller is in contact with a valve midway up the oven.

Component	Seller	Part ID
Fan for hot air circulation	EBM PAPST	R2K150-AC01-15
Ceramic insulated finned heater, 750W, 12"	RS	829-788
3 way ceramic terminal block	RS	703-3855

H3: Reaction chamber heating system

The reaction chamber is the part of the ALD heated to the highest temperature and has the strictest requirements on temperature uniformity. For this reason there are several more insulating layers surrounding the furnace tube than other areas of the ALD system, but these layers have been designed to be easily removable for access to the heating rope and thermocouples without needing to disassemble the vacuum system. The outer layer of insulation is a double layer of Masterboard with an air gap between the panels. Both front panels and the outer top and bottom panels can be removed together by the undoing of the screws indicated in Figures H3.1a, b. The panels can then just be slid out as shown in Figurer 3.1c leaving the side of the furnace box open for access.

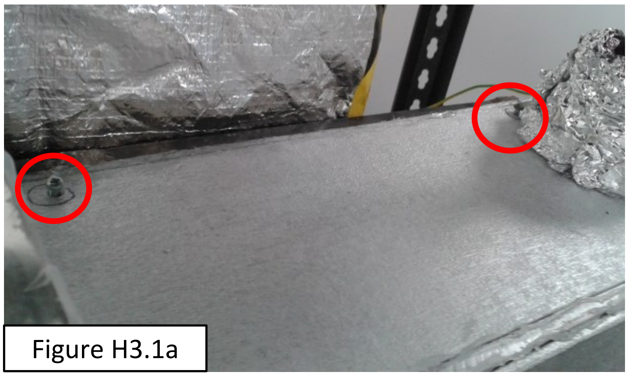

Figure H3.1a

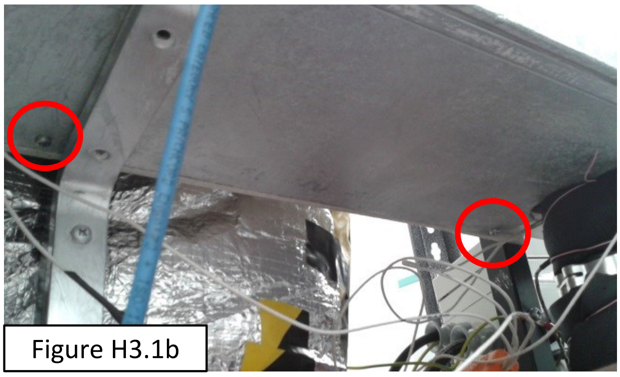

Figure H3.1b

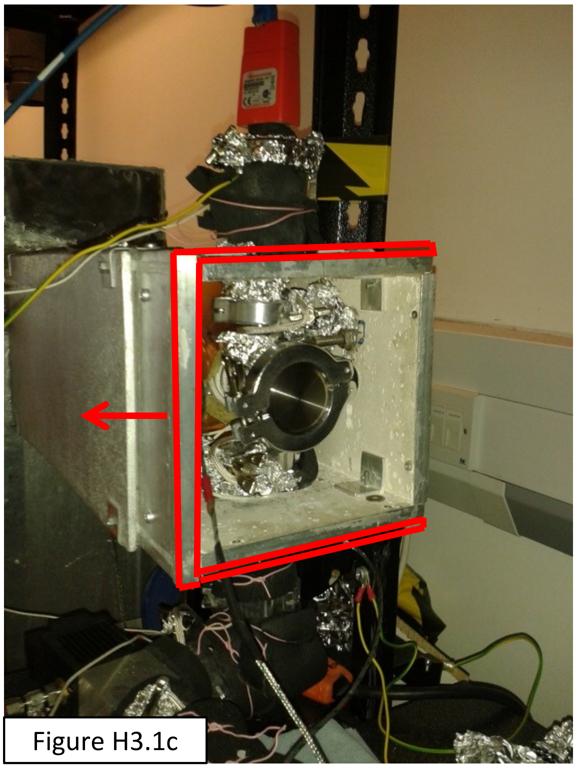

Figure H3.1c

Beneath the Masterboard, the reaction chamber tube is wrapped in two layers of Rockwool insulating wrap around a high temperature compatible Rockwool pipe. Underneath the insulation is the rope heater wrapped around a copper tube clamped to the reaction chamber tube wall for even heat distribution. The thermocouple is clamped to the tube adjacent to the end of the heated section. The Rockwool wrap is held tight around the chamber by wire and the end of the Rockwool insulation is covered by a metal sheet to protect it and contain the fibrous material.

Component	Seller	Part ID
Rope heater	Omega	FGR-100-240V
Inner Insulation - 20mm Wall 48mm Bore Rocklap H&V Pipe Section	Pipe Insulation and Lagging	-
Outer insulation - 25mm Thick Rockwool Ductwrap 1m Wide	Pipe Insulation and Lagging	-

H4: End of reaction chamber and line to pump heating systems

The heating of the end of the reaction chamber is done through rope heaters. Copper heat distribution sheets are clamped to the pipes and rope heaters are coiled around them. Aluminium foil and rubber insulation are wrapped around the vacuum pipes. The thermocouple for the "end of the reaction chamber" temperature controller is clamped to the pipe exiting the bottom of the reaction chamber box (Figure H4.1). The heater heats from the end of the reaction chamber, up to the pressure gauge and down to just before the pneumatic isolation valve. The "line to pump" heaters start from just before the pneumatic isolation valve and end at the particle trap.

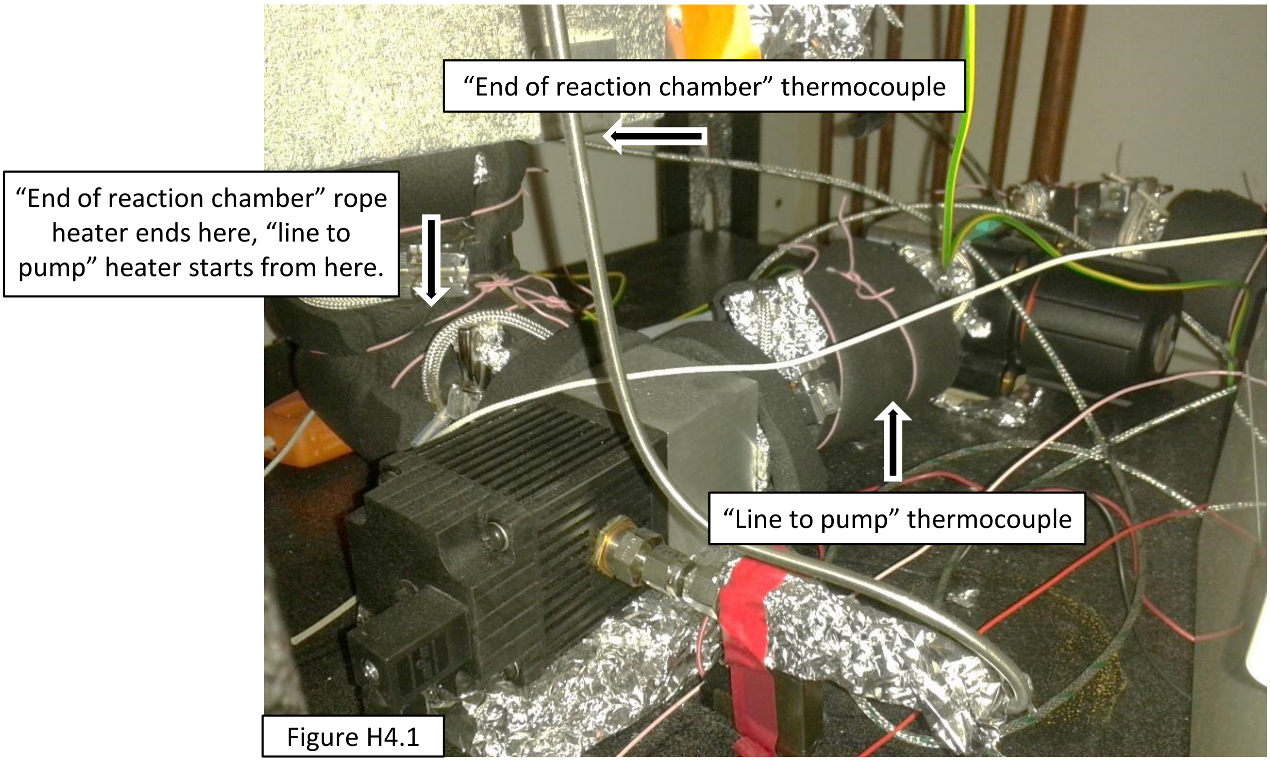

Figure H4.1

Component	Seller	Part ID
ZnPt MS worm-drive hose clip,25-35mm	RS	525-234
Black Nitrile Rubber Pipe Insulation, 48mm dia. x 13mm x 2m	RS	486-063
Copper Sheet, 300mm x 300mm x 0.35mm	RS	680-959

P1: Valve control relay boards

The pneumatic valves are controlled through a series of steps (see Figure A2.2), one step being USB controlled relays within the MAC solenoid valve circuits. The relays are wired to the normally open position so the solenoid MAC valves are normally off (consumes less power and safer in a power cut).

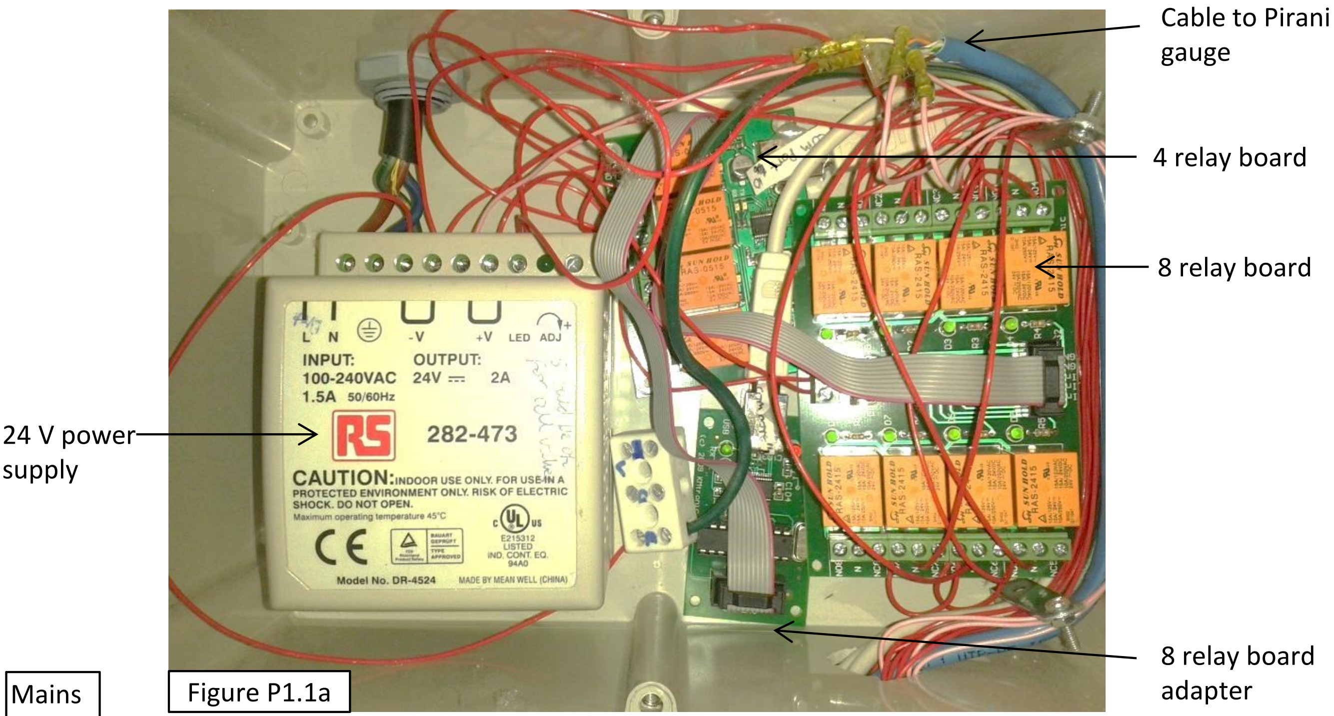

Figure P1.1a

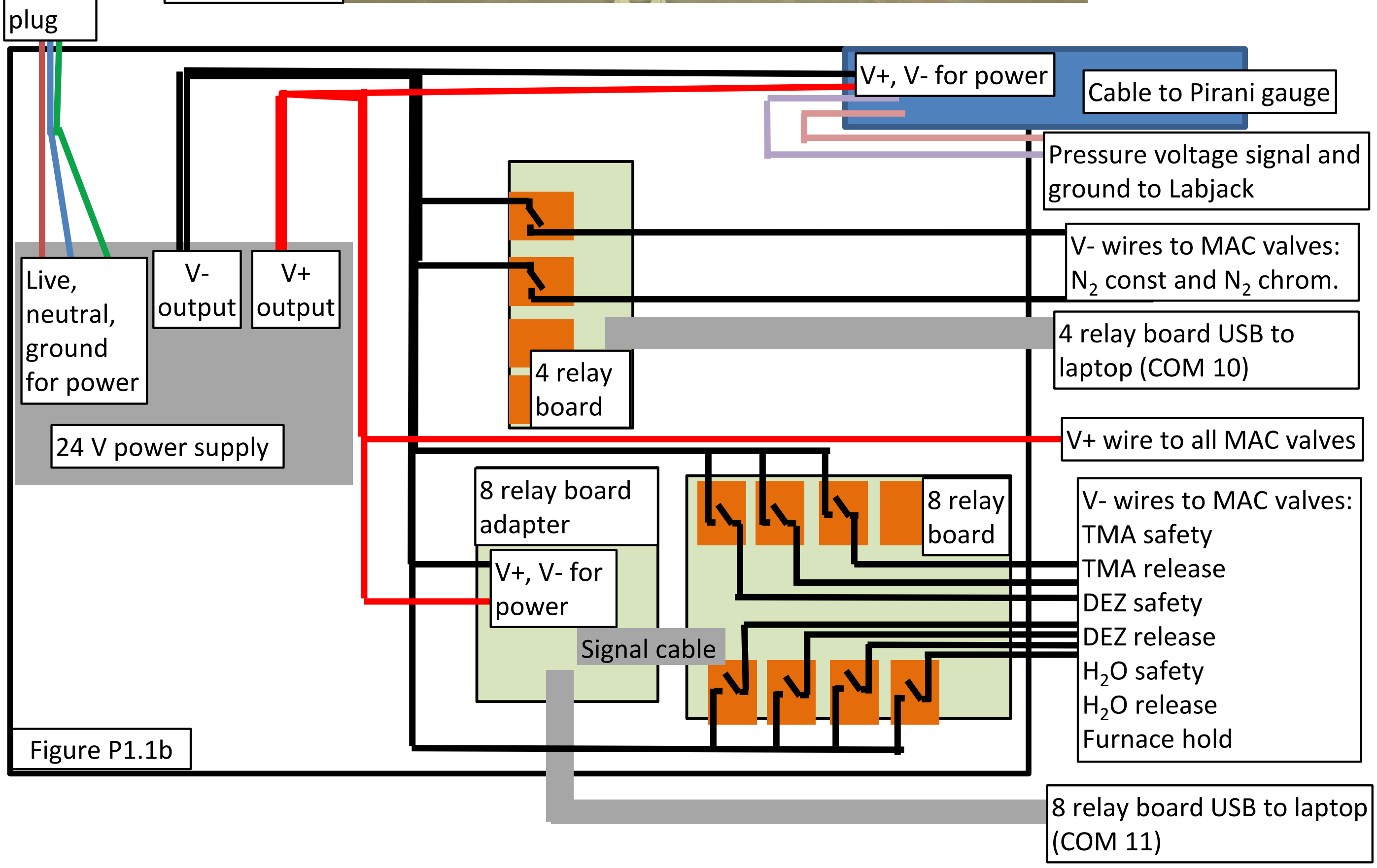

Figure P1.1b

Component	Seller	Part ID
USB Relay Controller Eight Channel - RS232 Serial controlled - 24V	KMtronic	SS_USB8REL24V
USB 4 Relay Board - RS232 Serial controlled, PCB	KMtronic	SS_USB4REL_PCB
RS POWER SUPPLY UNIT, DIN RAIL, 24V 2A	RS	282-473

P2: Valve control solenoid valves

The MAC solenoid valves have a recommended operation temperature of below 50 °C and so need to be kept separate from the heated sections of the ALD. The solenoid valves are outside the oven section with large separation to allow air circulation (Figure 2.1a), and a normal office standing fan to helps air flow around the ALD system. The tubes from the solenoid valves pass into the ALD oven section and connect to the ALD valves (Figure P2.1b).

The MAC solenoid valves have a red light to indicate when they are on (off in P2.2a, on in P2.2b). Check that the valves are in the correct state before each LabVIEW program is run. The circuit diagram for the MAC valves is shown in Figure P2.3 and contains diodes to suppress the back EMF from the solenoids which could damage circuitry. The diodes are arranged in an ABS box (Figure P2.4).

Figure P2.5 shows how the compressed air lines are connected to the MAC valve ports and the state when the solenoid is switched on and off. The centre diagram is the standard valve symbol and the diagrams at the side are the equivalent arrangements for those not familiar with valve diagrams. Aluminium foil covers on the valves help to protect the open ports from dust which may damage the valve. For the furnace isolation valve the lines into port 1 and 3 are swapped.

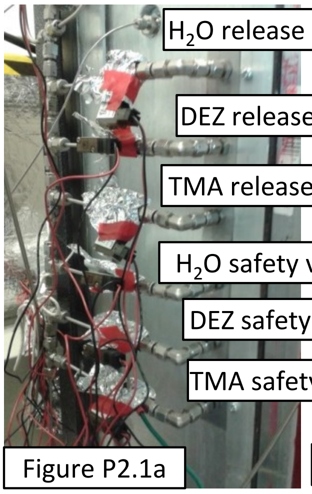

Figure P2.1a

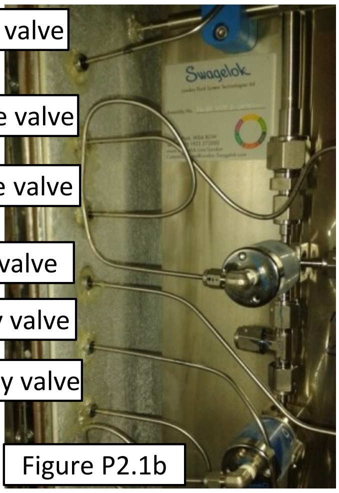

Figure P2.1b

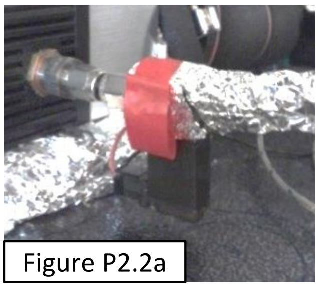

Figure P2.2a

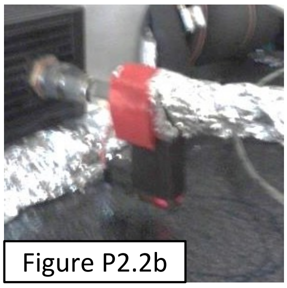

Figure P2.2b

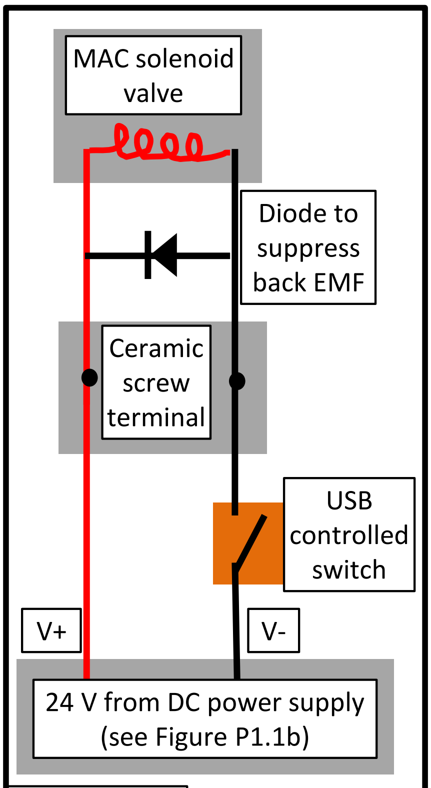

Figure P2.3

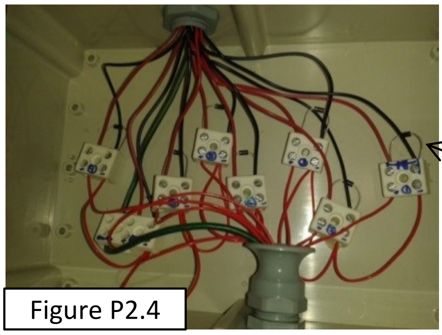

Figure P2.4

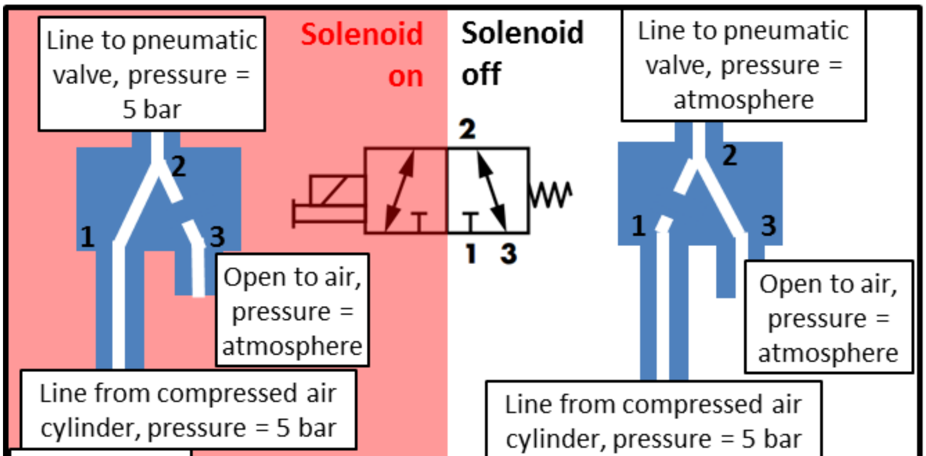

Figure P2.5

Component	Seller	Part ID
MAC solenoid valve	MAC	34C-AAA-GDFC-1KT
Diode 1A 1000V Standard Recovery Axial	RS	649-1143
Stainless Steel Swagelok Tube Fitting to #10-32 Male Thread for connecting tubes to MAC valves	Swagelok	SS-200-1-0157

V1: LabView program overview

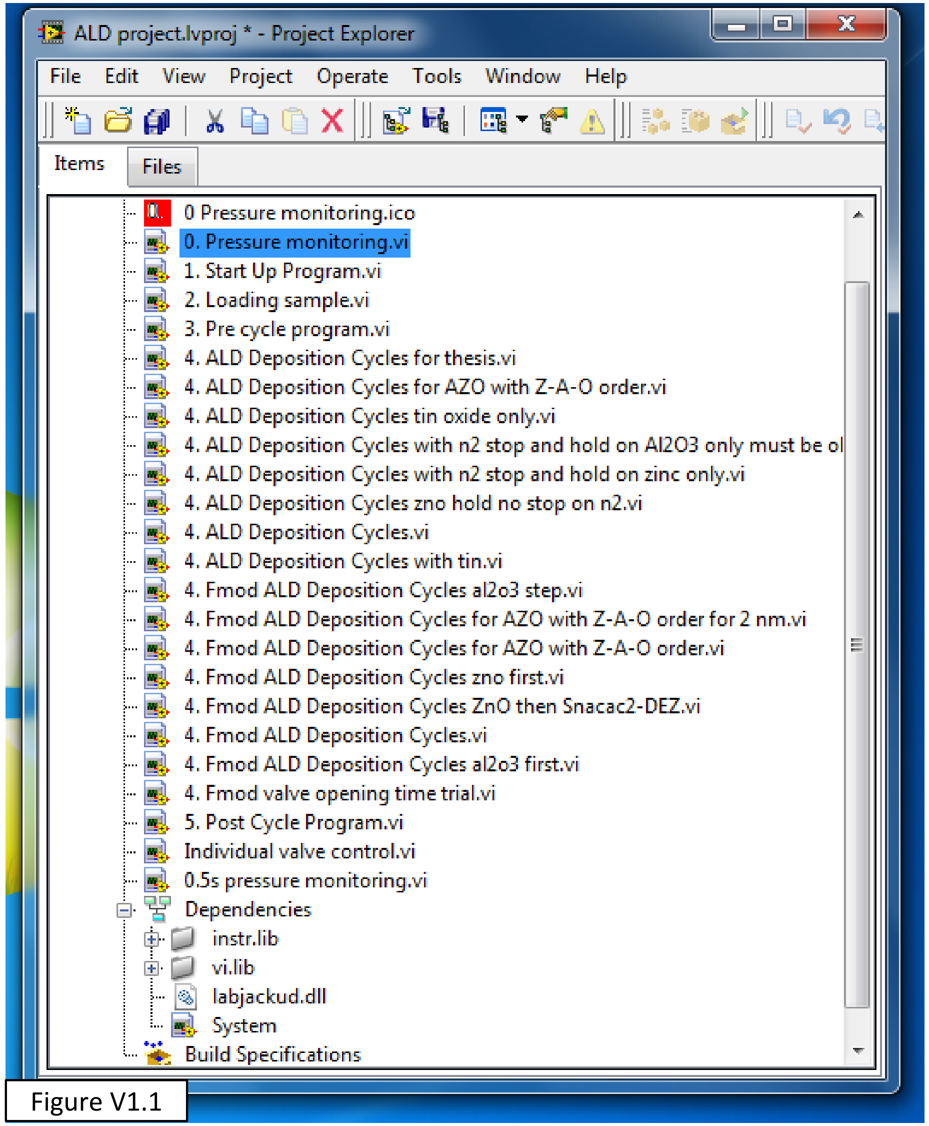

- 0 Pressure monitoring.ico
- 0. Pressure monitoring.vi
- 1. Start Up Program.vi
- 2. Loading sample.vi
- 3. Pre cycle program.vi
- 4. ALD Deposition Cycles for thesis.vi
- 4. ALD Deposition Cycles for AZO with Z-A-O order.vi
- 4. ALD Deposition Cycles tin oxide only.vi
- 4. ALD Deposition Cycles with n2 stop and hold on Al2O3 only must be ol
- 4. ALD Deposition Cycles with n2 stop and hold on zinc only.vi
- 4. ALD Deposition Cycles zno hold no stop on n2.vi
- 4. ALD Deposition Cycles.vi
- 4. ALD Deposition Cycles with tin.vi
- 4. Fmod ALD Deposition Cycles al2o3 step.vi
- 4. Fmod ALD Deposition Cycles for AZO with Z-A-O order for 2 nm.vi
- 4. Fmod ALD Deposition Cycles for AZO with Z-A-O order.vi
- 4. Fmod ALD Deposition Cycles zno first.vi
- 4. Fmod ALD Deposition Cycles ZnO then Snacac2-DEZ.vi
- 4. Fmod ALD Deposition Cycles.vi
- 4. Fmod ALD Deposition Cycles al2o3 first.vi
- 4. Fmod valve opening time trial.vi
- 5. Post Cycle Program.vi
- Individual valve control.vi
- 0.5s pressure monitoring.vi
- Dependencies
  - instr.lib
  - vi.lib
  - labjackud.dll
  - System
- Build Specifications

Figure V1.1

The ALD deposition LabVIEW project and the purpose of each program are described in Chapter 4. Figure V1.1 shows the project explorer page. There are the main 5 Vis (programs) to run in preparation for and after deposition and there are multiple ALD deposition cycle programs (program 4.), each adapted for a specific use. The old deposition programs were set up for a furnace isolation valve with MAC valve inlet/outlet tubes arranged so the isolation valve was normally closed. The new deposition programs lead with "Fmod" and are programmed for the new, improved arrangement of the tubes leading to the MAC solenoid valve so that the isolation valve is normally open (see Section P2). In addition to this program there is also an "individual valve control" control program, useful for troubleshooting and precursor loading.

In Sections V1-8 the parts of the ALD program are identified and described to help understanding and to allow easy modification. During programs messages will appear to the user with instructions and information on the program steps. These appear in message boxes (Figure V1.2), in this handbook the text in these messages is labelled on the program block diagram with blue boxes (Figure V1.2). The other important parts of the program are labelled in green boxes (Figure V1.3). In general when writing a new program, wiring the errors together in the program will help it proceed with the desired order of steps.

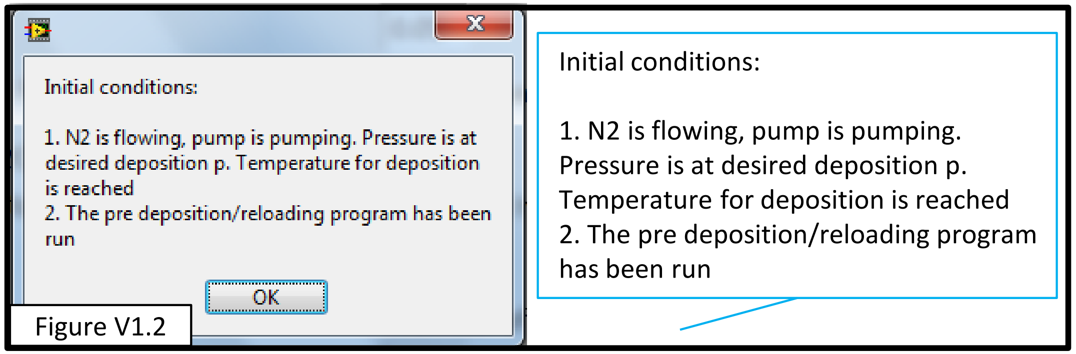

Initial conditions:

1. N2 is flowing, pump is pumping. Pressure is at desired deposition p. Temperature for deposition is reached
2. The pre deposition/reloading program has been run

Initial conditions:

1. N2 is flowing, pump is pumping.
Pressure is at desired deposition p.
Temperature for deposition is reached
2. The pre deposition/reloading program
has been run

Figure V1.2

The programs have wait times between messages and valve opening steps. This allows the user the opportunity to stop the program if an error has occurred as the program can not be stopped when a message box is on screen. It is possible to do the steps in programs 1, 2, 3 and 5 just by using the individual valve control program but this should only be done by very experienced users or if an error has occurred because if the wrong valves are opened simultaneously a fire or damaging reaction could occur.

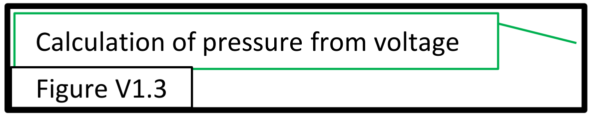

Figure V1.3

V2: LabView valve control

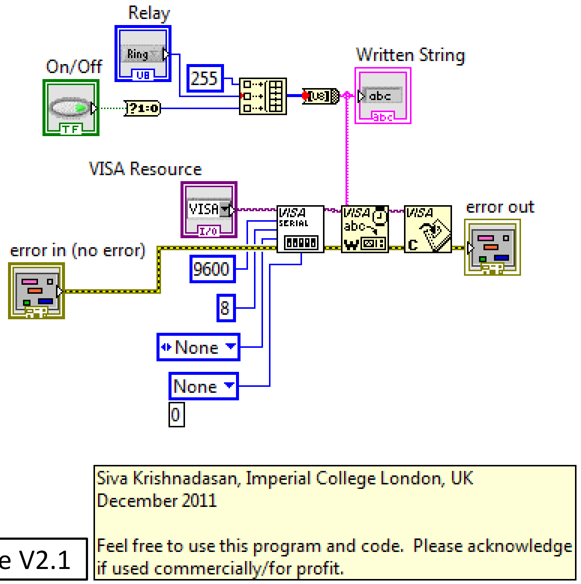

Siva Krishnadasan, Imperial College London, UK
December 2011

Feel free to use this program and code. Please acknowledge if used commercially/for profit.

Figure V2.1

All the programs in the ALD project have a "start deposition" button which needs to be pressed (turns green) before the program is run. There are other buttons and boxes for information which need to be selected/completed before pressing the run button, these are generally pointed out on the front panel. There are other buttons which become active only whilst the program is running e.g. emergency stop buttons. The block diagrams of each program can be accessed by pressing crtl+e when on the program front panel.

The opening of the pneumatic valves in the system is controlled through two relay boards controlled by LabVIEW via USB. The basis of the code is copied from the program in Figure V2.1. Just copying and using this program as a subVI to open and close valves, however, introduced a large time delay which prevented the ms precursor release times needed. The delay was due to having to open and close the VISA communication before and after each change in valve state. Therefore in the ALD programs the opening of the VISA communication is done only at the start of a valve opening sequence and closed after the whole sequence has finished. Also bare in mind that the N_2 valves are on a different relay board which needs a different serial port from the rest of the valves.

There are lots of other prewritten codes available online which are helpful when writing aspects of a new program e.g. the code for sending an email to the user was based from one online. The LabJack manufactures provide a library for data acquisition from their equipment along with example codes which was helpful when setting up the subprograms for pressure monitoring.

The temperature controllers are not controlled by the laptop and the MFCs are controlled by a program (Brooks smart interface) which is separate from the LabVIEW program. Instructions are given within the LabVIEW program on when to open Brooks smart interface program and how to set up the MFC flows. The VOR (valve override) needs to be set to off if a specific flow of N2 e.g. 30 sccm is needed, VOR can be set to closed to stop flow entirely and open to allow the fastest, uncontrolled flow through the MFC possible.

V3: Program - Individual valve control

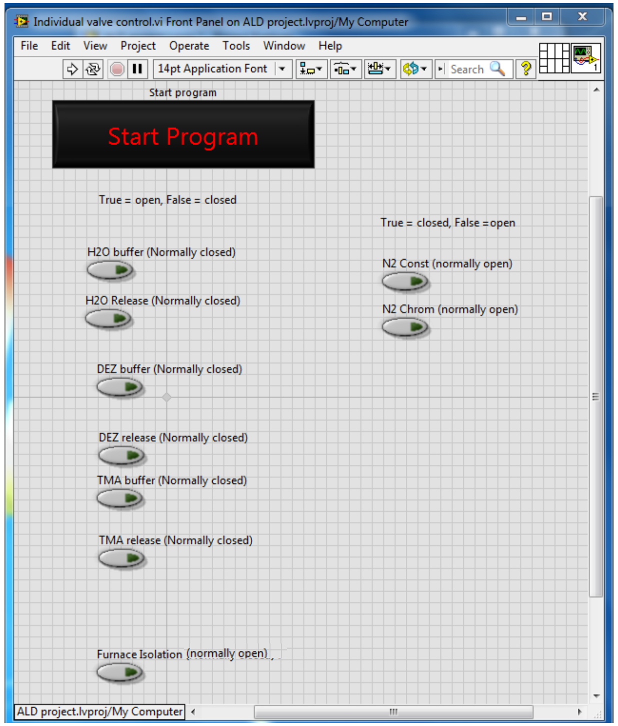

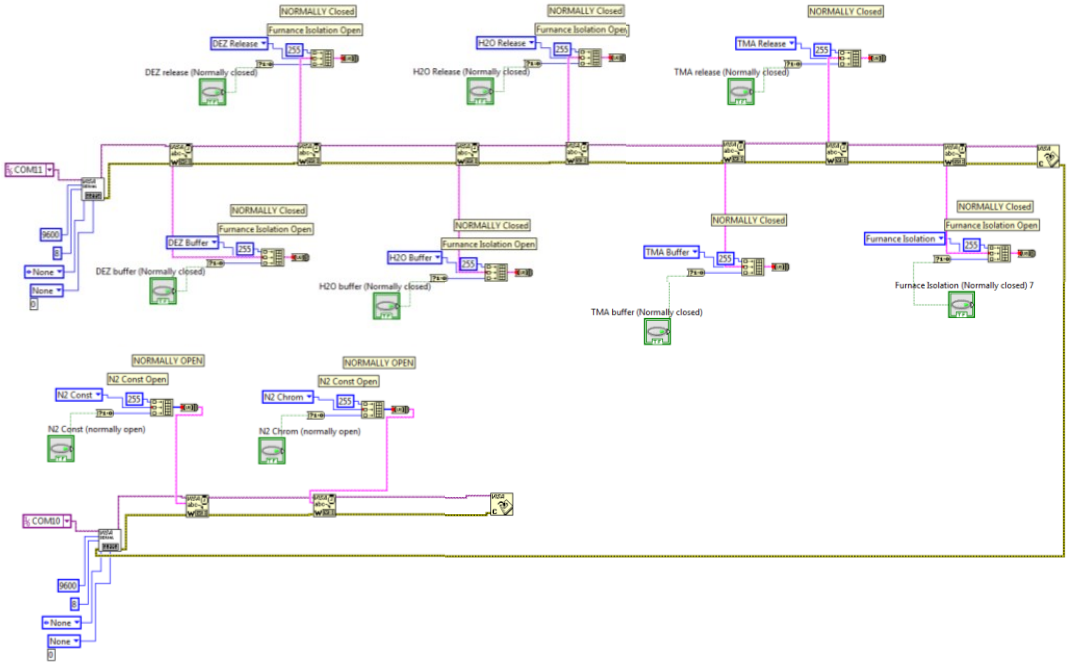

The individual valve control program consists of a series of on/off buttons which can be selected to operate the relevant valve. When the program is opened the buttons are all in the default off setting but this does not reflect the actual state of the MAC valves. There is no feedback on the valve states to the program, the program just sends commands to the relay switches. The state of the MAC valve can be known by looking to see if the red light is lit on the valve. This program should only be used by experienced operators as it could be very dangerous if the wrong valves e.g. precursor release valves are opened simultaneously.

V4: Program 0 - Pressure monitoring

The description of the purpose of this program and the other ALD programs is summarised in Chapter 4.

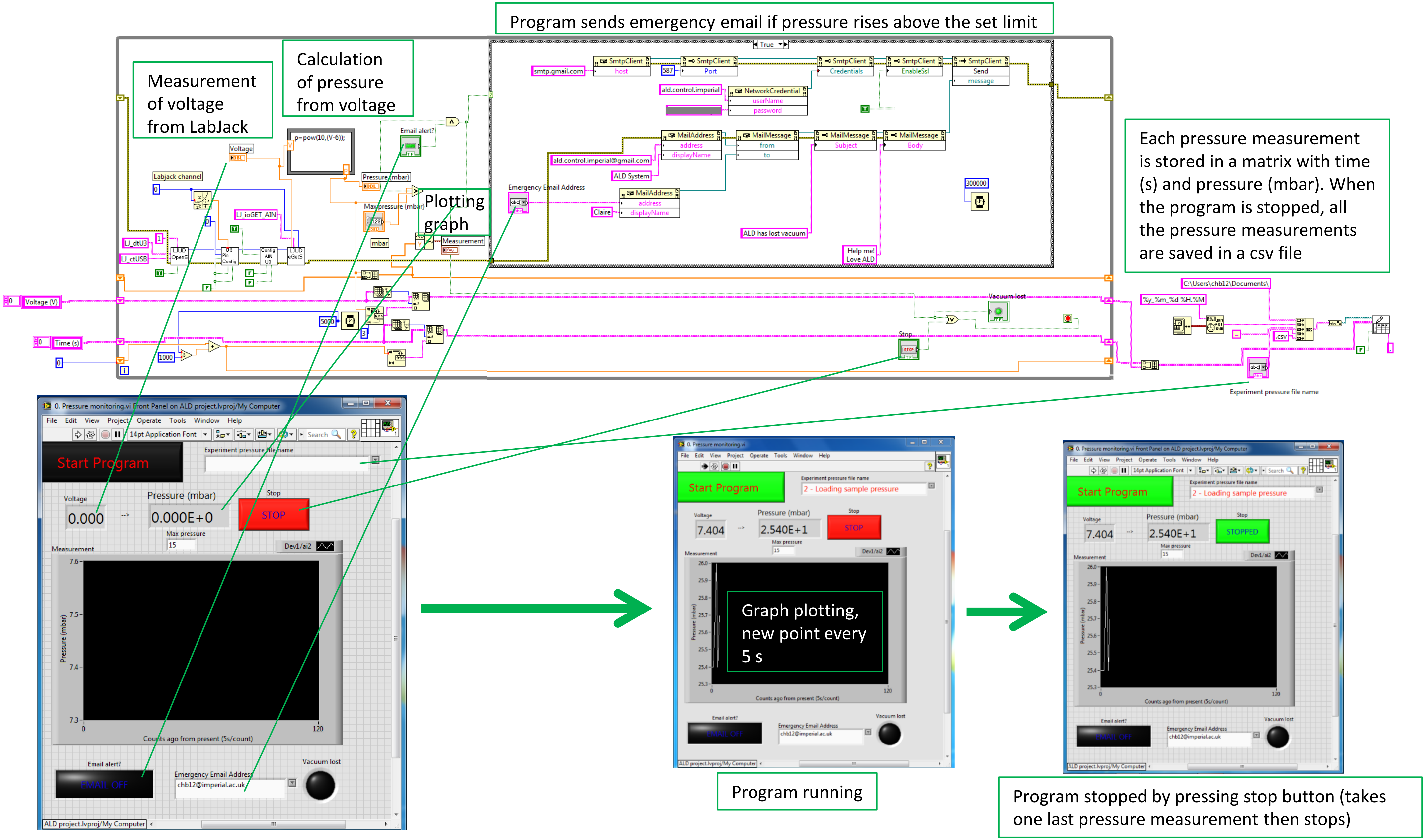

Program sends emergency email if pressure rises above the set limit

Measurement of voltage from LabJack

Calculation of pressure from voltage

Plotting graph

Each pressure measurement is stored in a matrix with time (s) and pressure (mbar). When the program is stopped, all the pressure measurements are saved in a csv file

Graph plotting, new point every 5 s

Program running

Program stopped by pressing stop button (takes one last pressure measurement then stops)

V5: Program 1 - Set up

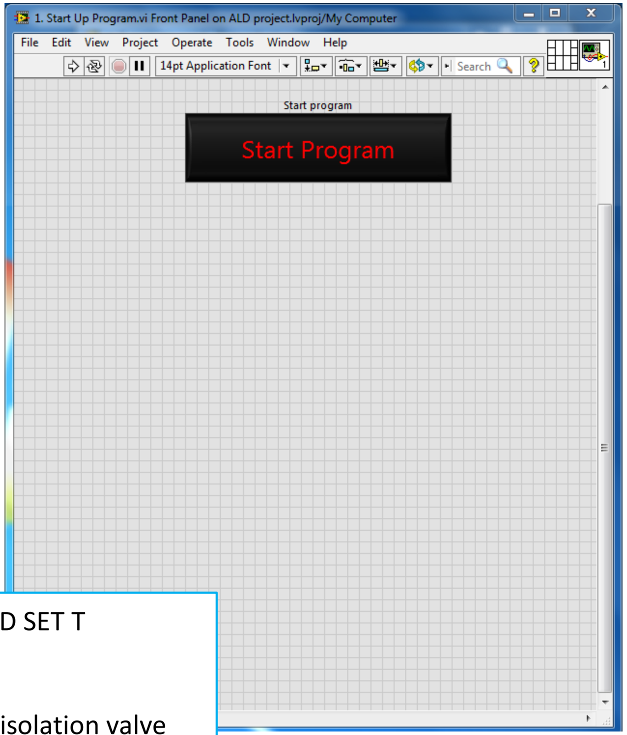

Initial conditions:

1. System has been left unused, unheated for a while
2. Check N2 pressure and that manual valves are closed
3. Check air pressure, should be = 0
4. Check all valves are off (red lights off)
5. Check manual furnace valves are closed
6. Check precursor valves are closed

PNUEM PRESSURISE AND N2 VALVES CLOSE

1. Slowly turn up air pressure to p=5
2. See if chamber is under vacuum
(3. Check manual furnace valve closed)

Next the N2 valves will close

START PUMPING CHAMBER AND SET T

1. Turn on vacuum pump
2. Slowly open manual furnace isolation valve
3. Watch pressure as it drops
4. Check manual oven valves are open
5. Set preliminary heater temperatures

PROGRAM FINISHED

Chamber is left being pumped and at a preliminary warm temperature.

Can turn pump off after a while if want to (close manual valve)

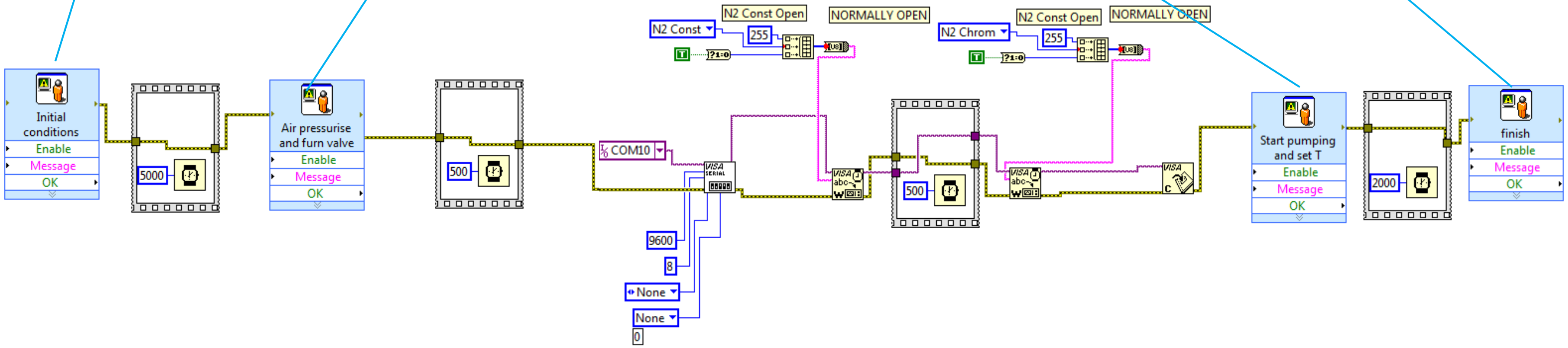

V6: Program 2- Sample loading

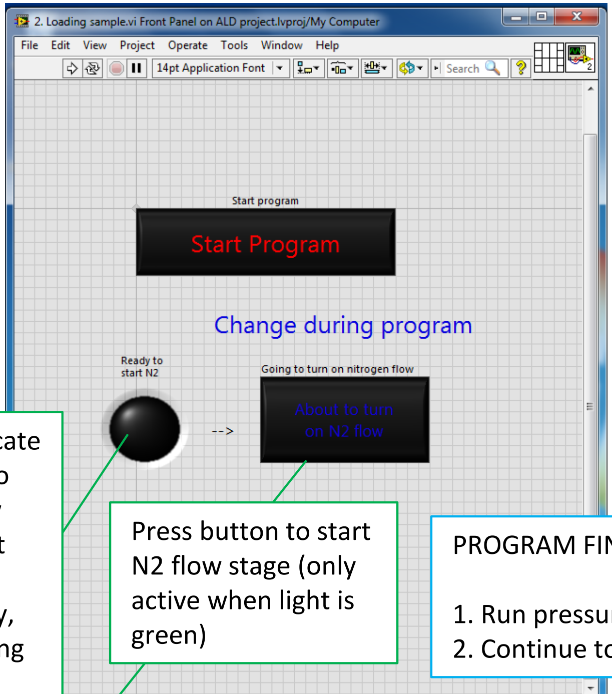

Initial conditions:
1. Chamber is being pumped and has been for a while, pressure is around 10^-2 mbar (if pump off, restart and slowly open manual furnace valve)
2. The chamber, oven and pump line are all partially heated
3. No N2 is flowing yet, manual valves are shut
4. The air and N2 pressures are ok.
5. The pneumatic N2 valves are closed (red lights on)
6. The precursor manual and pneumatic valves are shut

Lights up to indicate program ready to start the N2 flow stage (but do not have to start N2 flow immediately, wait until pumping down complete)

Press button to start N2 flow stage (only active when light is green)

PROGRAM FINISHED

1. Run pressure with alarm program when this is done
2. Continue to pre-cycle program when all heated and ready

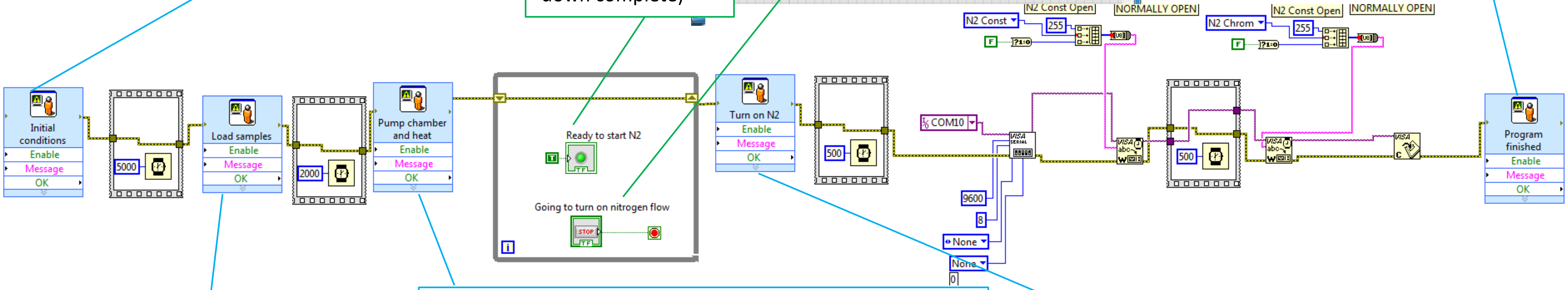

LOADING SAMPLES

1. Open manual N2 valves
2. Close manual furnace valve
3. Turn off pump
4. Vent chamber with manual valves
5. Load samples

PUMPING DOWN CHAMBER AND SETTING HEATERS

1. Close the chamber after samples are loaded.
2. Check the manual furnace and vent valves are closed, then turn on pump
3. Slowly open manual furnace valve
4. Set heaters to required temperature
5. Open isolation valves on precursors
6. When you want to use nitrogen push button

TURNING ON N2

1. Check manual N2 valves open
2. Open MFC program and start desired flow
3. Check pressures and vacuum when N2 starts flowing

V7: Program 3- Safety valve setup

Initial conditions:

1. N2 is flowing, pump is pumping. Pressure is at desired deposition p. Temperature for deposition is reached
2. This program opens precursor pneumatic safety valves and calculates purge settings

CALCULATIONS ABOUT TO RUN

press stop program to stop calculation

SELECTED SAFTEY PNEUMATIC VALVES ABOUT TO OPEN

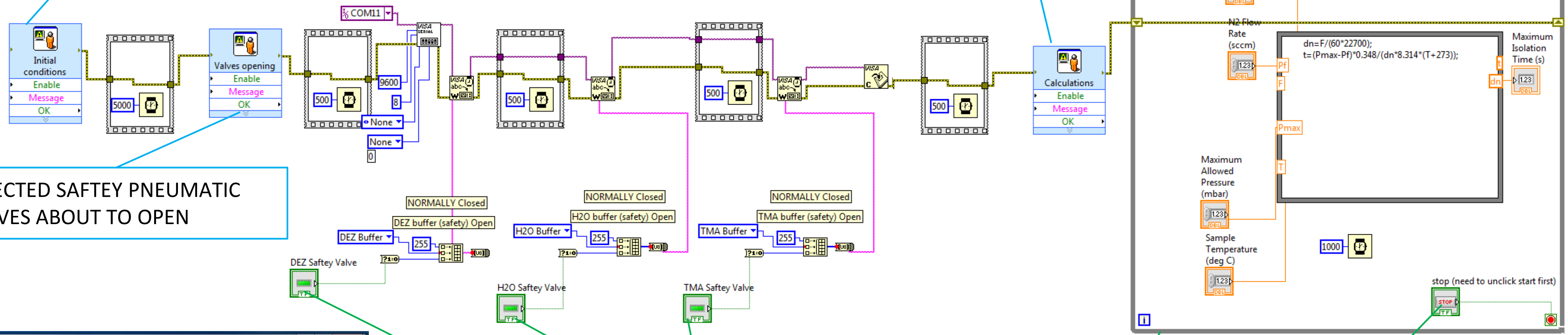

dn=F/(60*22700);
t=(Pmax-Pf)*0.348/(dn*8.314*(T+273));

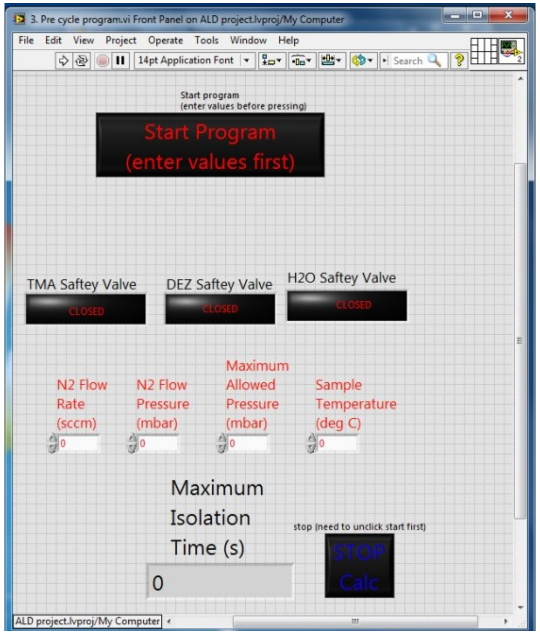

Typical button selection before running the program e.g. for Al doped ZnO deposition without a hold step

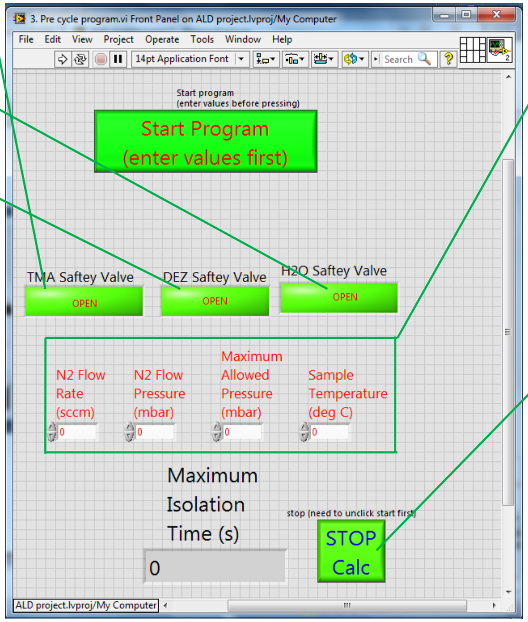

V8: Program 4- Deposition (1)

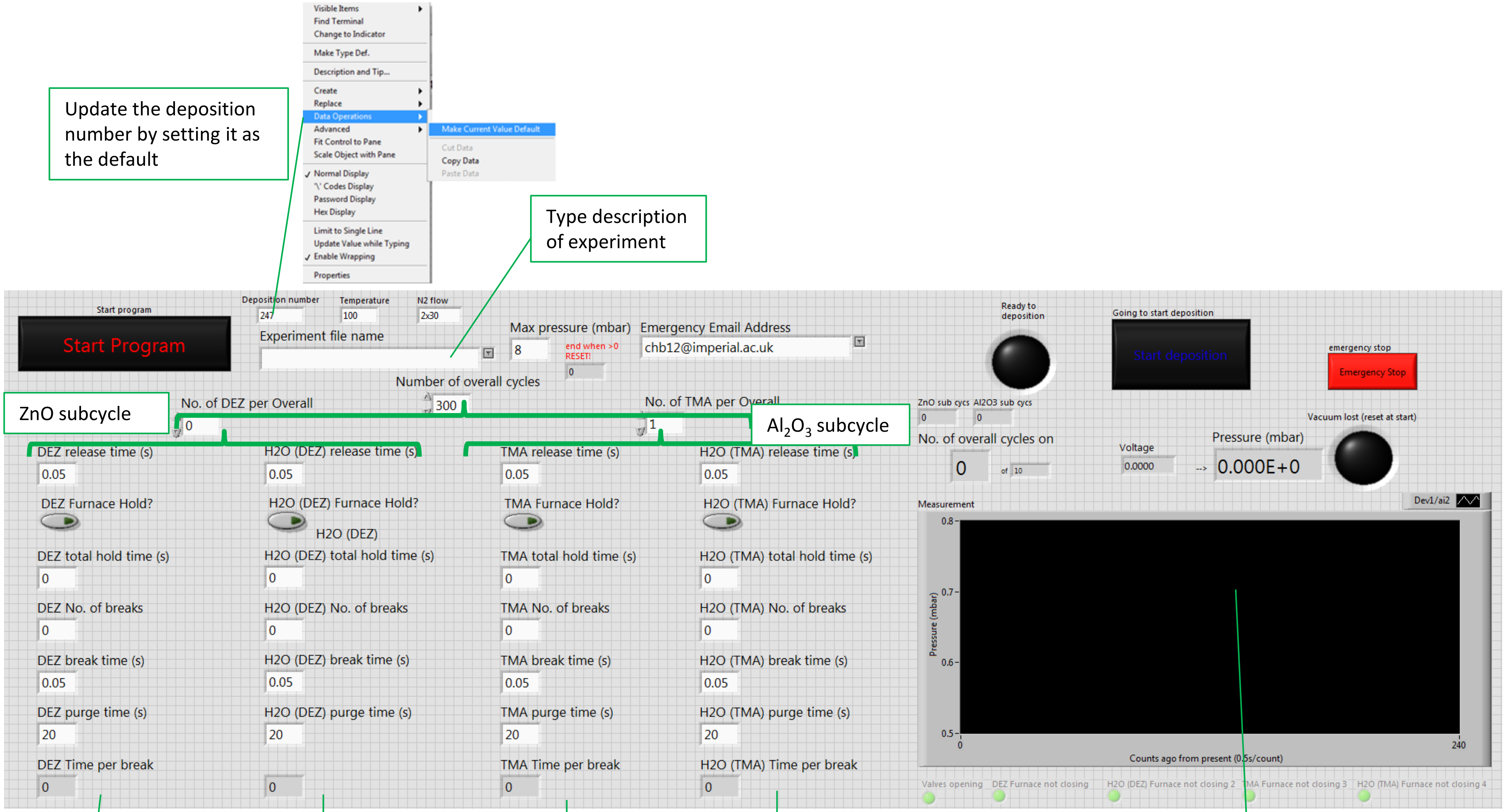

Update the deposition number by setting it as the default

Type description of experiment

ZnO subcycle

Al_2O_3 subcycle

Start program: Start Program

Deposition number: 247

Temperature: 100

N2 flow: 2x30

Experiment file name:

Max pressure (mbar): 8

end when >0 RESET!: 0

Emergency Email Address: chb12@imperial.ac.uk

Number of overall cycles: 300

No. of DEZ per Overall: 0

No. of TMA per Overall: 1

DEZ release time (s): 0.05

DEZ Furnace Hold?

DEZ total hold time (s): 0

DEZ No. of breaks: 0

DEZ break time (s): 0.05

DEZ purge time (s): 20

DEZ Time per break: 0

H2O (DEZ) release time (s): 0.05

H2O (DEZ) Furnace Hold?

H2O (DEZ)

H2O (DEZ) total hold time (s): 0

H2O (DEZ) No. of breaks: 0

H2O (DEZ) break time (s): 0.05

H2O (DEZ) purge time (s): 20

0

TMA release time (s): 0.05

TMA Furnace Hold?

TMA total hold time (s): 0

TMA No. of breaks: 0

TMA break time (s): 0.05

TMA purge time (s): 20

TMA Time per break: 0

H2O (TMA) release time (s): 0.05

H2O (TMA) Furnace Hold?

H2O (TMA) total hold time (s): 0

H2O (TMA) No. of breaks: 0

H2O (TMA) break time (s): 0.05

H2O (TMA) purge time (s): 20

H2O (TMA) Time per break: 0

ZnO sub cycs: 0

Al2O3 sub cycs: 0

No. of overall cycles on: 0 of 10

Voltage: 0.0000

Pressure (mbar): --> 0.000E+0

Diethyl zinc release conditions

H_2O release conditions

TMA release conditions

H_2O release conditions

Pressure monitoring graph showing the last 120 s, point plotted every 0.5s

V8: Program 4- Deposition (2)

This is the general layout of an ALD deposition cycle program, but the exact cycles are adapted to create new programs for specific cases. See Chapter 4 for more details.

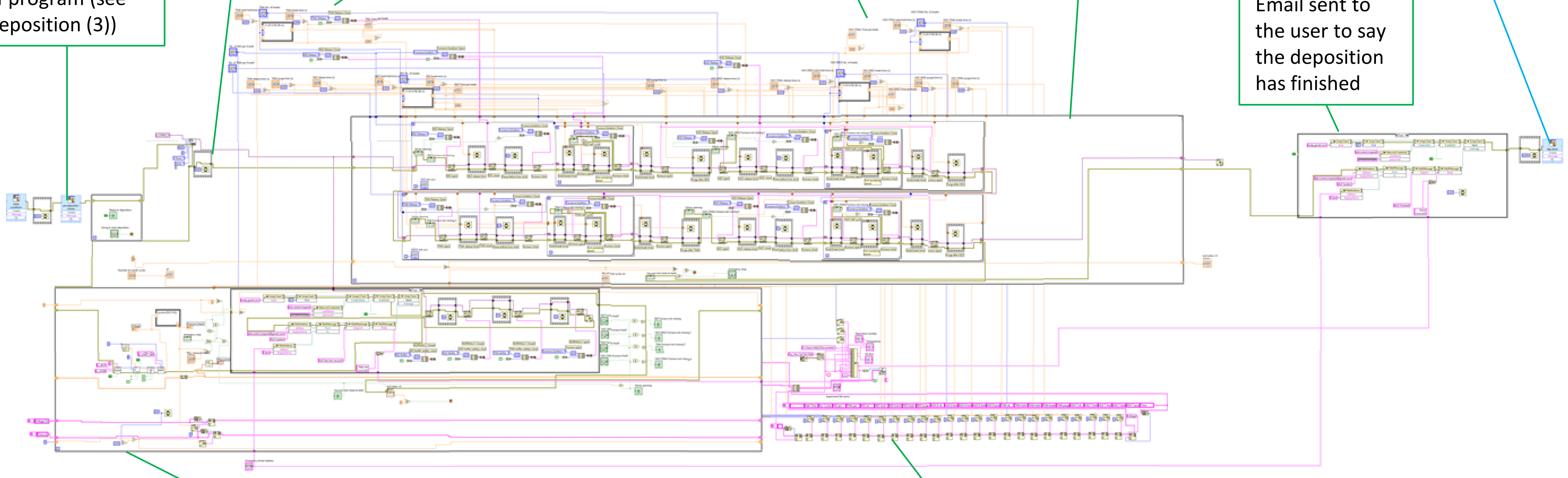

Starting sequence of program (see Deposition (3))

5 s of monitoring pressure before deposition cycles start

Deposition parameters e.g. release time, and the subVis for closing the release valves.

Deposition cycles, discussed in Chapte 4. The subVIs for opening the release valves are within the loop so if the deposition is emergency stopped then no release valves open

DEPOSITION IS DONE

Email sent to the user to say the deposition has finished

Similar to program 0. (Pressure Monitoring) with addition features explained in Deposition (4). Runs simultaneously with the deposition cycle loop and stops when deposition cycles end

Settings entered in the program saved to csv file along with pressure measurements (mbar) with time (s).

V8: Program 4- Deposition (3)

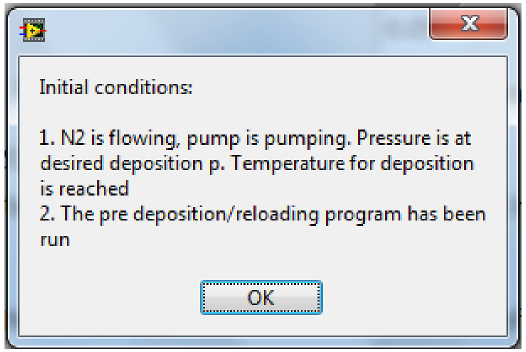

Initial conditions:

1. N2 is flowing, pump is pumping. Pressure is at desired deposition p. Temperature for deposition is reached
2. The pre deposition/reloading program has been run

Initial conditions:

1. N2 is flowing, pump is pumping. Pressure is at desired deposition p. Temperature for deposition is reached
2. The pre deposition/reloading program has been run

DEPOSITION IS READY TO START

1. Double check all the correct precursor and nitrogen manual valves are open
2. Close the pressure monitoring program if it is running
3. Double check all the parameters entered are correct
4. Click on "start deposition button" when ready

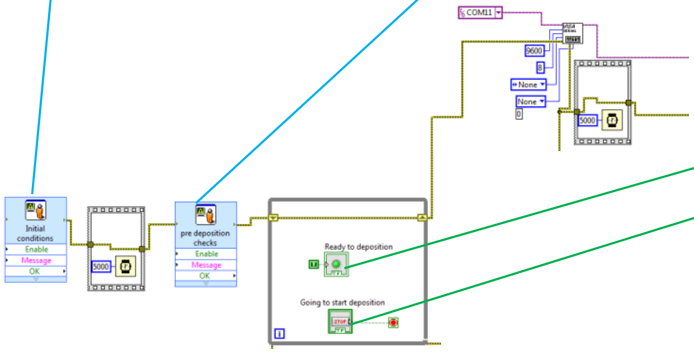

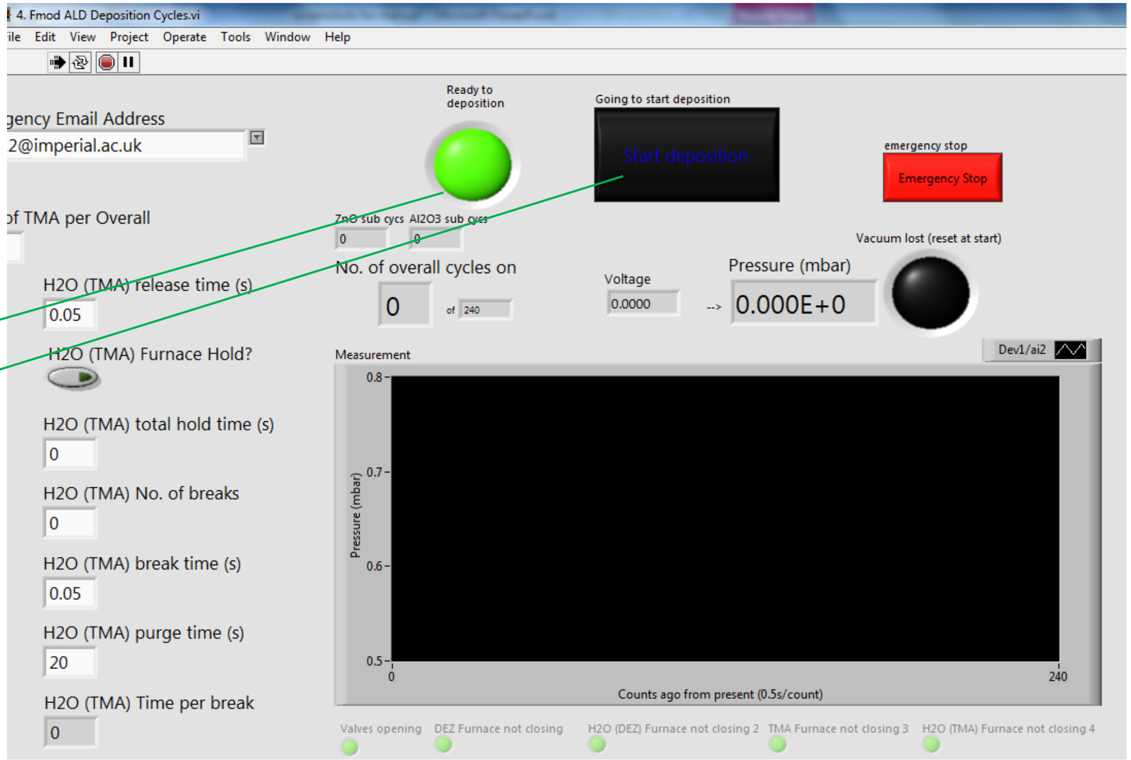

gency Email Address: 2@imperial.ac.uk

of TMA per Overall

Ready to deposition

Going to start deposition

emergency stop

ZnO sub cycs: 0

Al2O3 sub cycs: 0

No. of overall cycles on: 0 of 240

Voltage: 0.0000

Pressure (mbar): 0.000E+0

Vacuum lost (reset at start)

H2O (TMA) release time (s): 0.05

H2O (TMA) Furnace Hold?

H2O (TMA) total hold time (s): 0

H2O (TMA) No. of breaks: 0

H2O (TMA) break time (s): 0.05

H2O (TMA) purge time (s): 20

H2O (TMA) Time per break: 0

V8: Program 4- Deposition (4)

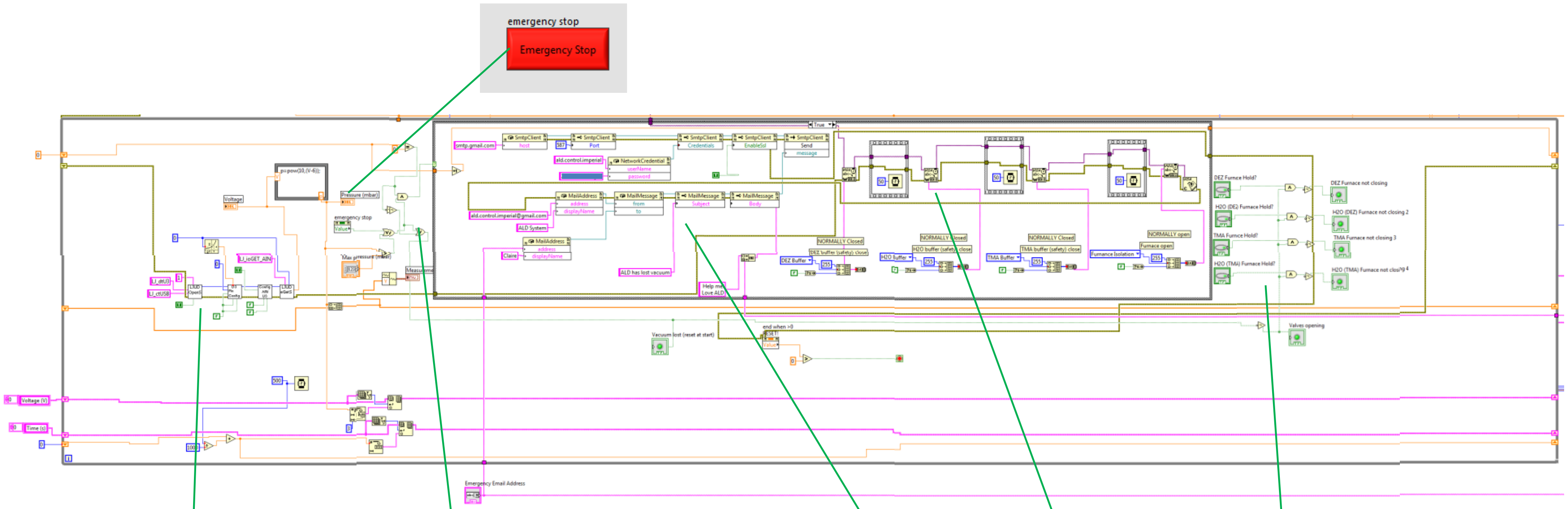

Measuring voltage signal from Pirani gauge, calculating pressure, plotting pressure graph, new point every 0.5 s. Same as the 0. pressure monitoring program

Conditions for emergency stopping the program mid deposition (pressure over set limit or emergency stop button pressed)

Email sent if deposition emergency stopped

Safety valves close when deposition emergency stopped

If emergency stopped these components tell release valves not to open

V9: Program 5- Unloading samples

Initial conditions:

1. Deposition finished. N2 is flowing, pump is pumping. Chamber is at temperature for deposition.
2. This program closes precursor pneumatic safety valves allows cooling and unloading, and returns system to idle state or next deposition

COOLING STAGE, N2 STILL RUNNING

1. Set the furnace (and other) temperatures to intermediate state and allow to cool
2. Press unloading button when cool enough for sample unloading.
3. Make sure "consecutive deposition" button selected if this is the case.

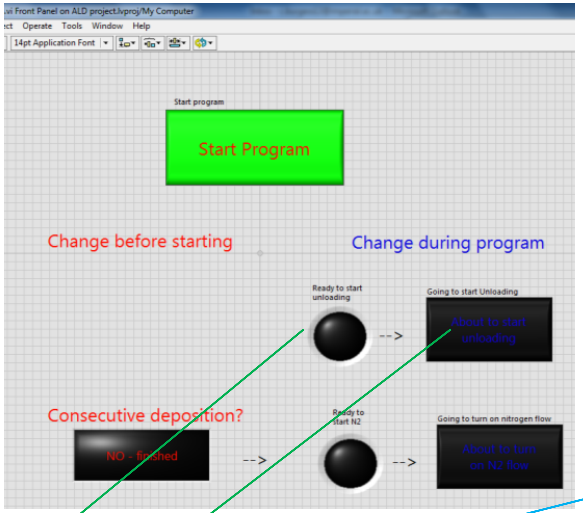

TURNING OFF N2

1. Open MFC program and stop flow
2. Next the N2 pneumatic valves will close

Check pressures and vacuum when N2 stops

SAFTEY PNEUMATIC VALVES ABOUT TO CLOSE

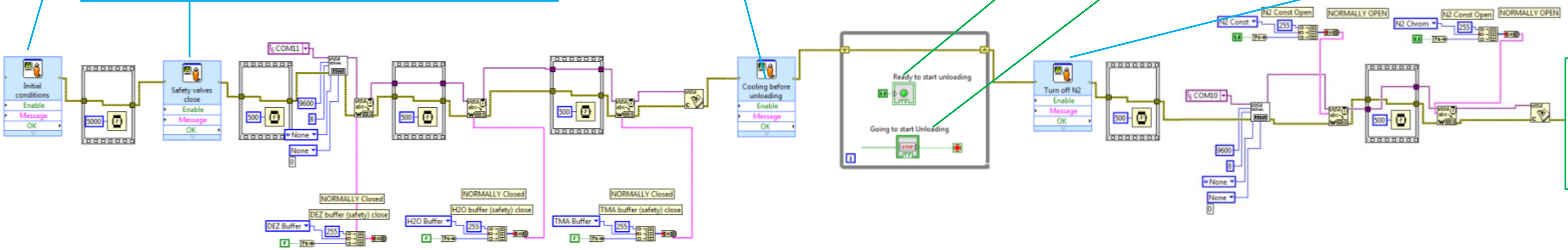

Leads to the true/false case structure below

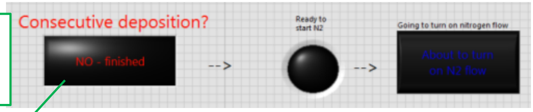

Consecutive deposition is not selected then shutdown sequence runs

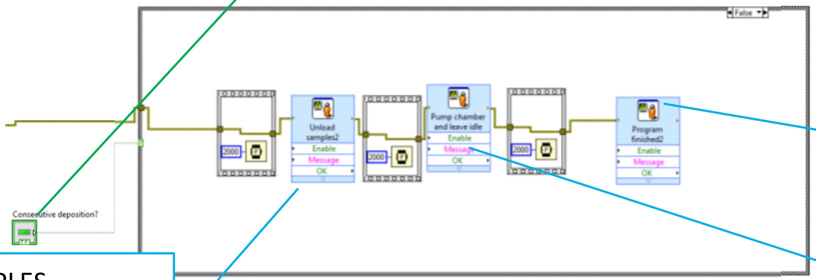

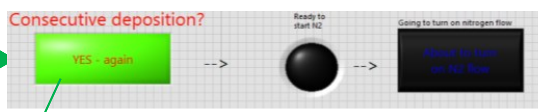

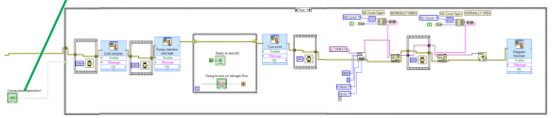

Consecutive deposition is selected (press button before starting program) then the program will run a final sequence identical to Program 2

PROGRAM FINISHED
System left at intermediate idle temperature and under vacuum

You can turn off vacuum pump after a while (remember to close manual furnace isolation valves)

JUST UNLOADING SAMPLES

1. Close manual furnace valve
2. Turn off pump
3. Vent chamber with manual valves
4. Unload samples

PUMPING DOWN CHAMBER

1. Close the chamber after samples unloaded
2. Check the manual furnace and vent valves are closed
3. Turn on pump and slowly open manual furnace valve
4. Check heaters are set to intermediate idle temperatures
5. Close isolation valves on precursors
6. Close N2 manual valves